MIT
International Center for
Air Transportation

Integrated Design of Solid Rocket Powered Vehicles Including Exhaust Plume Radiant Emission

Kelly J. Mathesius and R. John Hansman

This report is based on the Doctoral Dissertation of Kelly J. Mathesius submitted to the Department of Aeronautics and Astronautics in partial fulfillment of the requirements for the degree of Doctor of Philosophy at the Massachusetts Institute of Technology.

The work presented in this report was also conducted in collaboration with the members of the Doctoral Committee:
Prof. R. John Hansman (Chair)
Prof. Carmen Guerra-Garcia
Dr. Michael Knotts

Report No. ICAT-2023-01
May 2023

MIT International Center for Air Transportation (ICAT)
Department of Aeronautics & Astronautics
Massachusetts Institute of Technology
Cambridge, MA 02139 USA

Integrated Design of Solid Rocket Powered Vehicles Including Exhaust Plume Radiant Emission

by

Kelly J. Mathesius and R. John Hansman

Abstract

For aircraft and rockets where vehicle visibility is a concern, exhaust plume radiant emission is an important aspect of solid rocket powered vehicle performance. However, it is often not considered during the design phase, despite significant couplings with other vehicle disciplines, especially propulsion. Considering plume radiant emission during the design phase is important for ensuring vehicle design constraints and objectives can be met while accounting for the coupling of plume radiant emission with other disciplines.

Technology gaps exist for integrating exhaust plume radiant emission in solid rocket powered vehicle design. Typical modeling approaches are computationally expensive and rely on CFD and complicated integration schemes that are not well-suited for fast, iterative vehicle design. Existing data for solid rocket motor exhaust plume radiant emission is limited in the open-literature and does not include measurements for small, low-thrust motors or propellants containing the burn rate suppressant oxamide. Few design guidelines exist for the integrated consideration of exhaust plume radiant emission in solid rocket motor design.

This thesis provides advancements and solutions for these technology gaps to enable design phase consideration of exhaust plume radiant emission. The effects of chamber pressure and propellant oxamide content on exhaust plume infrared radiant emission were measured for small, low-thrust, end-burning solid rocket motors. Static fires utilized motors that were operated at approximately 1 MPa to 2 MPa with ammonium perchlorate composite propellants that were doped with 0 or 8 % oxamide. An end-to-end differentiable model for exhaust plume radiant emission was developed and implemented in the flexible AeroSandbox design optimization framework. The developed model shows reasonable agreement with measurements from this work and results from other studies, and it is robust over eight orders of magnitude of plume radiant intensity.

The model is used to explore the couplings between vehicle thrust, chamber pressure, oxamide content, and exhaust plume radiant intensity for a small ($<3\,\mathrm{kg}$), low-thrust ($5\,\mathrm{N}$ to $20\,\mathrm{N}$), fast ($>100\,\mathrm{m\,s^{-1}}$) solid rocket powered aircraft concept. For this class of vehicles, it was found that a large range of radiant intensities can be achieved for a given thrust requirement by varying the motor oxamide content and chamber pressure. Additionally, the effects of motor size on the progression of afterburning kinetics and plume radiant emission is explored and quantified; for

sufficiently small motors and plumes, it was found that the excess fuel in the plume remains largely unburnt, which reduces the plume radiant intensity.

The experimental data, practical modeling tools, and design guidelines developed in this thesis support the design phase consideration of exhaust plume radiant emission in solid rocket motor design. For vehicles where visibility is important, considering exhaust plume radiant emission during vehicle design enables a better understanding of motor design and performance tradeoffs and supports improved motor performance.

Contents

1 Introduction **11**

1.1 Motivation for integrating plume radiant emission in solid rocket powered vehicle design . . . 11

1.2 Overview . . . 12

1.2.1 Introduction to rocket exhaust plume radiant emission phenomenology . . . 12

1.2.2 Firefly: a small, fast aircraft concept . . . 14

1.2.3 Modeling and design optimization with AeroSandbox . . . 15

1.3 Technology gaps and thesis contributions . . . 16

1.4 Document structure . . . 18

2 Literature Review: Solid Rocket Propellants and Motors **19**

2.1 Solid rocket motor components and grain configuration . . . 20

2.1.1 Design of low-thrust motors for small, fast aircraft propulsion 22

2.2 Motor thrust, chamber pressure, and mass flow . . . 23

2.2.1 Mass flow . . . 24

2.2.2 Equilibrium chamber pressure and thrust . . . 24

2.3 Motor performance parameters . . . 25

2.3.1 Specific impulse . . . 25

2.3.2 Characteristic velocity . . . 26

2.3.3 Thrust coefficient . . . 26

2.4 Ammonium perchlorate composite propellants . . . 27

2.4.1 Composition . . . 27

2.4.2 Oxamide burn rate suppressant 28
2.4.3 Minimum burn pressure 30
2.5 Combustion modeling 31
2.6 Propellant characterization 31
2.7 Manufacturing and inspection 32

3 Literature Review: Radiation Processes 33
3.1 Origin of emission 34
3.2 Radiative transfer equation in participating media 36
3.2.1 Spectral radiant intensity 38
3.2.2 Total radiant intensity 38
3.2.3 Optical depth 38
3.2.4 Emissivity 39
3.3 Spectral line radiation for molecular gases 39
3.3.1 Natural broadening 41
3.3.2 Collision broadening 41
3.3.3 Doppler broadening 42
3.3.4 Voigt line profiles 42
3.4 Band modeling for molecular gases 42
3.4.1 Narrow band models 43
3.4.2 Wide band models 45
3.5 Radiative properties of particulate media 46
3.5.1 Overview 46
3.5.2 Radiative properties of a cloud of particles 47
3.5.3 Radiative properties of soot clouds 49

4 Literature Review: Typical Properties and Modeling Practices for Plume Radiant Emission 51
4.1 Representative radiant emission spectra for solid rocket motors 51
4.2 Typical practices in rocket exhaust plume radiant emission modeling . 53
4.2.1 Overview of exhaust plume radiant emission studies 53

4.2.2 Typical modeling approach 54
4.2.3 Typical modeling methods 55
4.3 General behavior and scaling laws for exhaust plume radiant emission 60
4.3.1 Scaling laws for motor thrust, mass flow rate, and size 60
4.3.2 Soot 62
4.3.3 Oxamide burn rate suppressant 63

5 Experimental Measurements for Small, Slow-burning Solid Rocket Motors 65

5.1 Experiment overview 66
5.2 Test motor design 67
5.3 Propellants 69
5.3.1 Propellant formula 69
5.3.2 Propellant combustion products 70
5.3.3 Propellant manufacturing 71
5.3.4 Propellant inspection 72
5.4 Test setup 74
5.5 Instrumentation and measurement procedures 74
5.5.1 Exhaust plume radiant emission 74
5.5.2 Thrust 82
5.5.3 Chamber pressure 83
5.5.4 Propellant burn rate 83
5.6 Experimental results 85
5.6.1 Radiant intensity and chamber pressure 86
5.6.2 Thrust 89
5.6.3 Burn rate 91
5.6.4 Minimum burn pressure 92
5.7 Alumina-silicate nozzle 93
5.7.1 Overview 94
5.7.2 Nozzle design and material 95

5.7.3 Thermal shock experiments 97
5.7.4 Nozzle manufacturing procedure 99
5.7.5 Nozzle testing 100
5.7.6 Nozzle thermal insulation performance 101
5.7.7 Nozzle cracking 106
5.8 Conclusions and recommendations regarding experimental measurements 107

6 Exhaust Plume Radiant Emission Model: Description and Implementation 111
6.1 Model overview 111
6.2 Implementation with AeroSandbox 114
6.2.1 Defining design problems 115
6.2.2 Model limitations 115
6.2.3 Surrogate modeling tools 116
6.3 Sub-model descriptions 117
6.3.1 Chamber thermodynamic equilibrium 117
6.3.2 Internal ballistics 119
6.3.3 Nozzle flow 120
6.3.4 Plume flow field 121
6.3.5 Afterburning kinetics 125
6.3.6 Radiative transfer 130

7 Exhaust Plume Radiant Emission Model: Results and Validation 139
7.1 Validation of sub-models 140
7.2 Comparison with measured data from this thesis 142
7.3 Comparison with data from Avital et al. 149
7.4 Comparison with modeled results from Alexeenko et al. 152
7.5 Recommendations for further model development 156

8 Integrated Design of Small, Low-Thrust Solid Rocket Motors Including Plume Radiant Emission 159

8.1 Effects of motor size scale on afterburning kinetics and radiant emission 160
8.1.1 Plume time scales . . . 160
8.1.2 Plume Damköhler number analysis . . . 162
8.1.3 Damköhler number scaling for frozen plumes . . . 164
8.1.4 Damköhler number scaling for equilibrium plumes . . . 165
8.1.5 Plume temperatures . . . 165
8.1.6 Radiant emission . . . 167
8.2 Effects of chamber pressure and oxamide content on radiant intensity for small solid rocket motors with fixed burn area . . . 169
8.2.1 Evaluation with developed model . . . 170
8.2.2 Comparison with first-order scaling law . . . 175
8.3 Small, low thrust motor design with integrated consideration of plume radiant emission . . . 177
8.4 Example: optimization of Firefly motor design . . . 180
8.4.1 Design problem setup . . . 180
8.4.2 Results . . . 182
8.5 Conclusions for integrated design of small, low-thrust solid rocket motors with plume radiant emission . . . 189

9 Conclusion 191

A Manufacturing of Propellant Insulator and Aft Insulator 195
A.1 Propellant insulator . . . 195
A.2 Aft insulator . . . 198

B Two-Piece Ceramic Nozzle with 3D Printed Cellular Ceramic Insulator 201

C Single Line Group Parameter Surrogate Models 205

D Validation of Developed Sub-models 211
D.1 Chamber thermodynamic equilibrium . . . 211

D.2 Flow field 214

E Scaling Law for Small Solid Rocket Motors with Fixed Burn Area 221

E.1 Derivation 222

Chapter 1

Introduction

1.1 Motivation for integrating plume radiant emission in solid rocket powered vehicle design

For applications where vehicle visibility is a concern, exhaust plume radiant emission is an important aspect of solid rocket powered vehicle performance. However, it is often not considered during the design phase or in conceptual design optimization studies, despite significant physical couplings with other vehicle disciplines, especially propulsion. Considering exhaust plume radiant emission during solid rocket powered vehicle design could lead to a better understanding of design tradeoffs and improved performance for vehicles where vehicle visibility, and therefore exhaust plume radiant emission, is important.

Technology gaps exist that prevent the integrated consideration of plume radiant emission during vehicle design. Typical modeling approaches are computationally expensive and rely on CFD and complicated integration schemes that are not well-suited for rapid design iteration or design optimization. Existing data for solid rocket motor exhaust plume radiant emission is limited in the open literature and does not include measurements for small, low-thrust motors or propellants containing the burn rate suppressant oxamide. Few tradespace analyses or design guidelines exist for

the integrated consideration of exhaust plume radiant emission in solid rocket motor design.

This thesis addresses these gaps to enable exhaust plume radiant emission to be practically considered during the design phase for solid rocket powered vehicles. This was achieved in this research through instrumented measurements of radiant emission for solid rocket motors, development of practical modeling tools, and analysis of the performance of solid rocket powered vehicles including plume radiant emission. A specific discussion of technology gaps, thesis work, scope, and contributions will be presented in greater detail in section 1.3. The next section provides an overview of exhaust plume radiant emission phenomena, as well as other topics that give context for the research in this thesis.

1.2 Overview

This section provides a brief overview of exhaust plume radiant emission phenomenology relevant to solid rocket motors. Additionally, a small, fast solid rocket powered aircraft concept and a flexible aircraft design optimization framework are introduced, both of which were utilized in the research in this thesis.

1.2.1 Introduction to rocket exhaust plume radiant emission phenomenology

A rocket exhaust plume is the formation of hot, high-velocity combustion products that exit the nozzle of a rocket. Depending on the propellants used, the combustion products may have only gaseous constituents, or may also include condensed particles. Rocket exhaust plumes are not uniform in structure, temperatures, velocities, or chemical composition.

A figure depicting the structure of a low-altitude exhaust plume is shown in Figure 1-1. At low altitudes, exhaust plumes consist of two distinct regions: an *inviscid core* near the central axis of the plume that is generally non-reacting; and

a *mixing layer* that entrains ambient air that may burn with exhaust fuel species in afterburning reactions depending on operating and ambient conditions [1, 2].

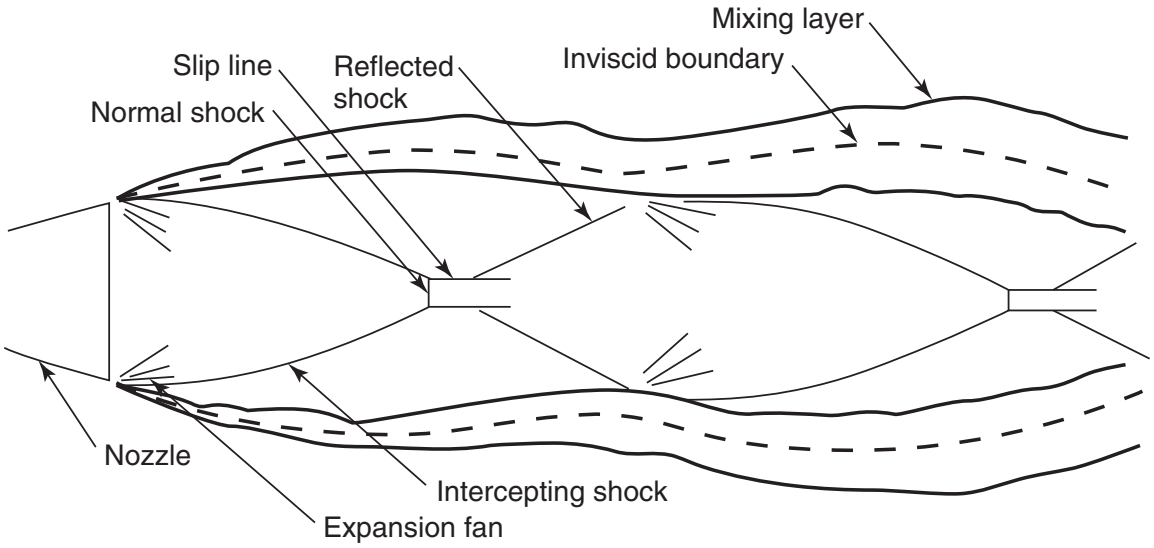

Figure 1-1: Low altitude exhaust plumes consist of an inviscid core and a mixing layer. Plumes entrain and mix with ambient air that may burn with fuel species in the exhaust. Reprinted from Ref. [1].

The hot gases and condensed particles (if present) in an exhaust plume radiate thermal energy, producing a characteristic plume spectral radiant emission "signature" for a particular propulsion system. Gaseous species in the exhaust plume – such as CO, CO_2, H_2O, and HCl – emit radiation within particular spectral bands; the strongest of these spectral bands emit in the infrared. Condensed phases – typically soot or alumina particles, if present – usually produce a continuous emission spectrum, which usually peaks in the infrared for typical temperatures prevailing in rocket exhaust plumes.

This thesis developed methods for considering this plume radiant emission during the design phase for solid rocket motors, and it also investigated the couplings between plume radiant emission and propulsion design and performance parameters. This involved understanding the relationships between the radiation processes that drive plume radiant emission, which is reviewed in chapter 3, and the motors and propellants that create the exhaust gases, discussed in chapter 2.

1.2.2 Firefly: a small, fast aircraft concept

The work for this thesis utilized many of the tools, hardware, and methods developed for Project Firefly, a technical effort to develop, demonstrate technical feasibility, and explore performance capabilities for small (<10 kg), fast (>100 m s^{-1}) aircraft. The Firefly vehicle is a demonstrator vehicle for small, fast aircraft explored as part of this development effort. The notional goals of the vehicle mission are to maximize vehicle range and endurance. It is powered by a small, low-thrust, end-burning solid rocket motor, and has a mass of <3 kg and a cruise speed of $\sim$ Mach 0.8 at an altitude of 10 km. The motor has a relatively low thrust to match the drag on the aircraft, about 5 N to 20 N. A class of slow-burning propellants using the burn rate suppressant oxamide is used in the motor to achieve the low thrust levels required; the development and characterization of these propellants were discussed by Vernacchia et al. in Ref. [3]. The proposed configuration of the vehicle is shown in Figure 1-2 and a summary of important vehicle parameters is given in Table 1.1. A recent discussion of the design, development, and performance of this class of vehicles was given by Vernacchia et al. in Ref. [4].

Research for this thesis focused on infrared radiant emission for small, low-thrust motors for Firefly-like aircraft. The Firefly vehicle was used as a case study (discussed in section 8.4) to demonstrate how the models and data from this thesis can be used to optimize the performance of small, fast, low-altitude aircraft.

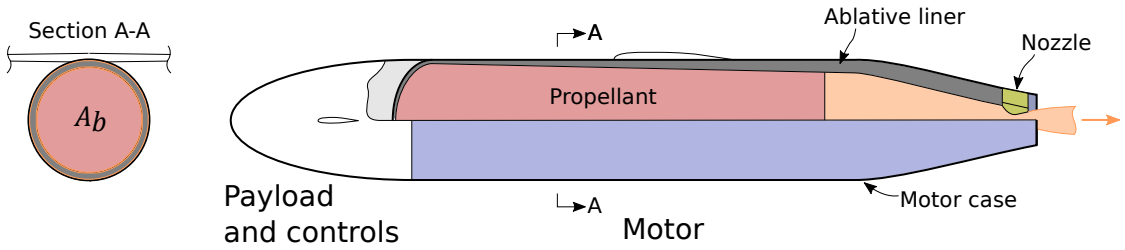

Figure 1-2: The Firefly vehicle is a demonstrator vehicle for a class of small, fast aircraft. A proposed configuration for such a vehicle has a circular cross-section, an ablative liner for insulating the motor case, and a forward/aft split between the payload and motor. Reprinted from Ref. [4].

Parameter	Value
Thrust	5 - 20 N
Burn time	100 - 200 s
Grain configuration	End burn
Burn length	$\sim$ 400 mm
Propellant	AP + HTPB + oxamide
Case diameter	65 mm
Burn area	$\sim$2500 mm^2
Throat diameter	2 - 5 mm
Chamber pressure	0.5 - 2 MPa
Specific impulse (delivered)	$\sim$ 110 s

Table 1.1: Summary of important vehicle design parameters for the small, low-thrust Firefly aircraft.

1.2.3 Modeling and design optimization with AeroSandbox

The modeling and optimization work in this thesis leveraged the AeroSandbox optimization framework, a python computational framework for high-dimensionality conceptual aircraft design optimization developed by Sharpe[†] [5]. AeroSandbox solves design problems using CasADi [6], a framework for automatic differentiation, and IPOPT [7], a robust gradient-based optimizer for non-linear programming. Automatic differentiation is a method for evaluating computational function derivatives by decomposing functions into elementary functions which have known derivatives, and then combining those derivatives using the chain rule [8]. Automatic differentiation can be used to compute derivatives for gradient-based optimizers such as IPOPT, and provides a computationally efficient method for AeroSandbox and other packages to solve high-dimensional engineering problems.

Sharpe recently used AeroSandbox to perform vehicle optimization and tradespace analyses for the Firefly vehicle (introduced in subsection 1.2.2). This thesis extended

[†]Peter Sharpe is a current graduate student in the MIT Department of Aeronautics and Astronautics working on Project Firefly.

the existing AeroSandbox models for aircraft design to incorporate models for solid rocket motor exhaust plume radiant emission. This subsequently enables radiant emission to be coupled with all of the existing tools and models for aircraft design optimization already available in AeroSandbox.

1.3 Technology gaps and thesis contributions

Technology gaps exist for integrating exhaust plume radiant emission in solid rocket powered vehicle design. To the author's knowledge, no exhaust plume radiant emission measurements for small, low-thrust motors at the Firefly (see subsection 1.2.2) size scale or propellants containing oxamide are available in the open literature. End-to-end differentiable models coupling solid rocket powered vehicle design with exhaust plume radiant emission are needed to enable optimization with gradient-based optimization frameworks such as AeroSandbox (see subsection 1.2.3). Analysis of plume radiant emission phenomena and performance tradeoffs unique to small, end-burning solid rocket motors are needed to support the design of future small, fast aircraft concepts such as Firefly.

The work for this thesis investigated these technology gaps. Exhaust plume radiant emission, chamber pressure, and thrust were measured in instrumented static fires utilizing a low-thrust, end-burning solid rocket motor with oxamide-doped propellants. Through the experimental work, a model for characterizing the minimum burn pressure of oxamide-doped propellants was refined and the feasibility of a machinable alumina silicate material for small, long-endurance motors was investigated. A differentiable model coupling solid rocket motor design to exhaust plume radiant emission was developed and implemented; it was validated with the experimental data for low-thrust, end-burning motors and data for other operating conditions from other works. The model was utilized to explore unique phenomena, design, and performance for small, low-thrust, end-burning motors such as those utilized for Firefly.

The scope of this thesis was limited to exhaust plume radiant emission in the infrared, specifically from 1.5 µm to 5.5 µm. This captures many of the strongest

emission bands for CO, CO_2, H_2O, and HCl. The modeling in this thesis also only considered exhaust products that are present in non-metallized propellants, such as those used for Firefly; models for scattering particulate such as alumina were not developed.

The results of this work provide advancements and solutions to enable design phase consideration of exhaust plume radiant emission. The specific contributions of this thesis are summarized below:

1. *Exhaust plume radiant emission measurements for small, low-thrust motors*: The effects of chamber pressure and oxamide content on radiant intensity for small, low-thrust motors were measured. The inclusion of oxamide in the propellant did not create any new measurable spectral peaks that would not have already been present for a composite propellant. To the author's knowledge, these measurements represent the lowest thrust levels for which rigorous plume radiant intensity measurements have been obtained and the only plume radiant intensity measurements for propellants containing oxamide in the open literature.

2. *Models and methods for designing and building small, fast aircraft*: A model describing the minimum burn pressure for oxamide-doped propellants originally proposed by Vernacchia et al. in Ref. [3] was updated with a new data point for a 8 % oxamide propellant burned at standard pressure. The feasibility of a low thermal conductivity alumina silicate material for novel use as a nozzle for a small, long-endurance motor was experimentally demonstrated.

3. *Modeling of exhaust plume radiant emission for solid rocket motors*: A reduced-order model for solid rocket motor afterburning kinetics was developed, as well as a procedure for fitting this model to a detailed kinetics scheme. This model is significantly less stiff than typical detailed kinetics mechanisms, and is more suitable for optimization with AeroSandbox. Additionally, interpolated differentiable surrogate models for molecular emittance parameters were developed to enable their implementation in AeroSandbox.

4. *Integrated design of solid rocket motors including exhaust plume radiant emission*: An end-to-end differentiable model for exhaust plume radiant emission coupled with solid rocket motor design was developed and implemented. This model enables design optimization for vehicles including constraints on plume radiant emission and integration of plume radiant emission with all existing aircraft design models in AeroSandbox. The importance of motor and plume size scale in afterburning kinetics and radiant emission was characterized, and for sufficiently small motors and plumes it was found that excess fuel in the plume remains largely unburnt. Additionally, the coupling between between oxamide content, chamber pressure, specific impulse, and radiant intensity in small, low-thrust motor design was characterized.

1.4 Document structure

The first several chapters are dedicated to discussing literature, theory, and typical practices relevant to the experimental, modeling, and analysis work discussed in this thesis. Chapter 2 provides a review of solid rocket motors and propellants. Chapter 3 reviews thermal radiation processes, properties, and modeling for gaseous and condensed media present in solid rocket motor exhaust plumes. Chapter 4 gives a more specific discussion of the typical properties and modeling practices for exhaust plume radiant emission.

The last chapters in this thesis focus on the thesis contributions discussed in section 1.3. Chapter 5 discusses experimental measurements collected for small, slow-burning solid rocket motors. Chapter 6 describes the end-to-end differentiable exhaust plume radiant emission model and its implementation; chapter 7 discusses the model results and validation. Lastly, chapter 8 explores phenomena and design guidelines pertaining to the integrated design of small, low-thrust solid rocket motors, and includes a case study for the optimization of a Firefly aircraft subject to constraints on the exhaust plume radiant emission.

Chapter 2

Literature Review: Solid Rocket Propellants and Motors

Solid rocket motors are used for several applications today, including launch vehicles, missiles, and gas generators [2]. They make attractive propulsion devices due to their relative mechanical simplicity and storability, among other reasons. The field of solid rocket motors and propellants is generally well-developed, and many sources throughout the open literature provide information on the relevant theory and best practices. *Rocket Propulsion Elements* by Sutton and Biblarz is one of the most well-known compilations of information relating to rocketry [2]. *Solid Rocket Propulsion Technology* by Davenas and *Mechanics and Thermodynamics of Propulsion* by Hill and Peterson provide more specific details on nozzle theory, manufacturing, and grain design, among others [9, 10]. McCreary also provides an excellent summary of practical knowledge for designing and manufacturing small solid rocket motors in *Experimental Composite Propellant* [11].

To enable plume emission to be considered during the design phase for solid rocket powered vehicles, it is important to understand the propulsion system that creates the vehicle thrust and exhaust plume. This chapter provides a review of solid rocket motor design, solid propellants, and the core physics that drives vehicle thrust and chamber pressure. Much of the review in the following subsections is summarized from the previously mentioned sources, and also borrows from the author's MS thesis

[12]. Specific considerations for the design of small, low-thrust, end-burning motors – such as the motors used for the small, fast Firefly aircraft concept introduced in subsection 1.2.2 – will also be included in the discussion.

2.1 Solid rocket motor components and grain configuration

Solid rocket motors are mechanically simple propulsion systems that produce vehicle thrust. The key components of a solid rocket motor are summarized here:

- The *propellant* is a solid grain containing both fuel and oxidizer. It burns to produce hot combustion products which give rise to the motor's chamber pressure and thrust.
- The *motor case* contains the propellant grain and acts as a pressure vessel for the combustion products during motor operation.
- The *insulation* protects the motor case from the hot gasses produced from the burning propellant.
- The *nozzle* expands and accelerates the high pressure combustion products in the motor case to produce thrust. The high-velocity exhaust that exits the nozzle forms the rocket exhaust plume.

The propellant geometry in solid rocket motors can be configured in a number of ways to achieve mission objectives. When designing a solid rocket motor, is important to choose a suitable grain configuration, as it has a significant impact on motor thrust, chamber pressure, and burn time. Some of the most common propellant configurations include end-burners, core-burners, and core-burners with slots. These configurations are illustrated in Figure 2-1. A brief description of these configurations is given below:

- *End-burners* have a single exposed propellant face with inhibited edges, which prevents the edges of the propellant from burning. The propellant regresses

axially along the length of the motor as the propellant burns. These motors have a typically neutral thrust profile, since the burning area of propellant remains constant for the duration of the burn.

- *Core-burners* have a typically cylindrical propellant grain with a hollow circular core. The entire interior surface of the core burns, and the surface of the core regresses radially outward as the propellant burns. As with end-burners, the edges of the grain are inhibited to prevent burning on the outer surface. Core-burning motors display a progressive thrust profile, since the burning area of the propellant increases as the propellant burning surface regresses outwards.

- *Core-burners with slots* are similar to simple core-burners as they both have hollow cores with interior burning surfaces. In addition to the simple cylindrical core, these motors have slots that add additional surface area to the core. The core regresses generally radially outward as the propellant burns, although the slots create tangential regression as well. The exact design of the core slots is usually chosen to achieve a desired thrust profile, which is typically neutral or progressive.

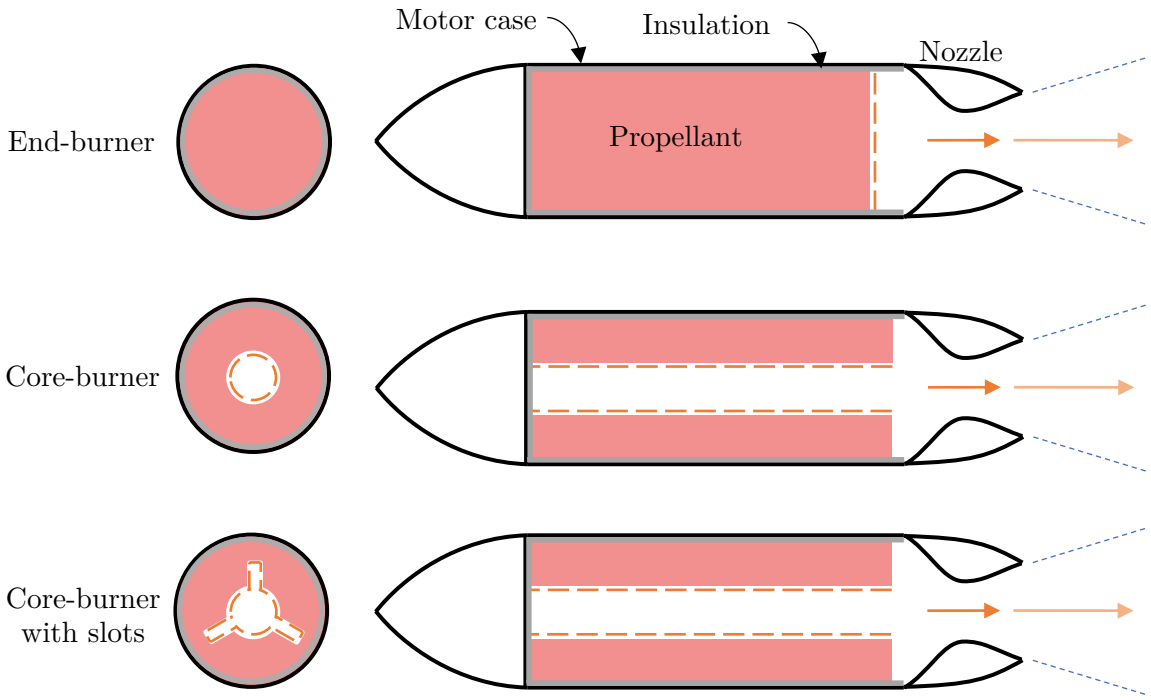

Figure 2-1: Different motor configurations have different burning surface areas and thrust profiles. Adapted from Ref. [13].

2.1.1 Design of low-thrust motors for small, fast aircraft propulsion

The small, fast Firefly vehicle concept (see subsection 1.2.2) utilizes an end-burning motor configuration. This configuration helps the Firefly vehicle to best achieve its thrust requirement and endurance objective. Because the burning area is relatively small for an end-burning motor, as opposed to a core-burner where the entire surface area of the inner core is burning, lower thrust levels can be achieved. Additionally, in an end-burning motor, the flame front regresses axially along the entire axial length of the motor. This produces a longer endurance motor in comparison to core-burning motors, where the flame front regresses through the typically smaller radial dimension of the motor. The end-burning configuration, as well as constrained and free design variables for the Firefly aircraft concept, are shown in Figure 2-2.

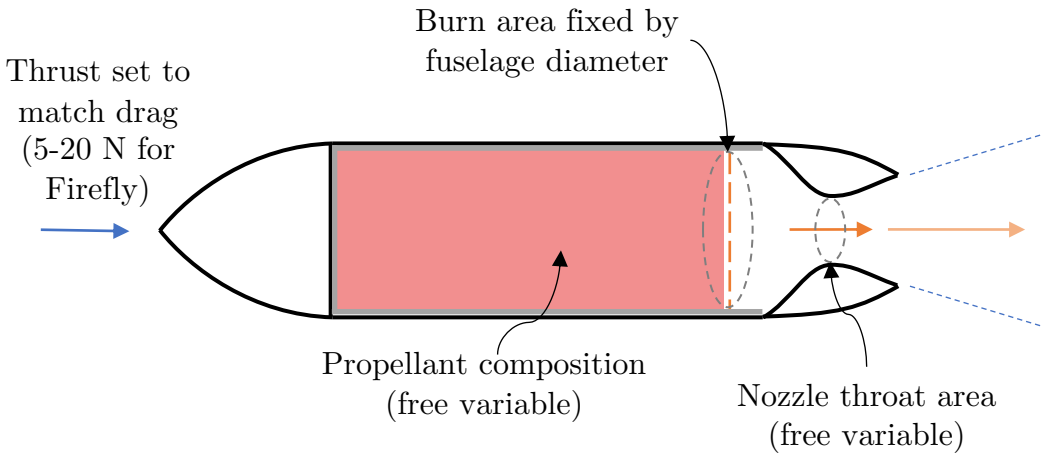

Figure 2-2: The burn area for the Firefly aircraft end-burning motor is fixed by the diameter of the aircraft fuselage. The propellant composition and nozzle throat area are free variables. Adapted from Ref. [14].

For an end-burning motor for a small, fast aircraft, the burn area is set by the diameter of the aircraft fuselage. To maintain steady flight, the thrust is constrained to match the drag. The propellant composition is a free design variable. The propellants used for the Firefly solid rocket motor dilute a standard baseline composite propellant formulation with varying amounts of the burn rate suppressant oxamide. These propellants are introduced in greater detail in section 2.4. The nozzle throat diameter is also a free variable, which directly affects the chamber pressure of the motor.

2.2 Motor thrust, chamber pressure, and mass flow

Solid rocket powered vehicles are typically designed with a specific thrust requirement to achieve some mission objective. For instance, the Firefly vehicle introduced in subsection 1.2.2 should have a thrust of approximately 5 - 20 N, which is set by the drag on the aircraft during flight. Thrust is coupled to chamber pressure and mass flows in a solid rocket motor, which influences important design parameters such as propellant burning area, nozzle throat area, and propellant composition. These concepts are reviewed in this section.

2.2.1 Mass flow

The rate of change of mass inside the combustion chamber for a solid rocket motor can be expressed as:

$$\frac{dm_c}{dt} = \dot{m}_{in} - \dot{m}_{out} \tag{2.1}$$

where m_c is the mass of gas in the combustion chamber, $\dot{m}_{in}$ is the mass flow rate of gas entering the combustion chamber due to the burning propellant, and $\dot{m}_{out}$ is the mass flow rate of gas exiting the combustion chamber through the nozzle. The mass flow rate of gas exiting through the nozzle can be found using

$$\dot{m}_{out} = \frac{p_c A_t}{c^*} \tag{2.2}$$

where p_c is chamber pressure, A_t is throat diameter, and c^* is characteristic velocity (defined in subsection 2.3.2). The mass flow rate of gas entering the chamber due to the burning propellant can be found using

$$\dot{m}_{in} = A_b \rho_p r \tag{2.3}$$

where A_b is the propellant burning area, ρ_p is the density of the solid propellant, and r is the propellant burn rate with units of velocity. In steady-state motor operation, the rate of change of mass inside the combustion chamber is zero, or

$$\frac{dm_c}{dt}\Big|_{steady} = \dot{m}_{in} - \dot{m}_{out} = 0 \tag{2.4}$$

2.2.2 Equilibrium chamber pressure and thrust

For a reasonable range of chamber pressures, the burn rate of a composite propellant can be related to the chamber pressure using an empirical burn rate law [2, 10]

$$r = a p_c^n \tag{2.5}$$

where r is the propellant burn rate, p_c is the chamber pressure, a is the burn rate coefficient, and n is the burn rate exponent. The values for a and n are determined experimentally; the process for obtaining the a and n values is described in section 2.6.

The equilibrium chamber pressure can be found by substituting Equations 2.2, 2.3, and 2.5 into Equation 2.4 and rearranging:

$$p_{c,eq} = (K_n \rho_p c^* a)^{\frac{1}{1-n}} \; ; \;\; K_n \equiv \frac{A_b}{A_t} \tag{2.6}$$

The thrust delivered by the motor can be found using:

$$F = C_F \left(\frac{p_c}{p_e}, \frac{p_a}{p_e}, \gamma \right) A_t p_c \tag{2.7}$$

where C_F is thrust coefficient (defined in subsection 2.3.3).

Equilibrium thrust can then be found by substituting the equilibrium chamber pressure given in Equation 2.6 into the equation for thrust given in Equation 2.7 and rearranging:

$$F_{eq} = p_c^n C_F \left(\frac{p_c}{p_e}, \frac{p_a}{p_e}, \gamma \right) c^* \left(R, \gamma, T_c \right) a \rho_p A_b \tag{2.8}$$

2.3 Motor performance parameters

A number of propulsive performance parameters exist for solid rocket motors, and are relevant for understanding the coupling between motor propulsion and exhaust plume radiant emission. A few of these parameters will be reviewed below.

2.3.1 Specific impulse

Instantaneous specific impulse is a measure of motor efficiency, and describes the motor thrust imparted per unit weight flow of propellant:

$$I_{sp} = \frac{F}{g\dot{m}} = \frac{c}{g} \tag{2.9}$$

where c is the motor effective exhaust velocity such that $F = \dot{m}c$. When the nozzle is matched such that $p_e = p_a$, then $c = v_e$. A higher specific impulse indicates a more efficient motor.

2.3.2 Characteristic velocity

The characteristic velocity c^* of a motor is a performance parameter that is useful for comparing the quality of different propellants. It is defined as

$$c^* \equiv \frac{p_c A_t}{\dot{m}} \tag{2.10}$$

where p_c is chamber pressure and A_t is nozzle throat area. Ideal characteristic velocity can also be written as a function of thermodynamic properties:

$$c^*(R, \gamma, T_c)_{ideal} = \left[\frac{RT_c}{\gamma \left(\frac{2}{\gamma+1} \right)^{\frac{\gamma+1}{\gamma-1}}} \right]^{\frac{1}{2}} \tag{2.11}$$

where R is the specific gas constant for the combustion products, γ is the ratio of specific heats, and T_c is the combustion chamber temperature. Because the characteristic velocity is only dependent on properties of the combustion products (and not on p_c), it is roughly constant for a particular propellant choice.

2.3.3 Thrust coefficient

The nozzle thrust coefficient is a measure of how effective the nozzle expansion process is at producing vehicle thrust. It is expressed as

$$C_F = \frac{F}{A_t p_c}. \tag{2.12}$$

Higher values indicate a more efficient nozzle expansion process.

For an ideal nozzle, thrust coefficient can be found using:

$$C_{F,ideal}\left(\frac{p_c}{p_e},\frac{p_a}{p_e},\gamma\right)=\left\{\frac{2\gamma^2}{\gamma-1}\left(\frac{2}{\gamma+1}\right)^{\frac{\gamma+1}{\gamma-1}}\left[1-\left(\frac{p_e}{p_c}\right)^{\frac{\gamma-1}{\gamma}}\right]\right\}^{\frac{1}{2}}+\frac{p_e-p_a}{p_c}\frac{A_e}{A_t} \quad (2.13)$$

where p_c is chamber pressure, p_e is the nozzle exit pressure, p_a is atmospheric pressure, A_t is the nozzle throat area, A_e is the nozzle exit area, and γ is the exhaust gas ratio of specific heats. $C_{F,ideal}$ is a function of p_c/p_e, p_a/p_c, and γ, since A_e/A_t is itself a function of p_c/p_e. It is not an explicit function of chamber temperature T_c, and is mostly independent of propellant chemistry and combustion[†]. For a given chamber pressure p_c, $C_{F,ideal}$ is maximized when the nozzle has matched expansion such that $p_e = p_a$.

2.4 Ammonium perchlorate composite propellants

Ammonium perchlorate composite propellants are a standard propellant used in high-performance solid rocket motors. These propellants have a number of desirable properties, including a high energy density, wide range of stable ambient temperatures, and good handling and storage qualities. The low-thrust, end-burning motors used in the Firefly vehicle concept (see subsection 1.2.2) use a class of ammonium perchlorate composite propellants containing varying amounts of the burn rate suppressant oxamide. This is also the type of propellant that was used for the experimental work in this thesis described in chapter 5. This section will review ammonium perchlorate composite propellants generally, and discuss some implications of adding oxamide.

2.4.1 Composition

Composite propellants are a heterogenous mixture of fuel, oxidizer, and other components. Ammonium perchlorate composite propellants (APCPs) typically consist of the following ingredients:

[†]The ratio of specific heats γ varies slightly with propellant chemistry and temperature.

- The *oxidizer* for this class of propellants is ammonium perchlorate (NH_4ClO_4). It has good compatibility with other propellant materials and a high oxidizing potential, and is the most commonly used oxidizer in solid propellant manufacturing.

- The *binder* is a polymer which provides a structural matrix for the rest of the propellant components. Binders are typically organic rubbers which also serve as a fuel.

- The *curative* is an agent that cross-links the prepolymers in the binder to form the solid rubber matrix for the propellant.

- The *plasticizer* is a low viscosity liquid which helps to improve the rheological properties and extend the pot life of the uncured propellant.

- An *opacifier* is an additive used to make propellant opaque, which prevents heat from the flame from being radiated deep into the solid propellant.

- *Metal fuels* are powdered metals optionally added into the solid propellant mixture to increase density, increase combustion temperature, and improve combustion stability.

- *Burn rate modifiers* are optional additives that can catalyze or suppress the burn rate, allowing the propellant burn rate to be modified.

2.4.2 Oxamide burn rate suppressant

A relatively slow propellant burn rate is required to achieve the low thrusts needed for propulsion systems for small, fast aircraft. Oxamide $(CONH_2)_2$ is an additive which can reduce the burn rate of APCPs by cooling the propellant surface. The decomposition of oxamide is endothermic and occurs at a temperature that is lower than the propellant surface temperature, and therefore absorbs a significant amount of energy at the propellant's surface [15, 16]. This slows down both the condensed- and gas-phase reactions at the surface, effectively reducing the burn rate [17].

2.4.2.1 Burn rate with oxamide

Vernacchia et al. derived a theoretical model to predict the effect of propellant oxamide content on burn rate [3]. The model assumes a baseline, undoped propellant with a known burn rate r^*, burn rate coefficient a^*, and burn rate exponent n is doped with some mass fraction w_{om} of oxamide. The model predicts the burn rate for the oxamide-doped propellant $r(w_{om})$ as a function of the oxamide mass fraction w_{om}, such that

$$r(w_{om}) = \phi_{om}(w_{om})r^* = \phi_{om}(w_{om})a^* p_c^n \tag{2.14}$$

where

$$\phi_{om}(w_{om}) = \frac{1 - w_{om}}{1 + \lambda w_{om}}. \tag{2.15}$$

The burn rate exponent n is not changed by the addition of oxamide. The dimensionless parameter λ is a function of gasification enthalpies for oxamide and the undoped propellant, defined as

$$\lambda \equiv \frac{\Delta h_{gas}^{om} - \Delta h_{gas}^*}{\Delta h_{gas}^*} \tag{2.16}$$

where Δh_{gas}^{om} is the gasification enthalpy of oxamide and Δh_{gas}^* is the gasification enthalpy of the undoped propellant.

2.4.2.2 Other propellant properties with oxamide

Vernacchia et al. also conducted combustion simulations of oxamide containing propellants using a thermodynamic equilibrium solver (explained further in section 2.5) to determine the relationships of propellant combustion temperature T_c, characteristic velocity c^*, and ratio of specific heats γ with propellant oxamide content [3]. The effect of oxamide content on propellant theoretical solid density was also calculated. The simulation results are plotted in Figure 2-3 below with curves of best fit. The effects of oxamide content on flame temperature and characteristic velocity are important, while its effects on ratio of specific heats and solid density are not significant.

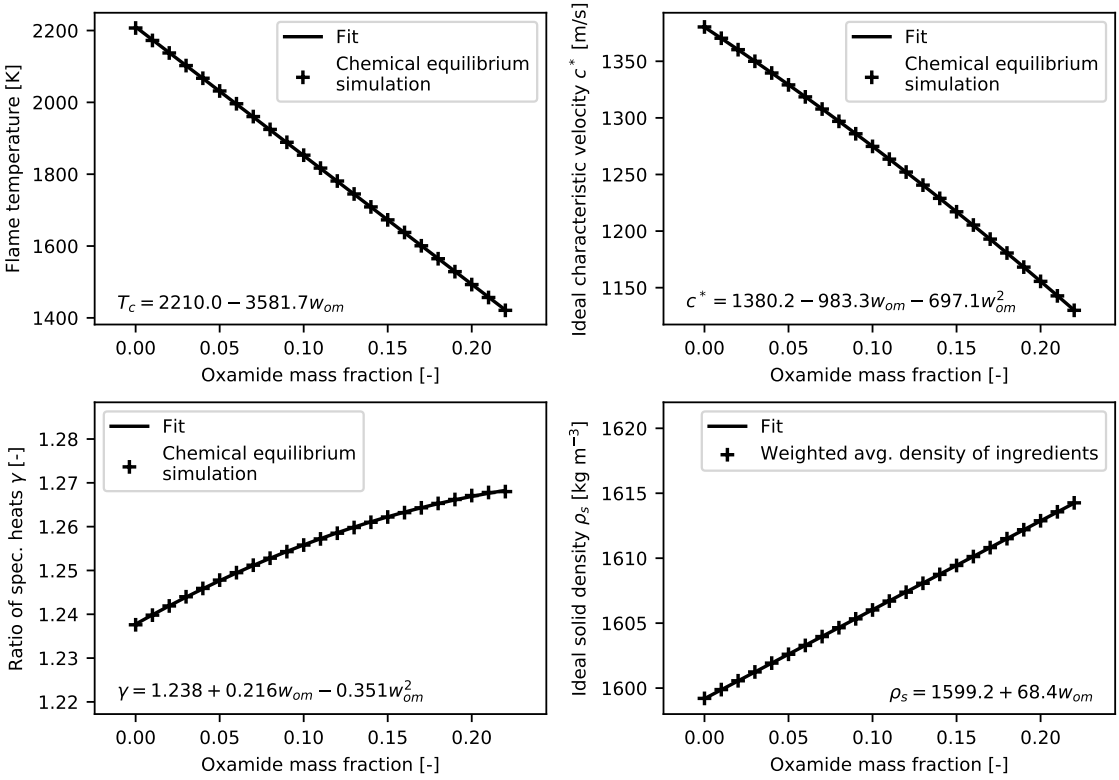

Figure 2-3: Equations for flame temperature, characteristic velocity, ratio of specific heats, and propellant solid density were fit as functions of propellant oxamide content. Flame temperature and characteristic velocity have a strong dependence on oxamide content. The ratio of specific heats and the ideal solid density do not vary significantly. Reprinted from Ref. [14].

2.4.3 Minimum burn pressure

Propellants can have a minimum pressure below which they do not burn. This minimum burn pressure is important for determining the lower bound on burn rate and thrust (see subsection 2.2.2) that can be achieved with a particular propellant. The minimum burn pressure for a particular propellant must be measured, as it cannot be determined from theory.

Vernacchia et al. characterized the minimum burn pressure for oxamide-doped propellants [3]. Ignition of propellants containing 0, 5, 10, 13, and 20% oxamide was attempted at various pressures at or above atmospheric pressure. An empirical minimum burn pressure curve with a quadratic shape was fit to the ignition data as

a function of oxamide content. This thesis presents an additional data point for an 8 % oxamide propellant and an updated curve fit for the minimum burn pressure in subsection 5.6.4.

2.5 Combustion modeling

Determining the equilibrium flame temperature and combustion gas product concentrations for a given propellant composition can be done using equilibrium thermodynamics [18]. For an adiabatic combustion reaction occurring at a constant pressure, if n combustion product species are assumed, then $n+1$ equations are required to solve $n+1$ unknowns: n different species concentrations and flame temperature. If α unique atoms are present in the reaction, then a mass balance for each atom provides α of these $n+1$ equations. Conservation of enthalpy for the reaction provides another equation. The remaining $n-\alpha$ equations are provided with chemical equilibrium equations, which enforce that the equilibrium gas species concentrations and temperature should minimize the Gibb's free energy of the system. The simultaneous solution of these $n+1$ equations provides the equilibrium species concentrations and flame temperature.

Combustion modeling and chemical equilibrium calculations are typically carried out with computer codes. A number of standard codes are available for these calculations, including Rocket Propulsion Analysis [19], NASA CEARUN [20], and Cantera [21].

2.6 Propellant characterization

Propellant burn rate is typically characterized using strand burner tests [2]. In these tests, samples (or "strands") of propellant with a constant burn area are burned at a known pressure. At each pressure, the burn rate of the propellant is measured, using embedded wires, thermocouples, optical observation, or other means [22]. The empirical burn rate law given in Equation 2.5 is then fit to the collected burn rate

data, and the values for a and n are determined for that propellant. Strand burner results typically show propellant burn rates 4 % to 12 % lower than if that propellant was burned in a full-size motor [2]. This is due to excessive heat loss resulting from the relatively large surface-area-to-volume ratio at the small-scale of the strand burner tests.

2.7 Manufacturing and inspection

To manufacture composite propellants, liquid binder and plasticizer are first mixed together. The solid ingredients, including oxidizer, metal fuel, opacifier, and any burn rate modifiers, are then added to the liquids, and the slurry is thoroughly mixed. The curative is added last, and then the propellant slurry is cast into a mold where it is left to cure.

Propellant mixing is typically done under vacuum to remove water and other volatiles from the mix [2, 11]. The mixing speed and time should be chosen appropriately to ensure the slurry is homogeneous and has acceptable rheological properties for casting. Muthaiah et al. recommend a mixing speed of $25\,\mathrm{rev\,min^{-1}}$ and a mixing time of 180 min [23]. Abdillah et al. recommend a mixing speed of $60\,\mathrm{rev\,min^{-1}}$ and a mixing time of 135 min [24]. It should be noted, however, that the optimal mixing time and speed is likely dependent on the mixer specifications and propellant batch size, and therefore values obtained in one study may not translate well to the next.

Cast propellant grains are inspected to ensure they are free of cracks, voids, or other flaws that may degrade propellant grain mechanical properties or lead to an unexpected increase in burning area [2]. Propellant grains can be inspected with non-destructive techniques, including x-ray imaging and ultrasound [2].

Chapter 3

Literature Review: Radiation Processes

Radiative emissions from solid rocket motor exhaust plumes are typically thermal in nature, with contributions from both gaseous and particulate media in the plume. Many factors influence plume radiant emission spectra, including the plume chemical constituents, temperature, and density, among others. These are in turn influenced by the chosen propellants and motor design, and the resulting motor performance parameters; these topics were introduced in chapter 2. This section will review relevant radiative processes involved in understanding and characterizing exhaust plume emission.

Much of this knowledge has been well-established for many decades. *Thermal radiation heat transfer* by Howell et al. and *Radiative heat transfer* by Modest are excellent texts on the general subject of radiation processes [25, 26]. *Rocket Exhaust Plume Phenomenology* by Simmons and *Handbook of Infrared Radiation from Combustion Gases* by Ludwig et al. provide more focused descriptions of topics specifically relating to exhaust plume radiant emission [1, 27]. Much of the review in the following subsections will summarize knowledge from these texts.

3.1 Origin of emission

Molecules can undergo changes to their internal energy state due to one of three transitions: transitions of electrons between different energy states; transitions between molecular vibration energy levels; and transitions between molecular rotation energy levels [1]. These changes in internal energy state are accompanied by a corresponding emission or absorption of radiative energy at some characteristic wavelength, known as a spectral line.

Transitions involving electrons are the most energetic, emitting radiation in the ultraviolet and visible regions of the spectrum [1, 28]. Vibrational transitions are less energetic, typically emitting in the near IR. Pure rotational transitions are less energetic still, with typical emissions in the mid and far IR. Given that this thesis will focus on infrared emission (discussed in section 1.3), this review will focus on emission due to vibrational and rotational transitions.

Molecules can vibrate and rotate in several different modes, depending on the number and arrangement of the constituent atoms. For each of these modes, a molecule can rotate, vibrate, or both, at a number of discrete energy levels, dictated by the selection rules of quantum mechanics [1, 26]. An excellent description of these selection rules is provided in section 10.3 of Ref. [26].

Changes in vibrational and rotational energies can – or are demanded by the selection rules to – occur simultaneously [26, 29]. These vibration-rotation transitions lead to the formation of characteristic vibration-rotation bands, which are groupings of spectral emission lines – each corresponding to a particular vibration-rotation transition – clustered around the characteristic wavelength of the pure vibration transition. A necessary molecular property for vibration-rotation transitions to occur is the existence of a dipole moment in the molecule, which creates a mechanism for the molecule to interact with electromagnetic radiation and subsequently emit or absorb radiative energy [28, 30]. For this reason, homonuclear diatomic molecules such as N_2 and H_2 do not emit or absorb in the infrared, since they do not have a dipole moment.

The concept of these characteristic vibration-rotation bands for a hypothetical diatomic molecule is illustrated in Figure 3-1. A vibrating diatomic molecule continually exchanges potential and kinetic energy at some discrete energy level v. Transitions between these energy levels v can occur through absorption or emission of a photon. Vibrational transitions that occur between the first energy level and the ground state are known as fundamental transitions; transitions between higher energy levels and the ground state are known as overtone transitions; transitions between two higher energy levels are known as "hot" transitions. For each vibrational transition, there is a substructure of possible rotational energies J. These simultaneous transitions between vibrational and rotational energy levels for some particular vibrational transition create the characteristic vibration-rotation bands.

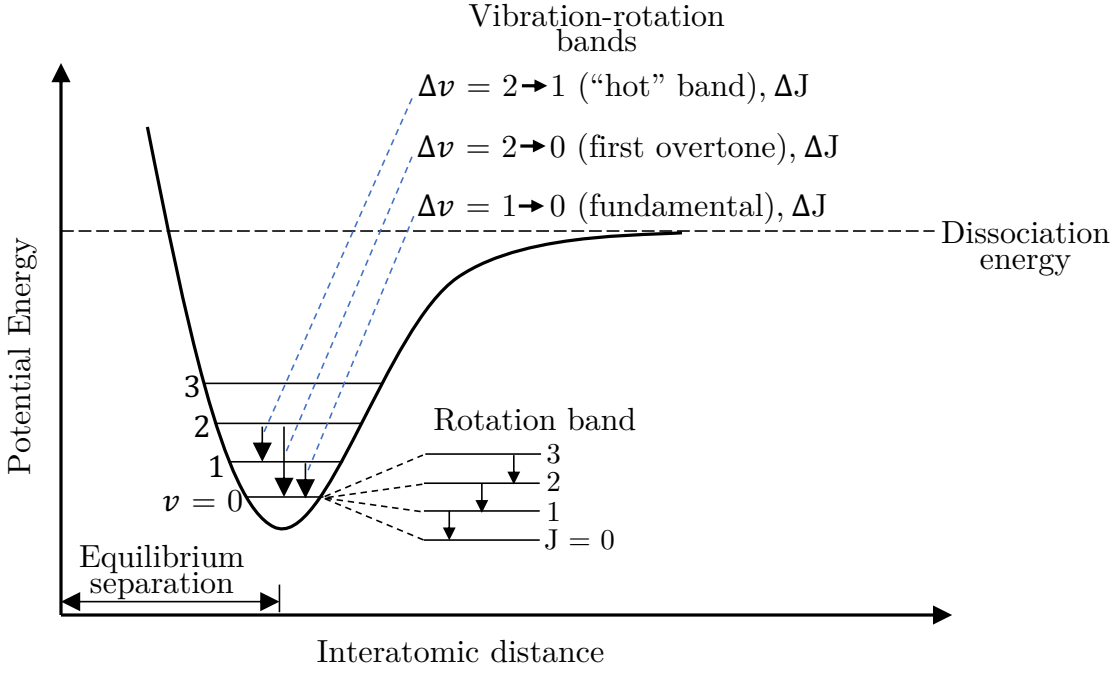

Figure 3-1: A hypothetical diatomic molecule exchanges energy between kinetic and potential energy at discrete vibrational energy levels v. Transitions between rotational energies J for a particular vibrational energy transition lead to the formation of characteristic vibration-rotation bands.

3.2 Radiative transfer equation in participating media

There are four processes that can change the energy of some beam of radiation along some path length [25, 26]:

- gains due to emission,
- losses due to absorption,
- losses due to out-scattering, and
- gains due to in-scattering.

These four processes, and their contributions to some arbitrary beam of energy along some small path length, are depicted in Figure 3-2.

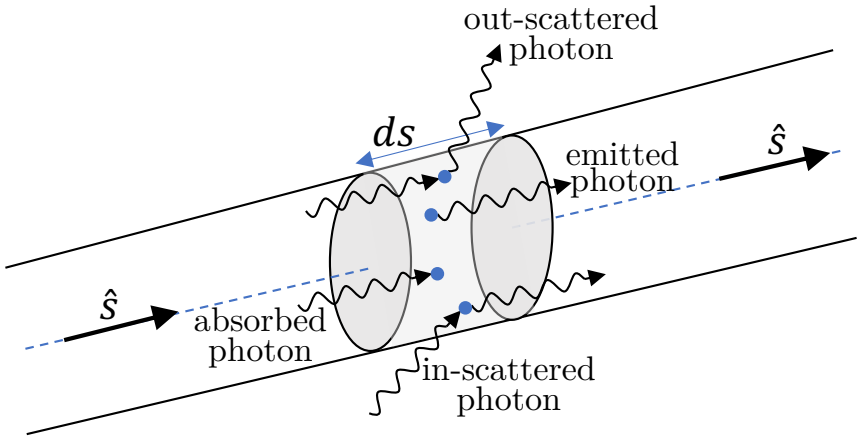

Figure 3-2: Along some path length ds, the radiative intensity in some arbitrary viewing direction $\hat{s}$ can change due to photon absorption, emission, in-scattering, or out-scattering.

The radiative transfer equation (RTE) represents an energy balance between these processes that add or subtract energy to a beam of radiative energy. A term for each of these processes appears in the RTE, written as follows:

$$\overbrace{\frac{dI_\lambda}{ds}}^{\substack{\text{change in}\\ \text{radiative energy}\\ \text{per path length}}} = \overbrace{+\kappa_\lambda I_{b\lambda}}^{\substack{\text{gain due to}\\ \text{emission}}} \overbrace{-\kappa_\lambda I_\lambda}^{\substack{\text{loss due to}\\ \text{absorption}}} \overbrace{-\sigma_{s\lambda} I_\lambda}^{\substack{\text{loss due to}\\ \text{out-scattering}}} \overbrace{+\frac{\sigma_{s\lambda}}{4\pi}\int_{\Omega_i=4\pi} I_\lambda(\hat{s}_i)\Phi_\lambda(\hat{s}_i,\hat{s})d\Omega_i}^{\substack{\text{gain due to}\\ \text{in-scattering}}} \quad (3.1)$$

where

- λ is wavelength (m)
- I_λ is spectral radiance ($\mathrm{W\,\mu m^{-1}\,sr^{-1}\,m^{-2}}$)
- $I_{b\lambda}$ is black body spectral radiance ($\mathrm{W\,\mu m^{-1}\,sr^{-1}\,m^{-2}}$)
- s is path (m)
- κ_λ is absorption coefficient ($\mathrm{m^{-1}}$)
- $\sigma_{s\lambda}$ is scattering coefficient ($\mathrm{m^{-1}}$)
- Φ_λ is scattering phase function, which describes the fraction of incident radiation that is scattered in a particular direction (-)
- Ω is solid angle (sr)

and parameters with the subscript λ are dependent on wavelength.

The solution of the RTE describes the spectral radiance I_λ (i.e. radiant power emitted per unit solid angle per unit emitting area per unit wavelength) for absorbing, emitting, and scattering media. The RTE in its complete form cannot be directly integrated, and consequently various approximations and solution methods have been developed; a summary of many available solutions methods is discussed in chapter 13 of Ref. [25]. Several other quantities relating to the RTE are also of interest, and are described in the following subsections.

3.2.1 Spectral radiant intensity

Spectral radiant intensity J_λ has units of $\mathrm{W\,\mu m^{-1}\,sr^{-1}}$, and describes the radiant power emitted per unit solid angle per unit wavelength. It is found by integrating the spectral radiance over the projected emitting area:

$$J_\lambda = \int_{A_{projected}} I_\lambda dA \tag{3.2}$$

This is the radiative property that will be measured for the exhaust plume experimental measurements discussed in chapter 5.

3.2.2 Total radiant intensity

Total radiant intensity J has units of $\mathrm{W\,sr^{-1}}$, and describes the radiant power emitted per unit solid angle. It is found by integrating the spectral radiant intensity over all wavelengths (or over a particular band of interest):

$$J = \int J_\lambda d\lambda. \tag{3.3}$$

3.2.3 Optical depth

Optical depth τ is a dimensionless quantity describing the number of mean free path lengths for a photon through some depth of participating media [31]. It is defined as

$$\tau_\lambda \equiv \int (\kappa_\lambda + \sigma_{s\lambda})\, ds \tag{3.4}$$

and is a spectral quantity proportional to both the physical thickness of the media, as well as the absorption and scattering coefficients. If $\tau_\lambda \gg 1$, then the media is optically thick, and photons entering the media will be scattered or absorbed many times before exiting. If $\tau_\lambda \ll 1$, then the media is optically thin, and photons entering the media will tend to pass through unperturbed.

3.2.4 Emissivity

For an isothermal, non-scattering ($\sigma_{s\lambda} = 0$) medium, the emissivity is defined as the ratio of radiant energy emitted ϵ_λ from the medium to the radiant energy emitted from a blackbody at the same temperature:

$$\epsilon_\lambda \equiv \frac{I_\lambda}{I_{b\lambda}} = \left(1 - e^{-\tau_\lambda}\right) \tag{3.5}$$

Emissivity has values between 0 and 1. $\epsilon_\lambda \ll 1$ corresponds to an optically thin medium ($\tau_\lambda \ll 1$). A linearization of ϵ_λ around $\tau_\lambda \approx 0$ gives $\epsilon_\lambda \approx \tau_\lambda$. $\epsilon_\lambda \approx 1$ corresponds to an optically thick medium ($\tau_\lambda \gg 1$), and the medium emits like a blackbody.

3.3 Spectral line radiation for molecular gases

As introduced in section 3.1, molecular gases can emit or absorb photons at discrete energies due to vibration-rotation transitions. These emitting and absorbing molecules can change the spectral radiance ($\mathrm{W\,\mu m^{-1}\,sr^{-1}\,m^{-2}}$) propagating along some path. Absorption decreases the spectral radiance I_λ along some path s, and that decrement can be written as

$$dI_\lambda = -\kappa_\lambda I_\lambda ds \tag{3.6}$$

where κ_λ, known as the absorption coefficient, is the proportionality coefficient between the decrement in spectral radiance and its path length [27]. Similarly, emission increases the spectral radiance along some path, and that increment can be written as

$$dI_\lambda = \kappa_\lambda I_{b\lambda} ds \tag{3.7}$$

where $I_{b\lambda}$ is the black-body spectral radiance, and κ_λ is the same proportionality coefficient as for absorption [27]. Both the absorption decrement (Equation 3.6) and the emission increment (Equation 3.7) appear as terms in the radiative transfer equation (Equation 3.1).

To evaluate Equations 3.6 and 3.7, the profile of the absorption coefficient κ_λ must be described. The profile of κ_λ can be determined for each spectral line, and therefore the profile of κ_λ for some particular bandwidth can be determined piece-wise if information about all existing spectral lines within the band is known [†]. The profiles of κ_λ for individual spectral lines – which are not truly "lines" since spectral lines are not truly monochromoatic – are driven by several spectral line broadening mechanisms that produce characteristic profiles for κ_λ [27]. The most important of these line profiles are illustrated in Figure 3-3. These profiles and their driving broadening mechanisms are reviewed in the following subsections.

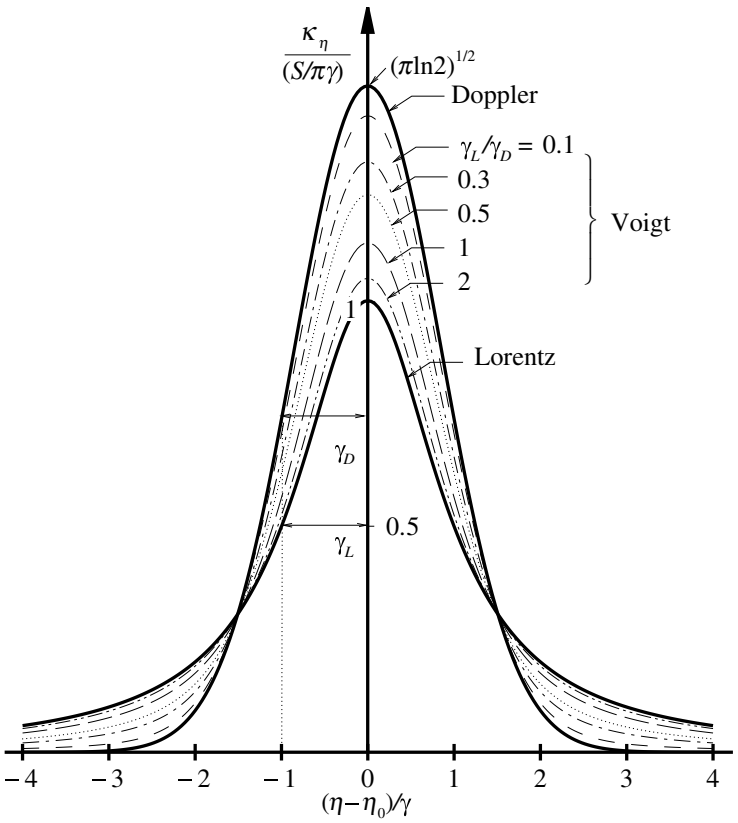

Figure 3-3: The shape profile of a spectral line changes due to different broadening mechanisms. At the limits are line profiles due to only collision broadening or only Doppler broadening; Voigt line profiles are a blend of the limits. This figure shows these spectral line shapes for equal line strength S (defined in Equation 3.8) and half-width γ. Reprinted from Ref. [26].

[†]The HITRAN database, a large online compilation of spectroscopic properties, is most commonly used for line-by-line calculations [32].

3.3.1 Natural broadening

Natural line broadening is due to natural variations in emitted photon energies because of the Heisenberg uncertainty principle [26]. These slight variations in energy give rise to spectral lines with finite widths. Natural broadening occurs when molecular energy levels are allowed to decay spontaneously, rather than due to some disturbance such as a molecular collision. The timescale for spontaneous emission is much larger than the timescale for molecular collisions, however, and therefore the effects of natural broadening are generally insignificant in comparison.

3.3.2 Collision broadening

Collision broadening occurs because of disruptions in the energy states of molecules due to molecular collisions [25]. The spectral line shape for collision broadening has a Lorentz profile (which is typically written using wavenumber as the spectral variable instead of wavelength) [33]:

$$\kappa_\eta = \frac{S}{\pi} \frac{\gamma_c}{(\eta - \eta_0)^2 + \gamma_c^2} \; ; \quad S \equiv \int_{\Delta\eta} \kappa_\eta d\eta \tag{3.8}$$

where η is the wavenumber (defined as the inverse of wavelength), S is the line-strength, γ_c is the spectral line half-width (also in wavenumber units) for collision broadening, and η_0 is the wavenumber of the line center. The line half-width γ_c can be predicted from kinetic theory [33]:

$$\gamma_c = \frac{2}{\pi^{1/2}} \frac{D^2 \, p}{c \, (m k_B T)^{1/2}} \tag{3.9}$$

where D is the effective diameter of the molecule, m is the mass of the molecule, p is the gas pressure, T is the gas temperature, k_B is the Boltzmann constant, and c is the speed of light. To first order, the line-strength S is proportional to gas density ρ [1, 25]. Collision broadening is typically dominant in exhaust plumes at lower altitudes, where densities are sufficiently high. This is expected to be the dominant broadening mechanism for plumes considered in this thesis.

3.3.3 Doppler broadening

Doppler broadening is the result of energy shifts due to molecular motion and the Doppler effect [25, 26]. The spectral line shape for Doppler broadening has a Gaussian profile:

$$\kappa_\eta = \left(\frac{\ln 2}{\pi}\right)^{1/2} \left(\frac{S}{\gamma_D}\right) \exp\left(-\ln 2 \left(\frac{\eta - \eta_0}{\gamma_D}\right)^2\right). \tag{3.10}$$

The line half-width for Doppler broadening γ_D is given by

$$\gamma_D = \frac{\eta_0}{c}\left(\ln 2 \, \frac{2k_B T}{m}\right)^{1/2}. \tag{3.11}$$

Doppler broadening tends to be the dominant broadening mechanism in high altitude exhaust plumes, where densities are lower.

3.3.4 Voigt line profiles

In some conditions, both collision and Doppler broadening mechanisms are important. The Voigt profile combines the effects of collision and Doppler broadening. It is the result of the convolution of the collision broadening profile given in Equation 3.8 and the Doppler broadening profile given in Equation 3.10 [34], and has no closed-form solution [26].

3.4 Band modeling for molecular gases

As discussed in section 3.3, the profile of the absorption coefficient κ_λ can be determined line-by-line for some desired band-width. However, carrying out line-by-line calculations involves large numbers of spectral lines and a rapidly changing profile for absorption coefficient that is difficult to integrate. For instance, of interest for this thesis is the analysis of a rocket exhaust plume, considering radiation from H_2O, CO, CO_2, and HCl in the 1.5 µm to 5.5 µm band. If only the most abundant isotopologue for each molecule is considered, querying the HITRAN database returns 164 988 spectral lines [32].

Given the complication of evaluating thousands of spectral lines, and the fact that the exact profile for absorption coefficient varies more rapidly with wavelength that other spectral quantities, smoothed approximations for the absorption coefficient are desirable [26]. This led to the development of various so-called band models. These band models can typically be grouped into two categories: narrow band models and wide band models. The model types are illustrated in Figure 3-4. Additional techniques can be applied to these band models to account for nonhomogeneous gases.

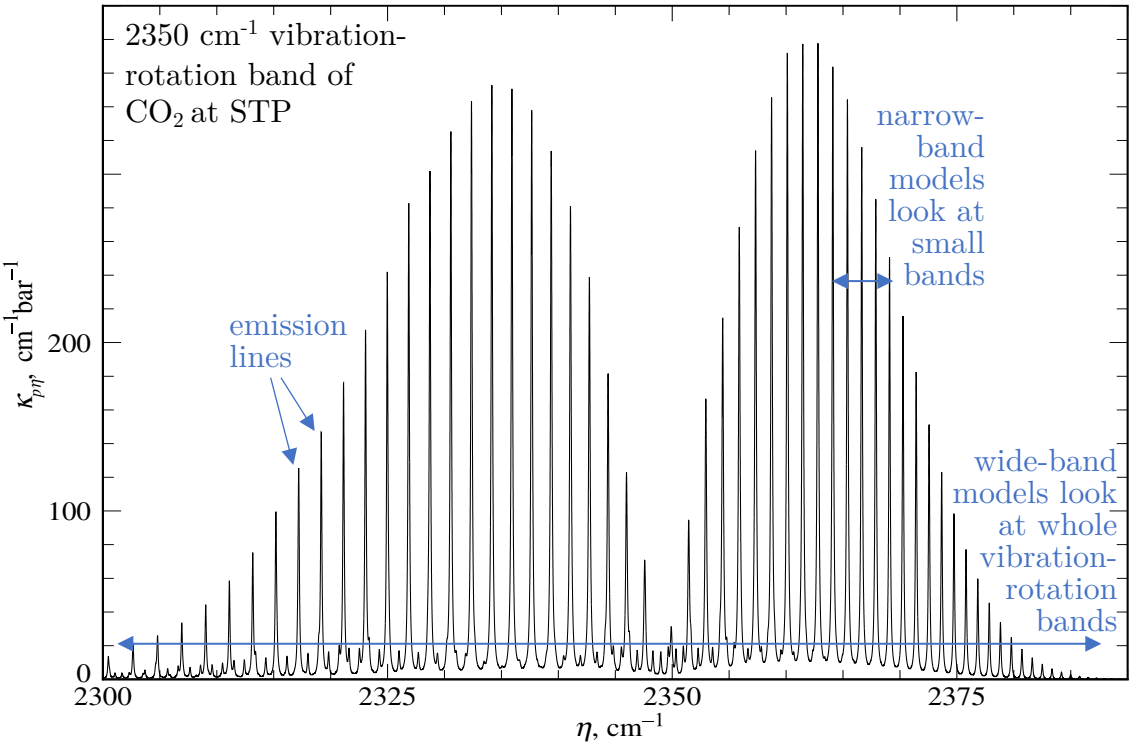

Figure 3-4: Molecular emission bands are modeled using line-by-line, narrow band, or wide-band models. Note that on the vertical axis, absorption coefficient is normalized by pressure. Modified from Ref. [26].

3.4.1 Narrow band models

Narrow band models consider spectral intervals that only cover a portion of a vibration-rotation band. They rely on the observation that, over small spectral intervals, variations in the intensity (i.e. the peak value of absorption coefficient for that spectral line) and spacing of spectral lines are typically relatively small [25, 27]. Following this

observation, narrow band models make assumptions about the distributions of line spacing, shape, and intensity within small spectral intervals.

Two broad categories of narrow band models exist: regular models, which assume a regular spacing of spectral lines; and random models, which assume a random spacing of spectral lines. Within these two categories, assumptions are made for the line shapes (collision, Doppler, or a hybrid), line widths, and the probability density function of the line strengths S. Some of the most commonly used narrow band models include:

- the regular Elsasser model, which assumes spectral lines with equal shape, spacing, half-width, and strength [35];
- the random Goody model, which assumes a random distribution of line positions, lines with equal shape and half-width, and an exponential distribution of line intensities (probability density function: $p(S) = \bar{S}^{-1} \exp(-S/\bar{S})$) [33]; and
- the random Malkmus model, which assumes a random distribution of line positions, lines with equal shape and half-width, and an exponential distribution of intensities for high-intensity lines and a distribution proportional to the inverse of the line strength for low-intensity lines (probability density function: $p(S) = S^{-1} \exp(-S/\bar{S})$) [36].

Based on the assumptions made for line shape, width, and strength, a narrow band model typically expresses optical depth τ (optical depth is defined in subsection 3.2.3) for homogenous media within a narrow spectral band as a function of two parameters. The first is the optical depth in the linear (optically thin, $\tau \sim \kappa L$) limit τ^*, calculated using

$$\tau^* = \frac{\bar{S}}{d} L \tag{3.12}$$

where $\bar{S}$ is the average line strength in the narrow spectral band, d is the average spacing between spectral lines, and L is path length. The second is the line overlap parameter β, calculated using

$$\beta = \pi \frac{\gamma}{d} \tag{3.13}$$

where γ is the line half-width.

3.4.1.1 The Curtis-Godson approximation for nonhomogeneous gases

For narrow band models, nonhomogeneous gases are typically treated with the Curtis-Godson approximation [37]. The approximation defines path-averaged parameters analogous to the two parameters described previously for narrowband models in subsection 3.4.1 that satisfy the optically thin and optically thick limits for optical depth. The Curtis-Godson approximation introduces error if there are large differences between line strengths or line spacings within the spectral band under consideration. A discussion of the procedures for calculating these path-averaged parameters is given in Section 10.6 of [26]. A random Goody narrow band model with the Curtis-Godson approximation was used for modeling exhaust plume radiant emission in this work.

3.4.2 Wide band models

Wide band models consider spectral intervals that cover entire vibration-rotation bands. Although typically less accurate than narrow band models, wide band models are simpler to implement and evaluate [26]. The most successful of these models is the exponential wide band model, originally developed by Edwards and Menard [38].

The exponential wide band model assumes that vibration-rotation bands have exponentially decreasing line intensities moving out from the band center [25, 26]. Each vibration-rotation band is characterized by a band strength parameter, a band width parameter, and a band center. The band strength and band width parameters are temperature dependent, and Edwards provides correlations for these in Ref. [39]. Further data compilations for computing these parameters can be found in section 9.3 of Ref. [25] and section 10.8 of Ref. [26].

Nonhomogeneity in wide band models is treated similarly to narrow band models. For the exponential wide band model, appropriate path-averaged values for the band strength and band width parameter can be used in calculations [39].

3.5 Radiative properties of particulate media

3.5.1 Overview

Some particulate media can be present in composite propellant exhaust plumes, notably soot and alumina (if an aluminum metal fuel was used) particles. Solid particles can cause changes to the spectral radiance in some viewing direction through both absorption and scattering. Energy losses due to particle absorption and scattering of energy away from the viewing direction is written in the same way as for gaseous absorption (see Equation 3.6):

$$dI_\lambda = -\kappa_{p\lambda} I_\lambda ds \tag{3.14}$$

$$dI_\lambda = -\sigma_{s\lambda} I_\lambda ds \tag{3.15}$$

where $\kappa_{p\lambda}$ is the absorption coefficient for particles and $\sigma_{s\lambda}$ is the scattering coefficient [26]. For compactness, attenuation of spectral radiance is often written in terms of an extinction coefficient β_λ such that

$$dI_\lambda = -\beta_\lambda I_\lambda ds \tag{3.16}$$

where the extinction coefficient accounts for attenuation due to both gases and particles:

$$\beta_\lambda = \sum_{gases} \kappa_{g\lambda} + \sum_{particles} \kappa_{p\lambda} + \sum_{particles} \sigma_{s\lambda}. \tag{3.17}$$

Energy gains due to in-scattering of radiant energy into some direction of study $\hat{\boldsymbol{s}}$ cannot be written simply as absorption and out-scattering. Determining the energy increment due to in-scattering requires knowledge of the radiant intensity in all incident directions which might scatter into $\hat{\boldsymbol{s}}$, as well as information regarding what fraction of the incident radiation is actually scattered into $\hat{\boldsymbol{s}}$. The increment due to in-scattering

is written as [26]

$$dI_\lambda = +\frac{\sigma_{s\lambda}}{4\pi}\left(\int_{\Omega_i=4\pi} I_\lambda(\hat{s}_i)\Phi_\lambda(\hat{s}_i,\hat{s})d\Omega_i\right)ds \tag{3.18}$$

where $\Phi_\lambda(\hat{s}_i,\hat{s})$ is the phase function, which describes what fraction of radiant energy from some incident direction $\hat{\boldsymbol{s}}_{\boldsymbol{i}}$ is scattering into the direction $\hat{\boldsymbol{s}}$. The term in the parentheses calculates the total amount of energy scattered from all directions into the direction $\hat{\boldsymbol{s}}$ (scaled by a factor of 4π due to the solid angle integral). The scattering coefficient $\sigma_{s\lambda}$ is then the proportionality coefficient between the increment in spectral radiance and its path length.

3.5.2 Radiative properties of a cloud of particles

Radiative properties of particles are typically determined under the assumption that particles have a spherical geometry. For a spherical particle, there are two main characterization parameters [25]:

- the complex index of refraction $m = n - ik$, and
- the particle size parameter $x = 2\pi a/\lambda$, where a is the particle radius and λ is the wavelength of radiation under consideration.

Several theories exist for predicting radiative properties for a spherical particle, depending on the particle's size parameter x. Particles with $x \ll 1$ are treated with Rayleigh theory [40], particles with with $x \gg 1$ are treated with geometric optics, and intermediate particles are treated with Mie theory [41, 42]. Given the wavelengths of interest (infrared, 1.5 µm to 5.5 µm) and the sizes particles present in exhaust plumes (soot and, depending on the propellant, alumina), Rayleigh and Mie particle treatments will be the most relevant.

For both treatments, the so called efficiency factors Q – which express the ratio of the event (i.e. absorption, scattering, or extinction) cross section C to the geometric cross section of a particle πa^2 – are used to determine absorption, scattering, and extinction coefficients for a particle. Efficiency factors for absorption, scattering, and

extinction are written as follows [26]:

$$Q_{abs} = C_{abs}/\pi a^2; \quad Q_{sca} = C_{sca}/\pi a^2; \quad Q_{ext} = C_{ext}/\pi a^2 \tag{3.19}$$

where $Q_{ext} = Q_{abs} + Q_{sca}$. Then, for a cloud of monodispersed particles, the absorption, scattering, and extinction coefficients can be found using:

$$\kappa_{p\lambda} = NC_{abs} = NQ_{abs}\pi a^2 \tag{3.20}$$

$$\sigma_{s\lambda} = NC_{sca} = NQ_{sca}\pi a^2 \tag{3.21}$$

$$\beta_{p\lambda} = NC_{ext} = NQ_{ext}\pi a^2 \tag{3.22}$$

where N is particle number density. If particles in the cloud are nonuniform in size, then absorption, scattering, and extinction coefficients are determined by integration over a particle size distribution function. The procedure for this is outlined in section 11.3 of Ref. [26].

For Mie theory, scattering and extinction efficiencies can be calculated using [25]:

$$Q_{sca}(m = n + ik, x) = \frac{2}{x^2}\sum_{n=1}^{\infty}(2n+1)\left(|a_n(m,x)|^2 + |b_n(m,x)|^2\right) \tag{3.23}$$

$$Q_{ext}(m = n + ik, x) = \frac{2}{x^2}\sum_{n=1}^{\infty}(2n+1)\,\Re(a_n(m,x) + b_n(m,x)) \tag{3.24}$$

$$Q_{abs}(m = n + ik, x) = Q_{ext}(m = n + ik, x) - Q_{sca}(m = n + ik, x) \tag{3.25}$$

where a_n and b_n are complex functions of m and x. A full derivation of Mie theory is given by Hulst [43]. The scattering phase function $\Phi_\lambda(\hat{s}_i, \hat{s})$ can be determined using an expression developed by Chu and Churchill:

$$\Phi_\lambda(\theta) = 1 + \sum_{n=1}^{\infty} A_n P_n(\cos\theta) \tag{3.26}$$

where θ is the angle between $\hat{\boldsymbol{s}}_{\boldsymbol{i}}$ and $\hat{\boldsymbol{s}}$, P_n are Legendre polynomials, and A_n is a function of a_n and b_n [44].

If particles are small enough, Rayleigh theory can be used instead of Mie theory, which offers many simplifications. In the Rayleigh treatment of particles, the efficiency factors can be written as [26]:

$$Q_{sca}(m = n + ik, x) = \frac{8}{3}\left|\frac{m^2 - 1}{m^2 + 2}\right|^2 x^4 \tag{3.27}$$

$$Q_{ext}(m = n + ik, x) = -4\Im\left(\frac{m^2 - 1}{m^2 + 2}\right) x \approx Q_{abs}. \tag{3.28}$$

Since, for small particles, $x^4 << x$, scattering is negligible in comparison to absorption, and $Q_{ext} \approx Q_{abs}$. The phase function for Rayleigh theory is also much simpler, given by [26]:

$$\Phi_\lambda(\theta) = \frac{3}{4}\left(1 + \cos^2\theta\right). \tag{3.29}$$

Rayleigh theory is typically used for soot particles, which is discussed more specifically in the following subsection. Mie theory would be used for alumina particles from aluminized propellants, however these propellants are not considered in this work, as mentioned in section 1.3.

3.5.3 Radiative properties of soot clouds

Soot is present in solid rocket motor plumes due to incomplete combustion of the hydrocarbon fuel [1]. Soot particle sizes are typically in the range of 5 nm to 80 nm [26], which makes Rayleigh theory appropriate for their spectral treatment when considering radiation wavelengths in the infrared.

Following from Equations 3.20 and 3.28, the scattering coefficient for a cloud of soot particles is negligible, and the absorption coefficient can be written as

$$\kappa_{p\lambda} = \frac{36\pi nk}{\left(n^2 - k^2 + 2\right)^2 + 4n^2k^2}\,\frac{f_v}{\lambda} \tag{3.30}$$

where f_v is the volume fraction of soot, n is the real part of the refractive index, k is the imaginary part of the refractive index, and λ is the wavelength [26]. Conveniently, $\kappa_{p\lambda}$ is not dependent on the particle size distribution for small particles such as soot, and can instead be determined from the volume fraction f_v [26]. The refractive index for soot is measured experimentally. Chang and Charalampopoulos provide data for soot refractive index, as well as polynomial fits for wavelengths in the range of 0.4 µm to 30 µm [45]:

$$n = 1.811 + 0.1263\ \ln\lambda + 0.0270\ln^2\lambda + 0.0417\ln^3\lambda \tag{3.31}$$

$$k = 0.5821 + 0.1213\ \ln\lambda + 0.2309\ln^2\lambda - 0.0100\ln^3\lambda \tag{3.32}$$

where the wavelength λ is in µm. These fits were used for modeling soot in the exhaust plumes in this work.

Chapter 4

Literature Review: Typical Properties and Modeling Practices for Plume Radiant Emission

Many previous studies have measured and modeled exhaust plume radiant emission for solid rocket motors. This chapter reviews specific characteristics for infrared spectra for solid rocket motor exhaust plumes. Typical modeling approaches used by other studies are also discussed, as well as general behavior and scaling laws for exhaust plume radiant emission.

4.1 Representative radiant emission spectra for solid rocket motors

Water vapor, carbon dioxide, carbon monoxide, and hydrochloric acid are the dominant emitting gaseous species in solid rocket motor exhaust plumes with ammonium perchlorate composite propellants [1]. The band center and band strength for several of the vibration-rotation bands for these species are given in Table 4.1. Hydrogen and nitrogen gas are also present in rocket exhaust plumes, however they do not emit

in the infrared since the molecules do not have a dipole moment, as discussed in section 3.1.

Molecular species	**Band center** μm [cm^{-1}]	**Band strength** $cm^{-1}/(g\,m^{-2})$
H_2O	2.7 [3660]	1.8
CO_2	4.3 [2350]	130
CO_2	2.7 [3660]	3.5
CO	4.7 [2140]	22
HCl	3.5 [2890]	10

Table 4.1: Several molecular species in propellant combustion products have vibration-rotation bands in the infrared. Data compiled from Ref. [32].

Calculated and measured emission spectra for a typical solid rocket motor using a non-aluminized AP/HTPB propellant is shown in Figure 4-1. The spectra show the vibration-rotation bands for the gaseous species in the exhaust at the expected locations given in Table 4.1.

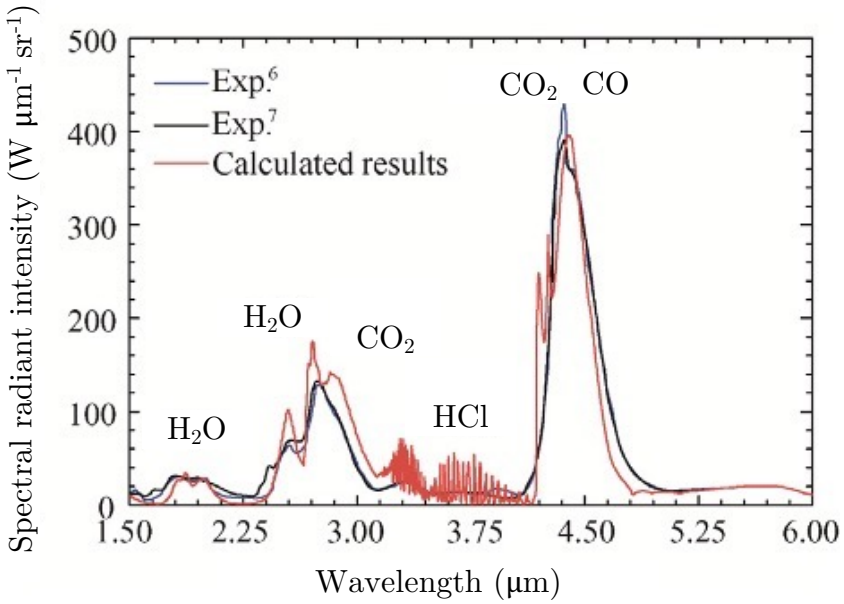

Figure 4-1: The infrared emission spectra for solid rocket motors contain emission bands for H_2O, CO, CO_2, and HCl. Adapted from Ref. [46].

4.2 Typical practices in rocket exhaust plume radiant emission modeling

This section will review modeling approaches used in other studies for predicting exhaust plume radiant emission and provide context for the radiant emission model developed for this work, which is presented in chapter 6.

4.2.1 Overview of exhaust plume radiant emission studies

Modeling of exhaust plume radiant emission is still an active area of research. A number of studies have investigated various plume modeling methods for motors with different characteristics. Avital et al. and Devir et al. compared spectral radiant intensity measurements from a small ballistic evaluation motor with a non-metallized ammonium perchlorate composite propellant to the output of a radiative transfer code [47, 48]. Wang et al. compared spectral measurements of three different double-base propellants with plume simulations that coupled plume flow field with radiative transfer [49]. Zhang and Li modeled plume emission for motors across one order of magnitude of size scales [50]. Stowe et al. compared results of a developed plume CFD code to radiometric imagery from a test motor with AP/HTPB propellant [51]. Rialland et al. compared radiation measurements from a sounding rocket with a metallized ammonium perchlorate composite propellant with outputs from developed CFD and radiative transfer codes [52]. Niu et al. developed a tool for modeling radiative outputs of non-metallized propellants; computational results were compared to radiative outputs of small ballistic evaluation motors with different operating conditions for afterburning, chamber pressure, and propellant formulation [46]. Niu et al. implemented a simplified method for evaluating plume radiant emission and compared results to Atlas II motor reference data [53]. Kim et al. simulated radiative outputs of motors with two different binders with varying altitudes, flight speeds, and motor size [54].

4.2.2 Typical modeling approach

Many of the studies mentioned in subsection 4.2.1 used the same overarching plume modeling approach, which is illustrated in Figure 4-2.

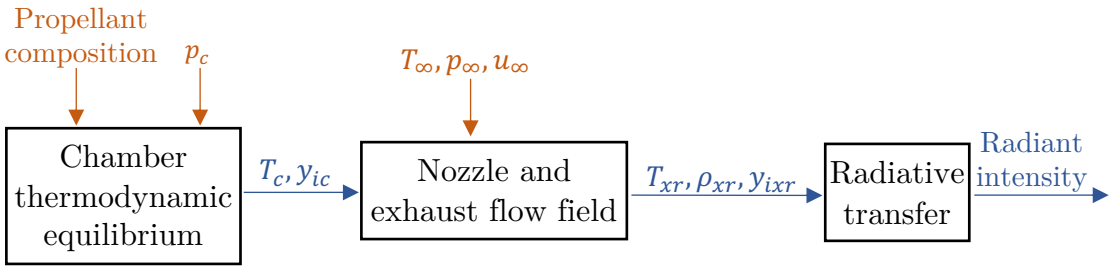

Figure 4-2: A typical exhaust plume modeling approach typically consists of three sub-models computed in series: chamber thermodynamic equilibrium, nozzle & exhaust flow field, and radiative transfer. This flow chart provides a summary of these sub-models along with their inputs and outputs.

There are three general modeling steps:

1. The *chamber thermodynamic equilibrium* model determines combustion gas properties – including combustion chamber gas temperature T_c and combustion gas mass fractions y_{ic} – from a known solid rocket propellant formulation.

2. The *nozzle and exhaust flow field* model determine flow properties throughout the nozzle and plume flow field, including density ρ_{xr}, temperature T_{xr}, and species mass fractions y_{ixr}. The nozzle and flow field properties can be computed separately or jointly. An afterburning kinetics scheme is coupled with the exhaust flow field calculations to capture the effects of afterburning in the plume.

3. The *radiative transfer* model determines the spectral radiance I_λ [W µm^{-1} sr^{-1} m^{-2}] and spectral radiant intensity J_λ [W µm^{-1} sr^{-1}] by evaluating the radiative transfer equation (see section 3.2). The radiation energy flow is typically several orders of magnitude smaller than other energy flows in the plume (mass flow, entrainment, or combustion), and therefore it is common practice to perform the radiative transfer calculations in series with the flow field calculations rather than in parallel [55]. An appropriate model for the species spectral properties in the exhaust plume is used to determine the optical depth of the plume.

For each of these modeling steps, there are a number of methods and approaches. A summary of the modeling methods used by a collection of other studies is presented in Table 4.2. All studies reviewed for this thesis that specified their methods for chamber properties used a thermodynamic equilibrium code, typically CEARUN [20]. The nozzle and exhaust flow field models were typically computed jointly with a 2D axisymmetric CFD code and using a finite rate kinetics mechanism for the afterburning kinetics. The radiative transfer models used discretization or line-of-sight methods for evaluating the radiative transfer equation; models and parameters for determining absorption coefficient and optical depths were typically based on Ref. [27]. Further discussion of some of these modeling methods is given subsequently in subsection 4.2.3. These modeling methods and approaches were used to inform the end-to-end differentiable radiant emission model developed for this thesis, which is discussed in chapter 6.

4.2.3 Typical modeling methods

For the general modeling steps and related models for evaluating exhaust plume radiant emission introduced in subsection 4.2.2, several modeling methods exist. The following sections provide additional details on these different modeling methods.

4.2.3.1 Chamber

Standard practice for determining combustion chamber temperature and mass fractions is to assume equilibrium conditions given the high pressures and temperatures. All studies reviewed for this thesis that specified methods for calculating chamber properties used a thermodynamic equilibrium code, as summarized in Table 4.2. Thermodynamic equilibrium codes follow a standard procedure, which was already outlined in section 2.5.

Study	Chamber	Nozzle	Flow field	After-burning kinetics	Radiative transfer	Spectral properties
[47], [48]	CEARUN [20]	Computed jointly with GASP code [56]		10 reaction mechanism	"Intuitive derivative" approach [57]	Model from [27]
[49]	Not specified	Computed jointly with 2D axisymmetric CFD		10 reaction mechanism	Discrete ordinates method [26]	Mean κ_λ for 7 spectral bands w/ HITRAN data
[50]	CEARUN [20]	Computed jointly with 2D axisymmetric CFD		17 reaction mechanism	Finite volume method	Model from [27]
[51]	CEARUN [20]	CEARUN [20]	2D axisymmetric CFD	25 reaction mechanism	Finite volume method	NBM w/ data from [58]
[52]	Custom thermodynamic equilibrium code	Computed jointly with 2D axisymmetric CFD		17 reaction mechanism	Spherical harmonics discrete ordinates method [59]	Multiple line group model [27]
[46]	CEARUN [20]	Computed jointly with 2D axisymmetric CFD		30 reaction mechanism	Line-of-sight method	Single line group model [27]
[53]	N/A	N/A	1D Woodroffe [55] model	10 reaction mechanism	Line-of-sight method	Single line group model [27]
[54]	CEARUN [20]	Computed jointly with 2D axisymmetric CFD		17 reaction mechanism	Line-of-sight method	Model from [27]

Table 4.2: Several approaches have been used in the literature to evaluate each of the modeling steps required for predicting exhaust plume radiant emission. This table provides a summary of the approaches used by studies in the literature.

4.2.3.2 Nozzle and exhaust flow field

The majority of studies summarized in Table 4.2 computed the nozzle and exhaust flow fields jointly using a computational fluid dynamics (CFD) code assuming 2D axisymmetric flow. The codes include coupled models for turbulence and afterburning kinetics. Some of the codes couple the effects of radiative transfer in the flow field energy calculations, although multiple studies have found that the effects of radiation on the flow field are small [51, 55].

Another approach is to consider the nozzle and exhaust flow field separately [51, 60]. In this case, flow parameters at the nozzle exit are determined assuming isentropic flow, and assuming either frozen or equilibrium chemistry in the nozzle. The flow field can still be calculated with CFD starting at the nozzle exit. Alternatively, a simplified 1D exhaust plume flow field model originally proposed by Woodroffe can be applied [55], which was utilized in a number of other studies [1, 53, 61].

4.2.3.3 Afterburning kinetics

For all reviewed studies, afterburning kinetics was modeled with a standard finite rate kinetics scheme (although the studies chose different sets of reactions and corresponding rate coefficients). Chemical reactions were modeled as either reversible elementary reactions or three-body reactions [62].

Elementary reactions have the form:

$$\mathrm{X_A A} + \mathrm{X_B B} \rightleftharpoons \mathrm{X_C C} + \mathrm{X_D D}$$

where A and B are reactants, C and D are products, and $\mathrm{X_i}$ are stoichiometric coefficients. Three-body reactions have the form:

$$\mathrm{X_A A} + \mathrm{X_B B} + \mathrm{M} \rightleftharpoons \mathrm{X_{AB} AB} + \mathrm{M}$$

where M is an unspecified third-body in a chemical reaction that can supply or remove energy that is necessary for the reaction to proceed. A forward rate coefficient k_f is modeled with an Arrhenius type expression:

$$k_f = AT^b e^{-E_a/\hat{R}T} \tag{4.1}$$

where A is the pre-exponential factor, T is temperature, b is temperature exponent, $\hat{R}$ is the ideal gas constant, and E_a is activation energy. The forward reaction rate r_f $[\mathrm{mol\,m^{-3}\,s^{-1}}]$ is calculated for elementary reactions using:

$$r_f = k_f \prod_{i=0}^{\substack{species,\\ reactant}} [i]^{\mathrm{X_i}} = k_f \, [A]^{\mathrm{X_A}} \, [B]^{\mathrm{X_B}} \tag{4.2}$$

where bracketed quantities are concentrations $[\mathrm{mol\,m^{-3}}]$. For three-body reactions, the forward reaction rate is calculated using:

$$r_f = k_f \prod_{i=0}^{\substack{species,\\ reactant}} [i]^{\mathrm{X_i}} = k_f \, [A]^{\mathrm{X_A}} \, [B]^{\mathrm{X_B}} \, [M] \tag{4.3}$$

$[M]$ is an effective third body concentration calculated with

$$[M] = \sum_i \epsilon_i \, [i] \tag{4.4}$$

where i is species and ϵ_i is the third-body efficiency of species i [62]. The backward reaction rate is calculated using:

$$r_b = k_b \prod_{i=0}^{\substack{species,\\ product}} [i]^{\mathrm{X_i}} \tag{4.5}$$

where k_b is the backward rate coefficient which can be calculated with $k_b = k_f / k_c(T)$, where $k_c(T)$ is the reaction equilibrium constant.

The net species production rate is then found using

$$\dot{\omega}_i = M_i \sum_{k=1}^{reactions} \left(X_{i,k}^{product} - X_{i,k}^{reactant} \right) \left(r_{f,k} - r_{b,k} \right) \tag{4.6}$$

4.2.3.4 Radiative transfer

Some of the most common methods for solving the radiative transfer equation (RTE) given in Equation 3.1 to evaluate the plume spectral radiance include the finite volume

method and the discrete ordinates method [26]. Many studies summarized in Table 4.2 used one of these methods. Finite volume methods solve the RTE by discretizing the computational domain into a mesh of finite volumes, and then evaluating fluxes at the bounding surfaces. The discrete ordinates method discretizes the RTE at some coordinate into a set of discrete directions that spans the total solid angle 4π. Integrals over solid angle in the RTE are then replaced with appropriately weighted summations.

If no scattering particles are present, then the plume spectral radiance along a line-of-sight through the plume is independent of gas properties along any other line-of-sight. In this case, line-of-sight methods are attractive, which simply integrate the RTE along a line-of-sight as viewed from some arbitrary position to determine the spectral radiance. The line-of-sight is often discretized into smaller lengths that can be assumed isothermal to further simplify the integration. The line-of-sight concept is illustrated in Figure 4-3.

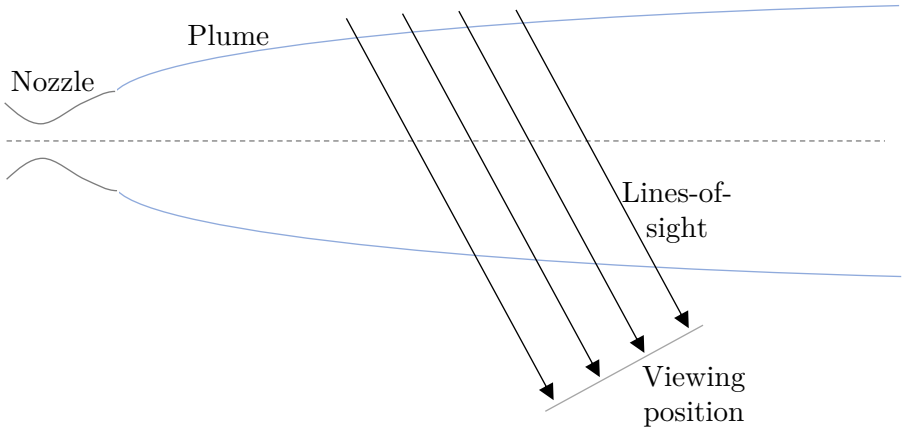

Figure 4-3: Integrated spectral radiance along lines-of-sight through a plume are independent of each other if no scattering particles are present.

4.2.3.5 Spectral properties

The spectral properties of the gas – namely absorption coefficient and optical depth – can be calculated using line-by-line models, narrow band models (NBM), and wide band models, as discussed in section 3.4. All of the reviewed studies used a narrow band model, which is typically a good compromise between complexity and accuracy.

The majority of the studies used one of two models developed by Ludwig et al. [27]: the single line group (SLG) model and the multiple line group (MLG) model. Both models use a functional relation for predicting the optical depth based on an approximation of a Voigt line profile (as mentioned in subsection 3.3.4, the Voigt line profile does not have a closed-form solution), which enables the effects of both Doppler and collision broadening to be included.

The single line group model assumes that there are no large differences between individual spectral line strengths within a narrow spectral band, and therefore the Curtis-Godson approximation (introduced in subsubsection 3.4.1.1) can be applied to all lines within a spectral band. If it cannot be assumed that lines within a spectral band are of similar strengths – for example, if there are large temperature gradients which might cause significant changes in line strengths within a spectral band along a line-of-sight – then the multiple line group model can be used. The MLG model breaks the lines within a spectral band into multiple groups, and then it is assumed that each group of lines has similar line strength and that the Curtis-Godson approximation can be applied to each group.

4.3 General behavior and scaling laws for exhaust plume radiant emission

4.3.1 Scaling laws for motor thrust, mass flow rate, and size

Following the definition of emissivity given in Equation 3.5, the spectral radiance I_λ for an isothermal, non-scattering medium can be written as $I_\lambda(T) = I_{b\lambda}(T)\epsilon_\lambda$. Following the equation for spectral radiant intensity J_λ given in Equation 3.2, $J_\lambda \sim I_\lambda(T)A_{projected}$. Combining these expressions, an approximate scaling relation for spectral radiant intensity is: $J_\lambda \sim I_{b\lambda}(T)A_{projected}\epsilon_\lambda$.

To first order, $F \sim \dot{m}$. Then, following the plume scaling analysis given by Simmons in section 6.3 of Ref. [1], for solid rocket propelled vehicles where the exhaust velocity greatly exceeds the vehicle velocity, a balance of forces acting on the exhaust

plume yields $D_{plume} \sim F^{1/2} p_a^{-1/2}$, where D_{plume} is the plume diameter and p_a is the ambient pressure. If the plume projected area is proportional to D_{plume}^2, then to first order it follows that:

$$J_\lambda \sim I_{b\lambda}(T)\epsilon_\lambda A_{projected} \sim I_{b\lambda}(T)\epsilon_\lambda D_{plume}^2 \sim I_{b\lambda}(T)\epsilon_\lambda \frac{F}{p_a} \sim I_{b\lambda}(T)\epsilon_\lambda \frac{\dot{m}}{p_a} \tag{4.7}$$

This scaling expression can be inspected for the limiting cases of emissivity ϵ_λ when the plume is optically thin ($\tau_\lambda \ll 1$) and optically thick ($\tau_\lambda \gg 1$), which are discussed in subsection 3.2.4. For the optically thin case, $\epsilon_\lambda \approx \tau_\lambda \sim \kappa_\lambda D_{plume}$. Therefore, for plumes that are optically thin, have scale-invariant temperature and species distributions throughout the plume, and where the ambient pressure is approximately constant, $J_\lambda \sim D_{plume}^3 \sim F^{3/2} \sim \dot{m}^{3/2}$. For the optically thick case, $\epsilon_\lambda \approx 1$. Therefore, for plumes that are optically thick, have scale-invariant temperature and species distributions throughout the plume, and where the ambient pressure is approximately constant, $J_\lambda \sim D_{plume}^2 \sim F \sim \dot{m}$. These relations are consistent with the scalings mentioned by Rudman and Hibbeln in Ref. [63]. These relations do not account for higher order effects, such as the effects of motor chamber pressure on radiant intensity J_λ for fixed burn area A_b. Radiant emission scaling for small, optically thin, fixed burn area motors will be discussed in section 8.2.

As already noted, these scaling laws are only valid for plumes where the temperature and species distributions remain scale-invariant throughout the plume. This is generally true for plumes exhibiting frozen flow (no afterburning reactions in the plume progress; excess fuel in the exhaust remains unburnt) or equilibrium flow (afterburning reactions occur quickly; excess fuel in the exhaust burns almost instantly with oxygen as it is entrained). Although the temperature and species distributions are scale-invariant within the equilibrium or frozen regimes, changes in size scale can cause a significant change between the regimes. The progression of afterburning kinetics is dependent on the size scale of the plume, and the flow can transition from frozen to equilibrium just by increasing the size scale of the motor. One of the contributions of this thesis is the characterization of the effects of motor size scale on afterburning kinetics in

the plume, and how this alters the temperatures and radiant intensity of the plume. These phenomena are discussed in section 8.1.

4.3.2 Soot

Exhaust plumes contain soot due to incomplete combustion of carbon-containing fuels. Few sources report data for actual soot loadings in solid rocket motor combustion products, although Vernacchia measured an average soot mass-loading of 1.35 % for an AP/HTPB propellant containing 5 % oxamide [14]. The addition of excess graphite in the propellant formulation and use of ablative insulators may also increase the amount of soot in the exhaust.

Following from the discussion of the radiative properties of soot clouds in subsection 3.5.3 and the absorption coefficient for soot given in Equation 3.30, to first order the absorption coefficient for a soot cloud scales like $\kappa_{\lambda,soot} \sim f_v/\lambda$. This scaling suggests that soot should have the largest effect on plume emittance at smaller wavelengths. This effect can be seen in Figure 4-4, which compares the plume spectral radiance for two same-thrust engine firings using different propellants: O_2/RP-1 and O_2/ethanol. The O_2/ethanol engine produces minimal soot, and shows a relatively small amount of plume emittance in the 1 µm to 2 µm band (top subfigure). Conversely, the O_2/RP-1 engine produces significant amounts of soot, and consequently the plume produces a blackbody-like emittance in the 1 µm to 2 µm band (bottom subfigure). The effect of the soot at longer wavelengths becomes negligible since $\kappa_{\lambda,soot} \sim 1/\lambda$.

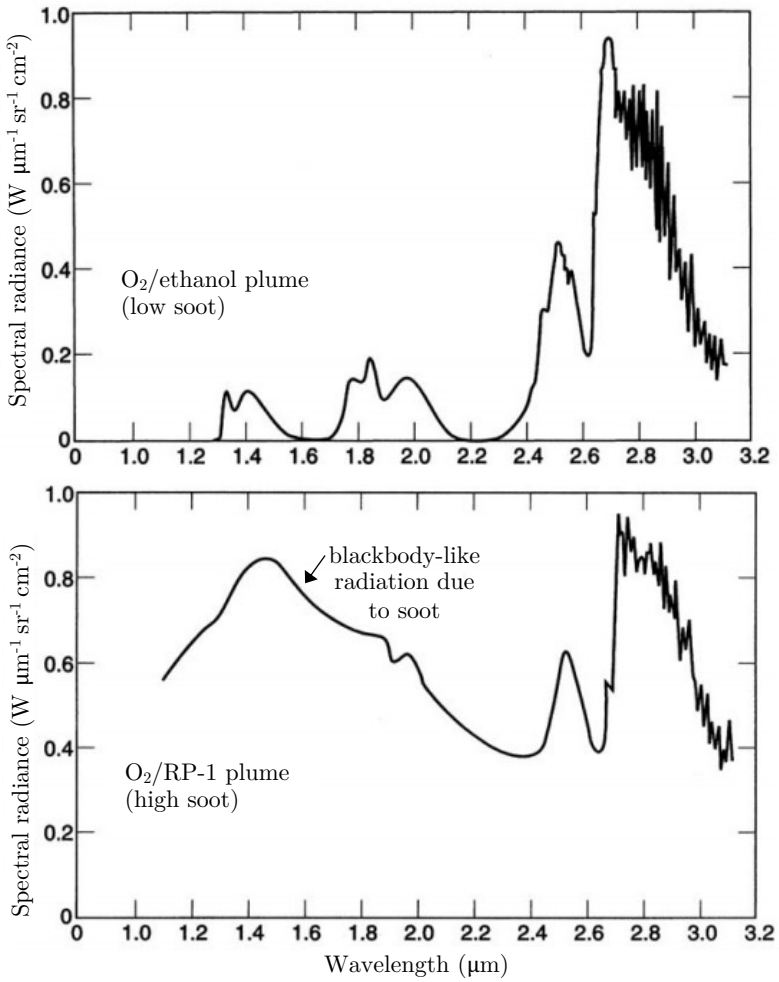

Figure 4-4: Exhaust plumes containing soot, such as from engines burning O_2/RP-1, show a black-body like emittance at small wavelengths, while exhaust plumes from cleaner-burning propellants such as O_2/ethanol do not. Reprinted from Ref. [1].

4.3.3 Oxamide burn rate suppressant

As discussed in subsection 2.4.2, oxamide is a coolant that can be added to a solid propellant to reduce its burn rate. Its decomposition at the burning surface of a propellant grain creates cyanogen $(CN)_2$ gas and water vapor [64]. Cyanogen subsequently burns with oxygen gas to form carbon dioxide and nitrogen gas [65]. Therefore the ultimate products of oxamide decomposition and combustion – H_2O, CO_2, and N_2 – are already present in solid rocket exhaust plumes. Consequently, the inclusion of oxamide in a propellant should not create any new vibration-rotation bands in the exhaust plume emission. Additionally, the reduced burn rate due to

the addition of oxamide should (for fixed chamber pressure) lead to reduced mass flow rate and subsequently reduced plume spectral radiant intensity and total radiant intensity, as discussed in subsection 4.3.1.

Chapter 5

Experimental Measurements for Small, Slow-burning Solid Rocket Motors

To understand radiant emission phenomena for small, low-thrust motors such as those used for the Firefly aircraft (introduced in subsection 1.2.2), a series of experiments measuring exhaust plume radiant emission for motors at this size scale were conducted. To the author's knowledge, these experiments represent the lowest thrust levels for which rigorous plume radiant intensity measurements have been obtained and the only plume radiant intensity measurements for propellants containing oxamide in the open literature. The experimental data are also used in chapter 7 to validate the performance of the differentiable radiant emission model discussed in chapter 6 for small solid rocket motors and propellants doped with oxamide.

This chapter describes the motor design and manufacturing, propellants, test setup, data processing, and results of these experiments. A small, low-thrust research motor – with similar size, thrust levels, and propellants as the Firefly aircraft – was designed, manufactured, and fired. Measurements of motor chamber pressure, thrust, and exhaust plume radiant emission were collected for varying nozzle diameters and propellant compositions.

5.1 Experiment overview

Experiments measured chamber pressure, thrust, and exhaust plume radiant emission for a small, end-burning solid rocket motor. The same end-burning motor configuration was used for all experiments, such that each motor firing had the same propellant burning area. The design of this motor is discussed in section 5.2. The propellant composition and nozzle throat diameter were varied for the motor tests; propellant composition and nozzle throat diameter were the free design variables for these end-burning motors as discussed in subsection 2.1.1.

In total, eight static fires (SF) of research motors were conducted in the course of these experimental efforts. SF1 and SF2 were early shakedown tests of the motor design; minor design changes were made to the motor after these tests, and the motor hardware was updated for subsequent tests. SF3 was a shakedown test of the updated motor design (presented in section 5.2), and the first test collecting exhaust plume radiant emission measurements. SF4-SF7 made up the core test matrix for the exhaust plume radiant emission measurements for this thesis; the results of these tests are presented in section 5.6. SF8 had thermocouples embedded in the bond line between the nozzle and aft closure to evaluate thermal performance of the nozzle; this static fire is discussed in subsection 5.7.6.

The core test matrix of static fires (SF4 - SF7), illustrated in Figure 5-1, evaluated the effects of oxamide content and operating chamber pressure on exhaust plume radiant emission for small solid rocket motors. A baseline propellant formulation containing either 0 or 8 % oxamide was used for the tests. These propellants are described further in section 5.3. For each of the two oxamide contents, two static fires with different throat diameters were conducted. The throat diameters were varied so that the operating chamber pressure of the motors would be approximately 1.1 MPa and 2.2 MPa.

		Chamber pressure	
		~ 1.1 MPa	~ 2.2 MPa
Oxamide content	0%	SF4	SF5
	8%	SF6	SF7

Figure 5-1: A core test matrix of four static fires (SF) evaluated the effects of oxamide content and chamber pressure on exhaust plume radiant emission.

5.2 Test motor design

A consistent end-burning motor configuration was used for these experiments. A rendering of the motor design is given in Figure 5-2. A picture of the disassembled components of the motor is shown in Figure 5-3.

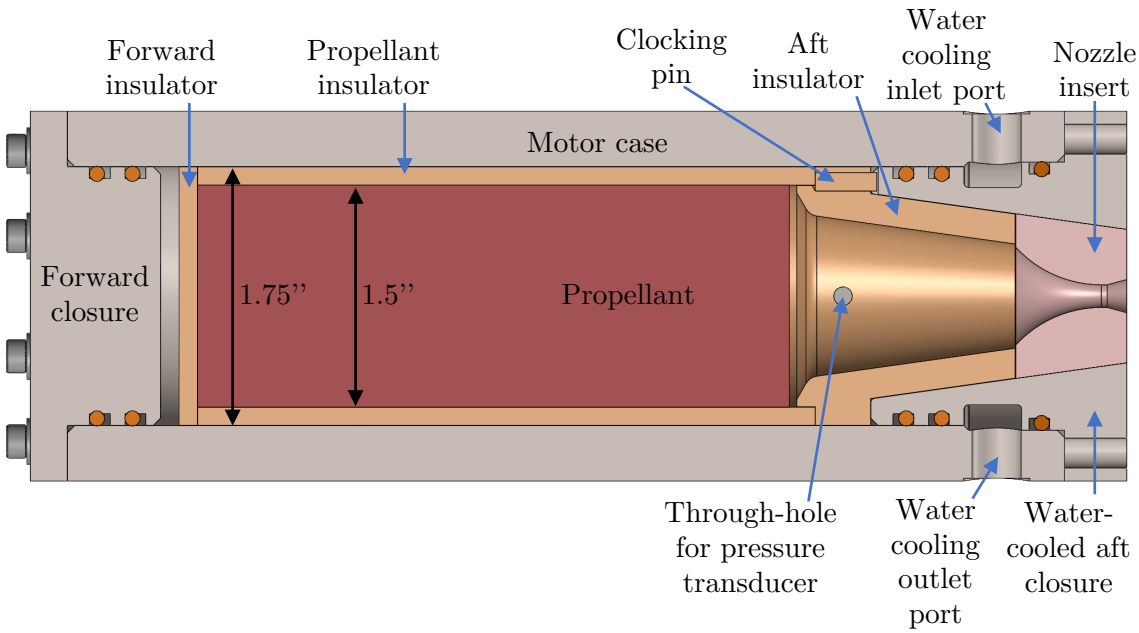

Figure 5-2: A consistent end-burning motor configuration was used for all motor tests. The motor design features a water-cooled nozzle and a replaceable nozzle insert. The gap between the forward insulator and forward closure was filled with silicone spacers during static fires.

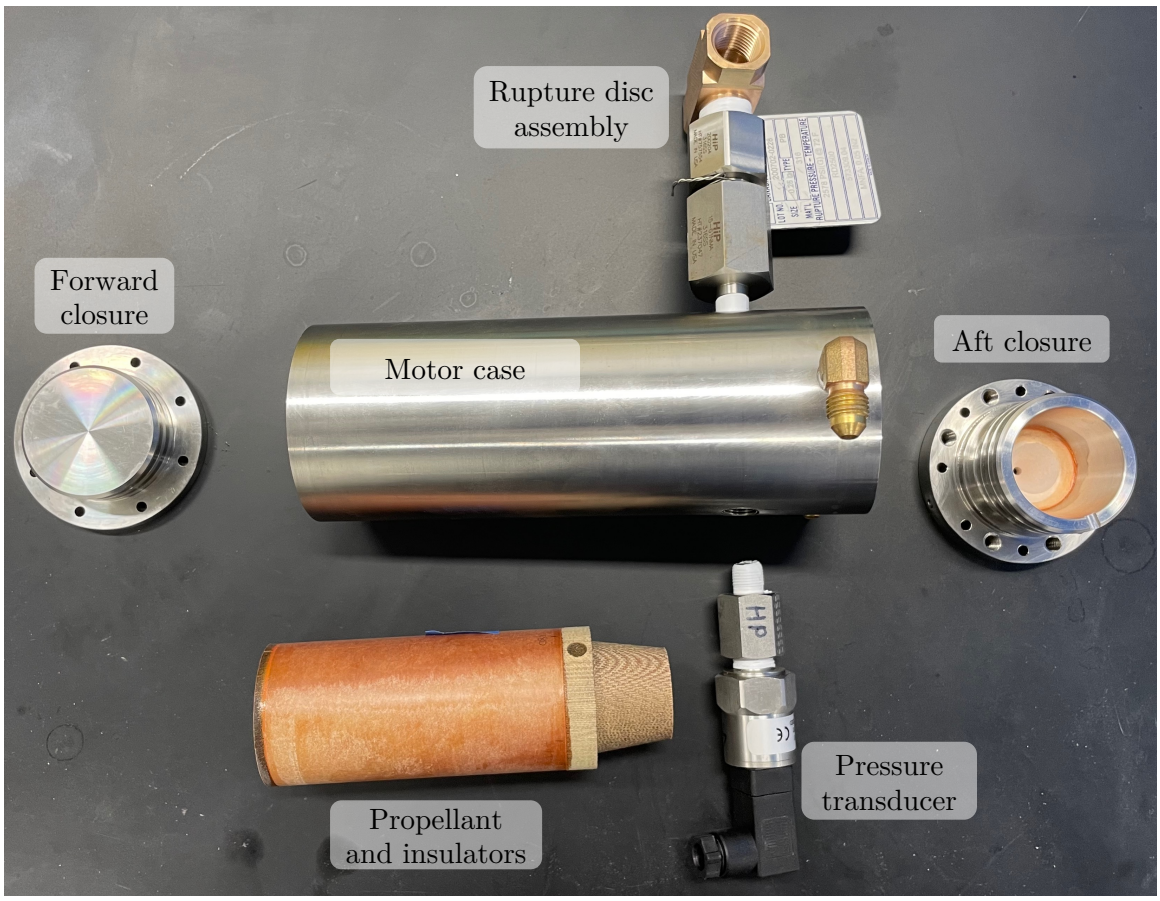

Figure 5-3: The test motor consisted of several components, including the motor case, closures, and propellant. A rupture disc assembly and pressure transducer were mounted to through-the-wall ports.

The thick-walled motor case, machined from 316 stainless steel to ensure corrosion resistance, allowed sufficient room for a through-the-wall NPT port for a pressure transducer to measure the motor chamber pressure. A rupture disc (not shown in Figure 5-2, but shown in Figure 5-3) was mounted to a through-the-wall NPT port to prevent hardware damage in the event of motor over-pressurization. The forward and aft closures were also machined from 316 stainless steel. The closures were each retained with eight axially oriented 6-32 screws. Redundant silicone o-rings were used for sealing each of the closures.

The aft closure was water-cooled to ensure the material maximum service temperature was not exceeded during the static fires. The aft closure assembly was designed such that there were no protrusions beyond the nozzle exit plane. This ensured that no

portion of the plume was shadowed during the plume radiant emission measurements. A slot on the aft closure interfaced with a pin in the aft insulator to ensure proper clocking. The interior of the aft closure was tapered to interface with the nozzle insert, which was bonded to the aft closure with a silicone adhesive. The tapered design was desirable, since the pressure load on the nozzle due to propellant combustion helped the nozzle insert to seal against the aft closure.

Swappable alumina-silicate nozzle inserts allowed the nozzle throat diameter (and thus the chamber pressure for a given propellant) to be changed by replacing a single component. This nozzle is discussed in further detail in section 5.7.

The forward insulator, aft insulator, and propellant insulator were all made from off-the-shelf phenolic composite. The propellant insulator also served as the casting tube, which streamlined the propellant manufacturing process described in subsection 5.3.3. The propellant insulator was made from Garolite XX phenolic tubing. More information on manufacturing the propellant insulator is given in section A.1. The forward insulator was waterjet cut from Garolite XX phenolic sheet. The aft insulator was turned from Garolite CE phenolic rod. More information on manufacturing of the aft insulator is given in section A.2.

5.3 Propellants

The motors tested in this work use a class of ammonium perchlorate composite propellants doped with the burn rate suppressant oxamide. This type of propellant and oxamide were introduced in section 2.4. This section provides specific details on the propellant formula, manufacturing, and characterization.

5.3.1 Propellant formula

Two different propellant formulations were used: a "baseline" formulation, and formulation with 8 % oxamide. The baseline propellant formulation for these experiments is shown in Table 5.1. It is an ammonium perchlorate and hydroxyl terminated polybutadiene propellant, and was previously characterized by Vernacchia et al. [3].

To create the 8 % oxamide formula, the baseline propellant formulation was diluted with the desired mass fraction of the additive. If a mass fraction w_{om} of oxamide is desired, then the new propellant formulation is created by scaling the mass fractions in Table 5.1 by a factor of $1 - w_{om}$, and then w_{om} oxamide is added.

Ingredient	**Chemical name**	**Manufacturer**	**Mass fraction**
Binder	Hydroxyl Terminated Polybutadiene (HTPB) Resin with HX-752 and CAO-5	RCS Rocket Motor Components	0.125
Plasticizer	Isodecyl Pelargonate (IDP)	RCS Rocket Motor Components	0.052
Opacifier	Graphite powder	Cretacolor	0.003
Oxidizer	Ammonium Perchlorate 400 Micron Blend	RCS Rocket Motor Components	0.800
Curative	Modified MDI Isocyanate	RCS Rocket Motor Components	0.020

Table 5.1: Baseline propellant formulation.

5.3.2 Propellant combustion products

The combustion products of the propellants are important since they determine which species are present and emitting in the motor exhaust plume. The combustion products of the baseline propellant described in subsection 5.3.1 doped with 0, 8, and 20% oxamide were computed, and are given in Table 5.2. The mole fractions of species were determined assuming equilibrium thermodynamics, a common assumption made when modeling hot, high pressure combustion reactions, as introduced in section 2.5. A custom thermodynamic equilibrium code was developed for this research, which is discussed in subsection 6.3.1.

Species	Mole fractions 0 % Oxamide	Mole fractions 8 % Oxamide	Mole fractions 20 % Oxamide
CO	0.251	0.259	0.265
CO_2	0.055	0.056	0.064
H_2	0.217	0.241	0.282
H_2O	0.250	0.220	0.170
HCl	0.149	0.135	0.114
N_2	0.076	0.088	0.106

Table 5.2: Equilibrium combustion products assuming 1 MPa chamber pressure for a few propellant oxamide mass fractions. Columns do not sum exactly to 1 due to rounding errors and existence of trace species.

5.3.3 Propellant manufacturing

Propellant grain manufacturing was completed in several steps. The oxidizer, opacifier, and burn rate suppressant were pre-measured. The binder and plasticizer were measured and machine mixed for several minutes. Then the opacifier and burn rate suppressant were added and mixed until incorporated. The oxidizer was then added slowly while the mixer was running. Once the oxidizer was incorporated, vacuum was pulled on the mixing bowl and the propellant was mixed under vacuum at a speed of $\sim$30 rev min^{-1} for two hours. Lastly, the curative was added to the mixing bowl through a valve in the mixer lid, and the propellant was mixed for an additional 10 minutes to incorporate the curative. The propellant was mixed in a custom vacuum mixer made from a heavily modified Bosch Universal Plus MUM6N10 kitchen mixer with a $\sim$6.2 L capacity, shown in Figure 5-4. A variac was used to provide further control of the mixing speed beyond the discrete speed options built into the mixer. Additional details regarding the propellant mixing process and the custom vacuum mixer can be found in the author's MS thesis [12].

After the propellant was mixed, the propellant was packed directly into pre-cut, primed off-the-shelf phenolic composite tubes, which also served as the propellant

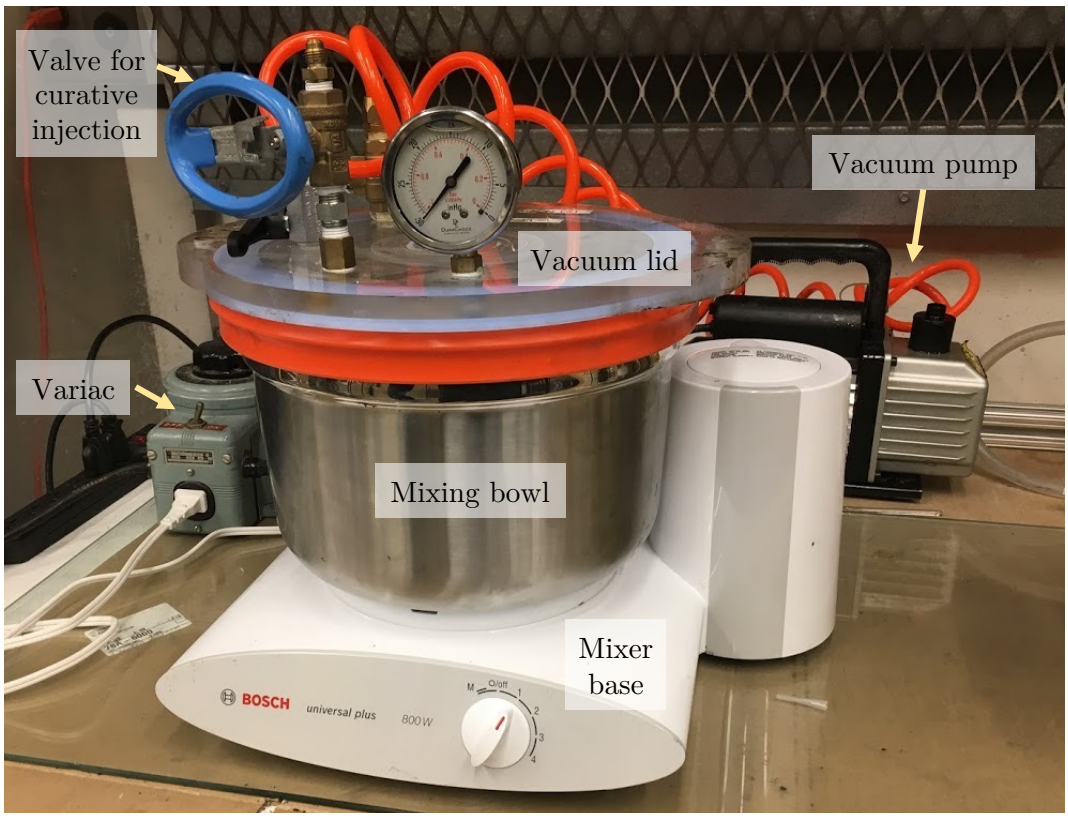

Figure 5-4: A custom propellant vacuum mixer was made from a heavily modified Bosch Universal Plus MUM6N10 kitchen mixer.

insulating liner as described in section 5.2. Many propellant grains were cast from each propellant mix.

5.3.4 Propellant inspection

All propellant grains were imaged with x-rays to inspect for voids or other defects within the grain. Two of these x-ray images are shown in Figure 5-5, showing grains with and without voids. Every x-ray image collected had two indicator propellant grains within the field of view. These indicator grains were the same size as the test grain, and had holes of known diameter drilled into the ends at different radial locations in the grain. The indicator grains provide verification in every image that any voids present in the test grain with dimensions greater than the holes in the indicator grains should be visible in the image.

Propellant grain with voids:

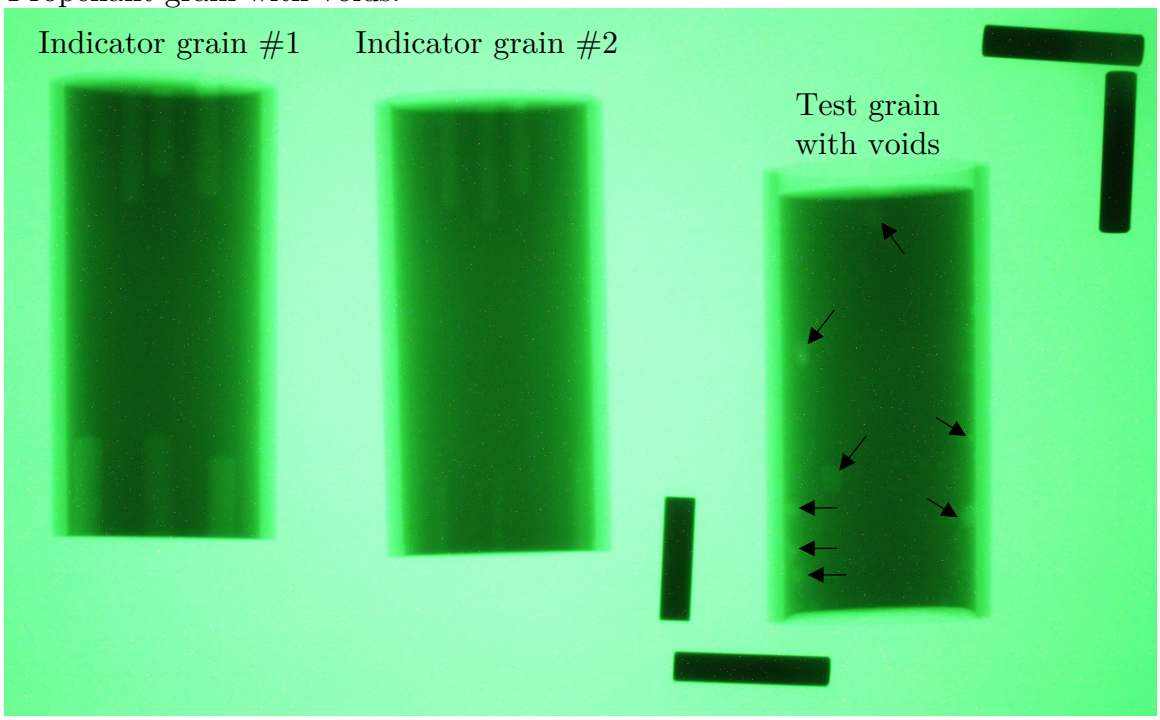

Propellant grain without voids:

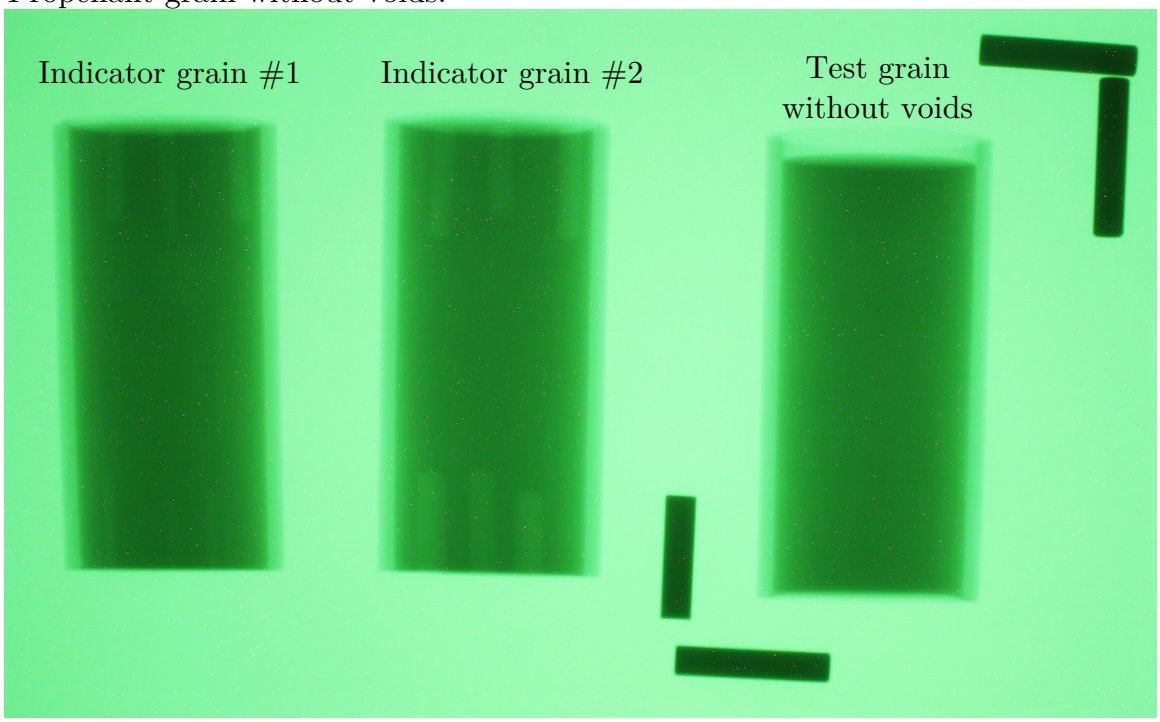

Figure 5-5: Propellant grains were inspected for voids with x-ray imagery. In the top image, a number of voids can be seen in the test grain, and consequently this grain was rejected for use in a static fire. The bottom image shows a void-free grain.

In the images shown in Figure 5-5, the two indicator grains are on the left, and the test grain is on the right. Many voids are visible in the test grain in the top image, which are pointed out with arrows. Propellants grains with significant voids were not used, since the voids would likely result in unpredictable propellant burning areas and motor chamber pressures. The propellant grain in the bottom image is a void-free example.

5.4 Test setup

All motor tests were conducted in a reinforced concrete blast chamber located on MIT campus, shown in Figure 5-6. The motors were mounted to a custom thrust stand (described in subsection 5.5.2) positioned in front of a high-emissivity background. Thrust, chamber pressure, and exhaust plume radiant emission measurements were collected for each motor; the instrumentation for these measurements is discussed in section 5.5. An exhaust duct was positioned downstream of the motor to collect the exhaust and vent it outside. This ventilation helped to prevent the exhaust gases from stagnating downstream of the motor and subsequently obstructing the exhaust plume radiant emission measurement.

5.5 Instrumentation and measurement procedures

5.5.1 Exhaust plume radiant emission

The exhaust plume radiant emission was measured using a CI Systems SR-5000N spectroradiometer. The radiometer used liquid nitrogen cooled indium-antimonide (InSb) and mercury-cadmium-telluride (MCT) photovoltaic detectors that together are sensitive to radiation from 1.2 µm to 14.2 µm. A continuous variable filter sampled the different wavelengths during measurements into 379 wavelength bins across the spectrum. The spectrum was scanned at a rate of 1 Hz at the maximum instrument gain setting. Measurements were made relative to a floating internal blackbody in the radiometer.

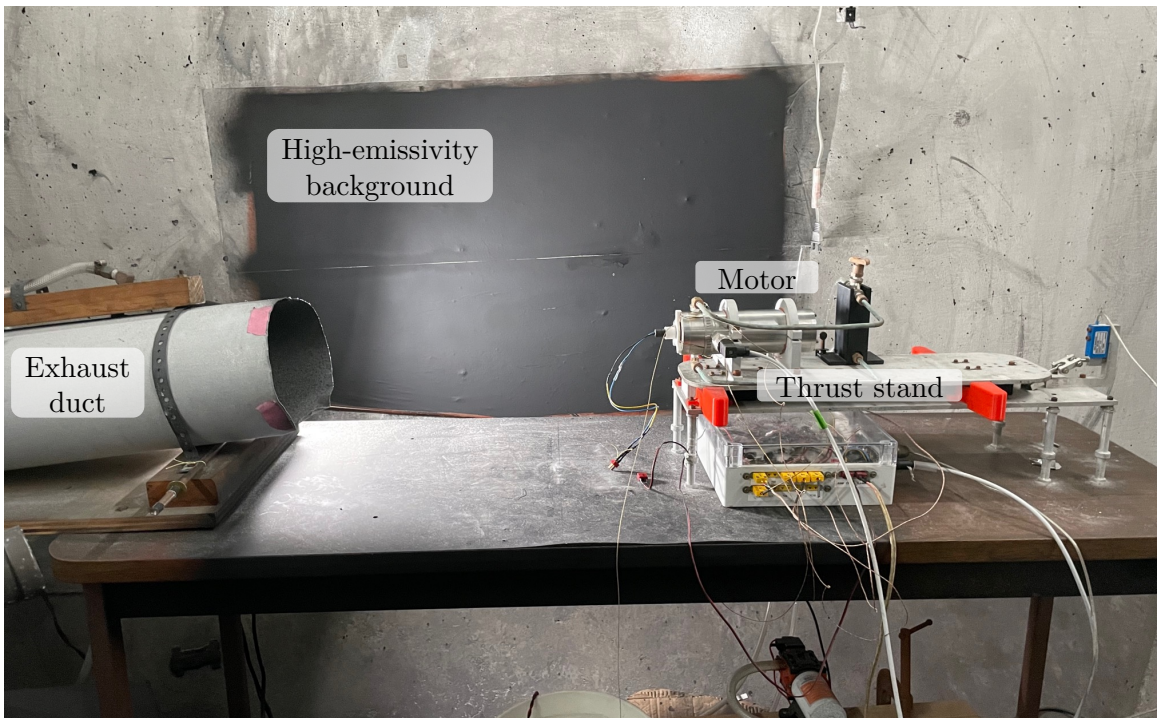

Figure 5-6: Test motors were mounted to a custom thrust stand positioned in front of a high-emissivity background. An exhaust duct helped to clear the blast chamber of exhaust products downstream of the motor.

The radiometer was kept in an enclosure[†] to protect it during the motor tests. For SF6 and SF7 (static fire numberings are discussed in section 5.1), the enclosure was continually cycled with air to cool the instrument electronics and maintain a constant instrument temperature (the importance of maintaining constant temperature is discussed in subsubsection 5.5.1.2). The enclosure had an optical window in front of the collecting optics of the radiometer. For SF4 and SF5, an uncoated zinc sulfide window with a transmittance from 60 % to 70 % for wavelengths from 0.4 µm to 12 µm was used. The measured signal level was small for these two tests, and so a different window with a higher transmittance was used for the next static fires. For SF6 and SF7, an uncoated calcium fluoride window with a transmittance of greater than 90 % for wavelengths from 0.2 µm to 7 µm was used.

Figure 5-7 illustrates the positioning of the radiometer with respect to the motor. The collection optics of the radiometer had an 18.7° field of view. The radiometer

[†]The author is very grateful to Dr. Michael Knotts for designing and building the enclosure.

was positioned 3.67 m away from the center axis of the exhaust plume, and the center of the optics were positioned to be 0.19 m downstream from the nozzle exit plane of the motor. The positioning was chosen to keep the plume within the center third of the field of view, which has a flatter measurement response from the radiometer optics. The concrete wall behind the motor served as a thermally stable background, given its large thermal mass. The wall was painted with a high-emissivity paint[†] to create a high-emissivity background for the radiant emission measurement, which prevented any reflection of radiation from the room or plume that might have altered the measurement.

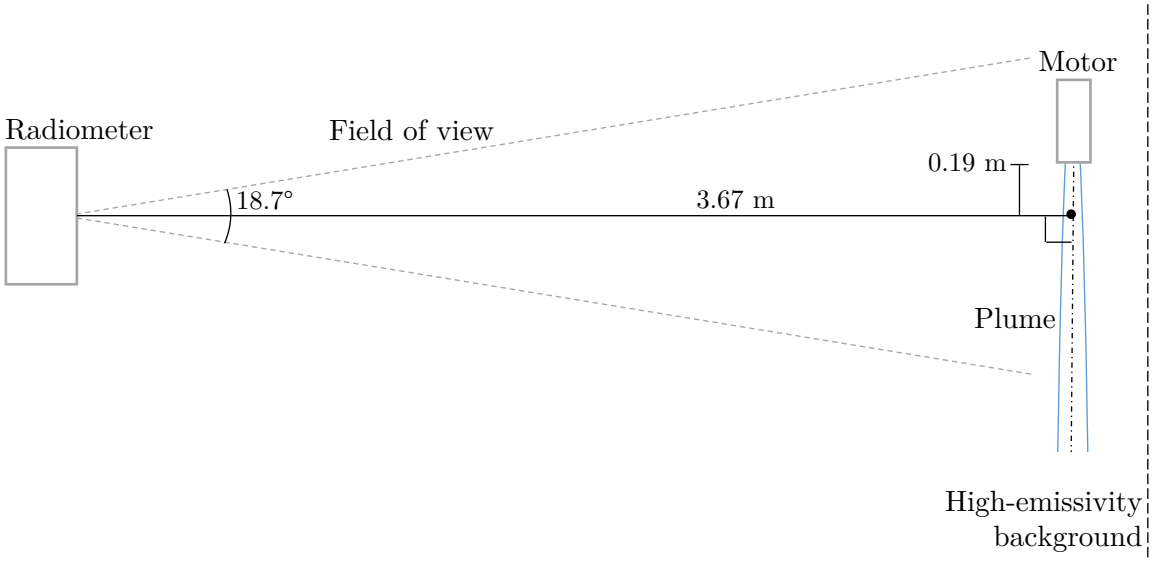

Figure 5-7: For exhaust plume radiant emission measurements, the radiometer was located 3.67 m away from the centerline of the plume. The center of the optics was positioned to be 0.19 m away from the nozzle exit plane on the motor.

5.5.1.1 Infrared radiation measurements

Four different radiometric measurements were needed for each motor static fire to enable the evaluation of exhaust plume radiant emission (see subsubsection 5.5.1.2). The radiometer measured incident infrared radiation in arbitrary units of "counts per unit detector gain", and so a calibration measurement of a known target was needed

[†]The wall behind the test setup was painted with Krylon Ultra Flat Black 1602 spray paint, which has an emissivity between 0.94 and 0.97 for wavelengths between 1.5 µm and 5.5 µm [66].

to map the plume measurements to "real world" units of $\mathrm{W\,sr^{-1}\,\mu m^{-1}}$. Additionally, since all measurements for this research were of targets that do not fill the field of view, measurements of the background were necessary so that the emittance of the targets relative to the background could be determined. For each motor static fire, the four collected measurements were:

Measurement 1: the exhaust plume, including all of the background within the field of view

Measurement 2: the background of the exhaust plume without the motor burning

Measurement 3: a calibrated laboratory blackbody with a known temperature and aperture area

Measurement 4: the background of the laboratory blackbody (i.e. a measurement of the laboratory blackbody with the aperture covered); this measurement is nearly identical to the background of the exhaust plume (Measurement 2)[†]

The calibration measurement (Measurement 3) was conducted immediately before the motor test firings with a Newport Oriel cavity style blackbody at a temperature of 1000 °C. The blackbody was placed the same distance away from the radiometer as the centerline of the motor plume (at 3.67 m away), and was positioned so that it was centered on the optics of the radiometer (at 0.19 m downstream of the nozzle exit plane), so that the radiometer did not need to be readjusted between calibration and plume measurements. Scans of the calibration blackbody were collected for 60 s. For the blackbody background measurement (Measurement 4), the aperture of the blackbody was covered with a piece of aluminum foil so that the background could be measured. Scans of the blackbody background were also collected for 60 s. The blackbody was subsequently removed, and the motor was fired. The radiometer measurements were collected starting 60 s before motor ignition and continuing through

[†]Measurement 4 was not collected separately for static fire SF4, and so Measurement 2 was substituted

the duration of the motor burn. The scans before motor ignition were used as the background measurement for the plume (Measurement 2), and the scans during the motor burn were used for the plume measurement (Measurement 1).

5.5.1.2 Evaluation of exhaust plume radiant intensity

The measurements described in subsubsection 5.5.1.1 had to be manipulated to determine the exhaust plume radiant emission $J_{\lambda,plume}$ in units of $\mathrm{W\,sr^{-1}\,\mu m^{-1}}$. The radiometer measures radiation contrast relative to an internal blackbody in units of "counts per unit detector gain". The signal reaching the detector for any measurement is proportional to the difference between (radiant intensity / [distance from detector]^2) for the environment within the detector field of view and the detector internal blackbody. For some measurement of a target not filling the field of view (such as the plume or laboratory blackbody), and assuming a constant background temperature and emissivity, this detector signal S can more formally be written as:

$$S_{target} \approx K_\lambda \left\{ \underbrace{\frac{J_{\lambda,target}}{L^2_{target}}}_{\text{target}} + \underbrace{\epsilon_{\lambda,bg} I_{b\lambda}(T_{bg}) \frac{A_{bg}}{L^2_{bg}}}_{\text{background}} - \underbrace{\epsilon_{\lambda,IBB} I_{b\lambda}(T_{IBB,target}) \frac{A_{IBB}}{L^2_{IBB}}}_{\text{detector internal black body}} \right\} \quad (5.1)$$

where L is distance from detector, A is projected area visible to the detector, ϵ is emissivity, and $I_{b\lambda}(T)$ is Planck blackbody intensity function $[\mathrm{W\,sr^{-1}\,m^{-2}\,\mu m^{-1}}]$. The quantity A/L^2 is the field of view (as seen by the detector) in units of steradians. K_λ is the response function, which is the proportionality constant that maps between detector signal and (radiant intensity / [distance from detector]^2) contrast within the field of view. Included in the response function are the effects of atmospheric transmittance along the path between the emitting environment and the detector, and the spectral width of the wavelength bins across the spectrum.

To eliminate the contribution of the background (the $\epsilon_{\lambda,bg} I_{b\lambda}(T_{bg}) \frac{A_{bg}}{L_{bg}^2}$ term in Equation 5.1), a second background measurement is collected:

$$S_{bg} \approx K_\lambda \left\{ \epsilon_{\lambda,bg} I_{b\lambda}(T_{bg}) \frac{A_{target}}{L_{target}^2} + \epsilon_{\lambda,bg} I_{b\lambda}(T_{bg}) \frac{A_{bg}}{L_{bg}^2} - \epsilon_{\lambda,IBB} I_{b\lambda}(T_{IBB,bg}) \frac{A_{IBB}}{L_{IBB}^2} \right\} \quad (5.2)$$

The difference between S_{target} and S_{bg} can then be evaluated, which eliminates the background term, assuming T_{bg} is approximately constant.

The response function K_λ can be determined by measuring a laboratory blackbody with a known temperature, area, emissivity, and distance to detector and evaluating $S_{LBB} - S_{LBB\_bg}$. Assuming emissivities $\epsilon_{\lambda,LBB}$, $\epsilon_{\lambda,IBB}$, and $\epsilon_{\lambda,LBB\_bg}$ are all ∼1, the response function is:

$$K_\lambda \equiv \frac{S_{LBB} - S_{LBB\_bg}}{\frac{A_{LBB}}{L_{LBB}^2} \left[I_{b\lambda}(T_{LBB}) - I_{b\lambda}(T_{LBB\_bg}) \right] - \frac{A_{IBB}}{L_{IBB}^2} \left[I_{b\lambda}(T_{IBB,LBB}) - I_{b\lambda}(T_{IBB,LBB\_bg}) \right]} \quad (5.3)$$

where S_{LBB} is the raw detector signal for measuring a calibrated laboratory blackbody (Measurement 3 in subsubsection 5.5.1.1), S_{LBB_bg} is the raw detector signal for the background of the blackbody (Measurement 4 in subsubsection 5.5.1.1), T_{LBB} is the temperature of the laboratory blackbody, T_{LBB_bg} is the temperature of the background of the laboratory blackbody (essentially ambient temperature), $T_{IBB,LBB}$ is the temperature of the internal blackbody during the laboratory blackbody measurement, and T_{IBB,LBB_bg} is the temperature of the internal blackbody during the blackbody background measurement.

The radiant intensity of the plume $J_{\lambda,plume}$ can be determined by evaluating $S_{plume} - S_{plume\_bg}$. Assuming $\epsilon_{\lambda,IBB}$ and $\epsilon_{\lambda,plume\_bg}$ are ∼ 1, and that the radiance of the background obstructed by the plume is much less than the radiance of the plume such that $I_{b\lambda}(T_{plume\_bg}) A_{plume} \ll J_{\lambda,plume}$[†], the radiant intensity of the plume can be

[†]This is a reasonable assumption since the temperatures in the plume (>1000 K at the nozzle exit) are significantly greater than the temperature of the background wall (room temperature, ∼300 K).

determined using:

$$J_{\lambda,plume} \approx L_{plume}^2 \left\{ \frac{S_{plume} - S_{plume\_bg}}{K_\lambda} + \frac{A_{IBB}}{L_{IBB}^2} \left[I_{b\lambda}(T_{IBB,plume}) - I_{b\lambda}(T_{IBB,plume\_bg}) \right] \right\} \tag{5.4}$$

where S_{plume} is the raw detector signal for the plume measurement (Measurement 1 in subsubsection 5.5.1.1), S_{plume_bg} is the raw detector signal for the plume background measurement (Measurement 2 in subsubsection 5.5.1.1), $T_{IBB,plume}$ is the temperature of the internal blackbody during the plume measurement, and $T_{IBB,plume\_bg}$ is the temperature of the internal blackbody during the plume background measurement.

If the temperature of the internal blackbody remains approximately constant across all measurements, then some important simplifications can be made. Namely, the response function K_λ in Equation 5.3 simplifies to:

$$K_{\lambda,T_{IBB,const.}} \equiv \frac{S_{LBB} - S_{LBB\_bg}}{\frac{A_{LBB}}{L_{LBB}^2} \left[I_{b\lambda}(T_{LBB}) - I_{b\lambda}(T_{LBB\_bg}) \right]} \tag{5.5}$$

and the exhaust plume radiant intensity in Equation 5.4 simplifies to:

$$J_{\lambda,plume,T_{IBB,const.}} \approx L_{plume}^2 \frac{S_{plume} - S_{plume\_bg}}{K_{\lambda,T_{IBB,const.}}} \tag{5.6}$$

These simplifications are desirable, since the effective field of view of the internal blackbody A_{IBB}/L_{IBB}^2, which is not an explicitly known quantity, is not needed in the simplified formulations.

The radiometer enclosure caused the temperature of the internal blackbody to drift upwards, since the instrument electronics were not being adequately cooled which subsequently increased the temperature in the enclosure. The temperature of the internal blackbody drifted by $\sim$0.5 K across the measurements for SF4 (static fire numbering is discussed in section 5.1 and in Table 5.3). For SF5, the measurements were collected several hours after the instrumentation was powered on so that the temperature of the radiometer and internal blackbody had time to stabilize. For SF6 and SF7, the radiometer enclosure was rigged to cycle external air through the enclosure, which cooled the electronics and stabilized the temperature. The

temperature drift for SF5-SF7 was $\leq$0.1 K. The internal blackbody temperature drift for SF4-SF7 was assumed small enough[†] that it could be treated as approximately constant, and Equations 5.5 and 5.6 were used to evaluate the exhaust plume spectral radiant intensity.

5.5.1.3 Data processing

Each of the four spectral radiation measurements described in subsubsection 5.5.1.1 collected for each motor static fire was actually a collection of individual scans from the radiometer, which scanned the spectrum at a rate of 1 Hz. For each measurement, all suitable scans collected were averaged for each wavelength, but were otherwise not filtered. The averaged measurements were used in Equations 5.5 and 5.6 for determining exhaust plume spectral radiant intensity.

As mentioned in subsubsection 5.5.1.1, the measurements for the plume and plume background were collected in the same radiometer scan run starting 60 s before motor ignition and continuing through the motor burn. The scans comprising the background and plume measurement were determined through simple visual inspection of the raw detector signal at each scan at 4.298 µm wavelength, which is the wavelength corresponding to CO_2 emission and has the largest signal. The plume measurement only included scans where the motor was at steady state (so excluding any peaks at startup). An example annotated figure of this raw detector signal is shown below in Figure 5-8.

[†]The effective field of view of the internal blackbody A_{IBB}/L_{IBB}^2 was roughly estimated by fitting a value to a series of background measurements collected before SF5 where the internal black body temperature drifted significantly, and an approximate value of $A_{IBB}/L_{IBB}^2 \approx 0.161$ was found. Comparing the values of $J_{\lambda,plume}$ plume for SF4 (which had $\sim$0.5 K drift between background and plume measurements) calculated using Equations 5.4 and 5.6 with $A_{IBB}/L_{IBB}^2 = 0.161$, the error across the plotted spectrum is <15 %, with the error being largest at larger wavelengths where $|I_{b\lambda}(T_{IBB,plume}) - I_{b\lambda}(T_{IBB,plume\_bg})|$ is largest.

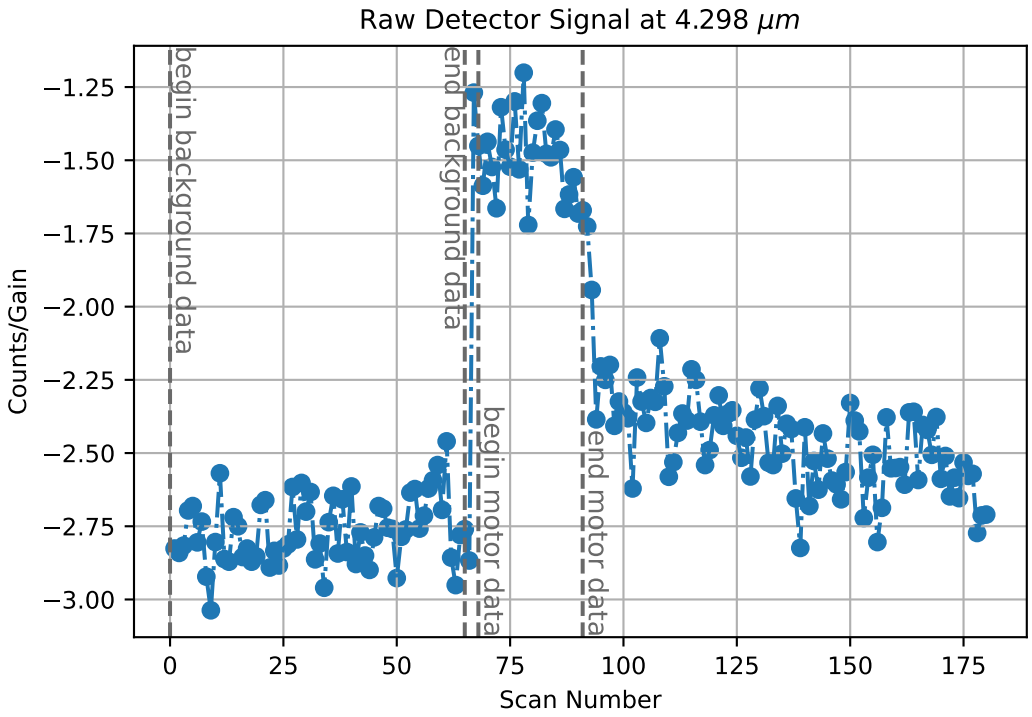

Figure 5-8: The raw detector signal for SF4 at 4.298 µm shows a sharp increase once the motor begins burning, and then drops off again after motor burnout.

5.5.2 Thrust

Thrust was measured using an Omega LCEB-5 load cell with a rated capacity of 5 lbf (22 N). The load cell was connected to a swung platform on a thrust stand[†], shown in Figure 5-9, on which the motor was mounted. Flexures supported the swung platform, which constrained the platform to have one degree of freedom in the thrust direction. The linkage between the swung platform and the load cell used a double-ball joint that only constrained movement in the thrust direction.

[†]The thrust stand was originally designed and built by Dr. Matthew Vernacchia for his doctoral thesis work [14]. Modifications were made for this work.

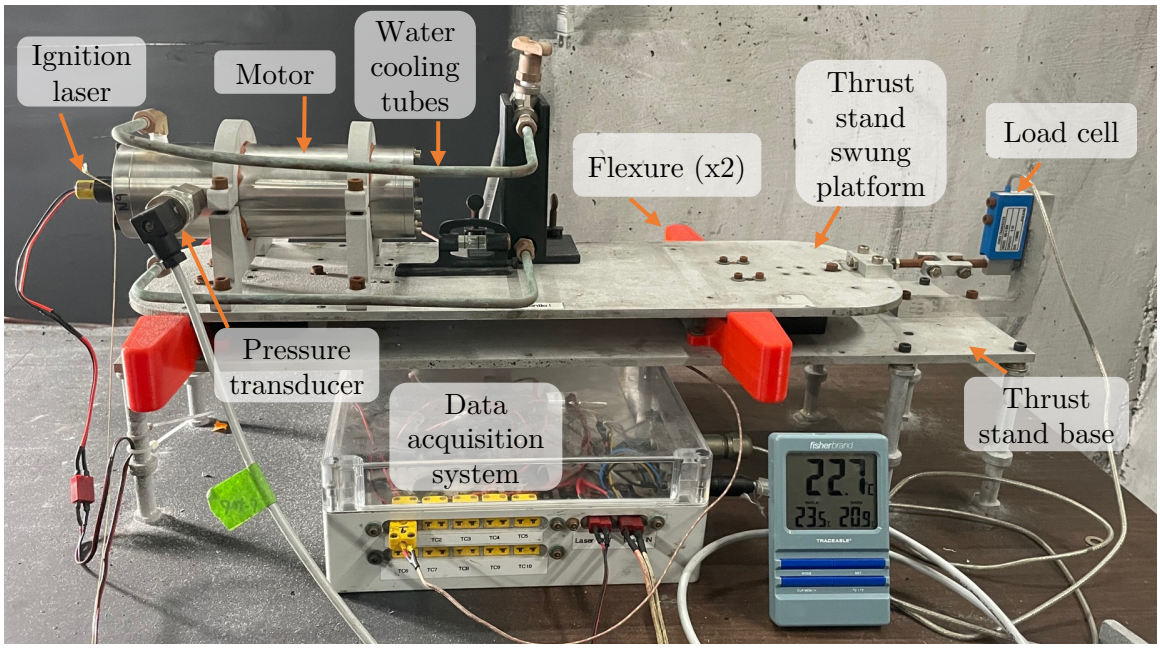

Figure 5-9: Motor thrust was measured using a load cell connected to a swung platform.

5.5.3 Chamber pressure

Chamber pressure was measured using an Omega PX119-600AI pressure transducer with a 600 psi (4.1 MPa) maximum pressure. The pressure transducer was mounted through the wall of the motor case as shown in Figures 5-2 and 5-3. Excess volume in the connections between the pressure transducer and the motor case was packed with low thermal conductivity silicone grease to protect the pressure transducer from the hot combustion gases of the motor. The pressure transducer mounted to a motor can be seen in Figure 5-9.

5.5.4 Propellant burn rate

To predict propellant mass flow rates and determine the appropriate nozzle throat areas required to achieve desired chamber pressures, the burn rates of the propellants must be determined. To do this, the propellant burn rate coefficient a and burn rate exponent n must be determined by fitting experimental burn rate measurements at different pressures to the $r = a\, p_c^n$ burn rate law introduced in section 2.6. Burn rate

coefficients and exponents for this class of propellants were already characterized by Vernacchia et al. for propellants doped with 0, 5, 10, 13, and 20% oxamide [3]. This work measured burn rate as well to provide additional data to support characterization of these propellants. Additionally, a new oxamide content of 8% was used in this work, which provided additional data to evaluate the theoretical oxamide burn rate model (see subsection 2.4.2) developed by Vernacchia et al. [3].

Propellant burn rate measurements were collected during the test motor firings introduced in section 5.1. The propellant a and n values can be determined in one of two ways:

1. *Average burn rate and n-averaged chamber pressure method*: A burn rate exponent n is assumed. For the propellants in this work, n is not sensitive to oxamide content and has a value of $n \approx 0.4$ [3]. Then the average burn rate $\langle r \rangle$ can be compared to the n-averaged chamber pressure $\langle p_c \rangle_n$ for each motor test. The collection of $(\langle r \rangle, \langle p_c \rangle_n)$ points for each motor can be fit to a $r = a\, p_c^n$ model to determine the a value. A more detailed explanation of this procedure can be found in Appendix A.1 of Ref. [14].

2. *c^*-based burn rate method*: The a and n values are estimated using the measured average characteristic velocity $\langle c^* \rangle$, the pressure during "steady" motor operation $p_{c,steady}$, and the equation for equilibrium chamber pressure: $p_{c,steady} = K_n \rho_b r_{steady,c^*} \langle c^* \rangle$. The collection of $(r_{steady,c^*}, p_{c,steady})$ points for each motor can be fit to a $r = a\, p_c^n$ model to determine the a and n values. A more detailed explanation of this procedure can be found in Appendix A.2 of Ref. [14].

Both methods were used for each motor firing. The measured burn rates for the test motor firings are given in subsection 5.6.3.

5.6 Experimental results

As introduced in section 5.1, eight static fires were completed during this research. The eight static fires are summarized in Table 5.3. SF1 and SF2 were early shakedown tests of the motor. SF3 was a shakedown test of an updated motor design and the operation of the spectroradiometer. Thrust and chamber pressure measurements were not collected for this static fire due to an issue with the data acquisition system. SF4-SF7 were the core test matrix that investigated the relationships between propellant oxamide content, motor chamber pressure, and exhaust plume radiant emission. SF8 had embedded thermocouples at the nozzle bond line to investigate thermal performance of the nozzle. All motors used a consistent end-burning motor configuration with a propellant burning area of 1140 mm^2, which was discussed in section 5.2.

Static fire	**Oxamide** [%]	**Ignition primer**	**Burn length** [mm]	**Burn time** [s]	**Steady chamber pressure** [MPa]
SF1	0	Grain	86.1	38.9	∼0.5
SF2	0	Grain	86.4	33.8	∼0.7
SF3	0	Grain	86.3	-	-
SF4	0	Coating	86.2	27.5	∼1.2
SF5	0	Grain	86.2	23.6	∼2.3
SF6	8	Coating	67.3	32.1	∼1.1
SF7	8	Coating	67.2	29.9	∼2.1
SF8	0	Grain	86.2	29.6	∼1.2

Table 5.3: Summary of the test motor firings discussed in this section.

One of two ignition primers was used in the static fires. Either a small piece (∼1 - 2 g) of a faster burning commercial propellant (CTI Classic propellant) was adhered onto the surface of the main motor grain with polyurethane adhesive, or the surface of the grain was coated with a commercial pyrogen coating (QuickBurst QuickDip coating). Both ignition primers were ignited with a 6 W 450 nm laser. After ignition,

the choice of primer did not affect the thrust, chamber pressure, or exhaust plume radiant emission measurement.

Two different propellant formulations were used: a baseline formulation, and a baseline formulation diluted with 8 % oxamide burn rate suppressant. The propellant formulations are discussed in subsection 5.3.1. Shorter propellant grains were used with the 8 % oxamide grains as compared to the 0 % oxamide grains, so that at a chamber pressure of ∼1 MPa, the burn time was near 30 s.

5.6.1 Radiant intensity and chamber pressure

The measurements in this subsection reference the core test matrix of static fires SF4-SF7. The radiant intensity and chamber pressure measurements for these motors are shown in Figure 5-10. The pressure traces for SF4, SF6, and SF7 were relatively flat, which is the desired behavior for an end-burning motor. SF5 showed an initial peak in pressure, which eventually decayed to a relatively steady chamber pressure, although the trace was still slightly regressive. The peak and decay were most likely due to the use of a relatively large starter grain for igniting the propellant (the other static fires used an ignition coating instead, as indicated in Table 5.3). This starter grain created an initial increase in burning area before being consumed, which explains the initial peak in chamber pressure. Its possible that the hotter, faster burning commercial propellant starter grain caused the main propellant grain near the starter grain to momentarily burn faster than the rest of the propellant surface, altering the propellant surface geometry such that the rest of the pressure profile was slightly regressive.

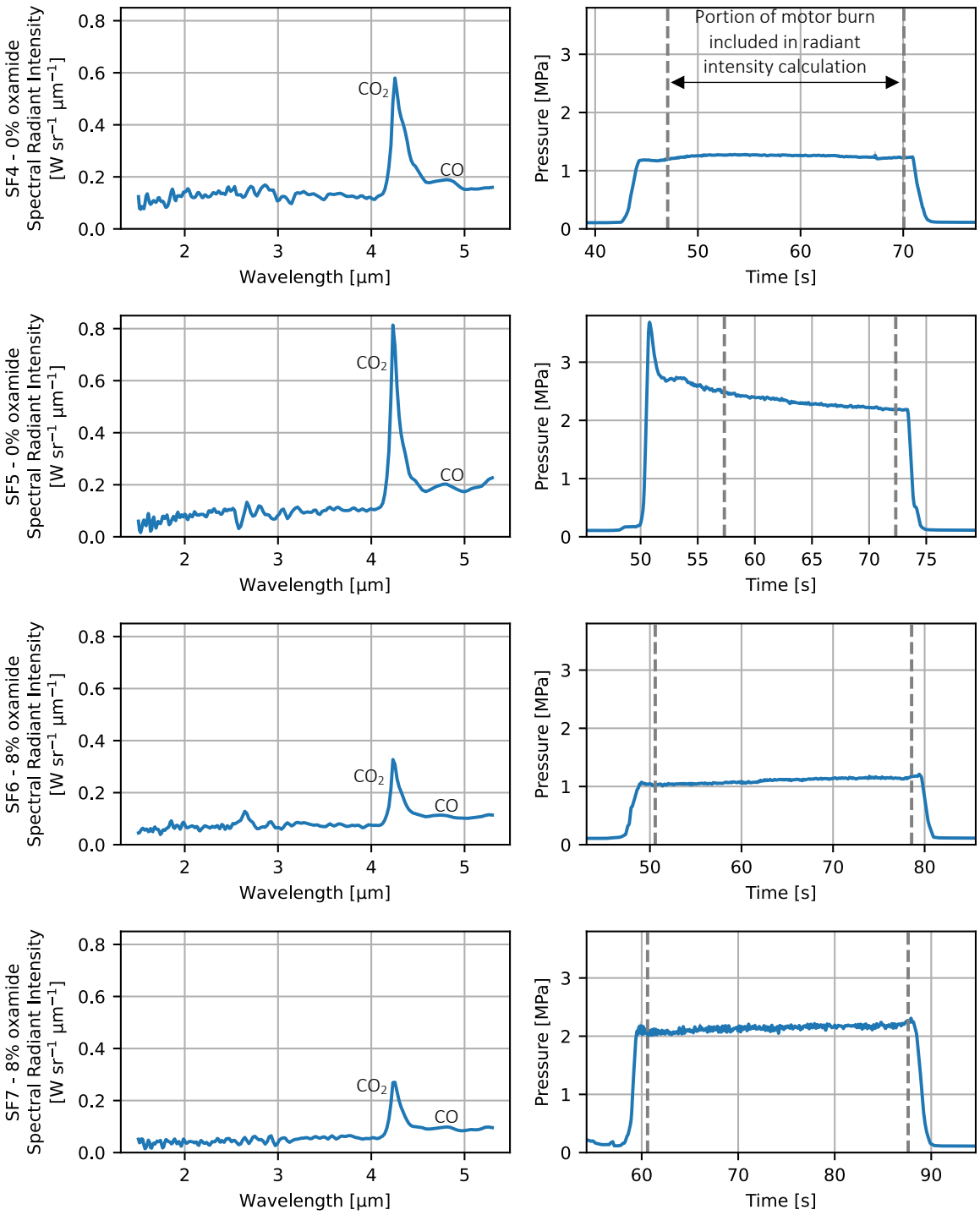

Figure 5-10: The exhaust plume spectral radiant intensity and chamber pressure were measured for four motors with different oxamide contents and chamber pressures. The dotted lines in the pressure plots show to the portion of the static fire where corresponding scans from the radiometer were included in the spectral radiant intensity plots for that motor.

Emission bands in the radiant intensity spectra for the motors correspond to the combustion products in the motor exhaust, which are given in subsection 5.3.2. The radiant intensity spectra for SF4-SF7 each had a strong peak at 4.3 µm. This peak was due to the CO_2 in the exhaust plume, which has a strong molecular emission band centered at 4.3 µm, as introduced in section 4.1. A weaker peak at 4.7 µm can also be seen, which is due to CO emission. The measurements for each motor test are unfortunately noisy. Measuring the radiant emission of these small, slow-burning solid rocket motors required operating the spectroradiometer near its lower sensitivity limit. Even at the maximum gain setting, the exhaust plume contrast measurements used, at most (at the 4.3 µm CO_2 band where the signal was strongest), 7.7 % of the dynamic range of the detector. For a larger motor with more emission, a band centered at 2.7 µm due to both H_2O and CO_2 and a band centered at 3.5 µm for HCl would be expected, given the expected combustion products in the motor's exhaust. However, these weaker emission bands were not very pronounced for these small, low-thrust motors. These measured spectra are compared to modeled spectra for these motors in section 7.2.

The peak spectral radiant intensities for SF4-SF7 are compared in Figure 5-11. The difference in peak spectral radiant intensity was greater due to the change in oxamide content than the change in chamber pressure. For the 0 % oxamide motors (SF4 and SF5), the increase of chamber pressure from ∼1.2 MPa to ∼2.3 MPa led to a ∼40 % increase in peak spectral radiant intensity; for the 8 % oxamide propellant (SF6 and SF7), the increase in chamber pressure from ∼1.1 MPa to ∼2.1 MPa led to a ∼12 % decrease. For motors operating near ∼1.1 MPa (SF4 and SF6), increasing propellant oxamide content from 0 % to 8 % led to a 47 % decrease in peak radiant intensity; for motors operating near ∼2.2 MPa (SF5 and SF7), increasing the oxamide content led to a 67 % decrease. These peak intensity results are compared to modeled results in section 7.2.

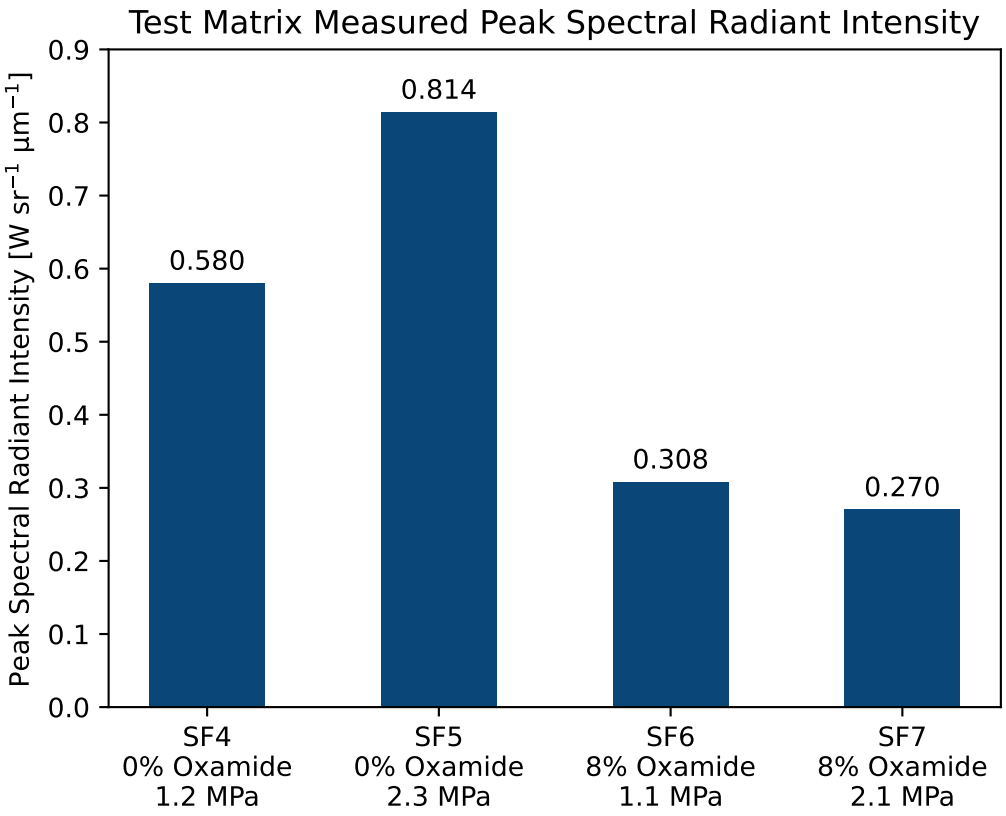

Figure 5-11: The difference in peak spectral radiant intensity was greater due to the change in oxamide content than the change in chamber pressure.

5.6.2 Thrust

The measurements in this subsection reference the core test matrix of static fires SF4-SF7. The thrust measurements for these motors are shown in Figure 5-12. Like the pressure traces in Figure 5-10, the thrust traces were also relatively flat, which was expected given the end-burning motor configuration. Also like the pressure trace for SF5, there was a peak in the thrust on motor startup due to the use of a larger starter grain for this motor. Stiction in the thrust stand due to a small amount of rubbing between the thrust stand swung platform and flexures (see Figure 5-9) caused the thrust measurements to not return all the way to zero after the thrust load was removed. As anticipated, thrust was higher for motors with higher chamber pressure and propellant with lower oxamide content.

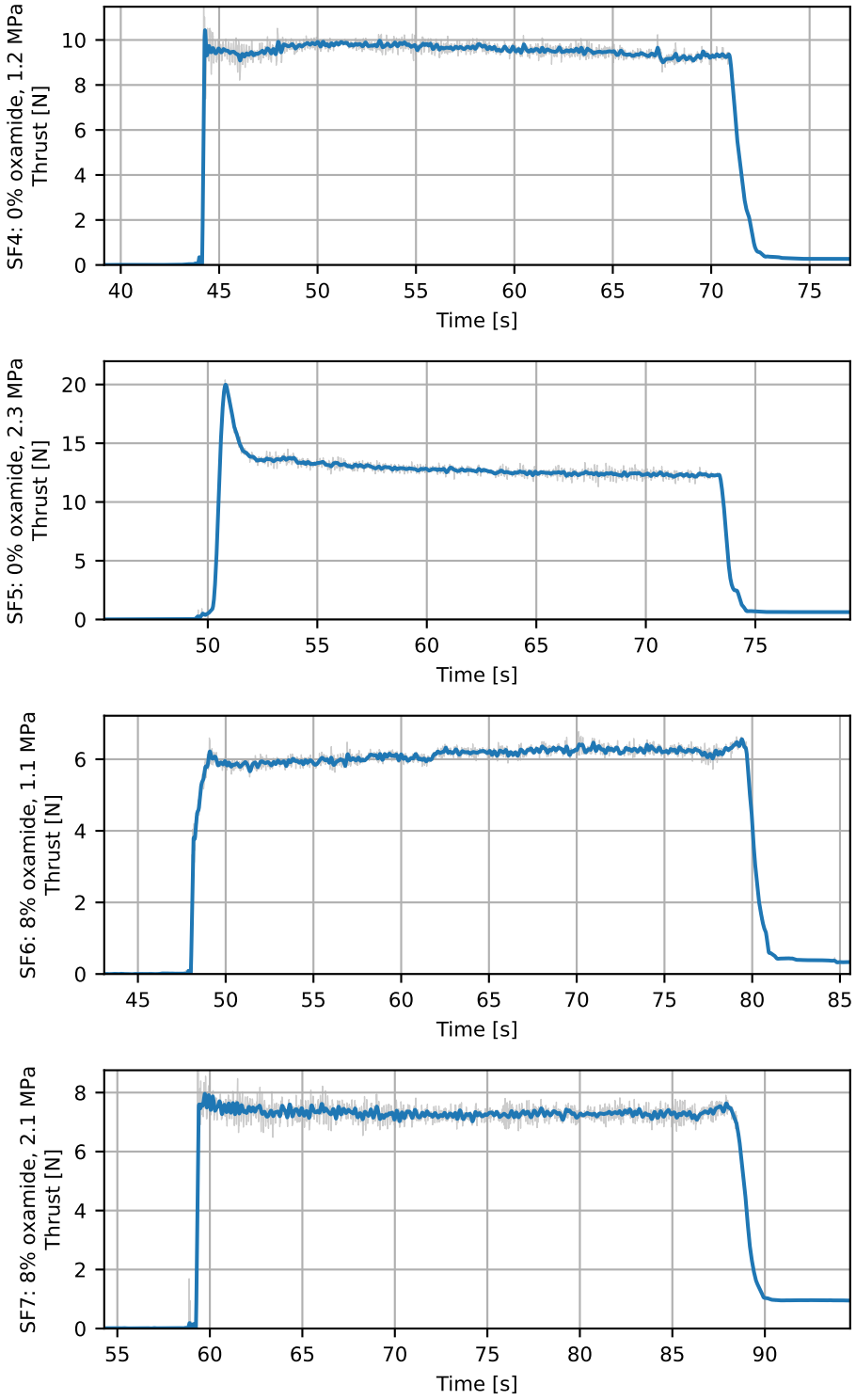

Figure 5-12: The thrust curves for these motors are relatively flat, which is the expected behavior for end-burning motors. Thrust is higher for motors with higher chamber pressure and propellant without oxamide.

5.6.3 Burn rate

Propellant burn rates for the static fires listed in Table 5.3 were measured. The burn rate was calculated for each static fire with two different methods: an average burn rate method and a c^*-based burn rate method. These burn rate calculation methods are described in more detail in subsection 5.5.4. A plot of the measured burn rate coefficients for this work, as well as the measured burn rate coefficients and model developed for oxamide doped propellants developed by Vernacchia et al. in Ref. [3], is shown in Figure 5-13.

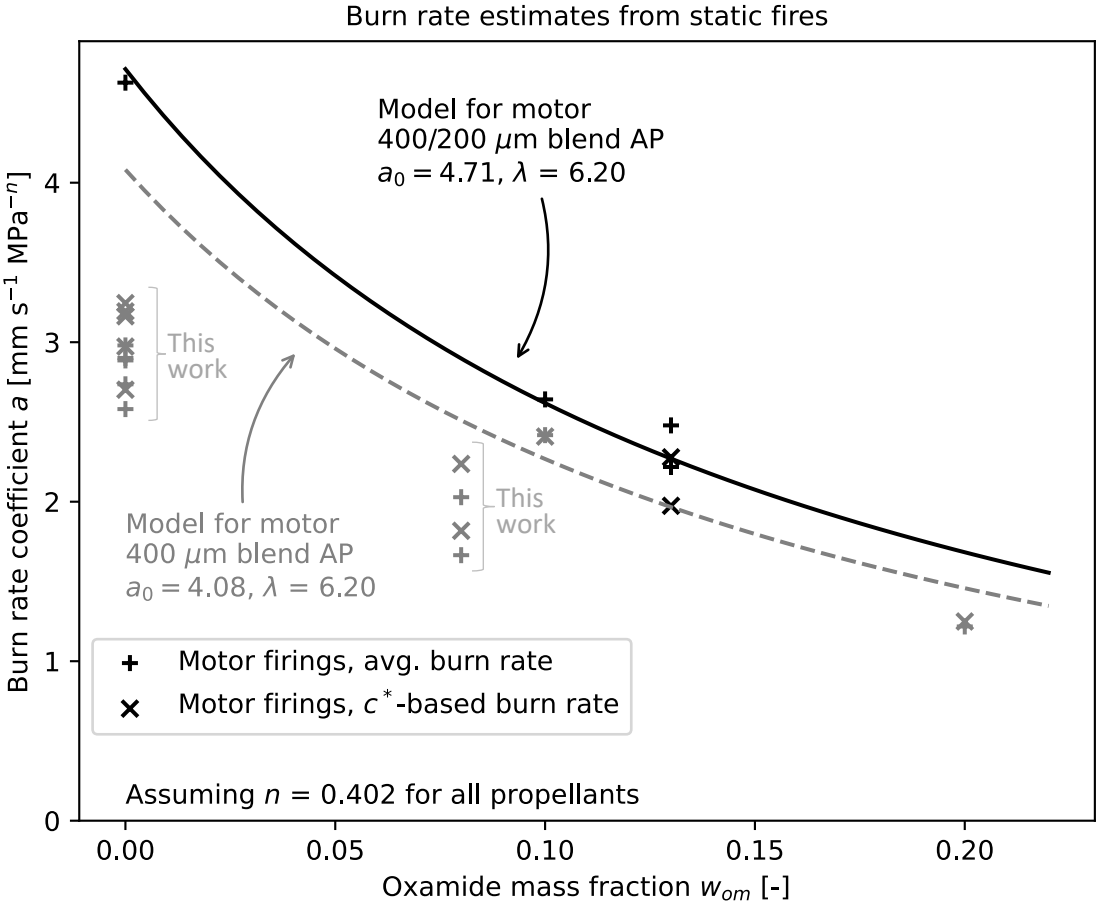

Figure 5-13: A comparison of the measured burn rate coefficients for the static fires given in Table 5.3 with the model and static fire measurements published in Ref. [3]. The propellants in this work used the 400 µm blend AP and should be compared to the gray dashed line. The burn rate coefficients from this work undershoot the model by ∼20 to 25%.

The burn rate coefficient versus oxamide model from Ref. [3] over-predicts the burn rate for the static fires completed in this work: the measurements from this work are ∼20 to 25% less than the model. This over-prediction could be due to the difference in motor designs between the motor in this work, discussed in section 5.2, and the motor design used in Ref. [3], which had a slightly larger burning surface area (1140 mm^2 for this work and 1257 mm^2 for Ref. [3]) and a much thinner motor case (9.5 mm thick for this work and 1.6 mm thick for Ref. [3]). The smaller burn area and larger heat capacity of the motor case for the motor used in this work could have resulted in greater thermal losses to the motor case walls as compared to the motors in Ref. [3], which would have the effect of slowing down the propellant burn rate.

5.6.4 Minimum burn pressure

As introduced in subsection 2.4.3, the family of propellants used in this work have a minimum burn pressure below which the propellant cannot stably burn. The minimum burn pressure was previously characterized for oxamide doped propellants by Vernacchia et al. in Ref. [3]. Ignition of propellants containing 0, 5, 10, 13, and 20% oxamide was attempted at various pressures at or above atmospheric pressure. A quadratic minimum burn pressure model was then fit to the ignition data as a function of oxamide content.

The original data and model in Ref. [3] suggested that the oxamide content where the propellant transitioned from unsuccessful to successful combustion at standard pressure (0.101 MPa) was between 5 and 10 %. Since testing propellant ignition at pressures below atmospheric pressure is difficult, reducing the known transition oxamide range at standard pressure is desirable since it is a relatively simple way to improve the accuracy of the model. Subsequently, ignition of 8 % oxamide propellant mixed for this work was attempted at standard pressure, and it was found to burn stably. This new ignition data point, as well as the data given in Ref. [3], are shown in Figure 5-14.

An updated empirical boundary for the minimum burn pressure was also determined, which is also given in Figure 5-14. As noted in Ref. [3], the choice of a

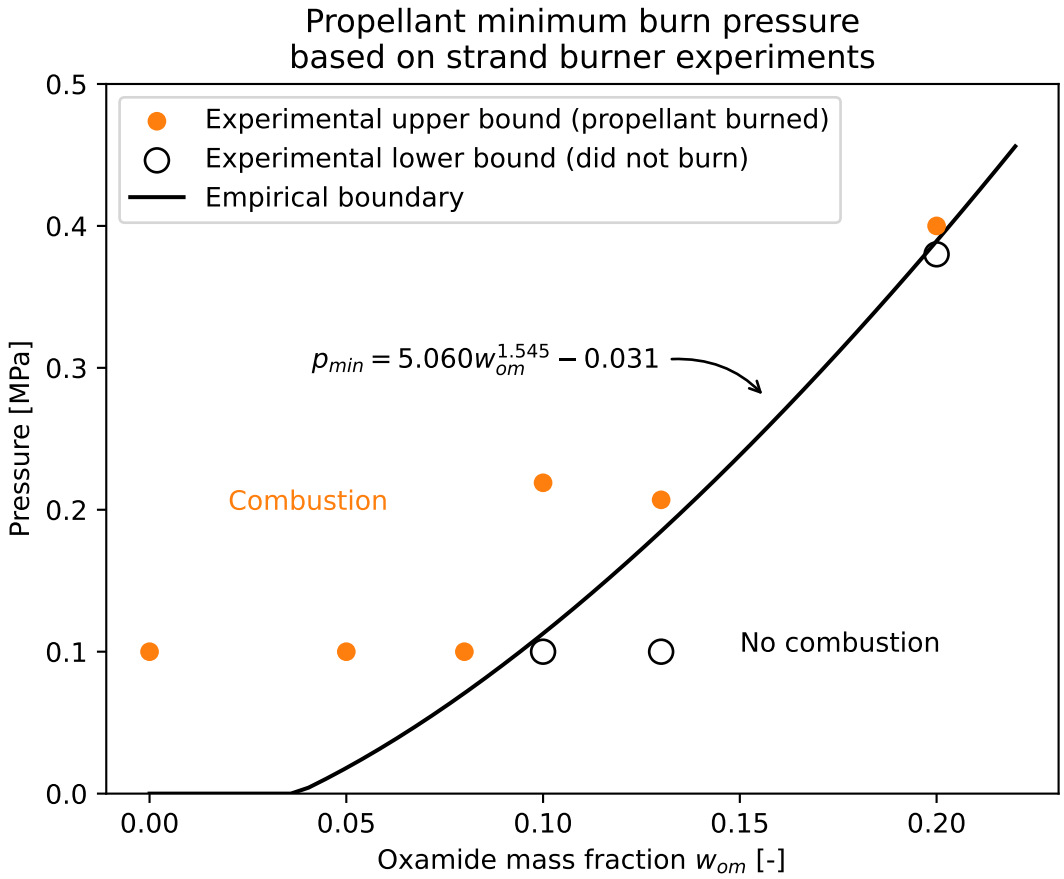

Figure 5-14: The minimum burn pressure is the minimum pressure that the propellant can stably burn. This plot presents data for the class of propellants used in this work originally published in Ref. [3], along with the addition of the data point at $w_{om} = 0.08$, which was collected using the propellant mixed for this work.

quadratic dependence on oxamide content was arbitrary, and there was no theoretical basis for it. For this work, a power law with constant offset model was used to fit the data. This model, like the quadratic, still has three fitted parameters. However, for this model the exponent was among the fitted parameters, which perhaps provides more intuition for the true dependence of minimum burn pressure on oxamide content than the quadratic model.

5.7 Alumina-silicate nozzle

A single-component nozzle with the novel application of an alumina-silicate material was developed for use with low-thrust, long-endurance solid rocket motors, such as the

motors used with the Firefly aircraft concept introduced in subsection 1.2.2. These nozzles were used in the motor static fires for this research for measuring chamber pressure, thrust, and exhaust plume radiant emission. This section describes the development, design, manufacturing, and testing of these alumina silicate nozzles.

5.7.1 Overview

Typical solid rocket motors rely on transient methods – such as ablation or heat-sinking – for managing heat transfer through the nozzle and maintaining acceptable temperatures in the motor case. A large motor can use an ablative nozzle, which might erode by several millimeters during the motor burn; since these few millimeters represent only a small fraction of the nozzle throat diameter, the motor's thrust barely changes. A short-duration motor can rely on simple heat-sinking methods; the heat capacity of the motor case is often sufficient such that the heat transferred to it during the short motor burn does not unreasonably increase the temperature. However, these methods do not work for a small, long-endurance solid rocket motors, such as the motor used for the Firefly vehicle. The nozzles for these motors require a steady-state insulation technique to ensure the temperature limits of the motor case material are not exceeded. Ideally, the chosen nozzle material and configuration would (following the analysis in Ref. [4]) provide a maximum service temperature $T_{max} > 1800\,\mathrm{K}$, a thermal conductivity $k < 5\,\mathrm{W\,m^{-1}\,K^{-1}}$ and good thermal shock properties with a critical fracture temperature change $\Delta T_f > 1000\,\mathrm{K}$. A survey of some material candidates for these nozzles is given in Table 10.1 of Ref. [14].

A two-piece nozzle configuration with a 3D-printed cellular ceramic nozzle insulator was previously proposed for use in low-thrust, long-endurance solid rocket motors for Firefly-like aircraft in Ref. [4]. The design and manufacturing challenges for these two-piece nozzles are discussed in more detail in Appendix B. The two-piece nozzle configuration used a nozzle insulator printed from a silica ceramic and a contoured nozzle insert turned from boron nitride which were bonded together with a silica adhesive. The nozzles were manufactured and tested successfully in small, long-endurance test motors. However, there were some manufacturing and performance drawbacks for this

nozzle design. The boron nitride showed significant nozzle erosion during the motor tests. Additionally, the manufacturing process for the 3D printed cellular ceramic insulator was unreliable and time-consuming. In response to these manufacturing challenges, a new single-component nozzle design with improved manufacturability was developed and tested. The rest of this section describes the material and design of this nozzle, as well as testing and performance.

5.7.2 Nozzle design and material

A new, single-component nozzle was designed and manufactured from an alumina-silicate material. The material and design for this nozzle were specifically chosen to simplify manufacturing, and address many of the manufacturing issues describe in subsection 5.7.1. This single-component configuration is shown in Figure 5-15.

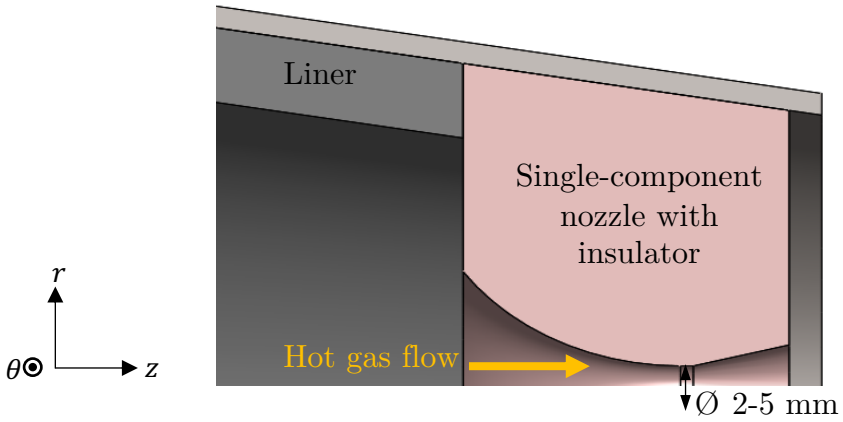

Figure 5-15: The single-component nozzle is manufactured from a single piece of an alumina-silicate material. The material is a thermal insulator, so the nozzle functions as an insulator as well.

The alumina silicate material used is the naturally occurring alumina silicate mineral pyrophyllite, and is often known by the trade names of "Wonderstone" or "Lava". The alumina silicate material has a low thermal conductivity in the range of $1.3\,\mathrm{W\,m^{-1}\,K^{-1}}$ to $2.5\,\mathrm{W\,m^{-1}\,K^{-1}}$ and a softening temperature of 1873 K [67].

Thermal shock properties for materials are typically indexed with a thermal shock resistance parameter R_s. For Biot number[†] $\gg 1$, thermal shock resistance is defined as:

$$R_s \equiv \frac{\sigma_{flex}(1-\nu)}{E\alpha_{LE}} \tag{5.7}$$

where σ_{flex} is flexural strength, ν is Poisson's ratio, E is Young's modulus, and α_{LE} is linear coefficient of thermal expansion [68–70]. Thermal shock resistance is related to critical fracture temperature change ΔT_f with:

$$\Delta T_f = R_s S \tag{5.8}$$

where S is a shape factor (typically of order unity), dependent on the part geometry and material property variation within a part. For thick-walled hollow cylinders with constant material properties, the shape factor S is a function of the ratio of inner and outer radii, and has values near or greater than 2 [70, 71].

The alumina-silicate has a low coefficient of thermal expansion $\alpha_{LE} = 3.6\times10^{-6}\,\mathrm{K}^{-1}$ and reasonable flexural strength of $\sigma_{flex} = 69\,\mathrm{MPa}$ which, following Equations 5.7 and 5.8, is suggestive of reasonable thermal shock properties. Many suppliers describe the thermal shock resistance as "good" or "excellent", although do not provide any quantitative values [72, 73]. Some simple experiments to gain more insight on the thermal shock resistance and critical fracture temperature change of the material were conducted, and are described in subsection 5.7.3.

The alumina-silicate material is purchased in a semi-fired state, and importantly it can be machined with standard tooling in this state. The material must be subsequently fired to achieve the full mechanical and thermal properties. The alumina-silicate expands in all dimensions when fired, and so all machined dimensions before firing must be under-sized accordingly. The measured material expansion is discussed in subsection 5.7.4.

[†]Biot number is defined as $\beta \equiv hl/k$, where h is convective heat transfer coefficient, k is thermal conductivity, and l is characteristic length. $\beta \gg 1$ indicates that there are strong temperature gradients within a body due to convection at a surface, and that material conductivity is not large enough to distribute heat away from the surface. For the nozzles in this work, $h \approx 3000\,\mathrm{W\,m^{-2}\,K^{-1}}$, $k \approx 2.5\,\mathrm{W\,m^{-1}\,K^{-1}}$, and $l \approx 1\,\mathrm{cm}$, and so $\beta \approx 12 \gg 1$.

The nozzle is bonded to the motor case using a high-temperature flexible silicone adhesive. The nozzle and motor case are designed with a tapered interface, as shown in Figure 5-15, such that if the material expansion is slightly different than anticipated, the nozzle can still seal against the motor case.

5.7.3 Thermal shock experiments

A series of simple thermal shock experiments using water quenching were conducted on the alumina silicate material[†]. Four samples of alumina silicate material were prepared from 2.5 cm diameter rod. The samples were cut on a bandsaw in 2.5 cm lengths. Edges were sanded to remove any sharp protrusions resulting from the cut. The samples were fired in a kiln according to the temperature schedule given in Table 5.5.

The prepared samples were then heated in a kiln to a series of incremental temperatures. After the samples were heated and thermally soaked at the desired temperature, they were removed from the kiln and quenched in a room temperature water bath, as shown in Figure 5-16. This quenching procedure provides an analogous thermal scenario to the nozzle: when the sample is quenched, the inside of the sample will be hot and the outside of the sample will be cool, as is the nozzle on motor startup. After the samples were quenched, they were visually inspected for surface cracks. If no cracks were present, the samples were heated in the kiln to the next temperature.

A summary of the kiln temperatures, thermal soak times, quench temperature change $\Delta T = T_{kiln} - T_{bath}$, and presence of cracking is given in Table 5.4. Samples were tested up to a maximum ΔT of 1000 K. None of the samples cracked at or below this temperature. This suggests that $\Delta T_f \gtrsim 1000$ K for the alumina-silicate material.

[†]The author thanks undergraduate researchers Insuh Na and Justin Schiavo for their work in setting up and conducting these experiments.

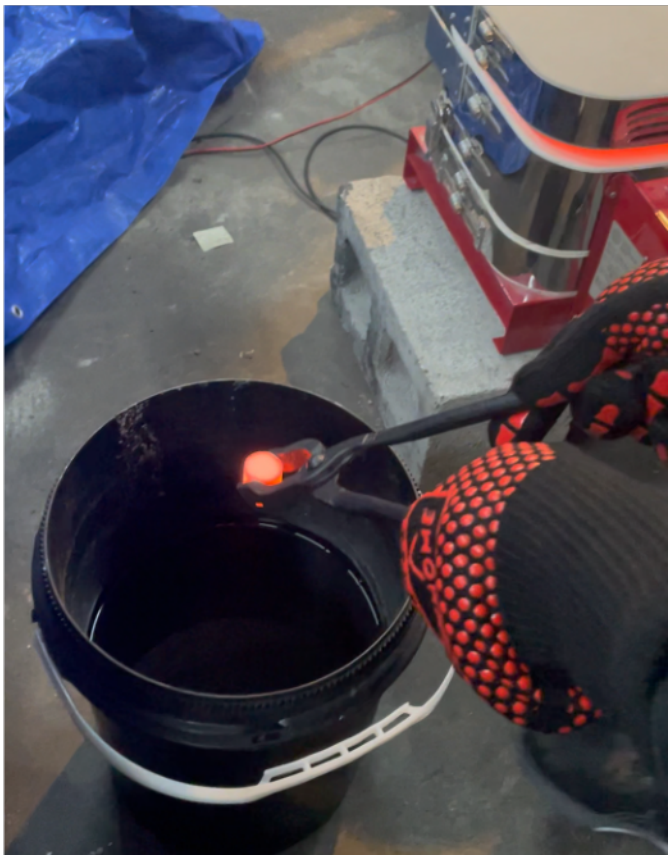

Figure 5-16: Alumina-silicate samples were heated in a kiln and then quenched in a room temperature water bath to evaluate material thermal shock properties. This image was taken just before the sample was quenched.

Increment	**Kiln Temperature** [K]	**Soak Time** [h]	ΔT [K]	**Visible cracks**
1	700	1	400	No
2	800	1	500	No
3	900	1	600	No
4	1000	1	700	No
5	1100	1	800	No
6	1200	2	900	No
7	1300	2	1000	No

Table 5.4: Summary of thermal shock experiments for alumina silicate samples.

5.7.4 Nozzle manufacturing procedure

The specific material for these nozzles was the "low thermal expansion alumina-silicate ceramic" purchased through McMaster-Carr. Their supplier at the time of purchase was Bar-Lo Carbon Products, Inc. The nozzle has a revolved geometry, as shown in Figure 5-15, and so the pre-fired nozzle was turned on a lathe. Because the alumina silicate material expands when fired, as mentioned in subsection 5.7.2, the part dimensions were undersized during machining. 11 nozzles were machined in total for this research, and the average material expansion after firing was $2.56 \pm 0.13\,\%$. A scaling factor of $1/1.0256 = 0.975$ was applied to all nozzle dimensions, except the throat diameter, for machining. The throat diameter was undersized further such that after firing, the nozzle throat could be drilled out to ensure the precision of the nozzle throat area, which is important for setting the motor chamber pressure as discussed in section 2.2. During the pre-fire machining, a scaling factor of 0.85 was applied to the throat diameter dimension.

After machining, the nozzles were fired in a Skutt Firebox 8x4 LT kiln. The kiln has a programmable controller where segments consisting of a ramp rate, hold temperature, and hold time can be specified. The firing schedule developed for the nozzles is given in Table 5.5. This firing schedule was based on recommendations provided by Aremco, although rates and hold times have been adjusted for this application [74].

Segment	**Rate** [$\mathrm{K\,h^{-1}}$]	**Temperature** [K]	**Hold** [h]
1	25	366	2
2	25	866	6
3	25	1394	2
4	75	432	0

Table 5.5: Firing schedule for alumina-silicate nozzles.

After firing, the nozzle throat was drilled out with a drill press to the final desired throat diameter. A TiAN or TiN coated carbide drill bit was used to drill out the nozzle throat at a speed of $300\,\mathrm{rev\,min^{-1}}$. The use of a high speed steel drill bit

was attempted, however it simply wore down the tool without drilling through the material.

5.7.5 Nozzle testing

The alumina silicate nozzles were used in all eight of the static fires described in section 5.1. An image of one of these nozzles being used in a static fire is shown in Figure 5-17. In SF1-SF7, the motor was water-cooled by flowing water through the water-cooling ports shown in Figure 5-2. These tests are still valuable for evaluating thermal shock performance of the nozzle, but are not suited for evaluating thermal insulation performance. In SF8, water was not flowed through the water cooling ports. This test was more suited to evaluating thermal insulation performance. Thermocouples were embedded in the bond line between the nozzle and aft closure for SF8 to evaluate the insulation performance, which is discussed in subsection 5.7.6.

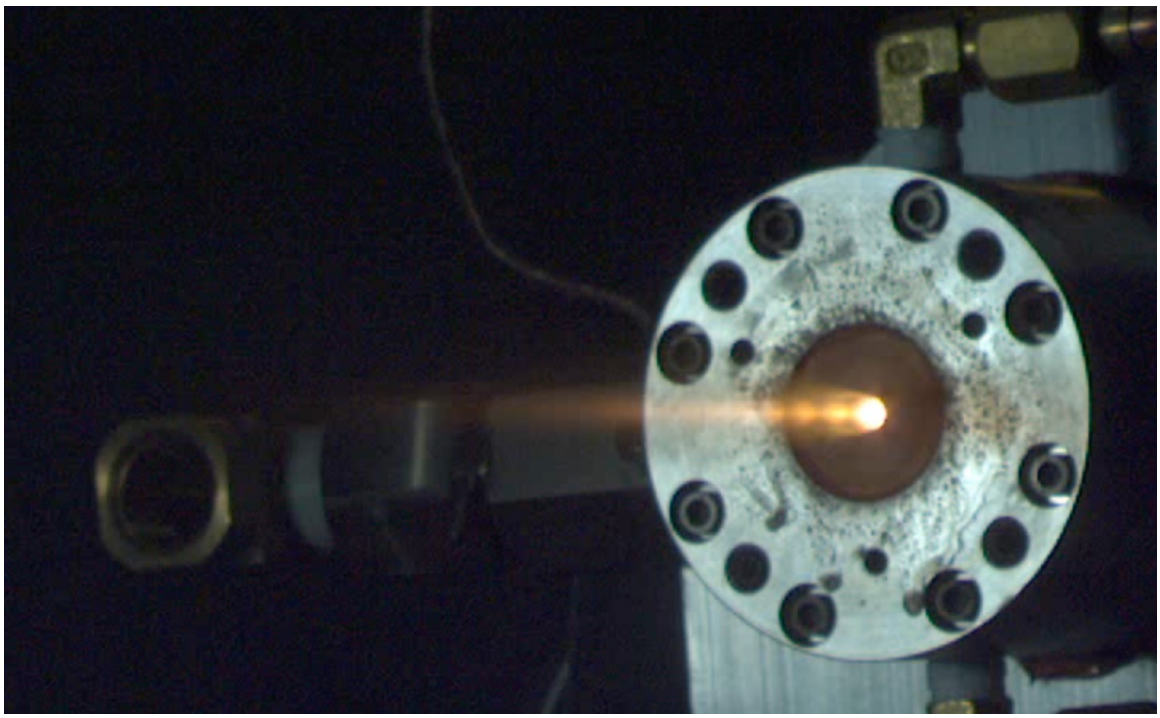

Figure 5-17: A novel alumina silicate nozzle material was tested in eight motor static fires.

5.7.6 Nozzle thermal insulation performance

In SF8, four Type K thermocouples were embedded in the bond line between the nozzle and the aft closure, as shown in Figure 5-18. Slots were cut with a rotary tool into the outer surface of the nozzle to accommodate the weld bead and wire of the thermocouples. The weld bead was potted into the silicone adhesive in the prepared slots at the bond line, approximately 2 mm from the aft face of the nozzle. The thermocouple wires were routed out the aft end of the motor and secured with a hose clamp around the outside of the motor. The thermocouple wires were potted with extra silicone at the aft face of the motor to protect them from the motor exhaust gases.

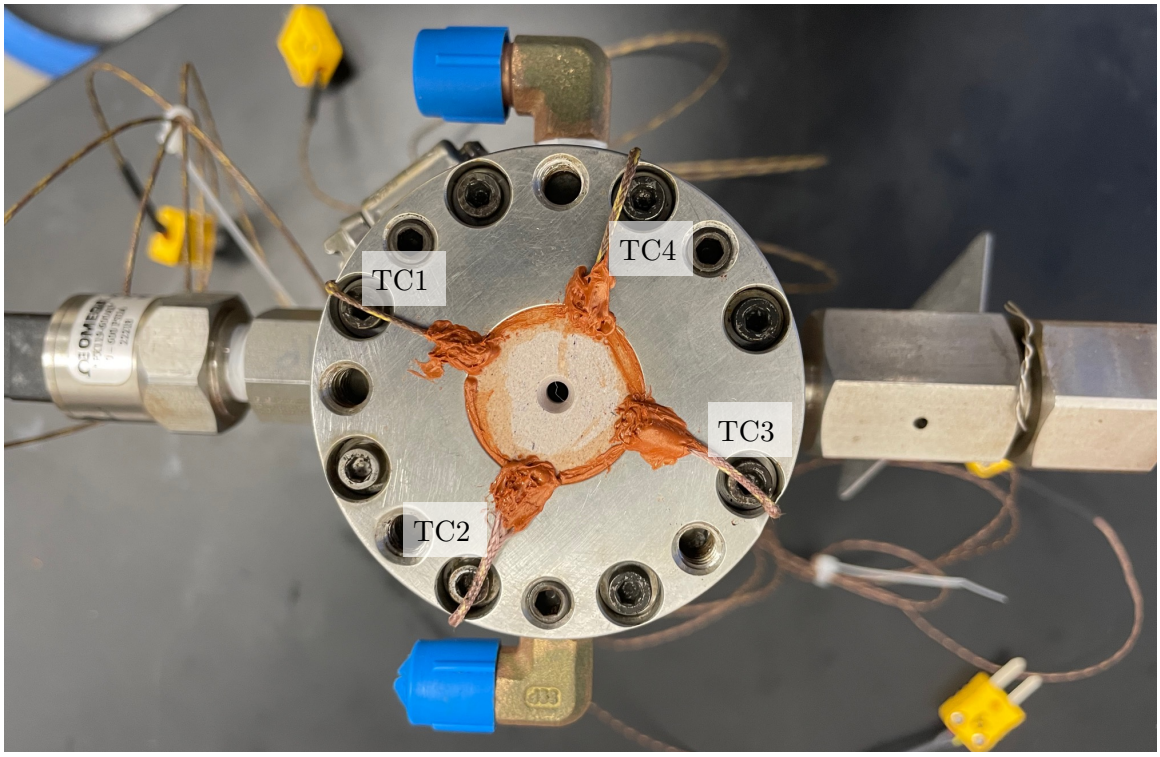

Figure 5-18: Thermocouples were embedded in the nozzle bond line for a motor to measure the thermal performance of the alumina silicate nozzle material.

The measured bond line temperatures of the four thermocouples are shown in Figure 5-19. The initial sharp rise and peak in measured temperatures after "laser on" was due to a design issue with the laser holder that caused flames to leak around the aft face of the motor before the laser holder released from the motor. This flame leakage

around the laser holder is shown in Figure 5-20. The excess heat from the flame leakage was distributed throughout the large heat capacity of the motor case after the laser holder fell away near "thrust start", and so the temperature decreased temporarily at that time. Then, the temperature rose again as the material and thermocouples were actually being heated by the heat transfer through the nozzle. The spread in the thermocouple measurements was possibly due to slight variations in the positions of the thermocouple weld beads or features in the motor case that are not radially symmetric (i.e. water cooling ports, rupture disc assembly, pressure transducer) that affect the thermal properties of the material around the thermocouples unevenly.

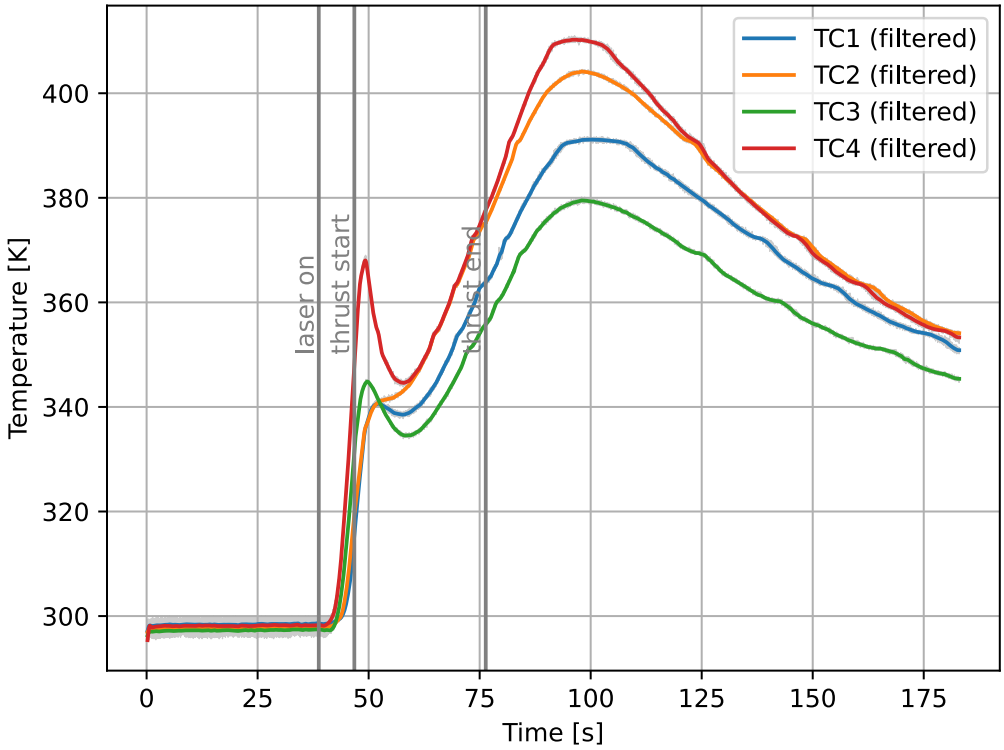

Figure 5-19: Thermocouples were embedded in the nozzle bond line of SF8 to measure the bond line temperature. The initial peak in temperature was due to flame leakage around the aft end of the motor before the laser holder released.

A transient thermal simulation of the nozzle was run to compare against the measured thermocouple data from SF8 and verify the alumina-silicate nozzle material thermal conductivity. A 2D axisymmetric finite element analysis was used to simulate the temperature at the nozzle bond line. Vernacchia provided averaged nozzle internal

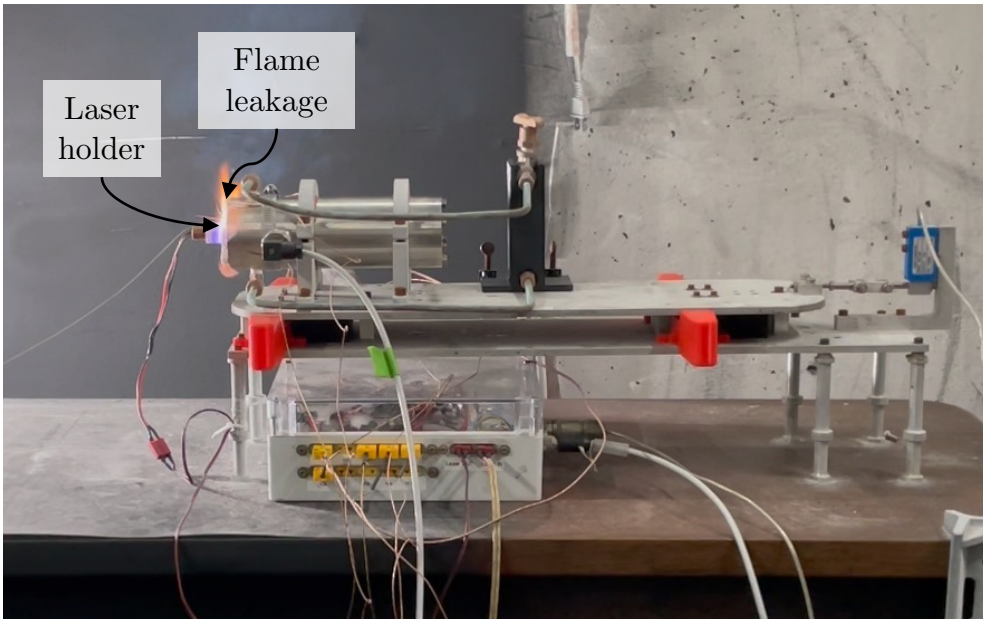

Figure 5-20: Flame leakage around the laser holder caused an initial spike in the measured bond line temperatures.

boundary convection coefficients and adiabatic wall temperatures based on CFD results for a small, low-thrust motor assuming a combustion gas temperature of 2000 K and a chamber pressure of 0.7 MPa [14]. The 0 % oxamide propellant used in SF8 has a predicted combustion temperature of 2188 K, which is near the temperature used in the CFD. The steady chamber pressure for SF8 was ∼1.15 MPa, which is significantly larger than the assumed chamber pressure used in the CFD. The convection coefficients from Ref. [14] are scaled using the Bartz heat flux correlation, which says that convection coefficient scales like $\sim p_c^{0.8}$ [10]. It is crudely assumed that the adiabatic wall temperatures are the same. The subsequent internal boundary conditions used for the simulation in the work are given in Table 5.6. An external convective boundary condition with an adiabatic wall temperature of 298 K and a convection coefficient of $10\,\mathrm{W\,m^{-2}\,K^{-1}}$ was assumed to account for natural convection at the surface of the motor. The boundary conditions and mesh for the simulation are shown in Figure 5-21. Ref. [67] reports a thermal conductivity of $2.5\,\mathrm{W\,m^{-1}\,K^{-1}}$ for the alumina silicate fired to 1473 K. This is near the firing temperature of 1394 K (see Table 5.5), and so this value is used in the simulation.

Region	**Convection coefficient** [$\mathrm{W\,m^{-2}\,K^{-1}}$]	**Adiabatic wall temperature** [K]
Converging	3384	1441
Throat	3593	1519
Diverging	1777	1499

Table 5.6: Alumina-silicate nozzle simulation internal boundary conditions. These values are based on CFD results presented in Ref. [14] adjusted for chamber pressure using the Bartz heat flux correlation [10].

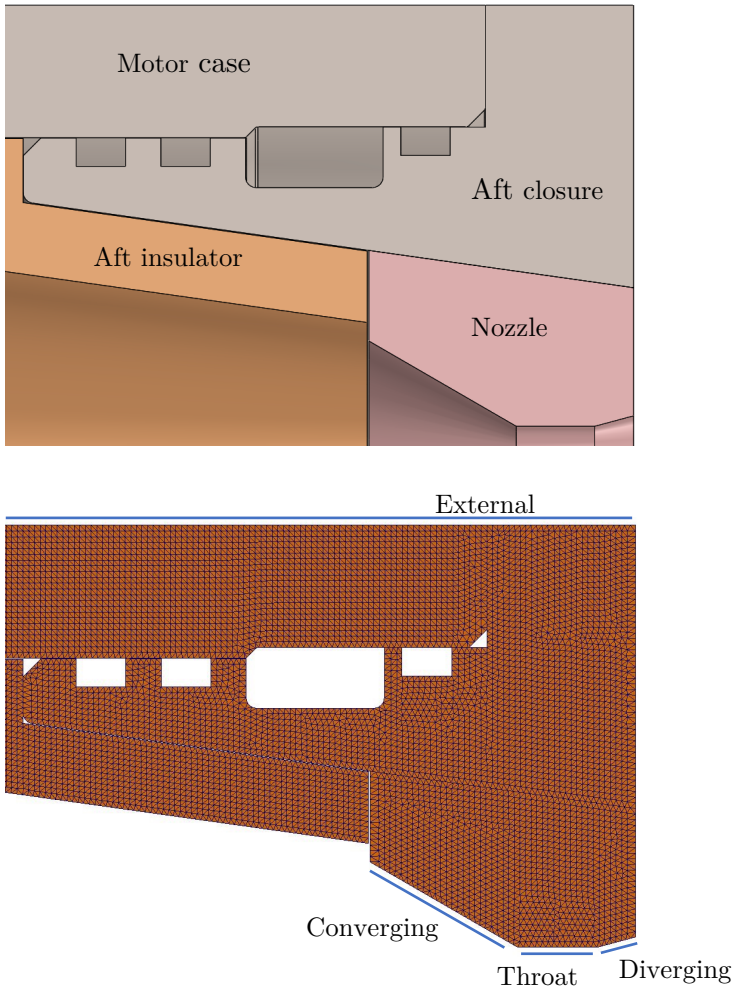

Figure 5-21: (top) A 2D axisymmetric finite element analysis of the motor was used to simulate the nozzle bond line temperature. (bottom) The mesh and boundary conditions for the simulation.

The simulated and averaged measured bond line temperatures are plotted in Figure 5-22 for times between "laser on" and "thrust off". The simulation shows a monotonic rise in temperature. This is the expected behavior before burnout as the heat transferred from the hot combustion gases flowing through the nozzle soaks through the nozzle. Again, the thermocouple data shows an initial peak due to the flame leakage around the laser holder before it released. The temperature then decreases after the laser holder fell away and the excess heat was distributed through the large heat capacity of the motor case. Then, the temperature increases again as the heat from the hot combustion gases soaked through the nozzle to the bond line.

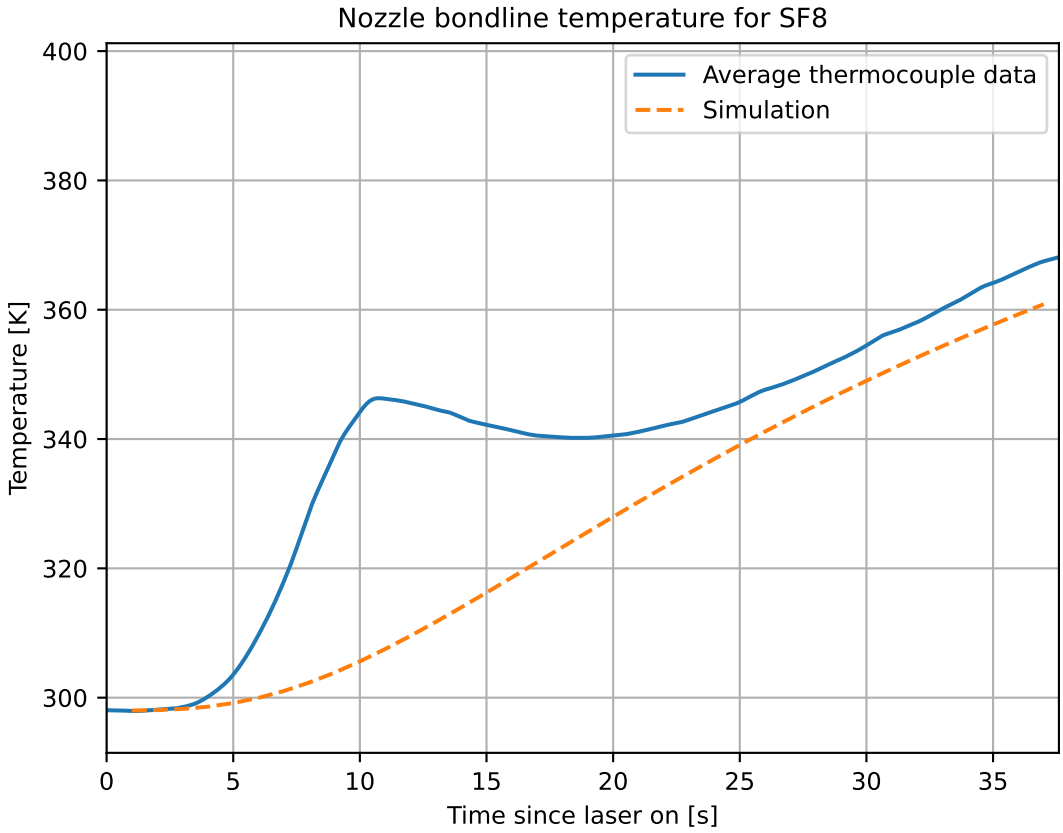

Figure 5-22: The simulated bond line temperature shows good agreement with the thermocouple data after the initial temperature peak due to flame leakage around the laser holder before it released.

After the initial peak in thermocouple temperature due to the flame leakage, the agreement between the thermocouple data and the simulation is surprisingly good.

Since the adiabatic wall temperatures used in the simulation (see table Table 5.6) were based on CFD data for combustion gas at 2000 K instead of 2188 K, a more significant under-prediction by the simulation was expected. However, as noted by Vernacchia in Ref. [14], the CFD analysis that the internal boundary conditions are based on did not account for cooling of the combustion gas due to heat loss to the motor chamber walls. These two effects may roughly cancel each other out in this simulation.

5.7.7 Nozzle cracking

Despite the results of the thermal shock experiments discussed in subsection 5.7.3, the nozzles cracked in all eight static fires. All cracks were in the rz plane of the nozzles (see Figure 5-15 for nozzle coordinate directions), which is consistent with cracking to relieve stress from thermal shock. An image of these cracks for a nozzle is shown in Figure 5-23.

There are several possible explanations for why the thermal shock water quench experiments discussed in subsection 5.7.3 did not show material cracking, while the nozzle motor tests did, including:

- the peak temperature change across the nozzle on motor startup was greater than the 1000 K benchmark used in the thermal shock experiments; or

- machining defects left stress concentrators in the nozzles that weren't present in the thermal shock test samples.

Despite the crack formation in the nozzles, the tapered interface between the nozzle and the aft closure meant that the pressure load on the nozzle from the combustion gases forced the cracks to seal. Because any leak area through the crack was significantly smaller than the nozzle throat area, it is not expected that there was any significant pressure loss due to the cracks.

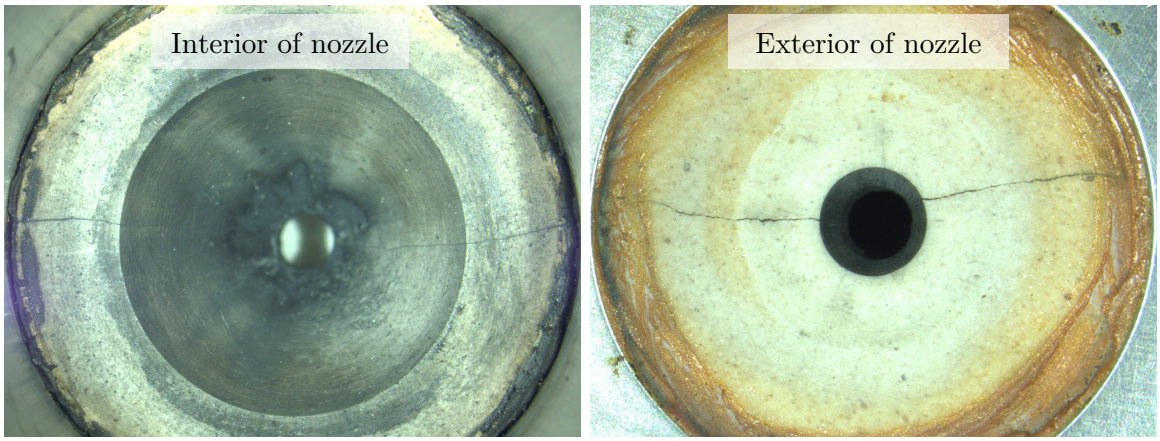

Figure 5-23: The alumina-silicate nozzles cracked during the static fires. However, the tapered interface between the nozzle and aft closure made it so the cracks self-sealed under the pressure load from the motor, so there was no significant loss in chamber pressure.

5.8 Conclusions and recommendations regarding experimental measurements

Experimental static fires measuring exhaust plume radiant intensity, chamber pressure, thrust, and burn rates for small, end-burning solid rocket motors were conducted using a developed research motor with a consistent configuration. A core test matrix of four static fires measured the effects of oxamide and operating chamber pressure on exhaust plume radiant emission: motors were operated with either 0 or 8 % oxamide, and at a chamber pressure of approximately 1.1 MPa or 2.2 MPa. To the author's knowledge, the measurements collected in this work represent the lowest thrust levels for which rigorous plume radiant intensity measurements have been obtained and the only plume radiant intensity measurements for propellants containing oxamide in the open literature.

For all the small solid rocket motor measurements, the strongest emission in the measured spectrum occurred at 4.3 µm, corresponding to CO_2 emission. There were no unexpected peaks in the spectrum, which supports the discussion in subsection 4.3.3 that the inclusion of oxamide in a solid rocket propellant should not create any combustion products in the exhaust that would not have already been present for a

typical composite propellant. From the peak radiant intensity measurements for the core test matrix of static fires, it appears that the radiant intensity is more sensitive to changes in propellant oxamide content than changes in operating chamber pressure.

In future experiments, it would be desirable to measure radiant intensity for small, end-burning solid rocket motors at a larger range of chamber pressures and at higher oxamide contents. As discussed in Ref. [3], the useful range of propellant oxamide mass fractions spans the range of 0 to 20 %. Testing motors at higher oxamide contents up to 20 % would allow the effects of oxamide on radiant intensity to be explored through its useful range, and the reduction in radiant intensity due to increased oxamide content could be validated for contents higher than the 8 % used in this work. It will be discussed in subsection 8.2.1 that for some motors operating at sufficiently low chamber pressures and expansion ratios, modeling results indicate that the afterburning behavior of the plume can change. Collecting radiant intensity measurements for low oxamide contents at lower chamber pressures would enable the validation of these observations.

A new single-component nozzle with the novel application of a machinable alumina-silicate material was also developed during these experiments. It was simpler to manufacture than a previous two-component nozzle design which used a 3D-printed fused silica insulator. This new nozzle was demonstrated in eight static fires, and showed no nozzle erosion and good thermal insulating performance. The nozzles did crack due to thermal shock in the motor firings, however the tapered design caused the cracks to seal under the pressure load, and there was no observed loss in chamber pressure. Future experiments for the nozzle should investigate the nozzle bondline temperature in a more realistic flight motor with less excess thermal mass. The excess thermal mass of the large test motor used in these experiments conducted heat away from the outside of the nozzle quickly, and created unrealistic thermal conditions for determining the thermal insulation performance.

Although the nozzle cracking did not appear to be problematic for these static fires, alternative nozzles should be considered that avoid these thermal shock issues. For future nozzle development, new nozzle manufacturing methods should be considered,

such as casting. Fused silica, which was used for the printed insulator in the previous nozzle iteration, has a high maximum use temperature, high thermal shock resistance, and low thermal-conductivity, and is available off-the-shelf as a castable material. If an appropriate casting process can be developed, cast fused silica nozzles might be an alternative option for a single-component nozzle.

Chapter 6

Exhaust Plume Radiant Emission Model: Description and Implementation

This chapter describes an end-to-end differentiable model developed for predicting exhaust plume radiant emission. The model is implemented in the flexible AeroSandbox design optimization framework introduced in subsection 1.2.3, and details specific to its implementation are provided. Implementing the radiant emission model in AeroSandbox enables fast, scalable optimization of rocket powered vehicles including constraints on radiant emission, and also enables radiant emission to be coupled with all other aircraft design tools available in AeroSandbox. Model validation, results, and recommendations for future model development are discussed in chapter 7.

6.1 Model overview

Predicting the exhaust plume radiant emission for a solid rocket powered vehicle requires the evaluation of a collection of interconnected models representing different physical phenomena in the motor and plume. As previously introduced in subsection 4.2.2, modeling approaches for plume radiant emission typically included sub-models for chamber thermodynamic equilibrium, nozzle & exhaust flow field, and

radiative transfer; afterburning kinetics was included in the calculation of the exhaust flow field.

The modeling for this thesis similarly divides the plume radiant emission problem into a collection of coupled sub-models that together can predict exhaust plume radiant emission. However, in contrast to other plume radiant emission modeling studies (see section 4.2), modeling for this thesis is done with the specific mindset of enabling conceptual design optimization of solid rocket powered vehicles including exhaust plume radiant emission with automatic differentiation and AeroSandbox.

Six sub-models of different coupled physical phenomena were developed and implemented in this thesis to predict exhaust plume radiant intensity. The approach for each sub-model was chosen as a balance between accuracy and simplicity: the simplest possible model was chosen that captured the necessary core physics for conceptual design and maintained compatibility with AeroSandbox modeling limitations discussed in subsection 6.2.2. Each sub-model was implemented as a separate python module using AeroSandbox syntax. The modules were then attached to a single AeroSandbox optimization environment, which coupled the inputs and outputs for the sub-models as illustrated in Figure 6-1. In-depth descriptions of each sub-model are given in section 6.3. A brief description of each of these sub-models is given below:

1. The *chamber thermodynamic equilibrium* sub-model predicts the motor combustion chamber temperature T_c and species mass fractions y_{ic} given the propellant composition and chamber pressure p_c. This sub-model uses equilibrium thermodynamics for these calculations, which is the typical approach used in the literature, as discussed in subsubsection 4.2.3.1.

2. The *motor internal ballistics* sub-model determines motor equilibrium mass flow $\dot{m}_{eq} = \dot{m}_e$, chamber pressure p_c, and nozzle throat diameter d_t given chamber temperature T_c, propellant a and n values, and desired thrust F. These values are solved using a mass flow balance between the burning propellant and the nozzle.

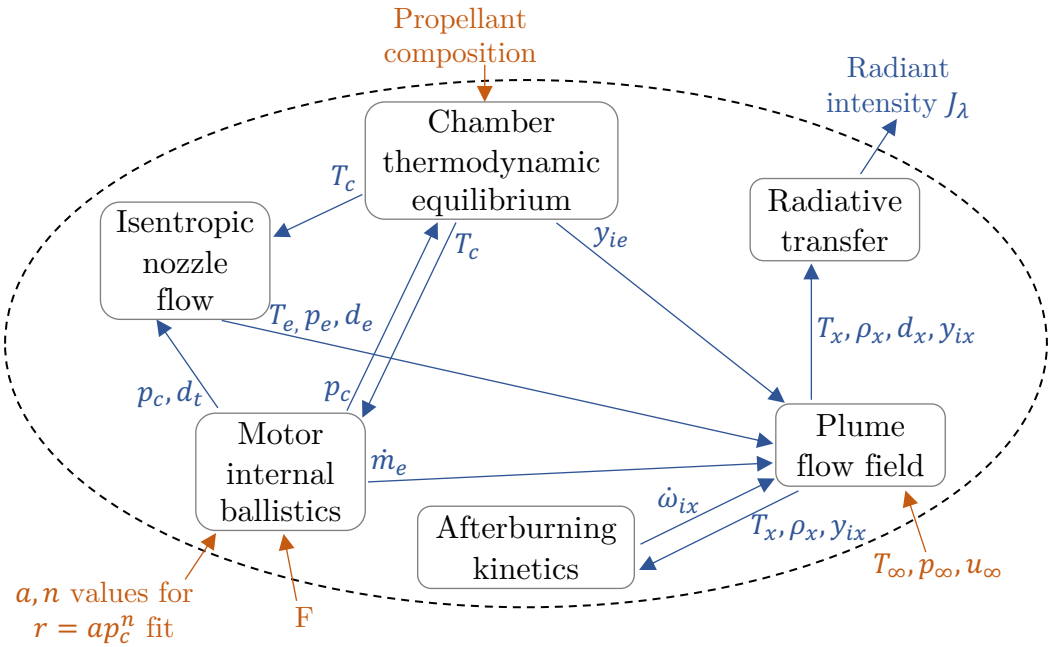

Figure 6-1: The end-to-end differentiable model for plume radiant emission consists of six sub-models for different coupled disciplines.

3. The *isentropic nozzle flow* sub-model determines nozzle exit temperature T_e, pressure p_e, and diameter d_e given chamber temperature T_c, chamber pressure p_c, and nozzle throat diameter d_t. For simplicity, these values are calculated using isentropic nozzle theory assuming frozen flow in the nozzle. This differs from the common approach in the literature to couple the nozzle flow into a joint CFD problem with the plume flow field, as discussed in subsubsection 4.2.3.2.

4. The *plume flow field* sub-model determines temperatures T_x, densities ρ_x, pressures, and species concentrations y_{ix} throughout the exhaust plume given nozzle exit properties and freestream conditions. A 1D simplified plume flow field model is implemented that captures the core effects of turbulent entrainment, jet expansion, and non-equilibrium chemistry. This 1D model is efficient and compatible with AeroSandbox, and does not rely black-box CFD codes used by many studies in the literature, as discussed in subsubsection 4.2.3.2.

5. The *afterburning kinetics* sub-model determines the species production rates $\dot{\omega}_{ix}$ throughout the plume given temperatures, densities, and species mass fractions

throughout the plume. This sub-model uses a simple, single reaction mechanism with a global reaction rate equation fit to reaction rates predicted by a 28 reaction mechanism. This fitted global reaction rate equation is significantly less stiff than the 10 or more reaction mechanisms used in the literature (see Table 4.2 and subsubsection 4.2.3.3 for a discussion of kinetics approaches used in the literature), and is therefore much easier to integrate in AeroSandbox.

6. The *radiative transfer* sub-model determines the plume radiant intensity J_λ given temperatures, densities, and species mass fractions throughout the plume. This sub-model integrates the radiative transfer equation using a line-of-sight method, and uses the Ludwig et al. single line group model [27]. This is a common approach used by other studies, as discussed in subsubsection 4.2.3.4 and subsubsection 4.2.3.5. Differentiable surrogate models were developed for this thesis for evaluating spectral band parameters for the single line group model.

6.2 Implementation with AeroSandbox

Models developed for this thesis are implemented in the AeroSandbox framework, which was introduced in subsection 1.2.3 [5]. AeroSandbox provides a flexible, scalable framework for implementing and solving high-dimensional design problems including fully- or under-constrained systems of nonlinear, implicit, and differential equations. Utilizing AeroSandbox enables the models developed for this thesis to be coupled with the other available aircraft design models for aerodynamics, structures, trajectory, and more already included in AeroSandbox. The following subsection provides additional details on syntax and modeling tools available in AeroSandbox, as well as some model limitations.

6.2.1 Defining design problems

All design problems implemented in AeroSandbox are defined as an optimization problem, even if the problem is fully constrained. Standard optimization problems are written using four elements:

1. *Variables* are quantities in the design problem that are not known; they are degrees of freedom and their values are solved for by the optimizer.

2. *Constraints* put bounds on variables or expressions that are functions of variables. They constrain the feasible design space. Constraints can be defined as equalities or inequalities.

3. The *objective* is the function in the design problem that is to be minimized by the optimizer. This is often a relevant performance metric.

4. *Parameters* are quantities in the design problem that have a pre-selected value that may be changed to update assumptions or perform design sweeps, but are otherwise treated as a constant by the optimizer during any particular optimization.

AeroSandbox provides straightforward syntax for implementing each of these optimization problem elements for a design problem. Each of the models introduced in section 6.1 are implemented in separate python classes as fully constrained systems of equations; that is, there are the same number of variables as there are constraints. Fully constrained systems do not need an objective function since the feasible space for solutions is already a single point. The developed models can be assembled into a larger optimization problem with additional variables, constraints, parameters, and an objective if desired.

6.2.2 Model limitations

Despite its great flexibility, the AeroSandbox framework does create some limitations on the types of models that can be used. The most important of these limitations are described below:

- *Glass-box models*: AeroSandbox uses automatic differentiation, which evaluates computational function derivatives by decomposing functions into elementary functions which have known derivatives, and then combining those derivatives using the chain rule [8]. To evaluate these derivatives, AeroSandbox needs direct access to the code for the model. Therefore models in AeroSandbox must be "glass-box", and coded directly in python using `AeroSandbox.numpy` syntax; "black-box" codes cannot be used.

- *C^1-continuity*: AeroSandbox uses gradient descent with automatic differentiation to solve optimization problems, which requires that models be C^1-continuous with respect to any problem variables. AeroSandbox has several tools for implementing surrogate models to meet the C^1-continuity requirement, which are described in subsection 6.2.3.

- *Non-stiff differential equations*: AeroSandbox integrates ODEs using a trapezoidal collocation method, which enforces integration as constraints between time steps assuming a trapezoidal integration scheme with non-adaptive time steps [75]. The constraints defined with the trapezoidal scheme are solved implicitly with IPOPT in AeroSandbox. This integration scheme does not converge well for some stiff systems of differential equations, and therefore stiff equations should be implemented with caution.

6.2.3 Surrogate modeling tools

AeroSandbox has a number of tools for developing differentiable models from otherwise discontinuous models. Several of these tools were used in the sub-models discussed later in this chapter. Piece-wise models can be blended using a sigmoid transition function, which is implemented in AeroSandbox with the `AeroSandbox.numpy.blend()` method. Models based on data points can be interpolated using a differentiable spline. In AeroSandbox, structured data can be modeled using the `InterpolatedModel()` class and unstructured data can be modeled using the `UnstructuredInterpolatedModel()` class.

6.3 Sub-model descriptions

Six key sub-models were implemented for this thesis to evaluate the plume radiant emission, as illustrated in Figure 6-1. These modules are described in this section.

6.3.1 Chamber thermodynamic equilibrium

Propellant combustion temperature and product species fractions are calculated in the chamber thermodynamic equilibrium module. These propellant combustion properties are determined in this model using equilibrium thermodynamics. Namely, combustion temperature and products are determined by minimizing their Gibbs free energy subject to conservation of mass and enthalpy, as introduced in section 2.5. Which species to include in the combustion products are simply guessed at using the common combustion products for solid rocket propellants (and species that are not present will simply solve to near-zero mole fractions). The implemented governing equations and methodology for determining species thermodynamic properties are described below.

6.3.1.1 Governing equations

The governing equations for the chamber thermodynamic equilibrium module are given below [76]:
Minimization of Gibbs free energy for gaseous products:

$$\hat{g_j^0}(T_c) + \hat{R}T_c \ln\left(\frac{n_j}{n_{gas}}\right) + \hat{R}T_c \ln\left(\frac{p_c}{p_0}\right) - \sum_{i=1}^{N_{elements}} \lambda_i a_{ij} = 0 \qquad \text{for } j = 1, \ldots, N_{species,gas} \tag{6.1}$$

Minimization of Gibbs free energy for condensed products:

$$\hat{g_j^0}(T_c) - \sum_{i=1}^{N_{elements}} \lambda_i a_{ij} = 0 \qquad \text{for } j = N_{species,gas} + 1, \ldots, N_{species} \tag{6.2}$$

Conservation of mass of chemical elements:

$$\sum_{j=1}^{N_{species}} a_{ij} n_j - \frac{b_{i0}}{\hat{m}_i} = 0 \qquad \text{for } i = 1, \ldots, N_{elements} \tag{6.3}$$

Conservation of enthalpy:

$$\sum_{j=1}^{N_{species}} n_j \hat{h}_j^0 - H_0 = 0 \tag{6.4}$$

Enforcement of molar sum of gaseous products:

$$\sum_{j=1}^{N_{species,gas}} n_j - n_{gas} = 0 \tag{6.5}$$

In the above equations, j are species, i are chemical elements, $\hat{g_j^0}$ is molar Gibbs free energy of species j, $\hat{h_j^0}$ is molar enthalpy of species j, H_0 is total system enthalpy, T_c is the chamber combustion temperature, p_c is the chamber pressure, p_0 is standard state pressure, n_j is number of moles of species j, n_{gas} is the number of moles of gas, a_{ij} is the number of moles of element i per mole of species j, b_{i0} is the total system mass of element i, $\hat{m}_i$ is the atomic mass of element i, λ_i are Lagrange multipliers, $N_{species}$ is the number of chemical species in the system, $N_{species,gas}$ is the number of gaseous species in the system ($N_{species,gas} \leq N_{species}$), and $N_{elements}$ is the number of chemical elements in the system. Gibbs free energy can be calculated using $\hat{g_j^0} = \hat{h_j^0} - T_c \hat{s_j^0}$, where $\hat{s_j^0}$ is molar entropy. Calculation of thermodynamic properties (including enthalpy and entropy) are discussed in subsubsection 6.3.1.2.

Lagrange multipliers λ_i are used, following the formulation given by Ponomarenko [76]. Using Lagrange multipliers allows the thermodynamic equilibrium problem to be solved as a system of constrained equations, rather than as a true minimization problem. This is important for implementation in AeroSandbox, so that the equations can be implemented as a set of problem constraints, rather than as a minimization problem which would be implemented as part of the problem objective.

6.3.1.2 Thermodynamic properties

Species thermodynamic properties – namely molar heat capacity at constant pressure $\hat{c}_p^0$ [$\mathrm{J\,mol^{-1}\,K^{-1}}$], molar enthalpy $\hat{h}^0$ [$\mathrm{J\,mol^{-1}}$], and molar entropy $\hat{s}^0$ [$\mathrm{J\,mol^{-1}\,K^{-1}}$] – are determined using the NASA 9-coefficient polynomial parameterizations [77]. The superscript 0 indicates that these quantities are for species in their standard state. These parameterizations have the following form:

$$\frac{\hat{c}_p^0(T)}{\hat{R}} = a_0 T^{-2} + a_1 T^{-1} + a_2 + a_3 T + a_4 T^2 + a_5 T^3 + a_6 T^4 \tag{6.6}$$

$$\frac{\hat{h}^0(T)}{\hat{R}T} = -a_0 T^{-2} + a_1 \frac{\ln T}{T} + a_2 + \frac{a_3}{2} T + \frac{a_4}{3} T^2 + \frac{a_5}{4} T^3 + \frac{a_6}{5} T^4 + \frac{a_7}{T} \tag{6.7}$$

$$\frac{\hat{s}^0(T)}{\hat{R}} = -\frac{a_0}{2} T^{-2} - a_1 T^{-1} + a_2 \ln T + a_3 T + \frac{a_4}{2} T^2 + \frac{a_5}{3} T^3 + \frac{a_6}{4} T^4 + a_8 \tag{6.8}$$

where T is temperature in K, $\hat{R}$ is ideal gas constant in $\mathrm{J\,mol^{-1}\,K^{-1}}$, and a_0 to a_8 are fitted coefficients specific to each species. Species coefficients are available in Ref. [77].

It should be noted that the enthalpy $\hat{h}^0$ for each species includes its heat of formation:

$$\hat{h}^0(T) = \Delta_f \hat{h}^0(298.15) + \left[\hat{h}^0(T) - \hat{h}^0(298.15)\right] \tag{6.9}$$

where the heat of formation has been arbitrarily assigned to equal the enthalpy at 298.15 K: $\Delta_f \hat{h}^0(298.15) = \hat{h}^0(298.15)$. This is important for writing the governing equations for the plume flow field, as discussed in subsubsection 6.3.4.1.

6.3.2 Internal ballistics

The internal ballistics module calculates motor equilibrium mass flow, chamber pressure, and thrust. It requires chamber temperature as an input, as well as properties of the propellant, including propellant solid density ρ_p, and a and n values to characterize the propellant using the empirical burn rate law $r = a p_c^n$.

The equilibrium chamber pressure and thrust are calculated according to the methods described in subsection 2.2.2. Namely, equilibrium chamber pressure is

calculated using (repeated from Equation 2.6):

$$p_{c,eq} = (K_n \rho_p c^* a)^{\frac{1}{1-n}} \; ; \;\; K_n \equiv \frac{A_b}{A_t} \tag{6.10}$$

and equilibrium thrust is calculated using (repeated from Equation 2.8):

$$F_{eq} = p_c^n C_F \left(\frac{p_c}{p_e}, \frac{p_a}{p_e}, \gamma \right) c^* \left(R, \gamma, T_c \right) a \rho_p A_b \tag{6.11}$$

The above equations are implemented using the `proptools` python library [78]. This module also enforces a minimum combustion pressure constraint as a function of oxamide mass fraction w_{om}:

$$p_c \geq \max \left(0, p_{c,min} \right) \tag{6.12}$$

where

$$p_{c,min} = 5.060 w_{om}^{1.545} - 0.031 \tag{6.13}$$

Minimum burn pressure for oxamide containing propellants is introduced in subsection 2.4.3, and an empirical model for minimum burn pressure is discussed in subsection 5.6.4.

6.3.3 Nozzle flow

The nozzle flow module calculates flow properties at the nozzle exit – including nozzle exit temperature, velocity, and area – assuming isentropic, frozen flow[†] in the nozzle. The calculations rely on the isentropic flow equations. For a given pressure ratio p_c/p_e, the nozzle exit mach number M_e is found by solving

$$\frac{p_c}{p_e} = \left(1 + \frac{\gamma - 1}{2} M_e^2 \right)^{\frac{\gamma}{\gamma - 1}} \tag{6.14}$$

where γ is the ratio of specific heats of the gas. γ is assumed equal to the ratio of specific heats in the combustion chamber γ_c following the frozen flow assumption. The

[†]Assuming frozen flow significantly simplifies the nozzle analysis, with typical errors <5 % for performance parameters (i.e. specific impulse I_{sp} or characteristic velocity c^*) [2].

nozzle temperature ratio T_c/T_e is found from M_e using

$$\frac{T_c}{T_e} = 1 + \frac{\gamma - 1}{2} M_e^2 \tag{6.15}$$

and the nozzle expansion ratio A_e/A_t is found using

$$\frac{A_e}{A_t} = \left(\frac{\gamma + 1}{2}\right)^{-\frac{\gamma+1}{2(\gamma-1)}} \frac{\left(1 + \frac{\gamma-1}{2} M_e^2\right)^{\frac{\gamma+1}{2(\gamma-1)}}}{M_e} \tag{6.16}$$

These equations are implemented using the `proptools` python library [78].

6.3.4 Plume flow field

The plume flow field module calculates temperature, density, velocity, and species mass fractions throughout the exhaust plume. This section describes the model used for determining the plume field, as well as methods for handling its various dependencies.

6.3.4.1 Governing equations

A 1D simplified plume flow field model is used to determine the temperature, density, velocity, diameter, and species mass fractions throughout the exhaust plume. This model concept is illustrated below in Figure 6-2.

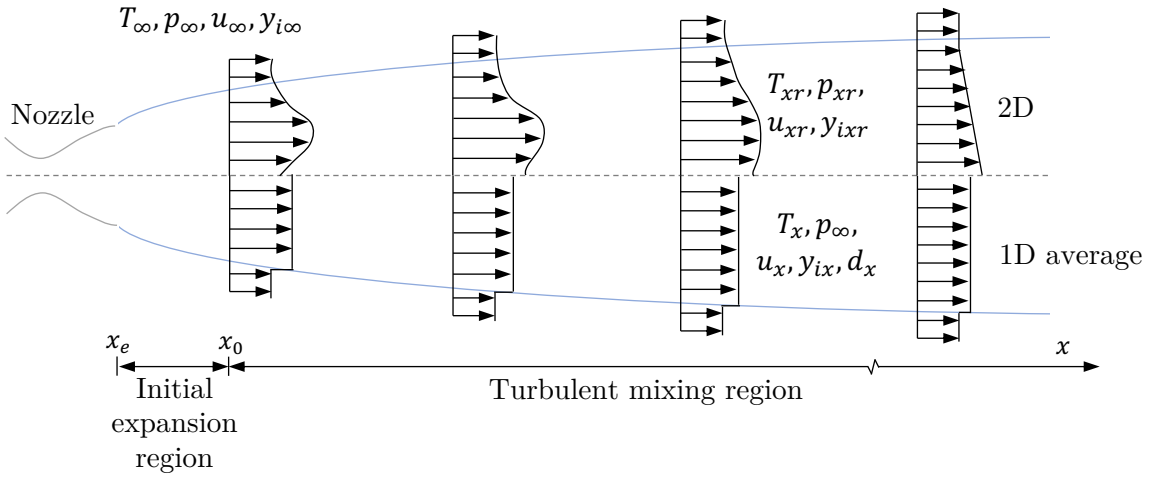

Figure 6-2: The 1D plume flow field model assumes average properties at each station in the plume in the turbulent mixing region, as opposed to a 2D model.

The model, originally proposed by Woodroffe [55], and used more recently by Mao et al. 2017 [61] and Niu et al. 2019 [53], makes the following assumptions:

- plume properties are averaged at each axial station (i.e. no radial variations in plume properties);
- entrained mass is mixed instantly and uniformly through the plume cross section;
- pressure in the plume is constant and equal to ambient pressure;
- nozzle expansion is near perfect, such that the plume initial expansion region is small and can be neglected; and
- radiation from the plume has no influence on the flow parameters throughout the plume.

After the flow exits the nozzle, there is an initial expansion region where the exhaust flow expands to ambient pressure. Once ambient pressure is achieved in the plume, the plume enters the turbulent mixing region, where it begins mixing and reacting with air from the freestream.

The governing equations for the 1D plume flow field model enforce conservation of mass, momentum, energy, and species flows, in addition to the ideal gas law state equation. These equations are given below.

Mass flow:

$$\frac{d}{dx}\left(\rho d^2 u\right) = 4d\alpha\sqrt{\rho\rho_\infty}\left(u - u_\infty\right) \tag{6.17}$$

Momentum flow:

$$\frac{d}{dx}\left(\rho d^2 u^2\right) = u_\infty \frac{d}{dx}\left(\rho d^2 u\right) \tag{6.18}$$

Energy flow[†]:

$$\frac{d}{dx}\left[\rho d^2 u\left(h + \frac{1}{2}u^2\right)\right] = \left(h_\infty + \frac{1}{2}u_\infty^2\right)\frac{d}{dx}\left(\rho d^2 u\right) \tag{6.19}$$

[†]For self-consistency, the energy flow equation is written differently here than how it is written by Woodroffe. Namely, a term on the right hand side accounting for the heat released due to afterburning reactions is omitted, since the heat release is accounted for by the heat of formation already included in the definition of enthalpy, as discussed in subsubsection 6.3.1.2.

Species flow:

$$\frac{d}{dx}\left(\rho d^2 u y_i\right) = y_{i\infty}\frac{d}{dx}\left(\rho d^2 u\right) + \dot{\omega}_i d^2 \tag{6.20}$$

Ideal gas law:

$$p_\infty = \rho R T \tag{6.21}$$

where ρ is density, d is diameter, u is velocity, α is entrainment coefficient, h is enthalpy [$\mathrm{J\,kg^{-1}}$], y_i is mass fraction of species i, $\dot{\omega}_i$ is the species production rate of species i [$\mathrm{mol\,m^{-3}\,s^{-1}}$], and subscript ∞ denotes freestream values. Handling of entrainment coefficient is discussed in subsubsection 6.3.4.4, enthalpy in subsubsection 6.3.4.3, soot in subsubsection 6.3.4.5, and species production rate in subsection 6.3.5.

6.3.4.2 Initial conditions

Equations 6.17 - 6.20 apply to the plume flow field once the plume has expanded to equilibrium pressure and is in the turbulent mixing region. Appropriate initial conditions must be used that consistently account for the effect of initial plume expansion on mass, momentum, energy, and species flow of the plume.

The initial conditions proposed by Mao et al. [61] are utilized in this module, which assume frozen flow and no entrainment effects in the plume initial expansion region. The following system of equations can be solved to determine the initial conditions at the start of the turbulent mixing region x_0:
Mass flow:

$$\rho_0 u_0 d_0^2 = \rho_e u_e d_e^2 \tag{6.22}$$

Momentum flow:

$$\rho_0 u_0^2 d_0^2 = \rho_e u_e^2 d_e^2 + \left(p_e - p_\infty\right) d_e^2 + \frac{1}{2} C_D \rho_\infty u_\infty^2 d_0^2 \tag{6.23}$$

Energy flow:

$$h_0 + \frac{1}{2}u_0^2 = h_e + \frac{1}{2}u_e^2 \tag{6.24}$$

Species flow:

$$y_{0i} = y_{ei} \tag{6.25}$$

where

$$C_D = \frac{16}{9\pi}\left\{\left[\left(1-\left(\frac{p_e}{p_c}\right)^{\frac{\gamma-1}{\gamma}}\right)^{1/2}+\frac{\epsilon\left(p_e-p_\infty\right)}{p_c C_{F,max}}\right]^{-1}-1\right\}; \tag{6.26}$$

$$C_{F,max} = \left[\frac{2\gamma^2}{\gamma-1}\left(\frac{2}{\gamma+1}\right)^{\frac{\gamma+1}{\gamma-1}}\right]^{1/2} \tag{6.27}$$

In the above equations, subscript e refers to conditions at the nozzle exit, subscript 0 refers to conditions at the start of the turbulent mixing region, C_D is the plume drag coefficient, $C_{F,max}$ is the maximum thrust coefficient, ϵ is the nozzle expansion ratio, and γ is the ratio of specific heats.

6.3.4.3 Enthalpy

Enthalpy h [$\mathrm{J\,kg^{-1}}$] of the gas mixture is calculated as a weighted sum of the enthalpies of the constituent species:

$$h = \sum^{species} y_i \frac{\hat{h}_i^0}{M_i} \tag{6.28}$$

where y_i is species mass fraction, M_i is species molecular weight, and $\hat{h}_i^0$ is the species molar enthalpy, which can be calculated using the NASA 9-coefficient polynomials discussed in subsection 6.3.1.

6.3.4.4 Entrainment coefficient

The entrainment coefficient α is determined using the fits developed by Witze [79]. The fits propose different values for α for subsonic and supersonic flows. Assuming that the flow at the start of the turbulent mixing region is supersonic, the expressions for entrainment coefficient for the supersonic and subsonic portions of the plume are:

$$\alpha = \begin{cases} 0.063\left(M_0^2-1\right)^{-0.15} & \text{for } M \geq 1 \\ 0.0672\left(\frac{\rho_\infty}{\rho_0}\right)^{-0.22} & \text{for } M < 1 \end{cases} \tag{6.29}$$

where M is Mach number and M_0 is Mach number at the start of the turbulent mixing region x_0. The two regions are blended together using the `AeroSandbox.numpy.blend()` method introduced in subsection 6.2.1.

6.3.4.5 Soot

The following assumptions are made when calculating the soot concentrations and temperatures in the plume flow field:

- soot in the plume is assumed non-reactive after it exits the nozzle, such that the mass flow rate of soot at any station in the plume is constant and equal to the mass flow rate of soot at the nozzle exit;
- the soot mass fraction is assumed to be small, such that its presence does not affect local plume temperatures, velocities, or gas densities;
- the soot particles in the plume are assumed small, such that soot in the plume has the same temperature and velocity as the local flow; and
- there are no radial variations in soot concentration in the plume.

Following these assumptions, the soot volume fraction $f_{v,soot}$ throughout the plume is determined using:

$$f_{v,soot} = y_{0,soot} \frac{\dot{m}_0}{\dot{m}} \frac{\rho}{\rho_{soot}} \tag{6.30}$$

where subscript 0 represents conditions at the start of the turbulent mixing region, $\dot{m}$ is mass flow rate, ρ is density in the plume, and $\rho_{soot} \approx 1770\,\mathrm{kg\,m^{-3}}$ is the solid density of carbon soot.

6.3.5 Afterburning kinetics

The differential equations representing finite rate reaction mechanisms, typically used to evaluate afterburning reaction kinetics in exhaust plumes (see subsubsection 4.2.3.3), are extremely stiff and difficult to integrate without specialized integrators. The integration scheme used by AeroSandbox (see subsection 6.2.2) is not well suited

for stiff systems of equations, and cannot reliably integrate a detailed chemical kinetics mechanism. To make the reaction kinetics more computationally tractable in AeroSandbox, a reduced-order global reaction mechanism kinetics model was developed. The model was developed with the goal of finding the simplest model for afterburning kinetics that captures the core physics and limiting behavior, and scales correctly. This model is not meant to be an equally rigorous replacement for detailed reaction rate mechanisms, but rather a simplified and practical tool for supporting conceptual level design and analysis of exhaust plumes.

The model assumes a global reaction mechanism with a single reaction rate. All fuel species are consumed at the same rate (relative to their initial quantities in the plume). An Arrhenius type rate equation is used to determine the reaction rate, with parameters fitted to results from a more detailed reaction mechanism. More details of the model are provided in the following subsections.

6.3.5.1 Global reaction mechanism

A global reaction mechanism is assumed:

$$X_{CO}\mathrm{CO} + X_{H_2}\mathrm{H_2} + X_{OH}\mathrm{OH} + X_{O_2}\mathrm{O_2} \longrightarrow X_{H_2O}\mathrm{H_2O} + X_{CO_2}\mathrm{CO_2} \tag{6.31}$$

where X_i are the stoichiometric coefficients for each species i. The global reaction is assumed to be irreversible, HCl is assumed to be nonreactive (following the treatment used in Ref. [47] for low altitude plumes), and reactions involving other species are ignored.

Appropriate stoichiometric coefficients X_i must be determined so that the reaction mechanism is balanced. The stoichiometric coefficients for the fuel species (CO, H_2, and OH) are taken as their respective initial mole fractions w_{ei} at the nozzle exit. The stoichiometric coefficients for O_2 and the product species can be calculated as a function of the coefficients for the fuel species to ensure the mechanism is balanced.

The equations for calculating these coefficients are as follows:

$$\begin{aligned} X_{CO} &= w_{e,CO} \\ X_{H_2} &= w_{e,H_2} \\ X_{OH} &= w_{e,OH} \\ X_{O_2} &= \frac{1}{2}X_{CO} + \frac{1}{2}X_{H_2} - \frac{1}{4}X_{OH} \\ X_{H_2O} &= X_{H_2} + \frac{1}{2}X_{OH} \\ X_{CO_2} &= X_{CO} \end{aligned} \tag{6.32}$$

6.3.5.2 Global reaction rate equation

The global reaction mechanism leads to a global reaction rate r (units: $\mathrm{mol\,m^{-3}\,s^{-1}}$) such that the species production rate $\dot{\omega}_i$ (units: $\mathrm{kg\,m^{-3}\,s^{-1}}$) can be defined as

$$\dot{\omega}_i \equiv \nu_i M_i r \tag{6.33}$$

where subscript i is species, $\nu_i = -X_i$ for reactant species, $\nu_i = +X_i$ for product species, and M_i is molecular weight.

The global reaction rate r is assumed to have an Arrhenius equation form, similar to what is used to model elementary reactions in detailed reaction mechanisms (see subsubsection 4.2.3.3):

$$r = Ae^{-E_a/RT}[fuel]^{n_{fuel}}[\mathrm{O_2}]^{n_{O_2}}[gas]^{n_{gas}} \tag{6.34}$$

where A is the pre-exponential factor, T is temperature, E_a is the reaction activation energy, R is the universal gas constant, n are concentration exponents, and bracketed quantities are concentrations. The concentration of fuel $[fuel]$ includes CO, H_2, and OH (i.e. $[fuel] = [\mathrm{CO} + \mathrm{H_2} + \mathrm{OH}]$). The general gas concentration term (the final term in the equation, $[gas]^{n_{gas}}$) allows for effects of third body reactions to be captured in the reaction rate model.

6.3.5.3 Global reaction rate parameter fits

The parameters A, E_a, n_{fuel}, n_{O_2}, and n_{gas} are fitted using a more detailed reaction kinetics mechanism implemented using the python package `Cantera` [21]. Specifically, the 28 reaction, 13 species mechanism recommended by Ecker et al. 2019 [80], which was intended for combustion modeling in solid rocket motor plumes, is used to fit the model parameters.

Reactions for combinations of initial temperatures from 600 K to 3000 K, pressures from 0.1 atm to 1 atm, and exhaust-to-air mass ratios[†] (EAR) from 0.01 to 100 were simulated in an ideal gas constant pressure and temperature reactor in Cantera. The large range of exhaust-to-air ratios is chosen to account for different conditions throughout the plume: near the nozzle exit, little air is yet to be entrained, so the gas mixture is fuel rich and EAR $\gg 1$; far away from the nozzle exit, much more air has been entrained than initial exhaust flow, so the mixture is fuel lean and EAR $\ll 1$. The relative ratios of fuel species are chosen to match the equilibrium combustion products of the baseline propellant formulation used in the work (see subsection 5.3.1).

For each simulated reaction, the concentration of O_2 versus time is recorded, along with initial concentrations of all species and the equilibrium concentration of O_2. An exponential decay model $[O_2] - [O_2]_{equilibrium} = \left([O_2]_{t=0} - [O_2]_{equilibrium}\right) e^{-t/\tau}$ is fit to the O_2 concentration versus time data using the `lmfit` python package [81]. The reaction rate for O_2 is taken to be the derivative of the fitted model at $t = 0$, or $r_{O_2} = -\left([O_2]_{t=0} - [O_2]_{equilibrium}\right)/\tau$. The value of r_{O_2} is recorded for each combination of pressure and EAR. The global reaction rate r is taken as $r = r_{O_2}/\nu_{O_2}$. These global reaction rates r are shown in Figure 6-3 as the plotted points.

The simulated global reaction rate r was fit to the global reaction rate model given in Equation 6.34 also using `lmfit`. A low-temperature and high-temperature regime is apparent in the reaction rate values r, so the reaction rate equation given in Equation 6.34 is fit to r separately for these two regimes, and the results are blended

[†]Exhaust-to-air ratio has an approximately linear relationship with equivalence ratio, defined as $\phi \equiv (w_{fuel}/w_{O_2})/(w_{fuel}/w_{O_2})_{stoich}$. They have values of the same order of magnitude for propellants in this work as well: for instance, for the combustion products of the baseline propellant formulation at stoichiometric conditions, $\phi = 1$ (by definition) and $EAR = 0.69$.

together using the `AeroSandbox.numpy.blend()` method described in subsection 6.2.3. The low-temperature regime reaction rate values r are evaluated using temperatures from 600 K to 800 K, and the high temperature regime values are evaluated using temperatures from 1000 K to 3000 K. The fitted parameters for the two regimes are given in Table 6.1. The fitted reaction rate model is plotted versus temperature for a number of exhaust-to-air ratios and pressures in Figure 6-3, along with the values for r determined using the above methods. This model should only be used for pressures >0.1 atm. At pressures below this, the assumption of irreversible reactions discussed in subsubsection 6.3.5.1 breaks down, and the global reaction rate model given in Equation 6.34 is no longer a good fit for evaluating the reaction rate.

	Low-Temperature	**High-Temperature**
A $\left[(\text{kmol m}^{-3})^{1-\Sigma n}\ \text{s}^{-1}\right]$ †	9.641×10^{12}	1.580×10^{11}
E_a/R [K]	24 834	9756
n_{fuel} [-]	1.403	1.861
n_{O_2} [-]	0.652	1.793
n_{gas} [-]	−0.471	−1.621

Table 6.1: Parameters for the global reaction rate model were fitted to results from Cantera.

†The pre-exponential factor A must have the appropriate units so that the reaction rate r has the correct units of $\text{kmol m}^{-3}\,\text{s}^{-1}$. The units for A account for the concentration terms in the reaction rate equation, where $\sum n = n_{fuel} + n_{O_2} + n_{gas}$.

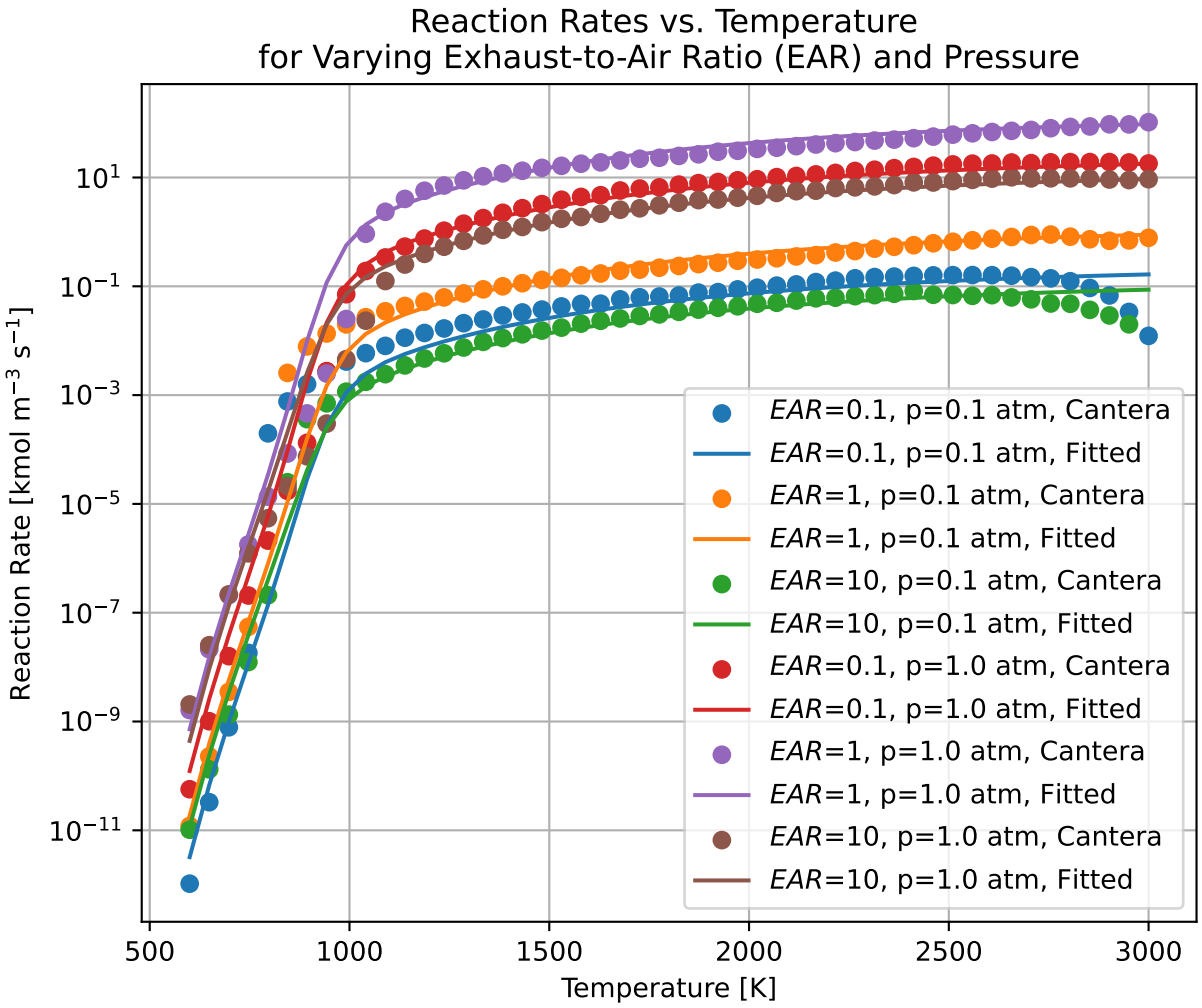

Figure 6-3: A global reaction rate mechanism was fitted to reaction rates calculated with Cantera for a range of pressures and equivalence ratios. Parameters were fit separately for temperatures below 800 K and above 1000 K, and the results were blended together.

6.3.6 Radiative transfer

The plume spectral radiant intensity is evaluated in the radiative transfer sub-model. It uses the temperature, density, and species distributions determined by the plume flow field module to determine the plume optical depth (defined in section 3.2), integrate the radiative transfer equation (Equation 3.1), and subsequently determine the plume radiant emission properties. This sub-model uses a line-of-sight method to integrate the radiative transfer equation and the Ludwig et al. single line group model for

determining the optical depth, which were both introduced in subsection 4.2.3 [27]. Further details are provided in the following sections.

6.3.6.1 Integration of the radiative transfer equation

The radiative transfer equation must be evaluated to determine the plume spectral radiance I_λ along each line-of-sight through the plume. The radiative transfer equation is given in Equation 3.1, and is reprinted below:

$$\overbrace{\frac{dI_\lambda}{ds}}^{\substack{\text{change in}\\ \text{radiative energy}\\ \text{per path length}}} = \overbrace{+\kappa_\lambda I_{b\lambda}}^{\substack{\text{gain due to}\\ \text{emission}}} \overbrace{-\kappa_\lambda I_\lambda}^{\substack{\text{loss due to}\\ \text{absorption}}} \overbrace{-\sigma_{s\lambda} I_\lambda}^{\substack{\text{loss due to}\\ \text{out-scattering}}} \overbrace{+\frac{\sigma_{s\lambda}}{4\pi}\int_{\Omega_i=4\pi} I_\lambda(\hat{s}_i)\Phi_\lambda(\hat{s}_i,\hat{s})d\Omega_i}^{\substack{\text{gain due to}\\ \text{in-scattering}}} \quad (6.35)$$

Equation 6.35 as written cannot be directly evaluated. To simplify the integration, it is assumed that no scattering particles are present in the plume[†]. Following this assumption, the scattering coefficient $\sigma_{s\lambda} = 0$ and the last two terms of the equation can be neglected. This greatly simplifies the radiative transfer equation because the radiance can be independently integrated along each line-of-sight, since each line-of-sight is independent of flow and radiation parameters elsewhere in the plume.

Next, the plume flow field model described in subsection 6.3.4 makes the assumption that there are no radial variations in flow parameters throughout the plume. Assuming a viewing angle perpendicular to the plume axis of symmetry, and following the assumptions made for the plume flow field model, the line-of-sight through the plume at any downstream station is isothermal and homogenous. This means that at any location throughout the plume, the absorption coefficient κ_λ along the line of sight is constant, and the optical depth can be determined simply using $\tau_\lambda = \kappa_\lambda L$, where L is the path length through the plume. Following these assumptions, the integration of

[†]Soot particles are small enough that they are treated as non-scattering (discussed in subsection 3.5.3), so this assumption does not affect the treatment of soot. This assumption does not account for scattering from alumina particles that would be present from aluminized propellants. This work uses a non-aluminized propellant.

the radiative transfer equation is straightforward:

$$I_\lambda = I_{b\lambda}\left(1 - e^{-\tau_\lambda}\right) \tag{6.36}$$

where I_λ is spectral radiance ($\mathrm{W\,\mu m^{-1}\,sr^{-1}\,m^{-2}}$), $I_{b\lambda}$ is black body spectral radiance ($\mathrm{W\,\mu m^{-1}\,sr^{-1}\,m^{-2}}$), and τ_λ is optical depth (dimensionless). Equation 6.36 is equivalent to the definition of emissivity for an isothermal, non-scattering medium given in Equation 3.5. The calculation procedure for determining τ_λ for soot is discussed in subsubsection 6.3.6.3 and for molecular gases in subsubsection 6.3.6.4.

6.3.6.2 Plume spatial integration for determining radiant intensity

As introduced in subsection 3.2.1, plume spectral radiant intensity J_λ is found by integrating I_λ over the projected viewing area of the plume:

$$J_\lambda = \int_{A_{projected}} I_\lambda dA \tag{6.37}$$

Because the spectral radiant intensity J_λ is a spatial integration of spectral radiance I_λ along every line-of-sight in the plume, it is dependent on the plume flow field and spectral radiance values at every location in the plume. Determining the derivatives of J_λ with automatic differentiation in AeroSandbox is computationally expensive because of this dense dependence on the many variables throughout the exhaust plume. Therefore some assumptions are made to simplify the spatial integration of the plume. The physical path length $L(x)$ through the plume at each downstream location in the plume x is assumed constant and set as $0.95d(x)$ following the mean beam length approximation [25]. This allows a single value of $\tau_{\lambda i}$ to be calculated at each location x. The effective projected plume height at each station is taken as $0.95d(x)$ at each station as well. With these assumptions, the spectral radiant intensity can be evaluated as an integration along the x direction only:

$$J_\lambda = \int_x I_\lambda(\tau_\lambda(x))\ 0.95d(x)\ dx \tag{6.38}$$

6.3.6.3 Optical depth for soot

The absorption coefficient for soot $\kappa_{\lambda,soot}$ is calculated according to the methods previously described in subsection 3.5.3. The soot particles in the plume are assumed small enough such that Rayleigh theory applies and the absorption coefficient can be calculated using (repeated here from Equation 3.30)

$$\kappa_{\lambda,soot} = \frac{36\pi nk}{\left(n^2 - k^2 + 2\right)^2 + 4n^2k^2} \frac{f_{v,soot}}{\lambda} \tag{6.39}$$

where $f_{v,soot}$ is the volume fraction of soot, n is the real part of the refractive index, k is the imaginary part of the refractive index, and λ is the wavelength. The soot volume fraction $f_{v,soot}$ is calculated using Equation 6.30. The refractive indices n and k can be determined using the fits given in Equations 3.31 and 3.32. Following the assumptions made to integrate the radiative transfer equation in subsubsection 6.3.6.1, the optical depth due to soot absorption is simply $\tau_{\lambda,soot} = \kappa_{\lambda,soot}L$, where L is the path length through the plume.

6.3.6.4 Optical depth for molecular gases

The optical depth τ_λ for molecular gases is determined using the "single line group" (SLG) model proposed by Ludwig et al. [27]. The single line group model is a narrow band model that proposes that the optical depth for a mixture of molecular gases in some small wavelength band is ultimately a function of gas temperature, gas pressure, species mass fractions, wavelength, and gas path:

$$\tau_\lambda = f\left(T, p, w_i, \lambda, s\right) \tag{6.40}$$

The SLG model is derived from a random Goody narrow band model for absorption coefficient with a hybrid Doppler-collision line shape (narrow band models are introduced in section 3.4). For each gas species, the optical depth due to collision broadening $\tau_{C\lambda i}$ and the optical depth due to Doppler broadening $\tau_{D\lambda i}$ are calculated separately:

$$\tau_{C\lambda i} = \tau^*_{\lambda i}\left(1 + \frac{\tau^*_{\lambda i}}{4a_{C\lambda i}}\right)^{-\frac{1}{2}} \tag{6.41}$$

$$\tau_{D\lambda i} = 1.7a_{D\lambda i}\left(\ln\left[1 + \left(\frac{\tau^*_{\lambda i}}{1.7a_{D\lambda i}}\right)^2\right]\right)^{\frac{1}{2}} \tag{6.42}$$

where $\tau^*_{\lambda i}$ is the optical depth in the linear (optically thin) limit, $a_{C\lambda i}$ is the fine structure parameter for collision broadening, and $a_{D\lambda i}$ is the fine structure parameter for Doppler broadening. Simplifying the SLG model for a homogenous, isothermal path (the same assumptions made for the integration of the radiative transfer equation in subsubsection 6.3.6.1), $\tau^*_{\lambda i}$, $a_{C\lambda i}$, $a_{D\lambda i}$ are calculated using:

$$\tau^*_{\lambda i} = \bar{\kappa}_{\lambda i}L; \qquad \bar{\kappa}_{\lambda i} = \bar{\kappa}_{\lambda i0}\frac{p}{p_0}\frac{T_0}{T} \tag{6.43}$$

$$a_{C\lambda i} = \frac{\gamma_{Ci}}{d_{\lambda i}} \tag{6.44}$$

$$a_{D\lambda i} = \frac{\gamma_{D\lambda i}}{d_{\lambda i}} \tag{6.45}$$

where $\bar{\kappa}_{\lambda i}$ is the mean absorption coefficient, $\bar{\kappa}_{\lambda i0}$ is the mean absorption coefficient at standard temperature and pressure, $1/d_{\lambda i}$ is the average line density, γ_{Ci} is the collision broadening half-width, $\gamma_{D\lambda i}$ is the Doppler broadening half-width, and L is the physical path length. Surrogate models for determining $\bar{\kappa}_{\lambda i0}$ and $1/d_{\lambda i}$ are discussed in subsubsection 6.3.6.5. γ_{Ci} and $\gamma_{D\lambda i}$ can be calculated following the procedure and data given in Chapter 5.3 of Ref. [27].

Once the the optical depth due to collision broadening $\tau_{C\lambda i}$ and the optical depth due to Doppler broadening $\tau_{D\lambda i}$ are determined, their combined optical depth is calculated using

$$\tau_{\lambda i} = \left(1 - z_{\lambda i}^{-\frac{1}{2}}\right)^{\frac{1}{2}}\tau^*_{\lambda i} \tag{6.46}$$

where

$$z_{\lambda i} = \left[1 - \left(\frac{\tau_{C\lambda i}}{\tau^*_{\lambda i}}\right)^2\right]^{-2} + \left[1 - \left(\frac{\tau_{D\lambda i}}{\tau^*_{\lambda i}}\right)^2\right]^{-2} - 1. \tag{6.47}$$

Lastly, the optical depth for all species (including soot) combined can be found simply using

$$\tau_\lambda = \sum^{species} \tau_{\lambda i}. \tag{6.48}$$

For this module, only emitting species with mole fractions greater than 0.01 in typical composite motor plumes are considered in the calculation of optical depth. These species are H_2O, CO_2, CO, and HCl. H_2 and N_2 do not emit in the infrared as discussed in section 3.1, and so their emission is not considered. The calculated value for τ_λ is then used to evaluate the simplified radiative transfer equation given in Equation 6.36.

6.3.6.5 Surrogate models for single line group parameters

Calculation of the optical depth using the single line group model described in subsubsection 6.3.6.4 requires appropriate values for the mean absorption coefficient at standard temperature and pressure $\bar{\kappa}_{\lambda i0}$ and the average line density $1/d_{\lambda i}$. Ludwig et al. provide average values for these parameters for different molecules within small bands at a selection of temperatures in Appendix A2 of Ref. [27]. However, to maintain compatibility with AeroSandbox (see subsection 1.2.3 for more information on AeroSandbox model requirements), C^1-continuous models for $\bar{\kappa}_{\lambda i0}$ and $1/d_{\lambda i}$ are needed. It should be noted that C^1-continuity is only needed with respect to temperature, and not with respect to wavelength. This is because temperature is defined within the AeroSandbox optimization environment as a variable (see subsection 6.2.1 for more information on implementation details with AeroSandbox) that must be implicitly solved, while wavelengths are selected explicitly as problem constants that do not need to be solved.

Differentiable, C^1-continuous surrogate models for $\bar{\kappa}_{\lambda i0}$ and $1/d_{\lambda i}$ were developed for each considered species (H_2O, CO_2, CO, and HCl) to meet this gap. The data tables in Ref. [27] were digitized. Missing values in the data were interpolated before fitting, and zero values in the data were replaced with small but nonzero values. Differentiable, cubic splines were fit to the logarithm of the data using the `UnstructuredInterpolatedModel()` class described in subsection 6.2.1. For values of

temperature and wavelength outside the data range, the surrogate model extrapolates values to the nearest model value at the boundary of the data range. An example of the surrogate models for $\bar{\kappa}_{\lambda i0}$ and $1/d_{\lambda i}$ are shown for CO in Figure 6-4. In the figure, points plotted with circles are data points given in the data tables in Ref. [27] and the curves are the output of the surrogate model in the given wavelength range for selected temperatures. Figures of the surrogate models for the other considered species are given in Appendix C.

The data in Ref. [27] for CO gives parameter values for wavenumbers (wavenumber is simply the inverse of wavelength) from $1100\,\mathrm{cm}^{-1}$ to $2350\,\mathrm{cm}^{-1}$ ($4.3\,\mu\mathrm{m}$ to $9.1\,\mu\mathrm{m}$) and temperatures from $300\,\mathrm{K}$ to $3000\,\mathrm{K}$. The surrogate models are C^1-continuous with respect to temperature for temperatures within the data range, and C^1-continuous with respect to wavelength for wavelengths within the data range. For wavelengths outside the wavelength range, the absorption coefficient $\bar{\kappa}_{\lambda i0}$ (and subsequently optical depth) is essentially zero, and the model extrapolation behavior will return the near-zero values at the boundary of the data range. Temperatures in the plume for propellants used in this work are within the data range, so the surrogate models will be C^1-continuous with respect to temperature at all wavelengths, even those outside the wavelength range in the data.

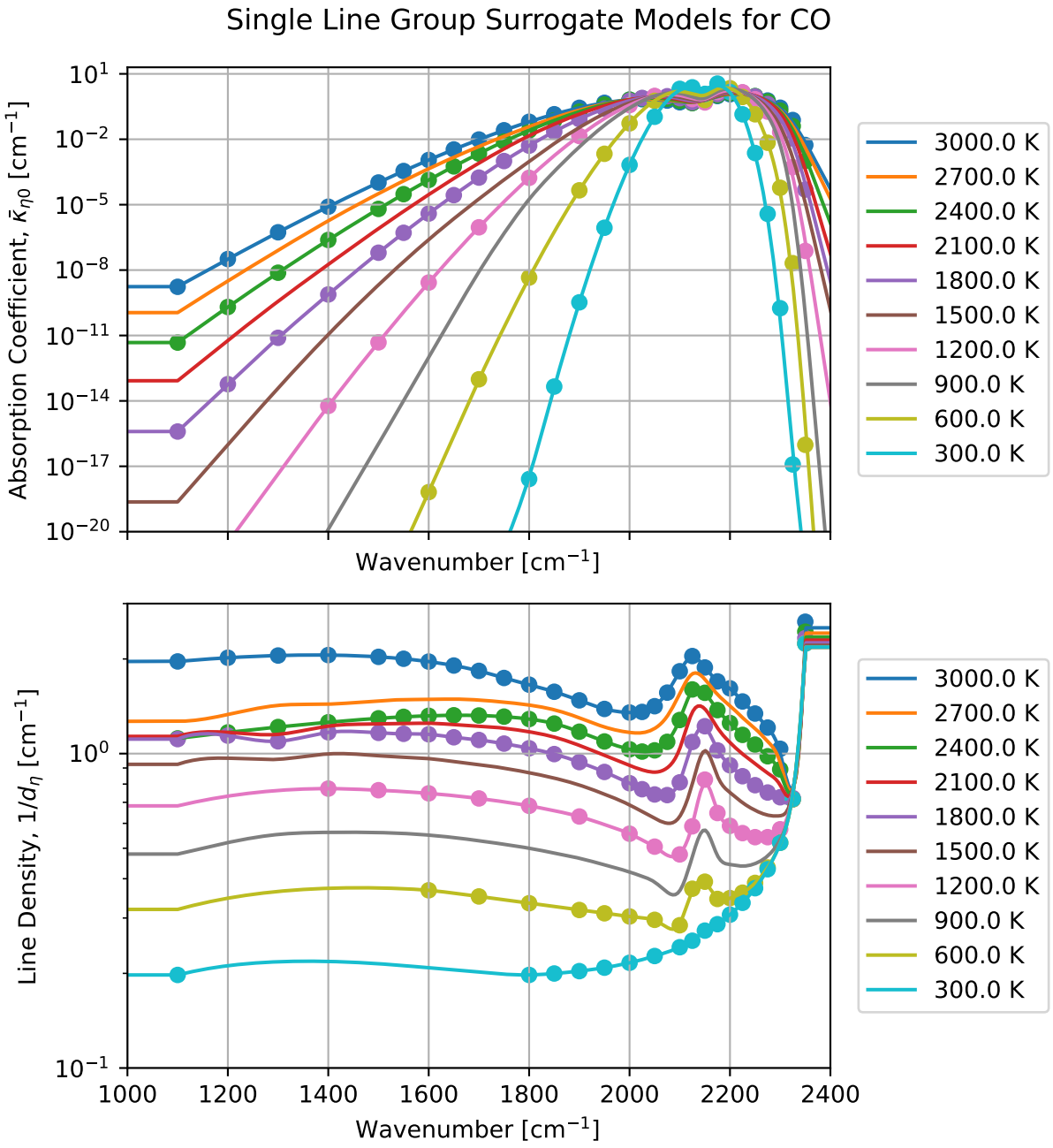

Figure 6-4: C^1-continuous (with respect to temperature) surrogate models for the mean absorption coefficient at standard temperature and pressure $\bar{\kappa}_{\lambda i 0}$ and the average line density $1/d_{\lambda i}$ (or equivalently with respect to wavenumber η, $\bar{\kappa}_{\eta i 0}$ and $1/d_{\eta i}$) were developed. For these figures, points plotted with circles are data points given in the data tables in Ref. [27]. The curves are the output of the surrogate model for the chosen wavelengths and temperatures.

Chapter 7

Exhaust Plume Radiant Emission Model: Results and Validation

An end-to-end differentiable model for exhaust plume radiant emission was developed and discussed in chapter 6. The model was developed to be compatible with AeroSandbox – a differentiable framework for aircraft design optimization – and can be coupled with all design tools available in AeroSandbox. This chapter discusses the methods for validation of the constituent sub-models introduced in section 6.3. Additionally, the results of the combined radiant intensity model are compared to three different test cases to validate its performance. The model is compared to the radiant intensity measurements of the core test matrix of static fires of low-thrust (6 N to 20 N), end-burning motors collected for this thesis given in subsection 5.6.1. Experimental measurements from a study conducted by Avital et al. [47] – which used a core-burning test motor with an estimated ∼1600 N thrust operated at sea level – and modeling results from a study conducted by Alexeenko et al. [82] – which analyzed a large Atlas II booster ($\sim 2.2 \times 10^6$ N thrust) plume at 15 km altitude – are also compared to the developed radiant intensity model.

7.1 Validation of sub-models

This section will provide a brief discussion of methods for validating the results of the sub-models described in section 6.3.

Chamber thermodynamic equilibrium To validate the chamber thermodynamic equilibrium sub-model (see subsection 6.3.1), the results of the sub-model were simply compared to results of the commercial Rocket Propulsion Analysis software [19]. Several test cases were evaluated using both Rocket Propulsion Analysis and the developed chamber thermodynamic equilibrium sub-model. For each test case, the chamber pressure and propellant formula were pre-selected, and then the resulting chamber temperature and species mass fractions were compared. The developed chamber thermodynamic equilibrium model shows excellent agreement with Rocket Propulsion Analysis. For several test cases using the oxamide containing propellants utilized in this work, the relative errors of the model outputs are $\leq 1 \times 10^{-4}$. These example test cases are given explicitly in Appendix D.

Motor internal ballistics The motor internal ballistics sub-model equations discussed in subsection 6.3.2 are implemented using the `proprools` python library, which has already been validated with a large number of published test cases [78].

Isentropic nozzle flow The isentropic nozzle flow sub-model equations discussed in subsection 6.3.3 are also implemented using the `proptools` python library, which has already been validated with a large number of published test cases [78].

Plume flow field The outputs of the plume flow field sub-model are compared to a set of explicit equations for modeling 1D exhaust plumes published by Woodroffe in Ref. [55] to model the plume temperature, velocity, diameter, and density assuming frozen flow. The two models show excellent agreement, which validates the results of the flow field sub-model for the frozen flow case. Additionally, the modeled temperature from the flow field sub-model is analyzed further to validate its behavior for non-frozen flow.

The behavior of the temperature results from the flow field sub-model are evaluated for a sweep of reaction rates spanning several orders of magnitude. The flow field model exhibits the correct limiting behavior in the frozen and equilibrium flow cases, and is compared to theoretical Cantera calculations, which agree well with the sub-model outputs. These validation efforts and results are discussed in detail in Appendix D.

Afterburning kinetics The afterburning kinetics sub-model discussed in subsection 6.3.5 is based on reaction rates determined from Cantera [21]. The agreement between the sub-model and the Cantera reaction rates can be seen in Figure 6-3.

Radiative transfer The radiative transfer model introduced in subsection 6.3.6 is validated using an example provided by Ludwig et al. in Appendix 1 of Ref. [27]. The example models an inhomogeneous column of CO_2 at atmospheric pressure. The natural logarithm of the optical depth calculations provided in Ref. [27] of different portions of the column at four different wavelengths and two different temperatures are compared to the natural logarithm of the optical depth outputs of the developed radiative transfer sub-model. The absolute error of the developed sub-model outputs are < 0.5 (so the sub-model outputs are within a factor of $e^{0.5} = 1.65$ of the calculations in Ref. [27]). Optical depth is a parameter that spans many orders of magnitude, and so this error is reasonable. It is also expected that the calculations given in Ref. [27] do not match the sub-model outputs exactly, since Ludwig et al. use a linear interpolation on the average line density $1/d_{\lambda i}$ and the mean absorption coefficient $\bar{\kappa}_{\lambda i}$, and this model uses a spline interpolation on $\ln(1/d_{\lambda i})$ and $\ln(\bar{\kappa}_{\lambda i})$. The good agreement of the surrogate models for $1/d_{\lambda i}$ and $\bar{\kappa}_{\lambda i}$ discussed in subsubsection 6.3.6.5 with the data provided by Ludwig et al. can be seen in the figures in Appendix C.

7.2 Comparison with measured data from this thesis

The radiant intensity measurements of static fires SF4 - SF7 discussed in subsection 5.6.1 were compared to the modeled radiant intensity. The model input parameters used for each of the static fires are summarized in Table 7.1. The measured data and modeled results for radiant intensity of SF4 - SF7 are shown in Figure 7-1.

The oxamide fraction and throat diameter are the actual values used in the static fires. The internal ballistics model described in subsection 6.3.2 was not used, and instead the chamber pressures are set to the approximate steady state values measured during the static fires. The exit pressure is assumed to be 0.101 MPa (standard sea level pressure) for all the static fires, which was the exit pressure for which each of the nozzles were designed. An altitude of 0 km and a freestream velocity of $1\,\mathrm{m\,s^{-1}}$ was also used. A soot mass fraction of 0.02 was assumed. This is slightly higher than the mass fraction of 0.0135 reported by Vernacchia in Ref. [13] for these propellants; however, the reported value was a lower bound because some soot escaped during the measurements. The flow field was integrated to a distance of $60\,d_0$ (d_0 is the initial plume diameter at the start of the turbulent mixing region, as introduced in subsubsection 6.3.4.2) downstream of the start of the turbulent mixing region, assuming a viewing angle of 90° (e.g. orthogonal to the plume axis of symmetry, as was the measurement condition).

Static fire	**Oxamide** [%]	**Throat diameter** [mm]	**Chamber pressure** [MPa]	**Exit pressure** [MPa]
SF4	0	3.00	1.2	0.101
SF5	0	2.30	2.3	0.101
SF6	8	2.53	1.1	0.101
SF7	8	1.93	2.1	0.101

Table 7.1: Radiant intensity model inputs for test matrix of static fires.

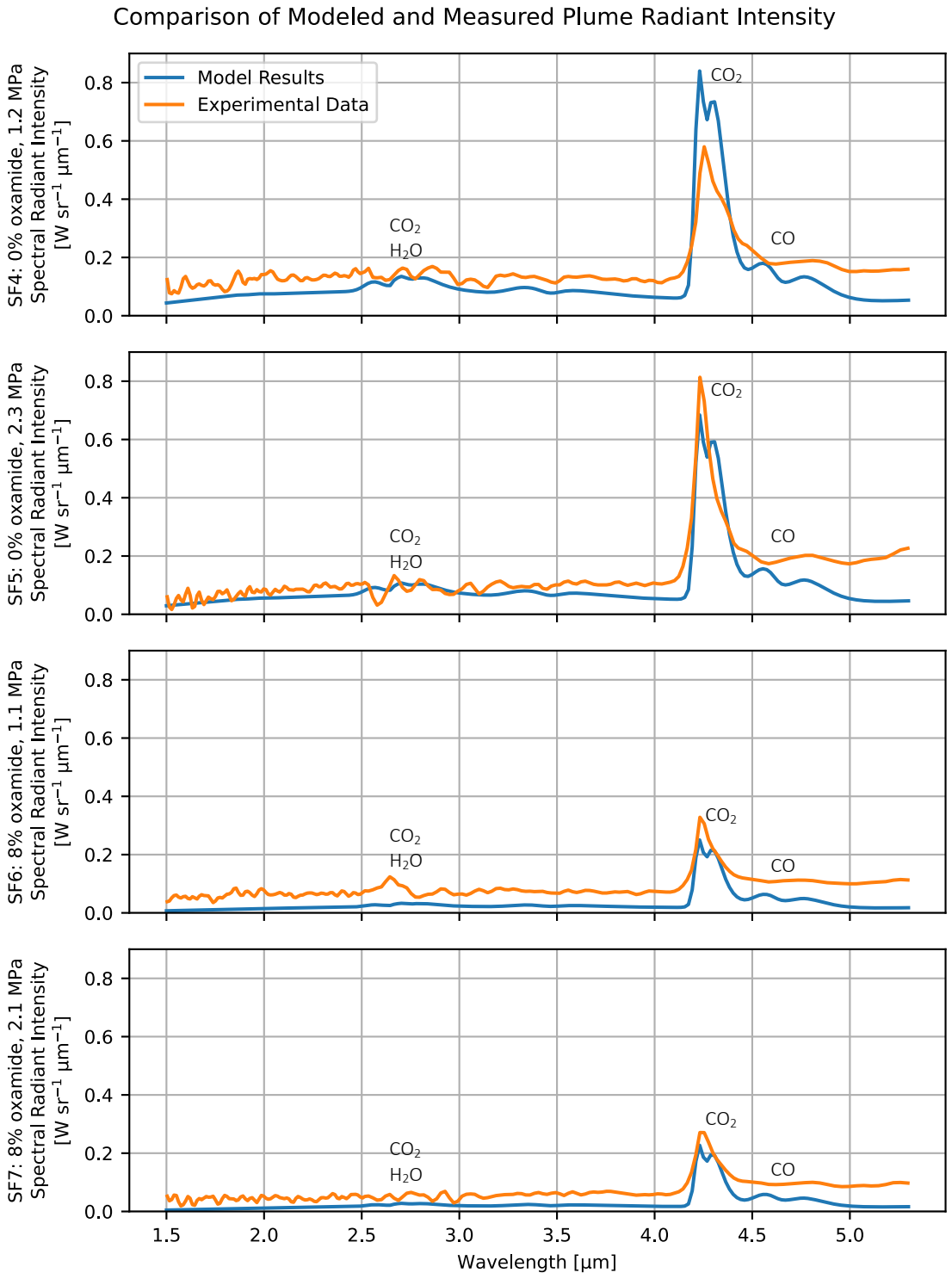

Figure 7-1: The measured and modeled radiant intensities for SF4 - SF7 show reasonable agreement across the spectrum. All show the largest peak at 4.3 µm corresponding to a CO_2 emission band. The data is unfortunately noisy due to sensitivity limitations of the instrumentation.

For all four static fires, both the measured and modeled spectra show a distinct peak at 4.3 µm corresponding to CO_2 emission. A CO emission band can be seen at 4.7 µm, although in the experimental data it appears as a relatively smooth plateau for all the static fires, while in the model it appears as two small peaks. A weaker peak exists at 2.7 µm corresponding to a combined CO_2 and H_2O emission band, although it is not particularly visible in the experimental data. The measured data and modeled results show reasonable agreement across the spectrum for all four static fires, although the measured experimental data is unfortunately noisy across the spectrum, especially away from the 4.3 µm CO_2 peak where the measured signal was weak. As mentioned in subsection 5.6.1, the radiant emission of these small, slow-burning solid rocket motors required operating the spectroradiometer near its lower sensitivity limit. Even at the maximum gain setting, the exhaust plume contrast measurements utilized, at most (at the 4.3 µm CO_2 band where the signal was strongest), 7.7 % of the dynamic range of the detector.

Because the signal is largest at the 4.3 µm peak, this point in the spectra is used to compare the measured and modeled spectra. The measured and modeled radiant intensities at this peak for SF4 - SF7 are compared in Figure 7-2. For SF5 - SF7, the modeled peak intensities are consistently between 15 % to 18 % less than the measured peak radiant intensity. For SF4, the modeled peak intensity is 45 % greater than the measured peak intensity. SF4 did have a larger temperature drift between the radiometer calibration and plume measuremets (see subsubsection 5.5.1.2) than the other static fires, which perhaps contributes to the larger error between the measurement and model seen for SF4.

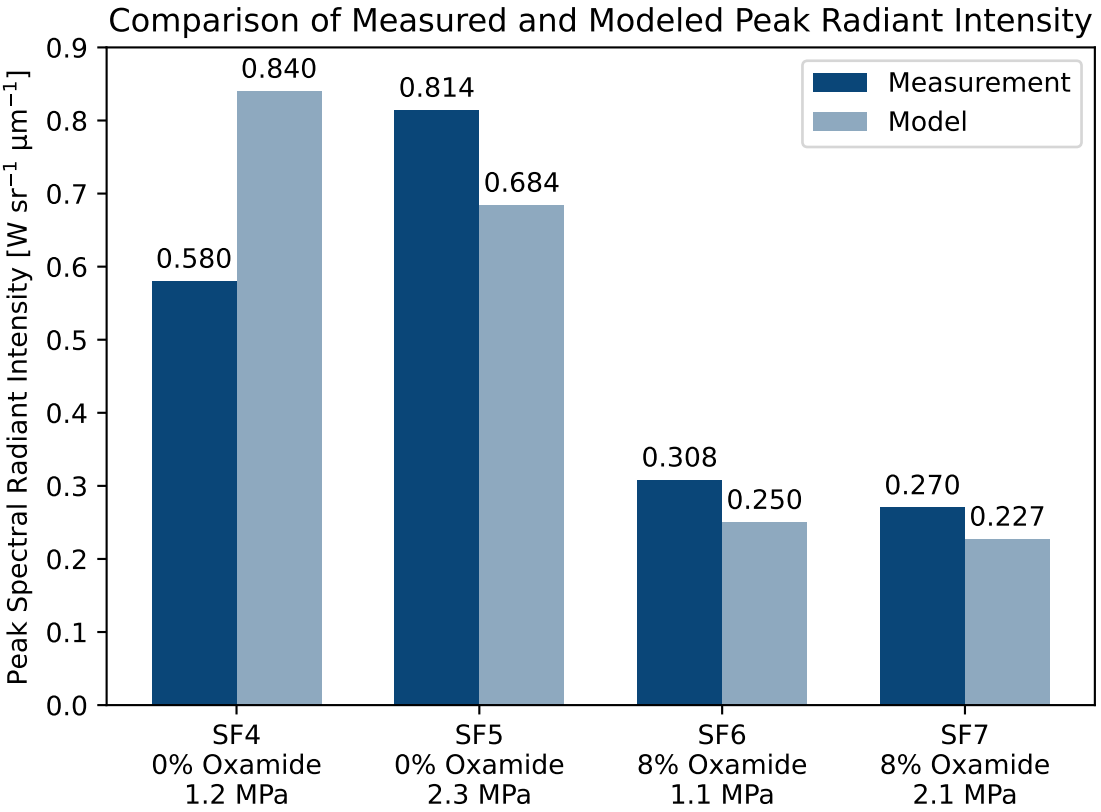

Figure 7-2: The measured and modeled peak radiant intensities agree fairly well. The model and measurements both show greater changes in radiant intensity due to a change in oxamide content than a change in chamber pressure.

As discussed in the experimental results in subsection 5.6.1, the peak radiant intensity measurements show greater sensitivity to changes in oxamide content than changes in chamber pressure. The modeled peak radiant intensities display this same trend as well. The reasons for this become more clear by examining the modeled flow field parameters for SF4 - SF7, which are shown in Figure 7-3.

Parameters are plotted against axial distance downstream from the start of the turbulent mixing region, normalized by the diameter of the plume d_0 at the start of the turbulent mixing region (the same d_0 introduced in subsubsection 6.3.4.2). For a given oxamide content (for instance, SF4 and SF5 at 0 % oxamide), although a change in chamber pressure causes the flow field properties to separate for a few d_0, they quickly converge to similar values as the plume mixes with entrained air and cools. However, across oxamide contents (SF4 and SF5 at 0 % oxamide versus SF6 and SF7 at 8 % oxamide) the flow field properties are significantly different throughout the

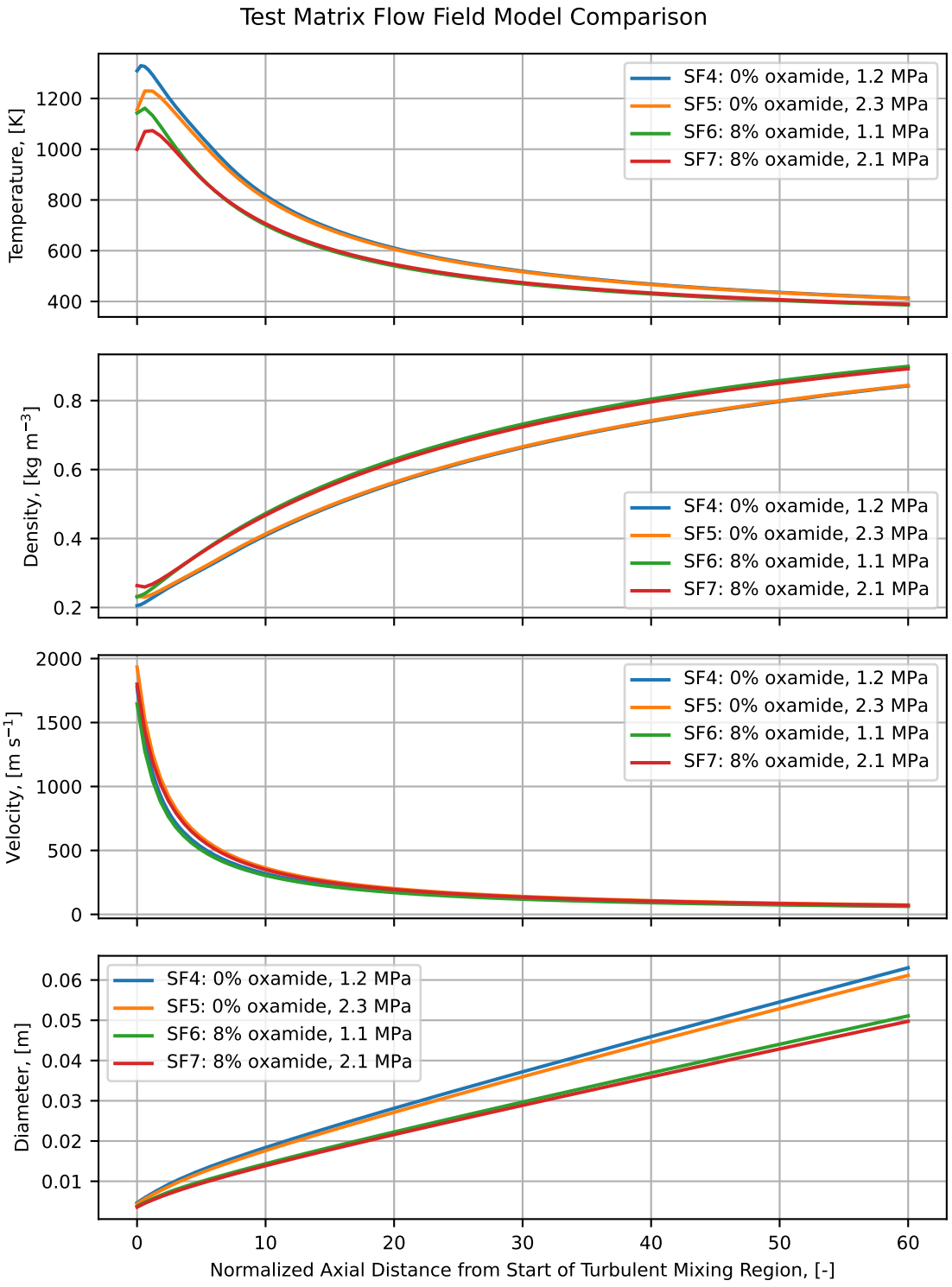

Figure 7-3: For a given oxamide content, the flow field parameters are similar throughout the flow field after the first few d_0 in the plume, even with a change in chamber pressure. Across the two oxamide contents (SF4 and SF5 at 0 % versus SF6 and SF7 at 8 %), the parameters are significantly different.

whole flow field, which ultimately leads to significantly different peak radiant intensity values for different oxamide contents. The effects of chamber pressure and propellant oxamide content on radiant intensity for small, end-burning solid rocket motors are explored further in section 8.2.

Also of interest is the behavior of the plume temperature model for the four static fires relative to theoretical lower bounds and upper bounds corresponding to frozen or equilibrium flow prevailing respectively throughout the plume. For each static fire, Figure 7-4 shows the plume flow field temperature curve plotted with theoretical curves for frozen flow and equilibrium flow (which should bound the possible temperatures throughout the plume) calculated using Cantera [21]. The methods for calculating the frozen and equilibrium flow curves with Cantera are explained in detail in Appendix D. For all four static fires, the flow field model predicts frozen or nearly frozen flow. Although low altitude plumes typically exhibit equilibrium flow, the small size scale of these plumes leads to Dahmköhler effects which ultimately cause frozen flow to prevail in these plumes. The effects of reduced motor size scale on afterburning kinetics in exhaust plumes is discussed further in section 8.1.

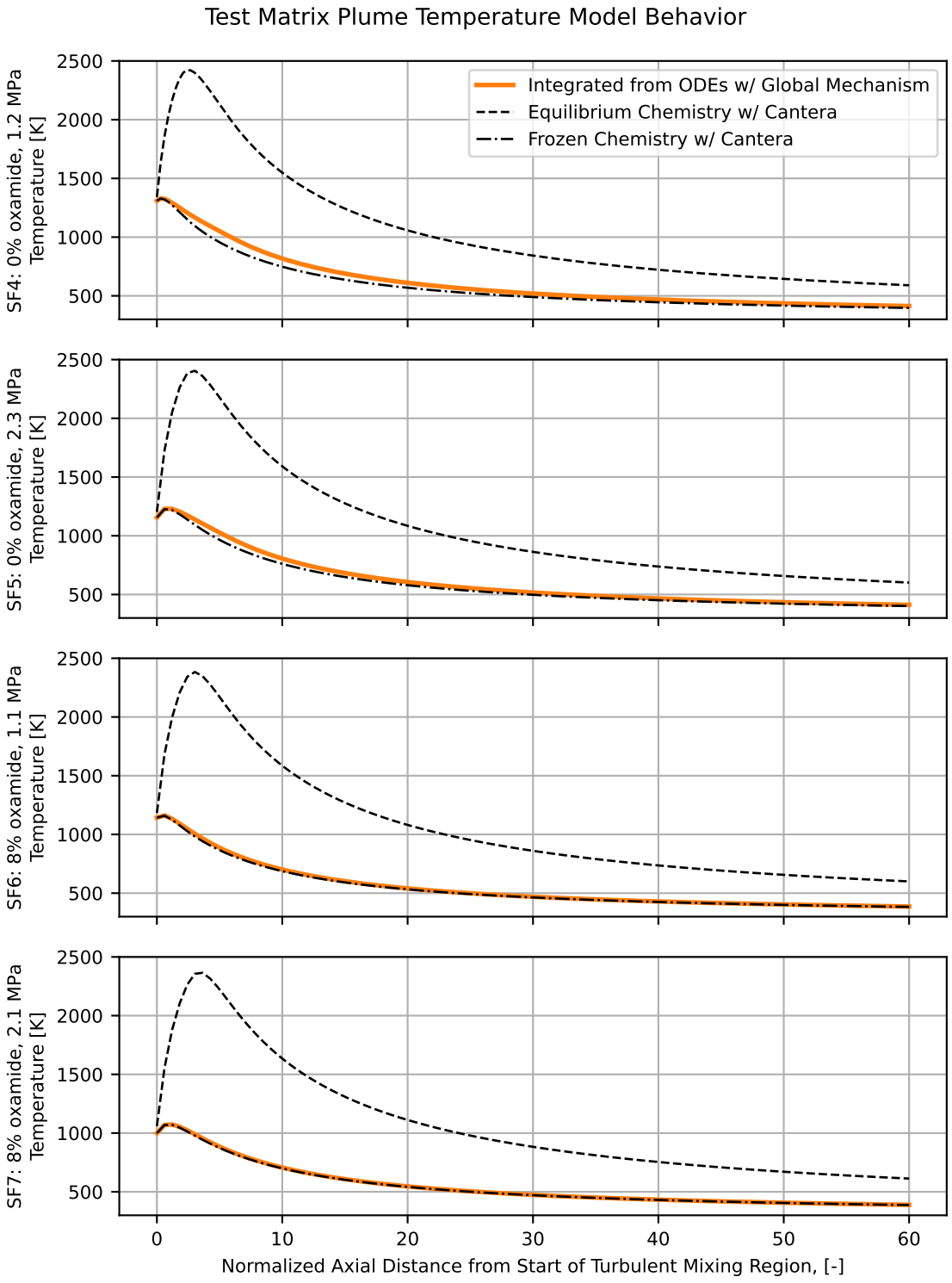

Figure 7-4: The modeled plume temperatures for SF4 - SF7 are frozen or near frozen for all of the static fires. This is a result of Dahmköhler effects due to the exceptionally small size scales of these plumes.

7.3 Comparison with data from Avital et al.

The developed radiant intensity model was compared to experimental data collected for a ~1600 N thrust test motor by Avital et al. in Ref. [47]. The test used a core-burning propellant grain consisting of 87 % ammonium perchlorate oxidizer and 13 % hydroxyl-terminated polybutadiene binder. A soot mass fraction of 0.1 % was assumed. The nozzle had a throat diameter of 15 mm, a chamber pressure of 3.8 MPa, and a nozzle exit pressure of 0.27 MPa. The plume was integrated to a downstream distance of 26 d_0, which is consistent with the detector field of view and distance to detector used by Avital et al. The experimental radiant intensity data given by Avital et al. in Ref. [47] is plotted with the output of the developed model for this thesis (using the motor parameters described above) in Figure 7-5.

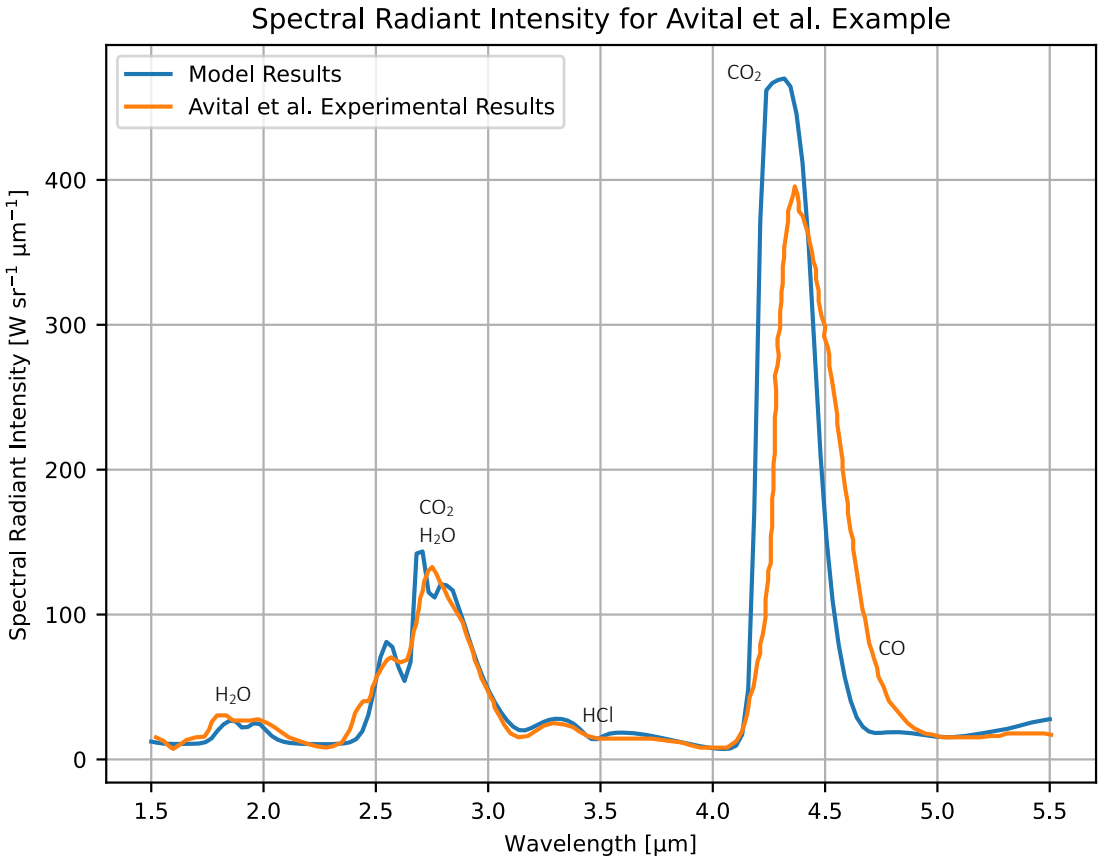

Figure 7-5: The agreement between the radiant intensity spectra for the Avital et al. experimental results and the developed model results is generally good, although the 4.3 µm CO_2 emission band peaks at slightly different values and at slightly different wavelengths between the data and model.

The agreement between the model and the Avital et al. experimental radiant intensity spectra is good. The model performs especially well for the 1.87 µm H_2O band, the 2.7 µm combined H_2O and CO_2 band, and the 3.5 µm HCl band. Some of these bands were not visible in the radiant intensity data or model results for the SF4 - SF7 static fires shown in Figure 7-1 due to the low temperatures and small size scales of those plumes. The model over-predicts the 4.3 µm CO_2 peak radiant intensity by ∼19 %. The center of the 4.3 µm CO_2 band between the model and Avital et al. measurement also differs, with the model predicting the band center near 4.31 µm and the data showing the center near 4.37 µm. The single line group model (discussed in subsubsection 6.3.6.4) used for modeling molecular emission in this thesis predicts the CO_2 band center very near 4.31 µm. It is not known why the model and Avital et al. band centers differ.

The plume flow field model temperature prediction is shown for the Avital et al. motor in Figure 7-6. The flow field model predicts a temperature curve that falls between the theoretical frozen and equilibrium chemistry curves predicted with Cantera. This is different from the temperature predictions for SF4 - SF7 in Figure 7-4, which predicted nearly frozen flow for the four motors. This suggests that the plume afterburning kinetics for the Avital et al. plume is best characterized as a finite rate process. Additionally, it suggests that the afterburning reactions are not rate-limited by the entrainment of oxygen into the plume, as this scenario would correspond to a temperature profile near the equilibrium flow theoretical curve.

The Avital et al. motor and plume was an interesting test case for the developed radiant emission model for several reasons. The Avital et al. plume had a peak radiant emission that was up to three orders of magnitude larger than the emission from the SF4 - SF7 static fires conducted for this work. The developed radiant emission model performs reasonably well for the Avital et al. plume and the SF4 - SF7 plumes, which demonstrates the model's robustness for modeling plumes spanning multiple orders of magnitude of radiant emission. The Avital et al. plume had enough thermal emission that the 1.87 µm H_2O band, the 2.7 µm combined H_2O and CO_2 band, and the 3.5 µm HCl band were much more visible than in the SF4 - SF7 plumes. The

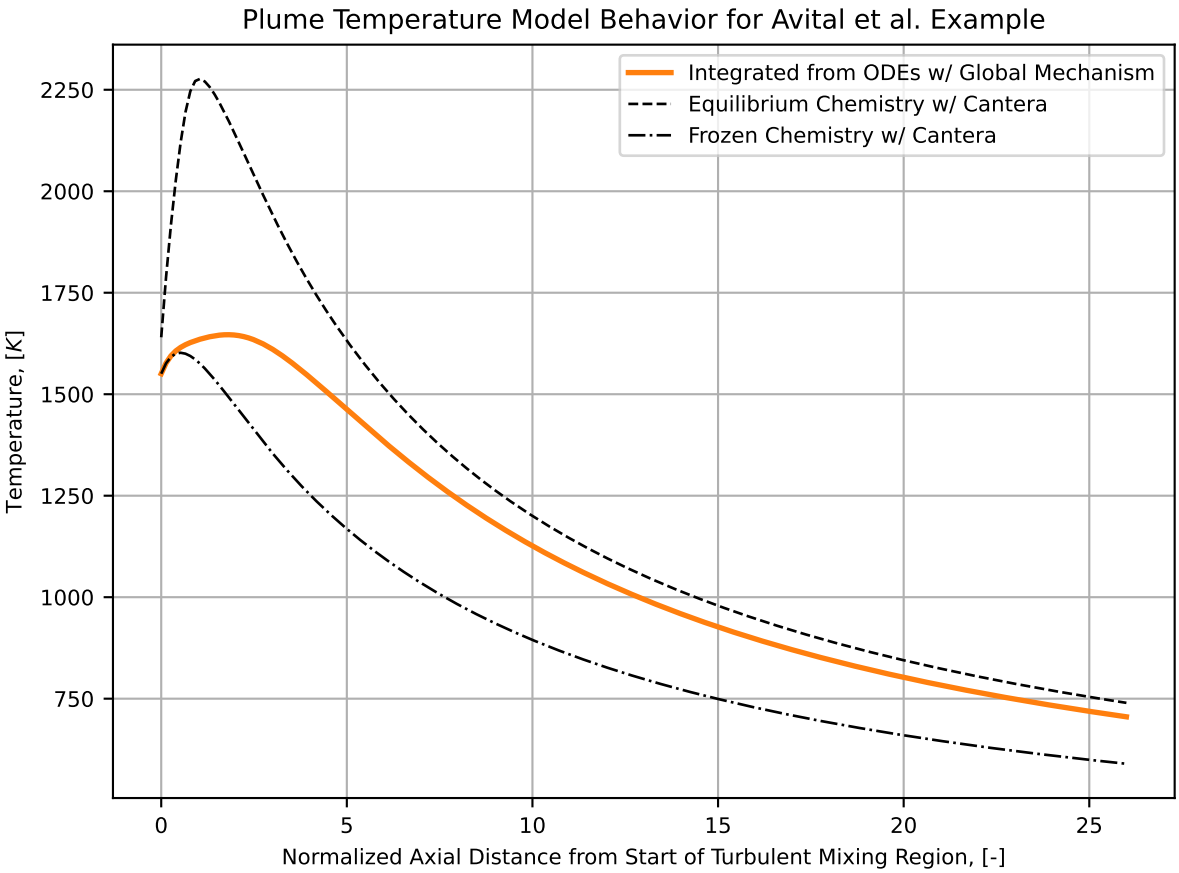

Figure 7-6: The flow field model predicts the Avital et al. plume temperature to lie between the theoretical frozen and equilibrium curves. This suggests that the afterburning kinetics for the Avital et al. plume has a finite rate, and is not limited by the entrainment of oxygen into the plume.

performance of the developed model around for these bands could be verified with the Avital et al. plume radiant emission measurement, since the radiant emission measurements for SF4 - SF7 did not have enough signal to capture these bands well. Additionally, unlike the predicted temperatures for SF4 - SF7 (see Figure 7-4) which corresponded to frozen or near frozen flow throughout the exhaust plume, the Avital et al. plume provided a test case for a plume that demonstrated finite rate kinetics, with temperatures throughout the flow field falling between the predicted theoretical frozen and equilibrium curves. This provides a good test case for the developed global finite rate mechanism introduced in subsection 6.3.5, and shows that it can make predictions of flow field temperatures driven by finite-rate kinetics processes that produce a reasonable exhaust plume radiant emission prediction.

7.4 Comparison with modeled results from Alexeenko et al.

The developed radiant emission model was compared to results from a model implemented by Alexeenko et al. in Ref. [82]. Alexeenko et al. modeled the plume of an Atlas II rocket flying at an altitude of 15 km assuming different soot mass fractions. The Atlas II rocket has three engines using kerosene and liquid oxygen propellants. Alexeenko et al. models the exhaust flow field of the three plumes simultaneously, capturing the interactions of the plumes with 3-dimensional CFD. However, following the approach of Viswanath et al. specifically for the Atlas II rocket, a simplified equivalent single-nozzle treatment is used here [83]. With the equivalent single-nozzle treatment, a single nozzle accounting for all three engines is assumed, with a chamber pressure of 1.95 MPa, an exit pressure of 0.69 MPa, an exit diameter of 2 m, an exit velocity of 2960 $\mathrm{m\,s^{-1}}$, an exit temperature of 2230 K, and nozzle exit mass fractions as given in Table 7.2. The freestream velocity given by Alexeenko et al. of 535 $\mathrm{m\,s^{-1}}$ is used, as well as a viewing angle of 90° (e.g. orthogonal to the plume axis of symmetry). The no-soot case presented by Alexeenko et al. is considered in this comparison.

Species	**Nozzle exit mass fraction**
CO	0.412
CO_2	0.302
H_2	0.012
H_2O	0.272

Table 7.2: Assumed nozzle exit mass fractions for Atlas II rocket using the equivalent single-nozzle assumption from Ref. [83]. All other minor species contributions are neglected.

The developed radiant emission model for this work was applied assuming all conditions at the nozzle exit plane were known. The chamber thermodynamic equilibrium, motor internal ballistics, and nozzle flow sub-models were not used. The appropriate initial conditions (as described above) were applied to the plume flow

field, afterburning kinetics, and radiative transfer sub-models directly to evaluate the exhaust plume radiant intensity. The plume was integrated to a distance of $37\,d_0$, which is consistent with the integration length used by Alexeenko et al. [82]. A comparison of the modeled results using the developed differentiable model for this work and the modeled results from Alexeenko et al. is shown in Figure 7-7.

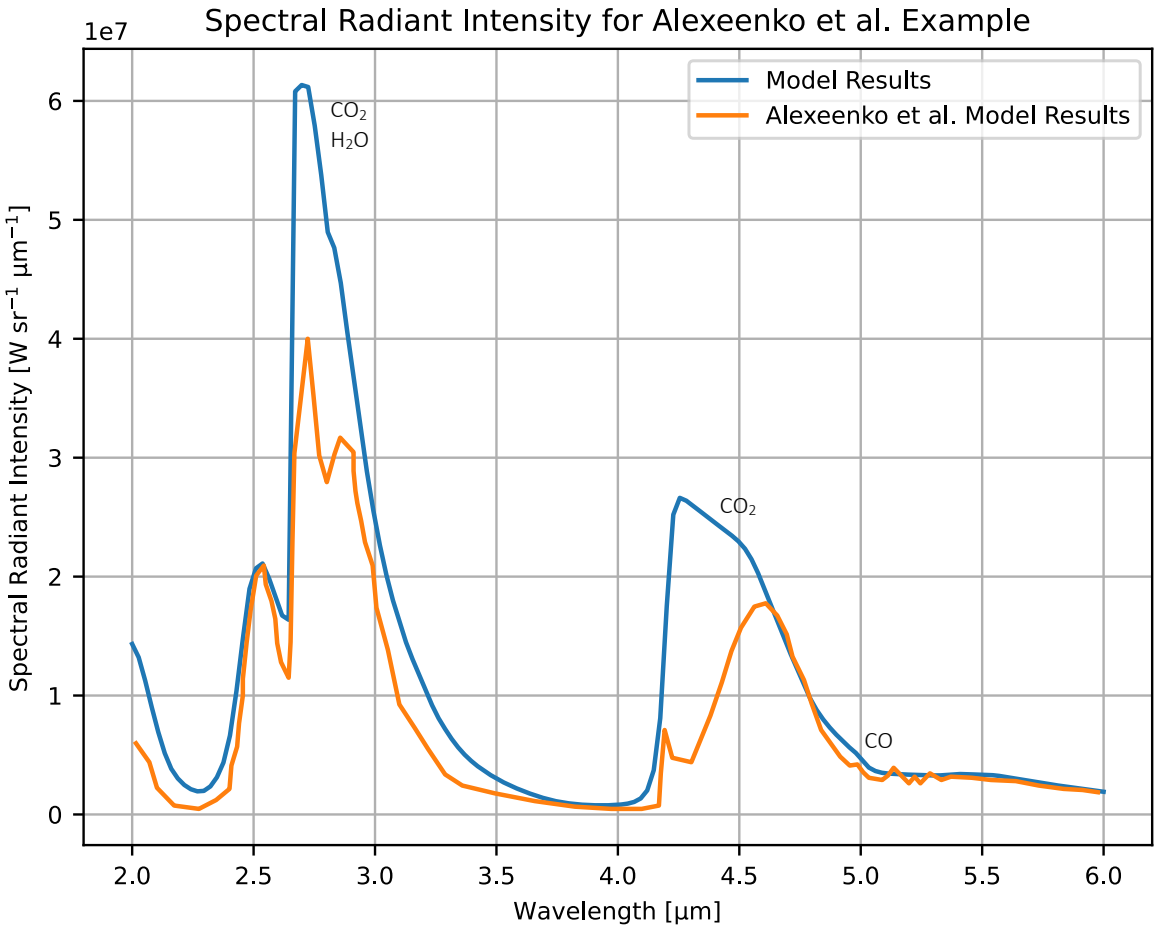

Figure 7-7: The developed differentiable model and the Alexeenko et al. model show results on the same order of magnitude, although the differentiable model does seem to over-predict the peak intensities at the the 2.7 µm combined H_2O and CO_2 band and the 4.3 µm CO_2 band peaks significantly.

The differentiable model seems to significantly over-predict the radiant intensity contributions from the CO_2 bands as compared to the Alexeenko et al. model, although both predict values of the same order of magnitude. However, the differentiable model results were based on the equivalent single-nozzle treatment, which was very different than the approach used by Alexeenko et al., which relied on 3-dimensional CFD of the

interacting plumes. It is possible that these very different approaches contribute to some of the difference between the two model results. Despite the over-prediction at the CO_2 bands, the two models show general agreement. Both produce results on the same order of magnitude and differ, at most, by a factor of a few (again, not orders of magnitude).

The flow field model prediction of plume temperature for this Atlas II plume is shown in Figure 7-8 along with the theoretical frozen and equilibrium flow temperature profiles. The flow field model plume temperature prediction converges with the equilibrium curve predicted with Cantera for the majority of the flow field, which suggests that equilibrium chemistry prevails throughout the plume. Between $2\,d_0$ and $10\,d_0$ downstream of the start of the turbulent mixing region, the flow field temperature prediction actually overshoots the predicted equilibrium chemistry curve, which is theoretically the upper bound on the temperatures that should exist throughout the exhaust plume. This over-prediction is most likely due to an unrealistic assumption made in the global reaction mechanism (discussed in subsection 6.3.5) that assumes combustion reactions in the plume occur exclusively in the forward direction. This assumption causes the kinetics model to predict further combustion progress of the fuel species in the plume than would actually be favored by a true equilibrium process at these altitudes and species concentrations. This in turn causes the temperature to be over-predicted by the flow field temperature model. This model tendency to predict temperatures larger than the theoretical Cantera equilibrium curve is discussed further in Appendix D.

This comparison of the developed differentiable model with the Alexeenko et al. modeling results for the Atlas II rockets enable validation of several aspects of the differentiable model. This test case enabled the differentiable model to be evaluated at an altitude of 15 km, as opposed to the Avital et al. and SF4 - SF7 examples which considered plumes at sea level. The higher altitude likely contributed to the over-prediction of the plume flow field temperature model (which predicted temperatures greater than the theoretical equilibrium Cantera in one region of the plume), which in turn likely contributed to the over-prediction of the radiant emission for the CO_2 bands.

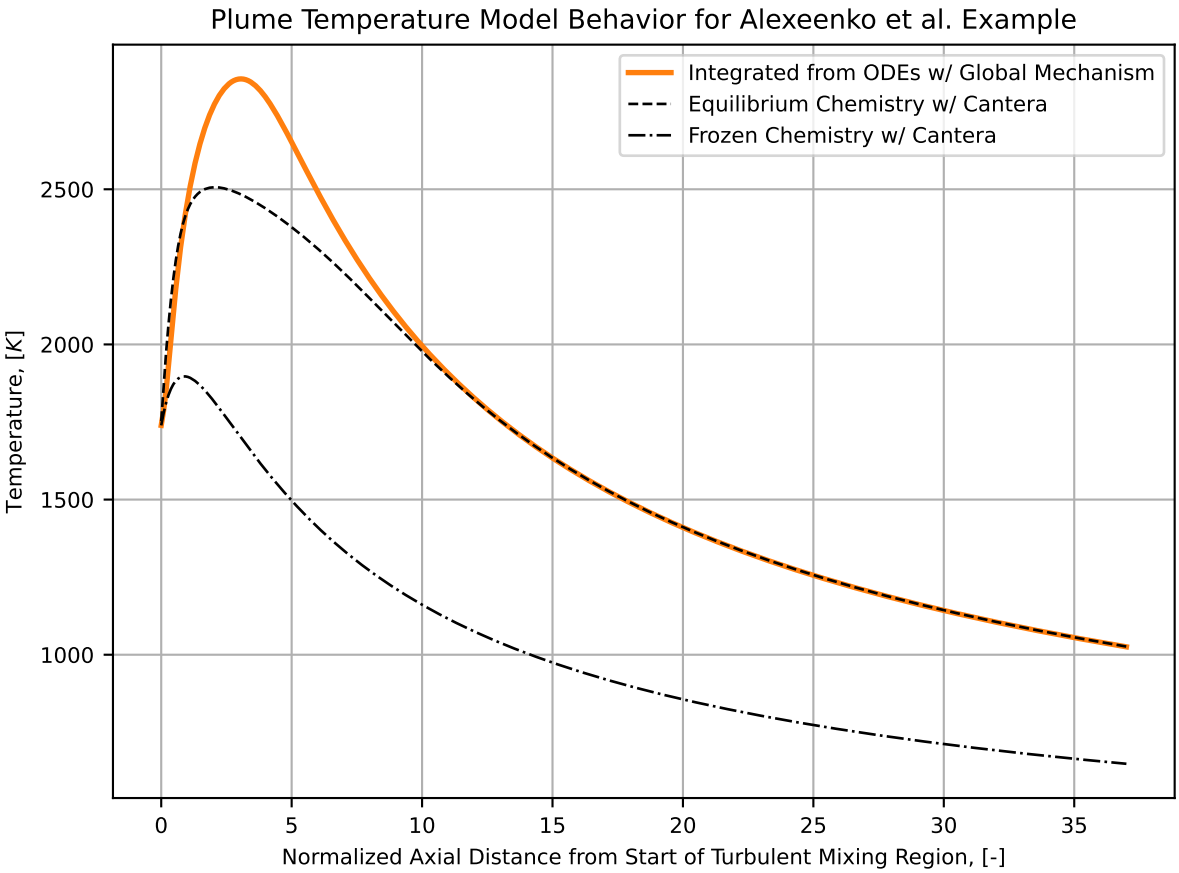

Figure 7-8: The plume flow field model predicts equilibrium flow behavior for the Atlas II plume at 15 km. The temperature curve exceeds the theoretical equilibrium upper bound predicted by Cantera most likely due to an unrealistic assumption of irreversible combustion reactions in the global reaction mechanism for plumes at this altitude.

Despite the over-prediction of the CO_2 bands, the developed differentiable model and the Alexeenko et al. model showed reasonable agreement, which demonstrates the performance of the flow field, afterburning kinetics, and radiative transfer sub-models for an example plume near equilibrium chemistry and at a higher altitude and significant freestream velocity. This test case also demonstrates the developed model's robustness for plume radiant emission scales even larger than the Avital et al. example. The developed differentiable model reasonably predicts radiant emission spanning eight orders of magnitude.

7.5 Recommendations for further model development

An end-to-end differentiable model for predicting exhaust plume radiant intensity was developed and implemented in the AeroSandbox design optimization framework. AeroSandbox provides a flexible framework for implementing and solving high-dimensional design problems, although the framework does have some limitations. Namely, models must be "glass box" and C^1-continuous. Additionally, stiff differential equations must be implemented with care, as AeroSandbox ultimately uses a trapezoidal integrator with non-adaptive timesteps.

The developed differentiable model consists of six sub-models of different coupled physical phenomena: chamber thermodynamic equilibrium, motor internal ballistics, isentropic nozzle flow, plume flow field, afterburning kinetics, and radiative transfer. The developed model shows reasonable agreement for a number of motors, and is robust over eight orders of magnitude of radiant intensity. Further model development should expand the types of propellants and operating conditions that can be modeled.

An important area for further development is the kinetics model, which is important for determining the temperatures and species concentrations throughout the plume. This work used a reduced-order global reaction mechanism (see subsection 6.3.5), which was dependent on the temperature and major species concentrations. Future work should focus on developing a kinetics model that can more accurately and robustly predict reaction rates, especially at higher altitudes where the reduced-order model performs poorly. The restrictions of implementing models in AeroSandbox make this challenging, as the trapezoidal integration scheme used by AeroSandbox (see subsection 6.2.2) is not robust to extremely stiff systems of differential equations, such as those used to model chemical reaction mechanisms. A reduced-order model that is not dependent on small concentrations of unstable species is still probably needed. A potential option for future kinetics models might be a reaction mechanism based on two or three reactions, instead of a single reaction as was used in this work. Separate reactions for hydrogen and carbon monoxide oxidation ($CO + O_2 \longrightarrow$

CO_2 and $H_2 + O_2 \longrightarrow H_2O$) could be fitted to a more detailed reaction mechanism, instead of only a single reaction. It might also be prudent to include a third water-gas shift reaction in the fitted model, which is often rate limiting for CO oxidation: $CO + H_2O \longleftrightarrow CO_2 + H_2$ [84].

A model for handling scattering in the exhaust plume should also be considered, as it would enable aluminized propellants to be included. However, modeling scattering within the AeroSandbox would involve a substantial effort of implementing a differentiable Mie theory (see subsection 3.5.2) module. Additionally, integrating the radiative transfer equation with scattering terms becomes more difficult, as every line-of-sight through the plume is then dependent on the scattering processes occurring everywhere in the plume. The line-of-sight method used for evaluating the radiative transfer integral (see subsubsection 6.3.6.1) and the simplifying 1D assumptions made for spatially integrating the plume (see subsubsection 6.3.6.2) would no longer be sufficient; a 2D discretization and integration scheme would probably be required, which would significantly increase the number of problem variables and make the radiant intensity integral more expensive.

The model should also be developed to enable radiant emission predictions for plumes viewed at arbitrary angles, as plumes on flying vehicles would typically not be viewed orthogonally. Additionally, more rigorous models for predicting soot mass fraction in the exhaust and accounting for soot oxidation in the plume should be considered, as soot can have a significant effect on the radiant intensity in the plume (see the discussion in subsection 4.3.2). Woodroffe provides data for soot concentrations in exhaust plumes as a function of oxidizer/fuel ratio for small liquid engines in Ref. [55]. This could perhaps be a starting point for a simple empirical model relating soot content to propellant composition and equivalence ratio, although the available data is still limited.

Chapter 8

Integrated Design of Small, Low-Thrust Solid Rocket Motors Including Plume Radiant Emission

An interesting class of solid rocket-powered vehicles includes small ($<10\,\mathrm{kg}$), fast ($>100\,\mathrm{m\,s^{-1}}$) aircraft such as the Firefly vehicle, which was introduced in subsection 1.2.2. The Firefly vehicle is a demonstrator vehicle designed to explore technical feasibility, manufacturing challenges, and performance capabilities for small, fast aircraft. The proposed design of the Firefly vehicle utilizes a small, end-burning solid rocket motor and a class of slow-burning propellants doped with the burn rate suppressant oxamide, similar to the motors developed, tested, and measured in the static fires described in chapter 5. The notional goals of the aircraft mission are to maximize vehicle range and endurance.

The developed differentiable plume radiant emission model introduced in chapter 6 was shown in chapter 7 to reasonably predict plume radiant emission for a wide range of rocket-powered vehicles, including the small, low-thrust, end-burning, Firefly-like motors characterized in chapter 5. Utilizing that radiant emission model and the experimental data collected for small, low-thrust motors, this chapter explores the integrated design of small, low-thrust solid rocket motors including plume radiant emission. Plume and radiant emission phenomena unique to small solid rocket motors

is discussed, such as the scaling of plume time scales and radiant emission with motor size. Design and performance tradeoffs between chamber pressure, oxamide content, thrust, specific impulse, and radiant emission are explored for small, low-thrust solid rocket motors, which enables the optimization of these aircraft with constraints on both thrust and radiant intensity. An example case study for the optimization of a Firefly class aircraft, including constraints on the plume radiant emission, is also presented.

8.1 Effects of motor size scale on afterburning kinetics and radiant emission

This section discusses the effects of motor size scale on afterburning kinetics and radiant emission. Effects unique to small solid rocket motors are discussed, and it is shown that sufficiently small plumes display frozen flow behavior and have a radiant intensity that scales like (size scale)^3. These effects are used in section 8.2 to discuss the relationships of chamber pressure and oxamide content on radiant intensity for small solid rocket motors.

8.1.1 Plume time scales

The presence of afterburning reactions in the exhaust plume plays an important role in determining the exhaust plume radiant emittance. If a significant amount of the fuel species exiting the nozzle burns with entrained oxygen in the plume, the flow field temperatures increase and species distributions can change significantly. The increased temperatures typically increase the radiant emittance from the exhaust plume.

Three time scales are relevant for analyzing the effective progression of afterburning in the plume: the time scale of the plume gas flow τ_{flow}, the time scale of oxygen entrainment into the plume τ_{ent}, and the time scale of the chemical reactions τ_{reac}. Two of these timescales are often compared using a dimensionless Damköhler number,

defined as:

$$Da \equiv \frac{\tau_{flow}}{\tau_{reac}} \tag{8.1}$$

If $Da \gg 1$ then the reaction timescale is much faster than the flow timescale, the plume flow field will exhibit equilibrium flow behavior, and excess fuel in the exhaust will burn with entrained oxygen. For sufficiently large Da, the progression of chemical reactions in the plume is rate-limited by the entrainment of oxygen, and τ_{reac} will converge to τ_{ent}. If $Da \ll 1$ then the flow timescale is much faster than the reaction timescale, the plume flow field will exhibit frozen flow behavior, and the excess fuel in the exhaust will remain unburnt.

These Damköhler effects with respect to changes in altitude and ambient pressure have been previously discussed in other studies [55, 85]. Woodroffe proposed that $Da \sim p_{\infty}^{3/2}$, with the intuition that as altitude increases, ambient pressures and reaction rates decrease, corresponding to $Da \to 0$ and flow transitioning from equilibrium flow at low altitudes to frozen flow at high altitudes [55].

A few other studies generally discuss the effects of motor size scale on afterburning and radiant intensity, but do not quantitatively analyze the plume time scales. Rudman and Hibbeln discussed scaling laws for optically thick, equilibrium plumes and briefly comment on the effects that altitude and size scale have on the progression of afterburning kinetics in the plume [63]. Kim et al. and Zhang et al. created empirical fits for radiant intensity scaling with motor size scale [28, 54]. Kim et al. mentioned that size scale plays a role in afterburning kinetics, but do not provide any further analysis. These studies do not investigate the effects that reduced motor size scale can have on the plume time scales or the Damköhler number, or how these effects can be used to quantify and explain afterburning progression and plume radiant emission scaling behavior. The next subsection suggests a quantitative process for evaluating time scales and Damköhler numbers for plumes, and how these relate to plume size scale and afterburning kinetics.

8.1.2 Plume Damköhler number analysis

Assuming fixed expansion ratio, chamber pressure, and propellant composition, the nozzle exit velocities should not change with size scale, and the time scale of the plume flow scales like:

$$\tau_{flow} \sim \frac{length\ scale}{velocity\ scale} \sim \frac{d}{u} \sim d \sim d_{exit} \sim d_t \tag{8.2}$$

The flow time scale should scale linearly with size scale regardless of the presence of afterburning, which suggests that the Damköhler number should have a significant dependence on motor size scale.

This scaling of the Damköhler number can be explored using the developed differentiable model. As an example, consider a family of motors using the baseline propellant formulation (see subsection 5.3.1) with a fixed chamber pressure of 1 MPa (these conditions imply fixed F/A_b and fixed $K_n = A_b/A_t$), operating at 10 km altitude and Mach 0.8. This family of motors can be scaled in size by changing the nozzle throat diameter. Local time scales can be crudely defined throughout the plume using:

$$\tau_{flow} \equiv \frac{10\,d_0}{u} \qquad \tau_{reac} \equiv \frac{[\mathrm{O_2}]}{r_{reac,O_2}} \qquad \tau_{ent} \equiv \frac{[\mathrm{O_2}]}{r_{ent,O_2}} = [\mathrm{O_2}]\left(y_{O_2,\infty}\frac{d\dot{m}}{dx}\frac{1}{M_{O_2}A}\right)^{-1} \tag{8.3}$$

where d_0 is the diameter of the plume at the start of the turbulent mixing region, u is velocity, $[\mathrm{O_2}]$ is concentration of oxygen in the plume, r_{reac,O_2} is the reaction rate of $\mathrm{O_2}$ in the plume (units: $\mathrm{mol\,m^{-3}\,s^{-1}}$), $y_{O_2,\infty}d\dot{m}/dx$ is the rate of change of oxygen entrainment into the plume with respect to position along the plume (like the plume mass flow conservation expression in Equation 6.17), M_{O2} is the molecular weight of oxygen, and A is the plume cross-sectional area. The reaction and entrainment time scales were chosen for $\mathrm{O_2}$ because, at least for the equilibrium case at large size scales, $\mathrm{O_2}$ is the rate-limiting reactant. The plume length scale is crudely taken as $10d_0$ for determining the flow time scale. Because the Damköhler number varies with downstream distance in the plume, the maximum Damköhler is used as a representative value for each plume, which occurs between 1 to $5d_0$ downstream of the start of the

turbulent mixing region for these plumes. These time scales and the maximum Damköhler number for a sweep of nozzle throat diameters are shown in Figure 8-1.

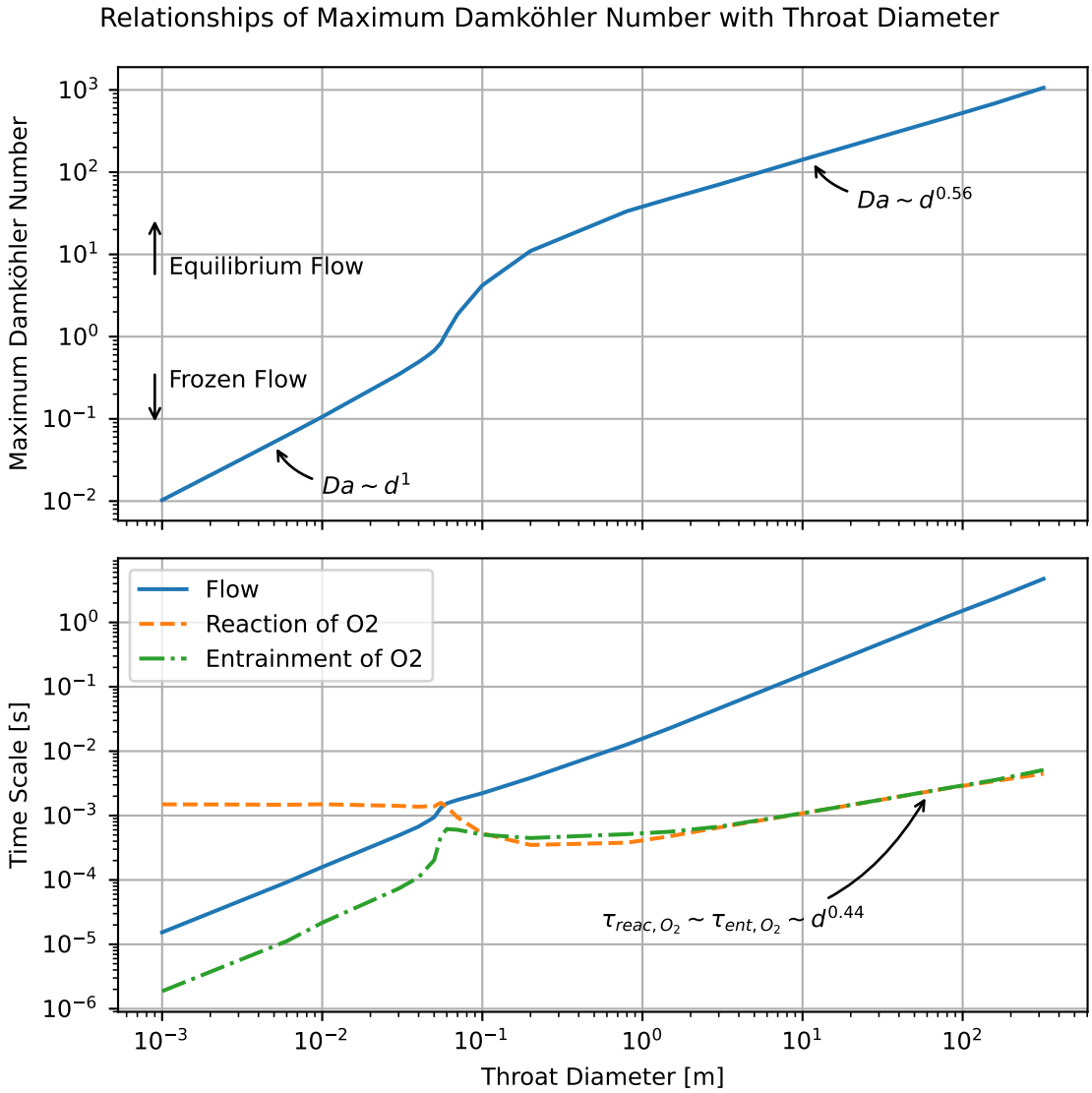

Figure 8-1: Relationship of maximum Damköhler number for a motor using the baseline propellant composition at 1 MPa chamber pressure, operating at 10 km altitude at Mach 0.8. For small throat diameters, the maximum Damköhler number is small and grows nearly linearly with throat diameter. For large throat diameter, the Damköhler number is large and grows like $\sim d^{0.56}$.

The plume can transition from $Da \gg 1$ and equilibrium chemistry to $Da \ll 1$ and frozen chemistry just by decreasing the size scale of the motor. For throat diameters $<4 \times 10^{-2}$ m, the flow is frozen and the maximum Damköhler number grows nearly linearly with throat diameter, which is consistent with the theoretical scaling for

frozen plumes that will be discussed in subsection 8.1.3. At a throat diameter of $\sim 5 \times 10^{-2}$ m, there is a kink in all of the curves in Figure 8-1 – this corresponds to the transition throat diameter where the size scale has become large enough for the plume to transition from frozen flow to equilibrium flow. For throat diameters significantly larger than this, the plume has transitioned to the equilibrium flow regime. The plume O_2 reaction rate is limited by the rate of O_2 entrainment (see the second subplot, where the reaction and entrainment timescales converge for large throat diameters) and, using the plots: $Da_{eq} \sim d^{0.56}$ and $\tau_{reac,O_2} \sim \tau_{ent,O_2} \sim d^{0.44}$. The theory for this scaling will be discussed in subsection 8.1.4. The Damköhler number continues to increase with increasing size scale for equilibrium plumes, but not as quickly as frozen plumes which scaled like $Da_{froz} \sim d^1$.

The Damköhler number should theoretically cross over unity near the transition throat diameter where the curves in Figure 8-1 change behavior. The choice of the plume length scale is important for determining the $Da = 1$ size scale, and the value of $10d_0$ is a good choice for this family of motors. With this choice of length scale, plumes with $Da < 10^{-1}$ exhibit frozen flow and plumes with $Da > 10^1$ exhibit equilibrium flow. For plumes in between, both reaction and flow time scales are important for evaluating plume behavior.

8.1.3 Damköhler number scaling for frozen plumes

For the frozen flow case, the flow field temperatures, velocities, and species concentrations are scale-invariant. The timescale of reactions τ_{reac}, which is dependent on temperature, ambient pressure, and species concentrations, is therefore not explicitly dependent on the motor size scale if frozen flow prevails: $\tau_{reac,froz} \sim d^0$. Combining these expressions, the Damköhler number for a frozen plume scales like:

$$Da_{froz} \equiv \frac{\tau_{flow}}{\tau_{reac,froz}} \sim \frac{d^1}{d^0} \sim d^1 \tag{8.4}$$

The Damköhler number should scale linearly with the motor size scale for frozen chemistry, which is consistent with the dependency in Figure 8-1.

8.1.4 Damköhler number scaling for equilibrium plumes

The $Da_{eq} \sim d^{0.56}$ dependency for large motor size scales can be explained by inspecting the reaction and entrainment rates and time scales. At equilibrium, the rate of reaction of oxygen in the plume r_{reac,O_2} should equal the rate of oxygen entrainment into the plume r_{ent,O_2}. For a constant temperature reaction where oxygen is the rate-limiting reactant, $r_{reac,O_2} \sim [\mathrm{O_2}]^{n_{O_2}}$, where n_{O_2} is some constant exponent. Following Equation 8.3, the rate of entrainment scales like $r_{ent,O_2} \sim (d\dot{m}/dx)(A^{-1}) \sim (d)(d^{-2}) \sim d^{-1}$. The scaling for the $d\dot{m}/dx$ term comes from the mass flow term in the plume flow field model in Equation 6.17, which says that $d\dot{m}/dx$ scales with the circumference of the plume. Equating these scaling expressions and solving yields a relationship between oxygen concentration and plume size scale: $[\mathrm{O_2}] \sim d^{-1/n_{O_2}}$. This is the scaling of the steady-state concentration of oxygen with size scale for equilibrium plumes. Larger plumes entrain oxygen less efficiently (smaller surface area to volume ratio), resulting in smaller oxygen steady-state concentrations and reaction rates.

This relationship between steady-state concentration of oxygen in the plume and size scale can be used to determine the scaling of the reaction time scale:

$$\tau_{reac,O_2} \sim [\mathrm{O_2}]/r_{reac,O_2} \sim [\mathrm{O_2}]^{1-n_{O_2}} \sim d^{(n_{O_2}-1)/n_{O_2}} \tag{8.5}$$

and the Damköhler number for an equilibrium plume:

$$Da_{eq} \equiv \frac{\tau_{flow}}{\tau_{reac,O_2}} \sim \frac{d^1}{d^{(n_{O_2}-1)/n_{O_2}}} \sim d^{1/n_{O_2}} \tag{8.6}$$

The fitted value of $n_{O_2} = 1.793$ determined for the global reaction rate mechanism from Table 6.1 is appropriate for the above analysis. Using this value with Equation 8.6 gives $Da_{eq} \sim d^{0.56}$, which is consistent with the dependence determined from Figure 8-1.

8.1.5 Plume temperatures

The effects of increasing Damköhler number and the transition from frozen flow to equilibrium flow on the plume temperature flow field is shown in Figure 8-2. This

plot shows plume temperature versus normalized axial distance from the start of the turbulent mixing region for a sweep of different nozzle throat diameters. The same motor and flight conditions are used for this analysis as were described in subsection 8.1.2, namely: a family of motors using the baseline propellant formulation (see subsection 5.3.1) with a fixed chamber pressure of 1 MPa (these conditions imply fixed F/A_b and fixed $K_n = A_b/A_t$), operating at 10 km altitude and Mach 0.8. The theoretical temperature profiles for frozen and equilibrium chemistry, determined using the procedure described in Appendix D, are also included in the plot.

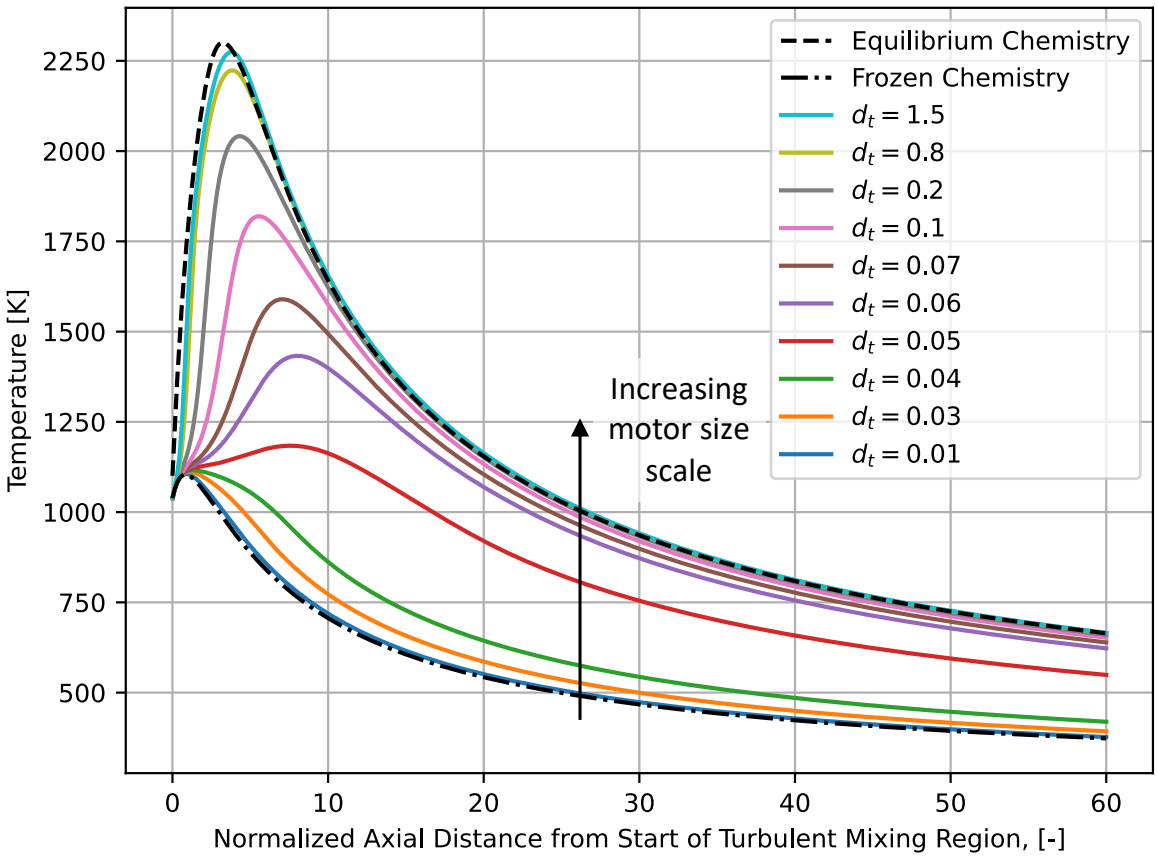

Figure 8-2: The temperature flow field in a plume can transition from frozen chemistry to equilibrium chemistry just by increasing the size scale of the motor. This plot assumes a motor using the baseline propellant composition at a chamber pressure of 1 MPa, an altitude of 10 km, and vehicle speed of Mach 0.8.

At $d_t = 0.01$ m, $Da \approx 10^{-1}$ (from Figure 8-1), the flow is frozen, and the temperatures throughout the plume are relatively cold. For $d_t < 0.01$ m, the temperature curves collapse onto the frozen flow curve which has a nearly identical profile as the

$d_t = 0.01\,\text{m}$ curve. As the throat diameter is increased, higher temperatures are found throughout the flow field. At $d_t = 0.05\,\text{m}$, the temperature profile falls between the lower and higher groupings of curves. This corresponds to $Da \approx 1$ (from Figure 8-1). The reaction and flow time scales are near the same size in this case, and this results in a relatively long temperature plateau where both flow and reaction processes are important. As d_t is increased further, temperatures throughout the flow field rise, and eventually converge onto the temperature profile for true equilibrium chemistry. $Da \approx 10^1$ at $d_t \approx 0.2\,\text{m}$ (from Figure 8-1), which shows nearly equilibrium temperatures in Figure 8-2. The plume transitions from frozen flow to near equilibrium flow over approximately one order of magnitude of motor size scale, and the Damköhler number is a good indicator of where this transition occurs. If motors and plumes are sufficiently small, frozen chemistry can prevail in the plume at any operating altitude, even with the high ambient pressures at sea level.

8.1.6 Radiant emission

The dependence of the plume afterburning kinetics and temperature flow field on the motor size scale also have important implications for the scaling of the plume radiant emission. The effects of increasing motor size scale on plume radiant intensity for several different wavelengths is shown in Figure 8-3. Again, the same motor and flight conditions are used for this analysis as were described in subsection 8.1.2, namely: a family of motors using the baseline propellant formulation (see subsection 5.3.1) with a fixed chamber pressure of 1 MPa, operating at 10 km altitude and Mach 0.8.

For sufficiently small motors and plumes, the flow field exhibits frozen flow, following the discussion from subsection 8.1.5. As long as the transition size scale is not approached, the plume flow field temperatures and species distributions are driven by mixing with entrained air, and are not dependent on the size scale. Small plumes are also typically optically thin, since optical depth scales like $\sim \kappa_\lambda d$ (optical depth is introduced in subsection 3.2.3). As previously discussed in subsection 4.3.1, for optically thin plumes with scale-invariant temperature and species distributions throughout the plume, and where the ambient pressure is approximately constant, the

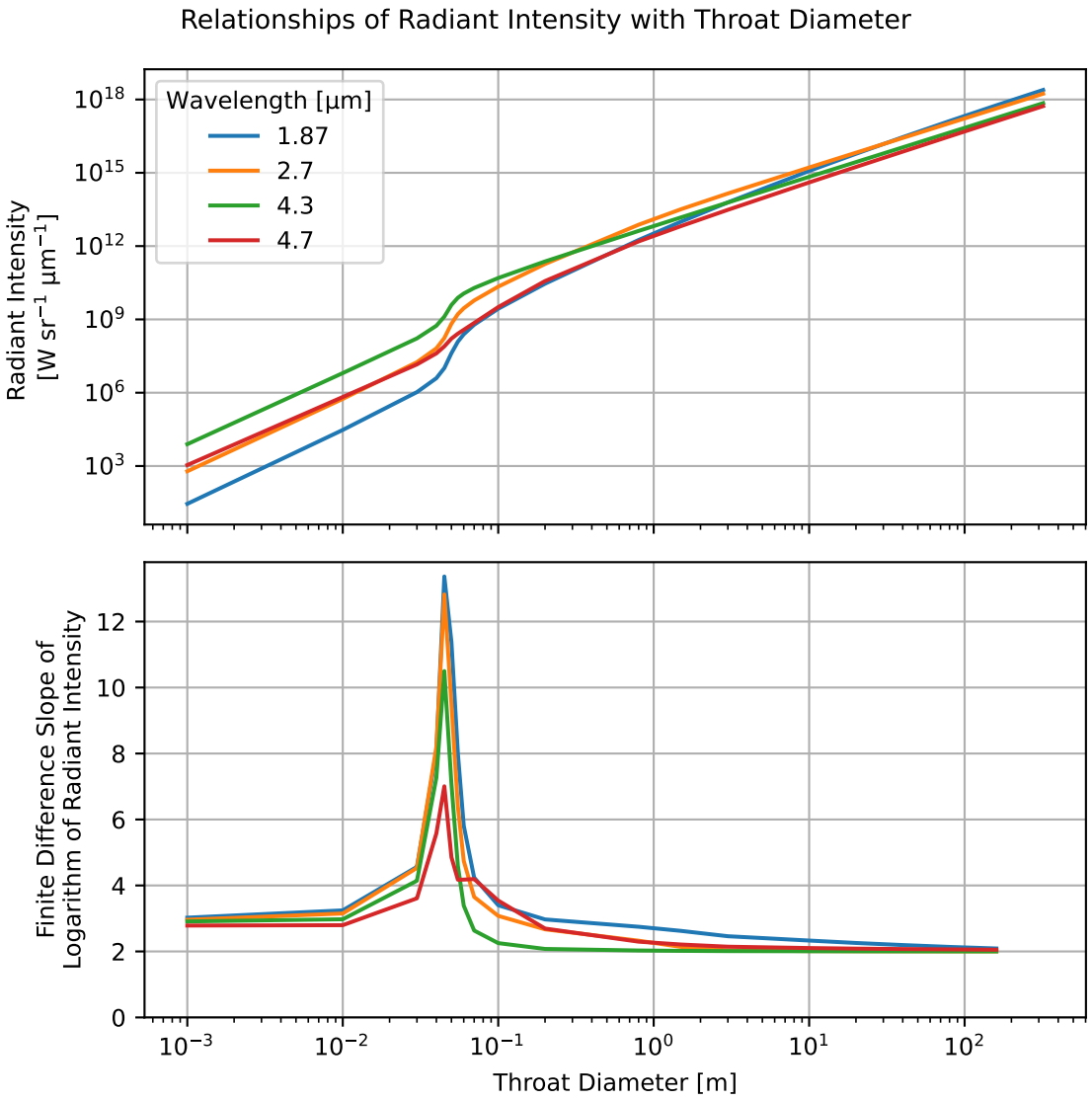

Figure 8-3: For small plumes, the plume flow field is typically frozen and the radiant intensity exhibits a $\sim d^3$ scaling with motor size scale. The radiant intensity increases rapidly during the transition from frozen to equilibrium behavior. For large plumes, the radiant intensity eventually scales like $\sim d^2$.

radiant intensity scales with the volume of emitting plume gas: $J_\lambda \sim \kappa_\lambda dA_{projected} \sim d^3$. Given that small plumes tend to be both optically thin and have frozen flow (which implies scale-invariant temperatures and species distributions), the above scaling law can be applied to small plumes more generally. This $J_\lambda \sim d^3$ scaling is evident in Figure 8-3 at motor throat diameters $<1 \times 10^{-2}$ m for all of the included wavelengths.

At the size scale where the plume transitions from frozen to equilibrium flow (near $d_t \approx 5 \times 10^{-2}$ m), the derivative of the radiant intensity becomes several times

larger for all of the included wavelengths. This is due to the increased temperatures throughout the flow field, which yield larger molecular absorption coefficients and blackbody radiance values.

For sufficiently large motors and plumes, the flow field will transition to equilibrium flow. The plume flow field temperature distribution converges to the equilibrium profile, where it is once again nearly invariant with size scale (for size scales where $Da \gg 1$). The emitting species distributions (CO, CO_2, HCl, and H_2O) also converge to equilibrium values. If the motor size scale is large enough, the plume becomes optically thick since optical depth scales like $\sim \kappa_\lambda d$, and the emissivity ϵ_λ converges to unity. As previously discussed in subsection 4.3.1, for plumes that are optically thick and have scale-invariant temperature and species distributions throughout the plume, and where the ambient pressure is approximately constant, $J_\lambda \sim \epsilon_\lambda A_{projected} \sim d^2$.

The radiant intensity at 4.3 µm almost immediately shows this d^2 dependence for $d_t > 2 \times 10^{-1}$ m. This suggests that the CO_2 band at 4.3 µm is almost immediately optically thick after the transition to equilibrium flow. For large enough throat diameters, the radiant intensity for the other wavelengths does eventually achieve the predicted d^2 dependence. However, these other bands are weaker than the 4.3 µm CO_2 band at these conditions, and so the motor size scale must be larger so that the optical depth $\kappa_\lambda d \gg 1$ and $\epsilon_\lambda \approx 1$. The 1.87 µm H_2O band does not show the $J_\lambda \sim d^2$ dependence until $d_t > 1 \times 10^2$ m, which is, of course, unrealistically large for any solid rocket motor.

8.2 Effects of chamber pressure and oxamide content on radiant intensity for small solid rocket motors with fixed burn area

The Firefly vehicle concept, introduced in subsection 1.2.2, uses an end-burning motor configuration. The constrained and free design variables for this vehicle concept are discussed in subsection 2.1.1. Notably, the motor burn area is constant and set by the

diameter of the aircraft fuselage, and the propellant oxamide content and nozzle throat area (which ultimately sets chamber pressure) are free variables. For this configuration of vehicles, understanding the influence of the free design variables (oxamide content and chamber pressure) on the radiant intensity is important for designing vehicles with constraints on the radiant emission. This section will discuss the coupling between chamber pressure, oxamide content, and radiant intensity for small, fixed burn area motors.

8.2.1 Evaluation with developed model

In section section 7.2, it was discussed that for the four point designs considered for the test matrix, both the measured and modeled radiant intensity showed little sensitivity to chamber pressure, but decreased significantly with the higher oxamide content. This section provides a more general analysis of the effects of chamber pressure and oxamide content on radiant intensity. The developed radiant intensity model was swept through a range of chamber pressures (0.2 MPa to 3 MPa) and oxamide contents (0 % to 20 %) to determine the resulting peak spectral radiant intensity and total radiant intensity in the 3 - 5 µm band, as well as the vehicle thrust and plume diameter. The oxamide burn rate law introduced in subsubsection 2.4.2.1 is used to relate the propellant burn rate to the oxamide content and determine the equilibrium chamber pressure. The nozzle is chosen to have a matched expansion ratio such that $p_e = p_a$. Figure 8-4 shows this design variable sweep for a stationary vehicle at 0 km altitude with a propellant burn area of 1140 mm^2, which is representative of the experiment conditions for the motor measurements in section 5.6. Figure 8-5 shows this design variable sweep for a vehicle traveling at Mach 0.8 at 10 km altitude with a propellant burn area of 2500 mm^2, which is representative of the Firefly vehicle concept.

For the experimental motor conditions (Figure 8-4), at chamber pressures >0.8 MPa, the radiant intensity is nearly invariant with chamber pressure for all of the oxamide contents in the plot. However, there is a significant dependence on oxamide content: the radiant intensity with 4 % oxamide is less than half that of the 0 % oxamide propellant at a given chamber pressure >0.8 MPa; the radiant intensity with 8 %

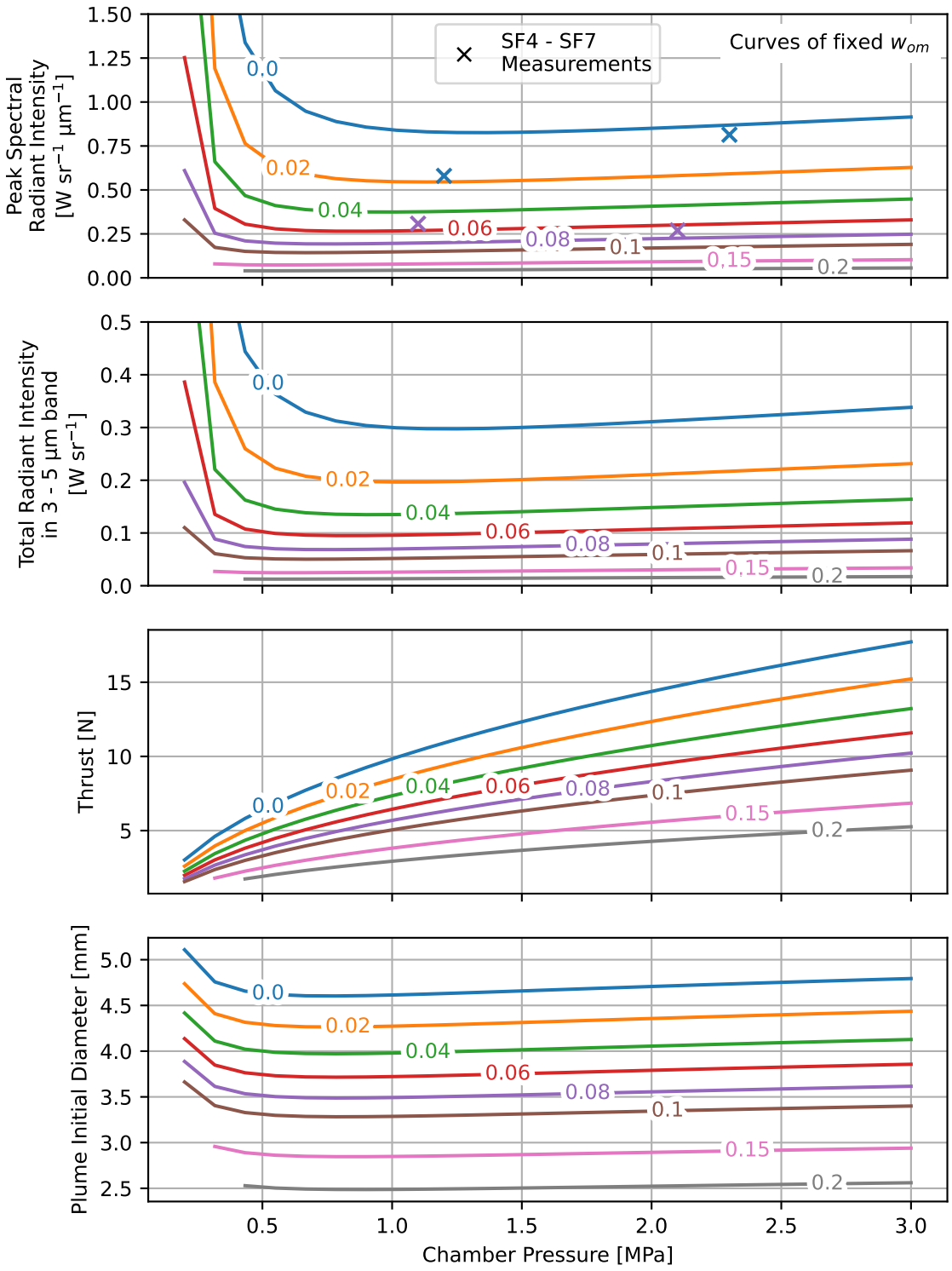

Figure 8-4: Modeled radiant intensity for a sweep of oxamide contents and chamber pressures at experimental measurement conditions: 0 km altitude, 0 m s^{-1} vehicle speed, 1140 mm^2 burn area. For chamber pressures >0.8 MPa, the modeled radiant intensity is nearly invariant with chamber pressure, but decreases significantly with increasing oxamide content.

oxamide is approximately a quarter of the 0 % oxamide propellant. These results are generally consistent with the measured results from subsection 5.6.1, which are also shown in Figure 8-4. There is very little difference between the peak spectral radiant intensity trend and the total radiant intensity trend, because the emission in the 3 - 5 µm band is dominated by the 4.3 µm emission band. For the experimental motor conditions and chamber pressures >0.8 MPa, to significantly change the peak or total radiant intensity of the motor, the oxamide content design variable must be manipulated, as radiant intensity at these conditions is nearly invariant with chamber pressure.

For a given propellant (and assuming fixed nozzle exit pressure), decreasing the chamber pressure decreases the nozzle exit velocity and increases the nozzle exit temperature. Both of these effects tend to increase the Damköhler number. An increased temperature increases the reaction rate – which is exponentially dependent on temperature – and decreases the reaction time scale. A decreased nozzle exit velocity increases the flow time scale, which is inversely dependent on velocity. At pressures less than 0.8 MPa, the increased temperatures and decreased velocities make afterburning relevant for many of the propellants. This significantly increases the radiant intensity, and is why many of the propellants in Figure 8-4 show a sharp increase in radiant intensity once the chamber pressure is sufficiently small.

The vehicle thrust is sensitive to both chamber pressure and oxamide content, and behaves as expected: thrust levels are higher for higher chamber pressures and lower oxamide contents, both of which drive faster propellant burn rates. The plume initial diameter (e.g. the plume diameter at the start of the turbulent mixing region, which is essentially identical to d_e since $p_e = p_a$) is relatively insensitive to chamber pressure for these fixed burn area motors, which suggests that plume size and volume are also similar. This is consistent with the fact that radiant intensity is also insensitive to chamber pressure (for $p_c > 0.8$ MPa, where there is no afterburning), since for these small motors, radiant intensity scales with the volume of emitting gas (see subsection 4.3.1).

For the Firefly flight vehicle conditions (Figure 8-5), the model sweep shows a dependence on both the chamber pressure and the oxamide content. The dependence on chamber pressure is still relatively weak: a 6× increase in chamber pressure (from 0.5 MPa to 3 MPa) only leads to a 1.8× increase in peak spectral radiant intensity for the 0 % oxamide propellant. The dependence is weaker for higher oxamide contents; for oxamide contents of 15 % and 20 %, the peak radiant intensity is again essentially invariant with chamber pressure. Again, there is a significant dependence on oxamide content at a given chamber pressure, with radiant intensity decreasing with increasing oxamide content. For the Firefly flight vehicle design as well, radiant intensity can be manipulated more successfully with the oxamide content design variable as opposed to the chamber pressure variable. Because of the lower ambient pressure at the operating altitude of 10 km for the Firefly example, the species concentrations and exit temperatures remain low enough that afterburning reactions do not progress significantly ($Da \ll 1$) for any of the propellants. This is why Figure 8-5 does not show a sudden increase in radiant intensities at lower chamber pressures, unlike the curves in Figure 8-4.

Similar to the experimental conditions, (Figure 8-4), the vehicle thrust for the Firefly vehicle conditions (Figure 8-5) is larger for higher chamber pressures and lower oxamide contents. The actual thrust values are significantly larger for the Firefly vehicle conditions due to the larger propellant burn area (2500 mm^2 versus 1400 mm^2) and higher nozzle expansion ratios p_c/p_e due to smaller ambient and exit pressures at 10 km altitude. Like the experimental conditions, the plume initial diameter for the Firefly conditions are relatively insensitive with chamber pressure, although it does increase slightly with increasing chamber pressure. The plume volume should therefore be relatively insensitive to chamber pressure, which again is consistent the radiant intensity results in Figure 8-5, which show only a weak dependence on chamber pressure.

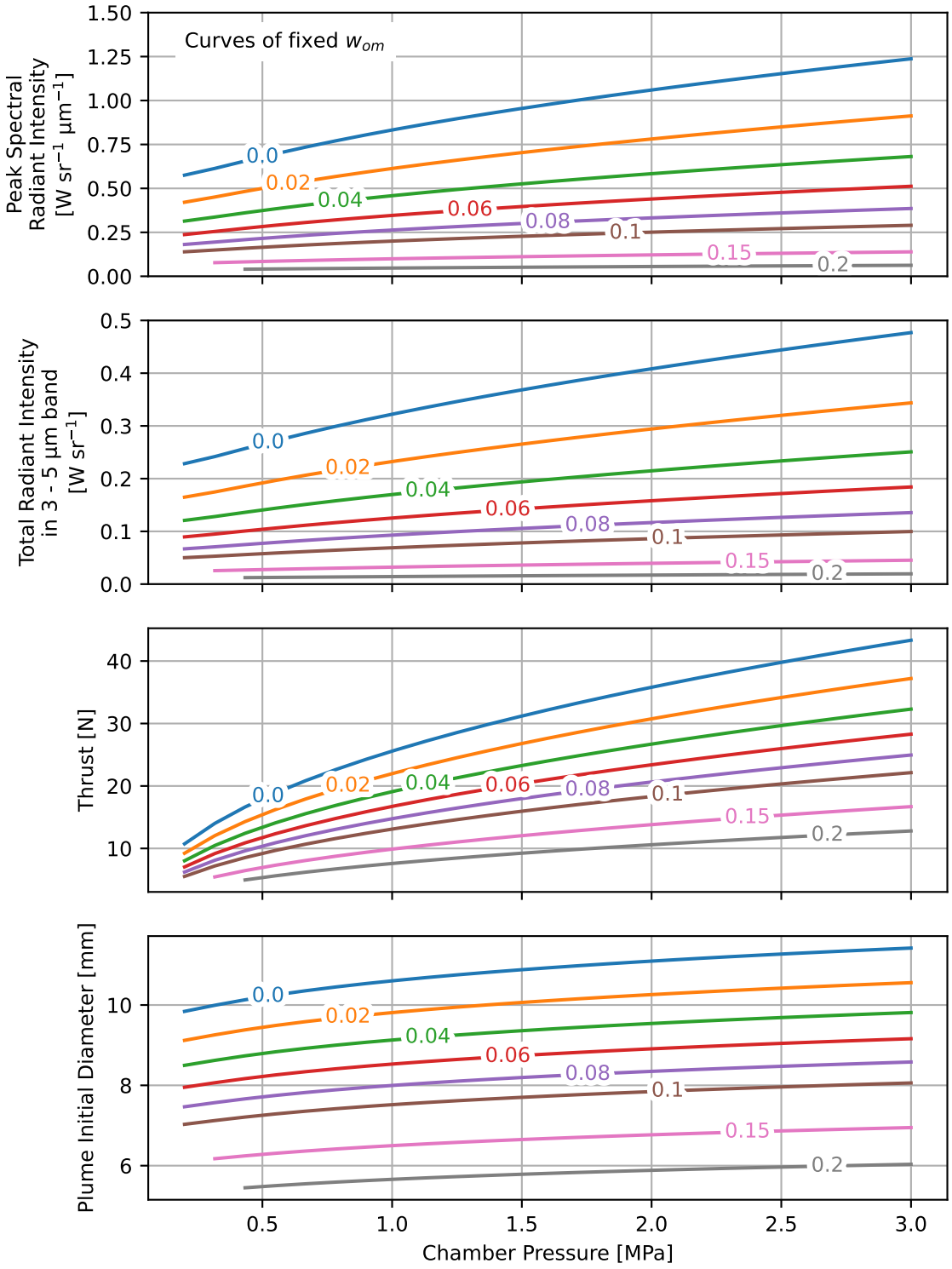

Figure 8-5: Modeled radiant intensity for a sweep of oxamide contents and chamber pressures at Firefly vehicle concept conditions: 10 km altitude, Mach 0.8 vehicle speed, 2500 mm^2 burn area. For low oxamide contents, the model shows a mild dependence of radiant intensity on chamber pressure.

8.2.2 Comparison with first-order scaling law

As a quick cross-check of the results discussed in the previous section, a first-order scaling law for exhaust plume radiant intensity for small motors with fixed burn area was derived (see Appendix E for the derivation). The derived scaling law is:

$$J_\lambda \sim I_{b\lambda}(T_e(p_c, w_{om}))\ \frac{p_a}{T_e(p_c, w_{om})}\ \left[\frac{A_e}{A_t}(p_c)\ \frac{A_t}{A_b}(p_c, w_{om})\right]^{3/2} \equiv S \qquad (8.7)$$

This scaling law assumes that the propellant burn area A_b is fixed, nozzles have matched expansion and motors are operated at a fixed altitude such that $p_e = p_a = constant$. It also assumes that motors are small enough such that the plumes are optically thin, the exhaust flow has frozen chemistry, and therefore radiant intensity scales like $\sim$ (size scale)^3. The assumptions of an optically thin plume and frozen exhaust flow are reasonable for motors of the Firefly size scale, following the discussion in subsection 8.1.6. Motor parameters at the nozzle exit plane, such as T_e and A_e, are assumed as representative of the plume. The scaling law does not account for any effects associated with plume mixing with entrained air or changes in molecular absorption coefficient due to temperature. The scaling parameter S, arbitrarily normalized[†] to the radiant intensity at $p_c = 1\,\mathrm{MPa}$ and $w_{om} = 0$, is given in the first subplot in Figure 8-6 versus chamber pressure for several different oxamide contents assuming an ambient pressure at 10 km altitude. Other terms appearing in the scaling law in Equation 8.7 – A_e/A_b, T_e, and $I_{b\lambda}(T_e)/T_e$ – are also given in Figure 8-6.

Again, from Figure 8-6, the radiant intensity has a relatively weak dependence on the chamber pressure. However, in Figure 8-6, the scaling parameters shows a slow decrease with increasing chamber pressure, while the modeled radiant intensities in Figure 8-5 show a slow increase with increasing chamber pressure. This is likely due to the effects neglected by the scaling law, including effects of plume mixing with entrained air and changes in molecular absorption coefficient due to temperature changes. The scaling of radiant intensity with oxamide content shows a similar trend

[†]The scaling parameter has nonsensical units of $\mathrm{W\,sr^{-1}\,m^{-2}\,\mu m^{-1}\,Pa\,K^{-1}}$. At $p_c = 1\,\mathrm{MPa}$ and $w_{om} = 0$, $S = 1.11 \times 10^3\,\mathrm{W\,sr^{-1}\,m^{-2}\,\mu m^{-1}\,Pa\,K^{-1}}$, which is also a nonsensical value, but is included here for completeness.

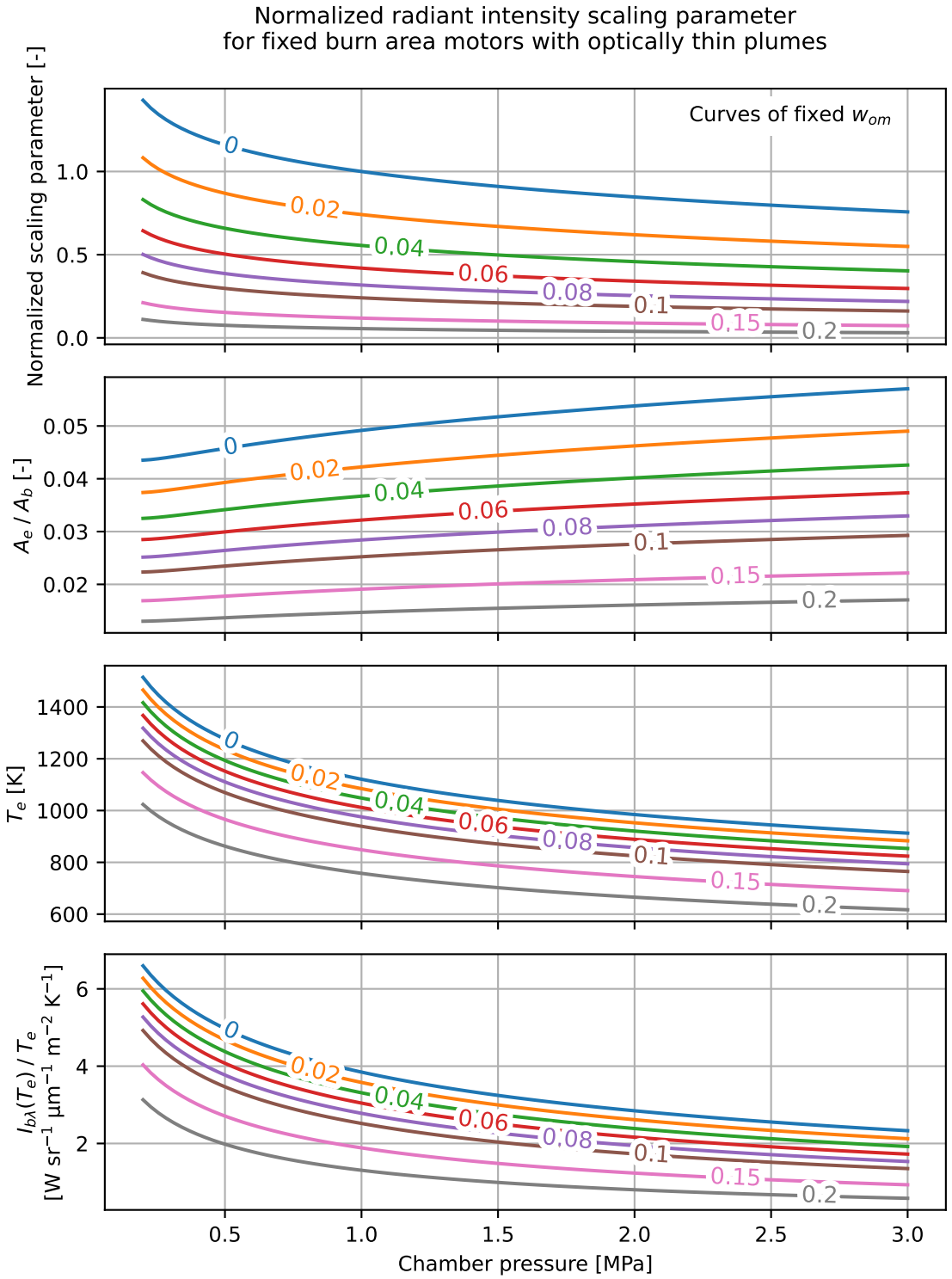

Figure 8-6: A first order scaling law for plume radiant intensity also reveals a relatively weak dependence of radiant intensity on chamber pressure for small, fixed burn area motors. The scaling law shows a similar dependence on oxamide content as the results in Figure 8-5.

to Figure 8-5. For the results in both Figure 8-5 and Figure 8-6, the 4 % oxamide propellant has approximately half the radiant intensity of the 0 % oxamide propellant, and the 8 % oxamide propellant has approximately a third the radiant intensity as the 0 % propellant.

The second subplot in Figure 8-6 shows how the exit area A_e varies with chamber pressure and oxamide content (A_b is fixed, so it does not affect the plotted trends). For any particular oxamide content, the exit area is nearly constant, slowly increasing with chamber pressure. The chamber pressure does not significantly affect the size of the plume, which partially explains why the radiant intensity is only weakly dependent on chamber pressure. The third subplot shows the exit temperature T_e, and the fourth subplot shows the temperature dependent terms – $I_{b\lambda}(T_e)/T_e$ – against chamber pressure for several different oxamide contents. Exit temperatures T_e are highest for lower chamber pressures (which corresponds to a smaller expansion ratio and higher exit temperatures) and lower oxamide contents. Because T_e is used as a representative temperature of the plume for this scaling law, the temperature dependent terms $I_{b\lambda}(T_e)/T_e$ show a decay with increasing chamber pressure. Realistically, however, mixing with entrained air would likely cause the plume temperatures to decay quickly, and would make the plume radiant intensity less sensitive to chamber pressure (this phenomena is discussed for the experimental test matrix of motors in section 7.2) than is predicted by the scaling law.

8.3 Small, low thrust motor design with integrated consideration of plume radiant emission

The radiant emission model discussed in chapter 6 was developed to enable improved design of solid rocket motors with integrated consideration of propulsion performance and plume radiant emission. In this section, the developed radiant emission model is used to explore design tradeoffs for the Firefly solid-rocket powered aircraft concept that was introduced in subsection 1.2.2. For this Firefly example, it is assumed that

the vehicle thrust is constant and is set to match the vehicle drag or another mission constraint. The motor has a 2500 mm^2 burning area, the nozzle has matched expansion such that $p_e = p_a$, and the aircraft is operating at 10 km altitude at a speed of Mach 0.8.

The vehicle thrust is treated as a problem constraint that a designer would choose depending on the mission requirements. The propellant oxamide content and motor chamber pressure are free design variables that can be manipulated to achieve the required thrust. For a selection of vehicle thrusts, the developed differentiable model was swept through a range of possible oxamide contents, and the resulting chamber pressure, motor specific impulse, and plume radiant intensity was solved. The results of this design sweep are plotted in Figure 8-7 with curves of fixed thrust.

This design chart helps to characterize the trade-offs between aircraft thrust, propellant oxamide content, chamber pressure, and plume radiant intensity. For a given vehicle thrust, a significant range of peak spectral and total radiant intensities can be achieved by varying the motor chamber pressure and propellant oxamide content. Operating at a higher oxamide content and chamber pressure yields lower radiant intensities at a given thrust. For a given propellant oxamide content, a different vehicle thrust constraint does not significantly change the radiant intensities. This is because, at a given propellant oxamide content, increasing the vehicle thrust is achieved by increasing the motor operating chamber pressure, and it was discussed previously in section 8.2 that radiant intensity is relatively insensitive to chamber pressure for small, fixed burn area motors.

For each vehicle thrust level, a different combination of propellant oxamide content and chamber pressure maximizes the motor specific impulse (marked with the ♦ markers in Figure 8-7). Increasing the propellant oxamide content decreases the propellant flame temperature and characteristic velocity (see subsubsection 2.4.2.2), which decreases the specific impulse. However, operating at a higher oxamide content means a higher chamber pressure is required to achieve a given thrust requirement; operating at a higher chamber pressure increases the nozzle thrust coefficient and increases the motor specific impulse. These opposing trends result in a specific impulse-

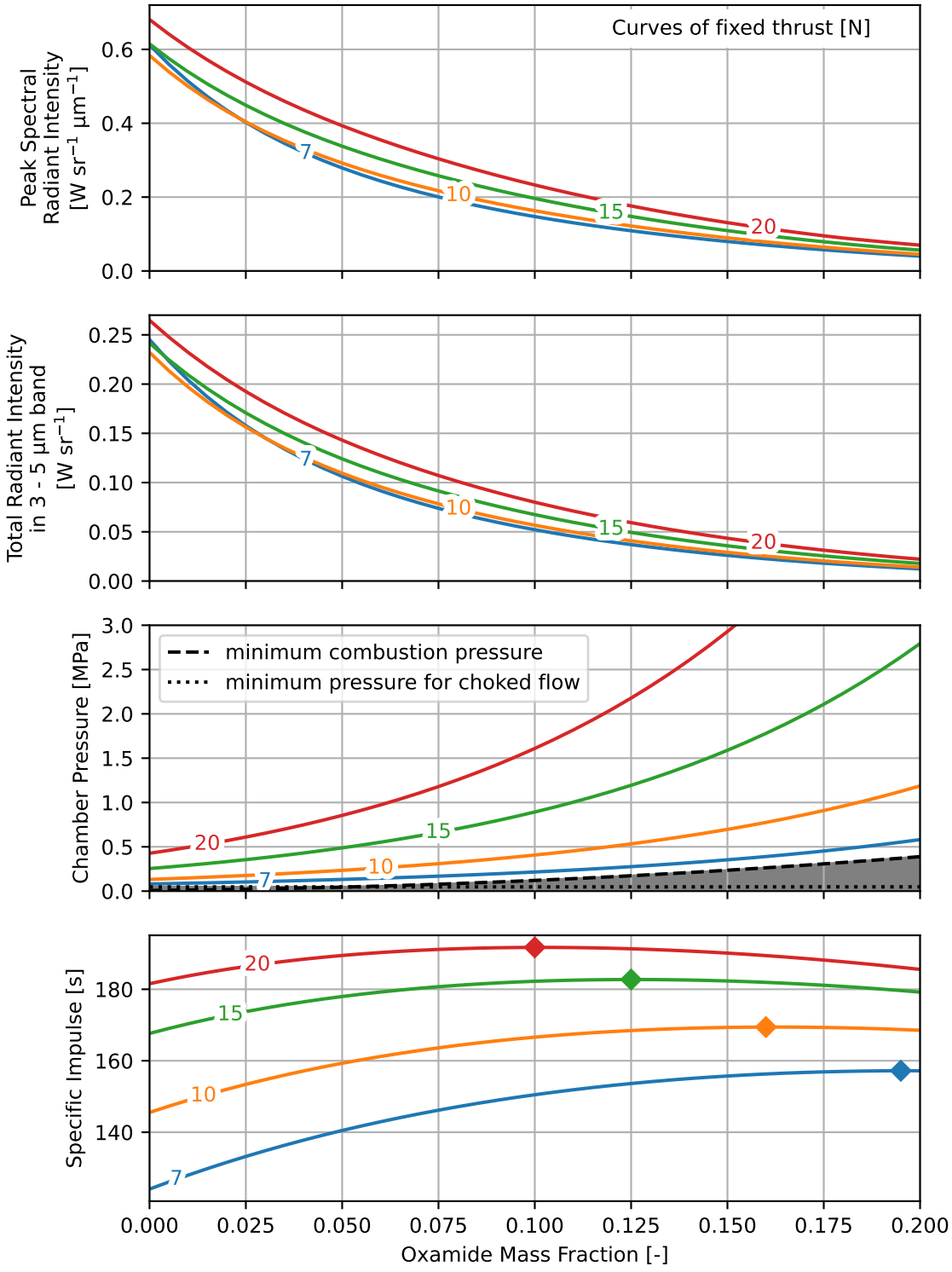

Figure 8-7: For a given vehicle thrust, a wide range of peak and total radiant intensities can be achieved by manipulating the motor chamber pressure and propellant oxamide content. The ♦ markers show the point of maximum specific impulse for each curve.

maximizing oxamide content for each thrust level, a phenomenon that was already highlighted by Vernacchia et al. in Ref. [4] for this class of oxamide-doped propellants.

8.4 Example: optimization of Firefly motor design

This section will provide an example case study for the design of a small, low-thrust Firefly class vehicle. The design problem will be formulated as an optimization problem. Two different vehicle scenarios will be considered: one with a constraint on radiant intensity, and one without. The optimized results will be discussed and compared.

8.4.1 Design problem setup

The Firefly vehicle concept is illustrated in Figure 8-8. The vehicle concept uses an end-burning motor with a fixed burn area that delivers a constant thrust. The propellant composition and nozzle throat area are free variables.

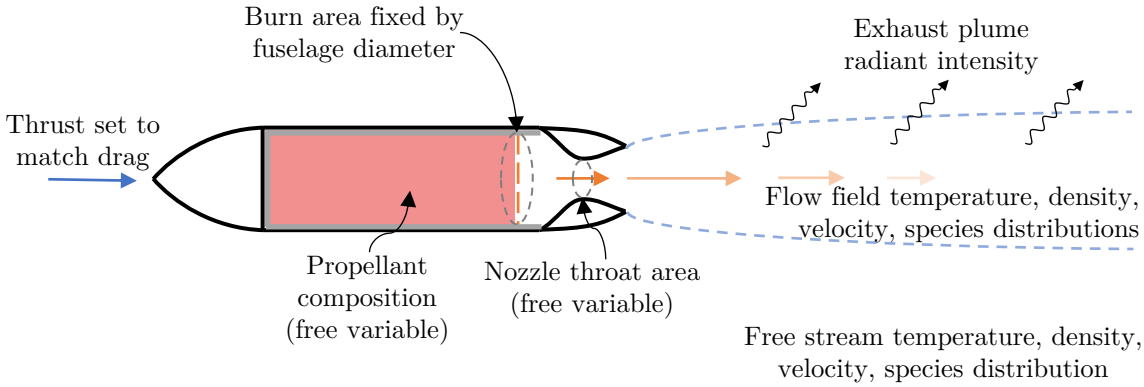

Figure 8-8: The Firefly vehicle concept has constrained thrust and propellant burn area, and variable nozzle throat area propellant oxamide content. The variable choices influence the plume flow field and subsequent exhaust plume radiant intensity.

A possible Firefly vehicle design might have a goal of maximizing the vehicle specific impulse (which maximizes vehicle burn time). It could also be of interest to constrain the radiant emission in the 4.3 µm CO_2 band to be less than some target value, if vehicle visibility is a concern. Two design optimization scenarios will be

considered in this case study. The first design scenario will optimize vehicle specific impulse with no constraint on radiant intensity (the "unconstrained" design). The second scenario will optimize specific impulse subject to a constraint that the radiant intensity at 4.3 µm is less than $0.1\,\mathrm{W\,sr^{-1}\,\mu m^{-1}}$ (the "constrained" design).

These scenarios can be formulated as design optimization problems, and can be defined using the appropriate problem variables, constraints, and objective for implementation in AeroSandbox (see section 6.2 for a discussion of AeroSandbox and the elements of an optimization problem). The problem elements for these case study scenarios are summarized below.

Constraints:

- Thrust, $F = 15\,\mathrm{N}$
- Burn area, $A_b = 2500\,\mathrm{mm^2}$
- Altitude, $h = 10\,\mathrm{km}$
- Free stream velocity, $u_\infty = \text{Mach } 0.8 \approx 240\,\mathrm{m\,s^{-1}}$
- Propellant oxamide mass fraction, $0 \leq w_{om} \leq 0.2$
- Radiant intensity, $J_{\lambda=4.3\,\mu\mathrm{m}}$
    1. Unconstrained design: no constraint on $J_{\lambda=4.3\,\mu\mathrm{m}}$
    2. Constrained design: $J_{\lambda=4.3\,\mu\mathrm{m}} \leq 0.1\,\mathrm{W\,sr^{-1}\,\mu m^{-1}}$

Variables:

- Nozzle throat area, A_t
- Propellant oxamide mass fraction, w_{om}

Objective:

- Maximize specific impulse, I_{sp}

Both scenarios were implemented in AeroSandbox with the additional constraints imposed by the six sub-models for modeling plume radiant emission discussed in section 6.1. The systems were solved for the propellant throat area and propellant oxamide mass fraction that maximized specific impulse subject to the constraints. The results are discussed in the following subsection.

8.4.2 Results

The scenarios described in the previous subsection were solved using AeroSandbox to determine the maximum specific impulse design. The optimized design and performance parameters are summarized in Table 8.1.

	Unconstrained	Constrained, $J_{\lambda=4.3\,\mu m} \leq 0.1\,W\,sr^{-1}\,\mu m^{-1}$
Oxamide content, w_{om} [-]	0.126	0.155
Throat diameter, d_t [mm]	3.24	2.71
Chamber pressure, p_c [MPa]	1.20	1.68
Radiant Intensity at 4.3 µm, $J_{\lambda=4.3\,\mu m}$ [$W\,sr^{-1}\,\mu m^{-1}$]	0.14	0.10
Specific impulse, I_{sp} [s]	184	183

Table 8.1: Comparison of vehicle design and performance parameters for Firefly scenarios.

The constrained and unconstrained designs have very different $J_{\lambda=4.3\,\mu m}$ values. The unconstrained design has $J_{\lambda=4.3\,\mu m} = 0.14\,W\,sr^{-1}\,\mu m^{-1}$. The constrained design has $J_{\lambda=4.3\,\mu m} = 0.10\,W\,sr^{-1}\,\mu m^{-1}$, which is significantly smaller than the unconstrained design. The value is also at the boundary of the $J_{\lambda=4.3\,\mu m} \leq 0.1\,W\,sr^{-1}\,\mu m^{-1}$, and so this constraint drives this design. The reduced $J_{\lambda=4.3\,\mu m}$ in the constrained design is achieved by operating the motor at a higher oxamide content w_{om} and higher chamber pressure p_c (which is set by a smaller throat diameter d_t) than the unconstrained design. This is consistent with the results in the design chart in Figure 8-7.

Despite the significant differences in peak radiant intensity, oxamide content, chamber pressure, and throat diameter, the specific impulse is nearly identical between the two designs. Including the $J_{\lambda=4.3\,\mu m} \leq 0.1\,W\,sr^{-1}\,\mu m^{-1}$ constraint for this design problem incurs almost no specific impulse performance penalty. The developed radiant intensity model enables the direct optimization of this constrained design, and revealed for this case study a new design that reduces plume radiant intensity and maintains a nearly identical specific impulse.

The vehicle design scenarios are explored further in the following figures. The predicted radiant intensities for the constrained and unconstrained Firefly designs are shown in Figure 8-9. The emission for the constrained design is smaller across the spectrum than the unconstrained design. This is expected given the driving $J_{\lambda=4.3\,\mu m} \leq 0.1\,W\,sr^{-1}\,\mu m^{-1}$ constraint, which selects for a higher oxamide content design with significantly smaller motor chamber and nozzle exit temperatures which reduces emission everywhere. The emission spectra show distinct peaks for the 2.7 µm combined H_2O and CO_2 band, the 3.5 µm HCl band, the 4.3 µm CO_2 band, and the 4.7 µm CO band. The emission for both designs is still relatively weak, due to the small vehicle size, high propellant oxamide content, low propellant mass flow rate, and low ambient pressure and species concentrations at 10 km altitude.

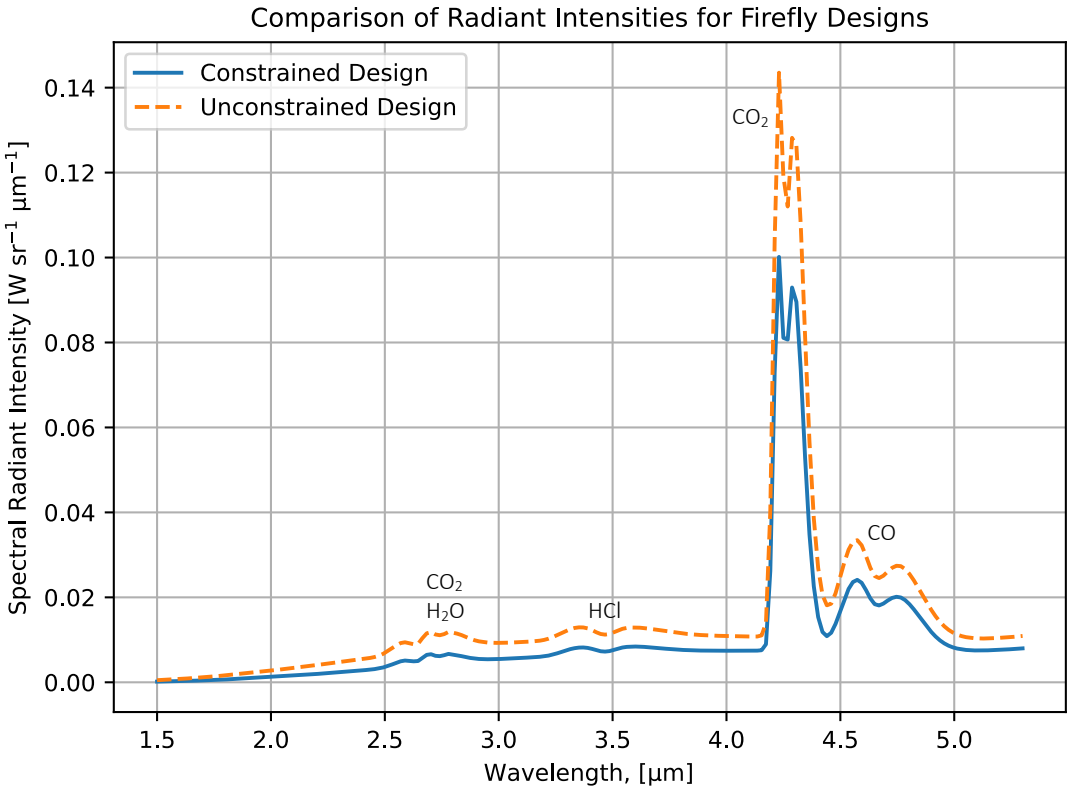

Figure 8-9: The constrained design shows lower radiant intensities across the spectrum than the unconstrained design. The predicted radiant intensity for both Firefly designs peaks at the 4.3 µm CO_2 band. The emission is weak across the spectrum for both designs due to the small vehicle size, high propellant oxamide content, and low ambient pressure and species concentrations at 10 km altitude.

The plume flow field temperature is plotted in Figure 8-10 for both designs along with theoretical lower bounds and upper bounds corresponding to frozen or equilibrium flow prevailing respectively throughout the plume (see Appendix D for a discussion of how the bounds were calculated). The temperatures throughout both plumes are relatively cold. The constrained design has a slightly smaller exit temperature than the unconstrained design due to the higher oxamide content and higher expansion ratio. The integrated temperature profiles for both designs converge with the theoretical frozen chemistry curve. This suggests that both plumes have $Da \ll 1$ with frozen flow, and that fuel species exiting the nozzle remain unreacted.

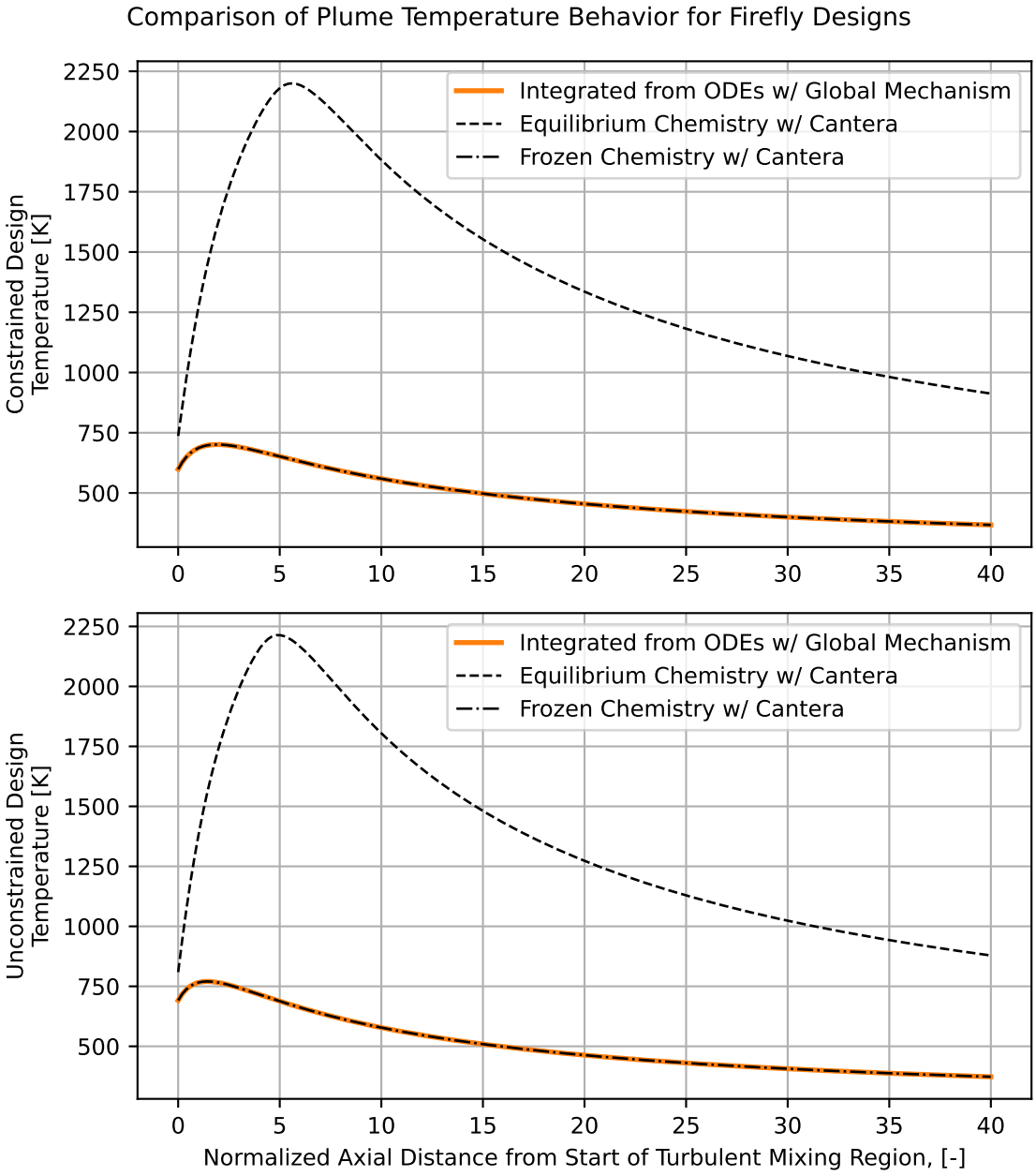

Figure 8-10: The flow field temperatures for these Firefly designs are relatively cold. The integrated temperature curve is convergent with the frozen chemistry curve for both plumes, which suggests $Da \ll 1$. The plumes are frozen due to the low temperatures, small size scale, and low ambient pressures.

Other modeled parameters characterizing the plume flow fields for this case study are shown in Figure 8-11. For both designs, the plume flow field is characterized by mixing with entrained air, since the flow is frozen and fuel species are not reacting with entrained oxygen. The temperature curves are the same curves plotted in Figure 8-10. The unconstrained design shows slightly higher temperatures and lower densities throughout the plume due to its lower oxamide content and higher nozzle exit temperature. The velocities are nearly identical between the designs, while the plume diameter is slightly larger for the unconstrained design.

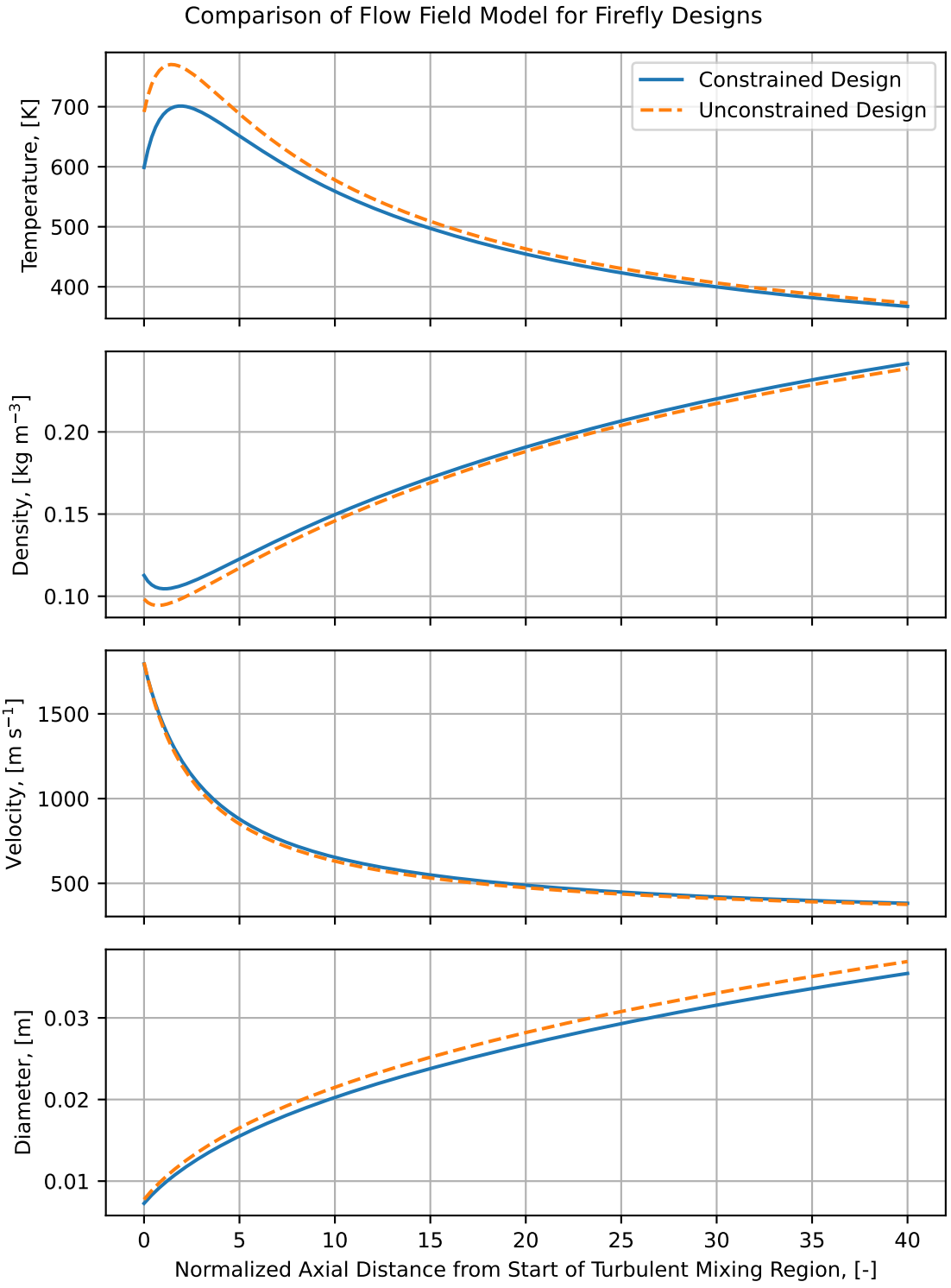

Figure 8-11: The flow fields for the Firefly designs are both characterized by mixing with entrained air, as the flow is frozen and fuel species in the exhaust are not reacting with oxygen. The unconstrained design has higher temperatures and lower densities than the constrained design due to its smaller oxamide content.

The species mass fractions throughout the exhaust plumes are plotted in Figure 8-12. Both plumes show very similar species mass fractions throughout the flow field. Again, the characteristics of the plume flow fields are driven by mixing processes only, as both plumes are frozen. At $x/d_0 = 0$, the species mass fractions are equal to the mass fractions at the exit plane of the nozzles. As the plumes entrain and mix with air from the freestream, the O_2 and N_2 mass fractions increase, while all other species mass fractions decrease as their concentration becomes diluted with entrained air. The concentrations of O_2 and N_2 eventually converge to their respective freestream mass fractions.

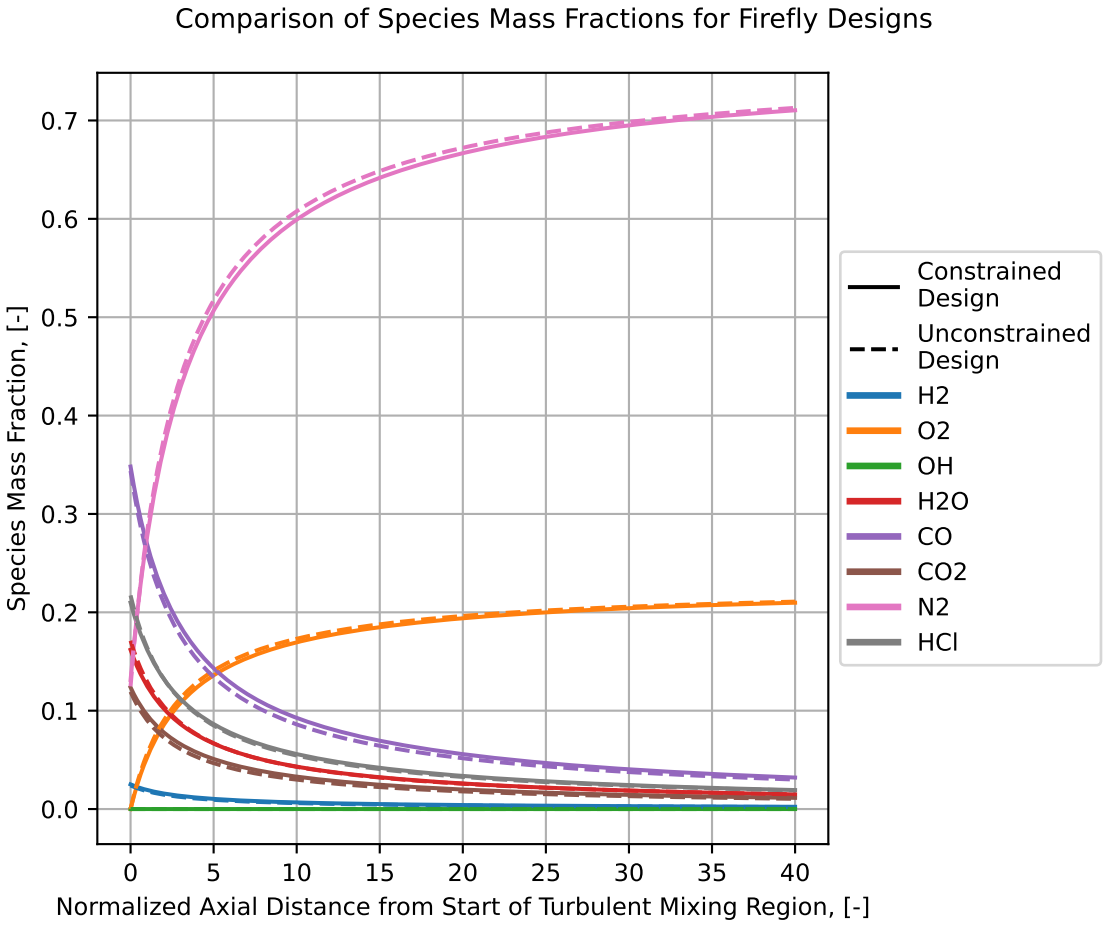

Figure 8-12: The species mass fractions for both plumes are similar. The mass fractions of N_2 and O_2 trend towards their values in the freestream air as more air is entrained into the plumes. The rest of the species trend toward zero mass fraction as their concentration is diluted with entrained air.

8.5 Conclusions for integrated design of small, low-thrust solid rocket motors with plume radiant emission

The developed differentiable model and the experimental data for small, low-thrust solid rocket motor were used to explore unique phenomena and performance tradeoffs relating to solid rocket motor design and the coupled plume radiant emission. These phenomena and design explorations can be used to inform the design of future solid rocket motors where plume radiant emission is important.

Motor and plume size scales have important effects on temperatures and the significance of afterburning in the exhaust plume. Damköhler effects (see section 8.1) can cause the plume to transition from frozen flow – where fuel species in the exhaust remain unburnt – to equilibrium flow – where fuel species react with oxygen as soon as its entrained into the plume – just by increasing the size of a motor. Assuming motors with fixed chamber pressure, expansion ratio, and propellant composition, this transition from frozen flow to equilibrium flow occurs over approximately an order of magnitude of size scales. During this transition, the flow field temperatures increase significantly (peak temperatures in the plume can more than double), which significantly increases the plume radiant emission as well. The size scales where this transition occurs is dependent on the propellant formulation, chamber pressure, and expansion ratio, among other parameters, and the transition size scale might be unrealistically large or small for a particular configuration. However, awareness of the transition is important for designers considering vehicles near it, and it could possibly be exploited to create large changes in radiant intensity with small changes in size.

For sufficiently small motors and plumes, the flow field will exhibit frozen flow, the plume will be optically thin since optical depth scales like $\sim \kappa_\lambda d$ (see subsection 3.2.3), and the plume radiant intensity scales with the volume of emitting gas in the plume: $J_\lambda \sim d^3$ (see subsection 8.1.6). This scaling law enables the relative change in radiant intensity to be evaluated for perturbations in the size scale of a small solid rocket

motor around its design point. Additionally, since vehicle thrust scales as $F \sim d^2$, at small size scales, these scalings imply that radiant intensity is more sensitive to changes in size scale than thrust. This could be exploited to manipulate the plume radiant intensity of a small solid rocket motor, such as vehicles on the size scale of the Firefly aircraft, with only small changes in the vehicle thrust.

For sufficiently small solid rocket motors ($Da \ll 1$ and $\kappa_\lambda d \ll 1$) with fixed burn area, the radiant intensity is relatively insensitive to changes in chamber pressure (see Figure 8-5 and the discussion in subsection 8.2.2). This phenomena arises from the fact that for fixed burn area, the nozzle exit area and subsequently plume size and volume do not change significantly with changes in chamber pressure. Because the radiant intensity is not strongly dependent on chamber pressure, vehicle thrust can be altered by changing the chamber pressure without significantly changing the plume radiant emission. For a given motor, this enables a designer to achieve different thrust requirements by changing the nozzle diameter without significantly affecting the plume emission. Alternatively, if both nozzle throat area and propellant oxamide content are varied, for a given thrust requirement, a designer can achieve a large range of radiant intensities (see the design chart in Figure 8-7).

For motors operating near $Da = 1$, the plume radiant intensity is very sensitive to motor chamber pressure (see subsection 8.2.1) and size scale (see subsection 8.1.6). Small, end-burning motors are already vulnerable to perturbations in chamber pressure due to nozzle clogging or defects in the propellant grain [4]. For steady and repeatable radiant intensity for small, end-burning solid rocket motors, it is best to operate the motor away from the $Da = 1$ size scales and pressures, where the radiant intensity is less sensitive chamber pressure. This does not seem to be an issue for the Firefly aircraft concept, where the flow appears to have $Da \ll 1$ and frozen chemistry for all points in the feasible design space (see the discussion in subsection 8.2.1).

Chapter 9

Conclusion

For applications where vehicle visibility is a concern, exhaust plume radiant emission is an important aspect of solid rocket powered vehicle performance. However, plume radiant emission is often not considered during the design phase for solid rocket powered vehicles. Typical modeling approaches are computationally expensive, and rely on CFD and complicated integration schemes that are not well-suited for fast, iterative vehicle design. The previously available experimental data for exhaust plume radiant emission did not include measurements for small, low-thrust motors, such as those used in the Firefly aircraft introduced in subsection 1.2.2. This thesis developed tools to address these gaps and enable the practical consideration of exhaust plume radiant emission in the design phase. The specific contributions of this thesis are discussed below.

Measurement of exhaust plume radiant emission for small, low thrust motors Exhaust plume radiant emission was measured for small, low-thrust, end-burning solid rocket motors (chapter 5). Static fires utilized motors that were doped with either 0 or 8 % oxamide operated at chamber pressures of approximately 1.1 MPa or 2.2 MPa. The effects of chamber pressure and oxamide content on radiant intensity were measured, with measured peak radiant intensities as low as $0.270\,\mathrm{W\,sr^{-1}\,\mu m^{-1}}$. The peak intensities for all the static fires coincided with the 4.3 µm CO_2 emission band, and the inclusion of oxamide in the propellant did not create any new measur-

able peaks in the spectrum that would not have already been present for a typical composite propellant. To the author's knowledge, the measurements collected in this work represent the lowest thrust levels for which rigorous plume radiant intensity measurements have been obtained and the only plume radiant intensity measurements for propellants containing oxamide in the open literature.

Models and methods for designing and building small, fast aircraft A model describing the minimum burn pressure for oxamide-doped propellants originally proposed by Vernacchia et al. was updated with a new data point for a 8 % oxamide propellant burned at standard pressure. The feasibility of a low thermal conductivity alumina silicate material for novel use as a nozzle for a small, low-thrust, long-endurance motor was demonstrated. The nozzle was demonstrated in eight static fires, and showed no measurable nozzle erosion and good thermal insulating performance. The nozzles did crack due to thermal shock in the static fires, however the tapered design caused the cracks to seal under the pressure load, and there was no observed loss in chamber pressure. This combination of material and design constitute a feasible option for nozzles for small, long-endurance solid rocket motors that are easier to manufacture than a previous design discussed in Ref. [4].

Modeling of exhaust plume radiant emission for solid rocket motors Six inter-connected disciplines for modeling exhaust plume radiant emission were identified, and differentiable models were implemented for each (see section 6.1): chamber thermodynamic equilibrium, motor internal ballistics, isentropic nozzle flow, plume flow field, afterburning kinetics, and radiative transfer. A simple, differentiable, reduced-order global reaction rate model was developed, as well as a procedure for fitting this global rate equation to a detailed kinetics scheme (see subsection 6.3.5). The fitted global model shows good agreement for the reaction rates of oxygen in the plume across a range of temperatures, ambient pressures, and exhaust-to-air ratios. This reduced-order model is significantly less stiff than typical detailed kinetics mechanisms, and is much more suitable for optimization with AeroSandbox and

IPOPT (see subsection 6.2.2). Additionally, interpolated C^1-continuous surrogate models for molecular emittance parameters were also developed, which enables the implementation of the radiative transfer model (see subsubsection 6.3.6.5).

Integrated design of solid rocket motors including exhaust plume radiant emission The six sub-models were implemented as a combined model in the AeroSandbox optimization framework. The combined radiant intensity model couples solid rocket motor design parameters with exhaust plume radiant emission, shows reasonable agreement with a number of motors, and is robust over eight orders of magnitude of radiant intensity (see chapter 7). The model enables exhaust plume radiant emission to be optimized with respect to motor design variables and coupled with all of the aircraft design tools available in AeroSandbox. Its utility was demonstrated in an optimization case study of the Firefly vehicle.

The importance of motor and plume size scale in afterburning kinetics and radiant emission was identified. Damköhler effects (see section 8.1) can cause the plume to transition from frozen flow to equilibrium flow just by increasing the size scale of a motor. This has important implications for small solid rocket motors at low altitudes, which can display frozen flow with all fuel species in the exhaust remaining unburnt despite relatively high ambient pressures. For sufficiently small solid rocket motors, such as motors on the size scale used for the Firefly vehicle, the radiant intensity scales like the volume of emitting gas: $J_\lambda \sim d^3$ (see subsection 8.1.6). This scaling law enables the relative change in radiant intensity to be evaluated for perturbations in the size scale of a small solid rocket motor around its design point.

The coupling between oxamide content, chamber pressure, specific impulse, and radiant intensity for small, end-burning solid rocket motors – such as the Firefly motor – was characterized, and several design principles for small, end-burning solid rocket motors were identified. For sufficiently small solid rocket motors with fixed burn area, such as the Firefly motor, the radiant intensity is relatively insensitive to changes in chamber pressure (see section 8.2). This phenomena enables vehicle thrust to be altered for an end-burning motor by changing the chamber pressure

(by varying the nozzle throat area) without significantly changing the plume radiant emission. Alternatively, if both nozzle throat area and propellant oxamide content are varied, a designer can achieve a large range of radiant intensities for a given thrust requirement. Understanding these relationship between free design variables (oxamide content and chamber pressure) and radiant intensity is important for designing vehicles with constraints on the radiant emission. The developed radiant intensity model can be used create design charts for exploring design and performance tradeoffs for solid rocket powered vehicles (see section 8.3), or can be used to optimize a solid rocket motor with constraints on the plume radiant intensity directly (see section 8.4).

The new experimental data, practical modeling tools, and design guidelines developed in this thesis support the design phase consideration of exhaust plume radiant emission in solid rocket motor design. For vehicles where vehicle visibility important, considering exhaust plume radiant emission during vehicle design enables a better understanding of motor design and performance tradeoffs and supports improved motor performance.

Appendix A

Manufacturing of Propellant Insulator and Aft Insulator

This appendix details some of the manufacturing methods for the propellant insulator and aft insulator discussed in section 5.2.

A.1 Propellant insulator

The propellant insulator was cut from a Garolite XX paper-phenolic composite tube. The outer diameter of the tube was turned down by a few thousandths of an inch to ensure a close slip fit with the motor case. A custom insulator holder tool was machined to mount the propellant insulator on the lathe, as shown in Figure A-1.

To ensure a good bond between the propellant (which is cast directly into the propellant insulator) and the propellant insulator, a primer was developed that can be applied to the inner surface of the insulator. The primer was developed to be chemically similar to the binder of the propellant, but with a significant excess of curative to promote cross-linking between the propellant and the primer. The primer is therefore made from many of the same components as the propellant itself (the propellant formula is given in subsection 5.3.1).

The developed primer maintains the same ratio of (binder + curative) to plasticizer as the propellant formula given in subsection 5.3.1. The binder to curative ratio is

Figure A-1: A tool was made for mounting the liner pieces to a lathe for turning down the outer diameter.

chosen so that the primer has a cure index ratio[†] of 2, assuming a binder OH equivalent weight[§] of 1219.5 g eq^{-1} and a curative NCO equivalent weight of 185 g eq^{-1}. The cure index of 2 should ensure that there are plenty of excess NCO groups in the primer to bond with available OH groups in the propellant during casting. The primer formula is given in Table A.1.

All components were mixed together by hand. The oxamide was ground and sifted before being mixed with the other components. After all ingredients were thoroughly mixed, the mixture was degassed in a vacuum chamber. The inside of the propellant insulator was sanded using a flap wheel mounted to a drill and cleaned with acetone before applying the primer. The primer was applied in a thin layer with a small paint brush. A picture of an unprimed insulator and a primed insulator is shown in Figure A-2.

[†]The curing reaction for these polymers takes place between available hydroxyl groups in the binder and available isocyanate groups in the curative, and is known as the urethane reaction: R − OH + NCO − R'. The cure index ratio is the ratio between moles of NCO from the curative and moles of OH from the binder. Therefore a cure index ratio of 2 means there are twice as many moles of available NCO compared to available OH.

[§]Equivalent weight is the grams of an ingredient per mole of reactive group. It is typically written with the units of "grams per equivalent".

Ingredient	Chemical name	Manufacturer	Mass fraction
Binder	Hydroxyl Terminated Polybutadiene (HTPB) Resin with HX-752 and CAO-5	RCS Rocket Motor Components	0.51
Plasticizer	Isodecyl Pelargonate (IDP)	RCS Rocket Motor Components	0.24
Opacifier	Graphite powder	Cretacolor	0.02
Coolant	Oxamide	Sigma Aldrich	0.08
Curative	Modified MDI Isocyanate	RCS Rocket Motor Components	0.15

Table A.1: Insulator primer formulation.

Figure A-2: A primer is applied to the inner surface of the propellant insulator to promote good bonding between the insulator and the propellant. Left subfigure: unprimed insulator. Right subfigure: primed insulator.

A.2 Aft insulator

The aft insulator was machined from Garolite CE linen-phenolic composite rod. Garolite XX grade rod was used for some of the early attempts at manufacturing the aft insulator, but it cracked frequently during machining.

The internal and external geometries of the aft insulator were turned separately using programmed tool paths on a 2-axis CNC lathe. An aft insulator holder tool was made to mount the aft insulator to the lathe to machine the outer geometry. A partially machined aft insulator mounted to a lathe with this tool is shown in Figure A-3.

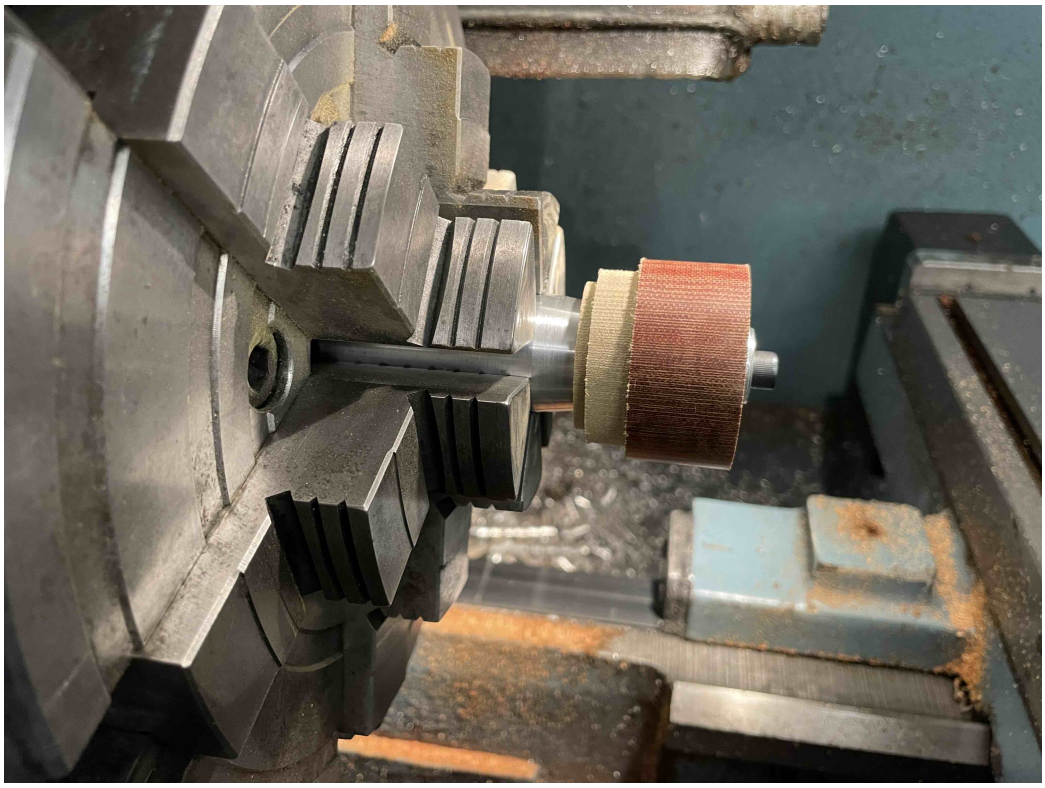

Figure A-3: A custom tool was developed for mounting the aft insulator to the lathe for machining the external geometry.

The aft insulator also has three drilled holes (one for a clocking pin, shown in Figure 5-2; one for a through-hole to the pressure transducer, shown in Figure 5-2; one for a through-hole to the rupture disc, not shown) which had to be machined separately. A custom drill jig was designed and 3D printed to ensure the holes could

be drilled simply and accurately, and is shown in Figure A-4. The revolved geometry of the aft insulator made it difficult to secure in a vice for drilling, and so the jig was designed to completely enclose the aft insulator and provide flat surfaces that could be secured in a vice. The jig had drill bushings pressed into it to enable easy alignment of drill bits for drilling.

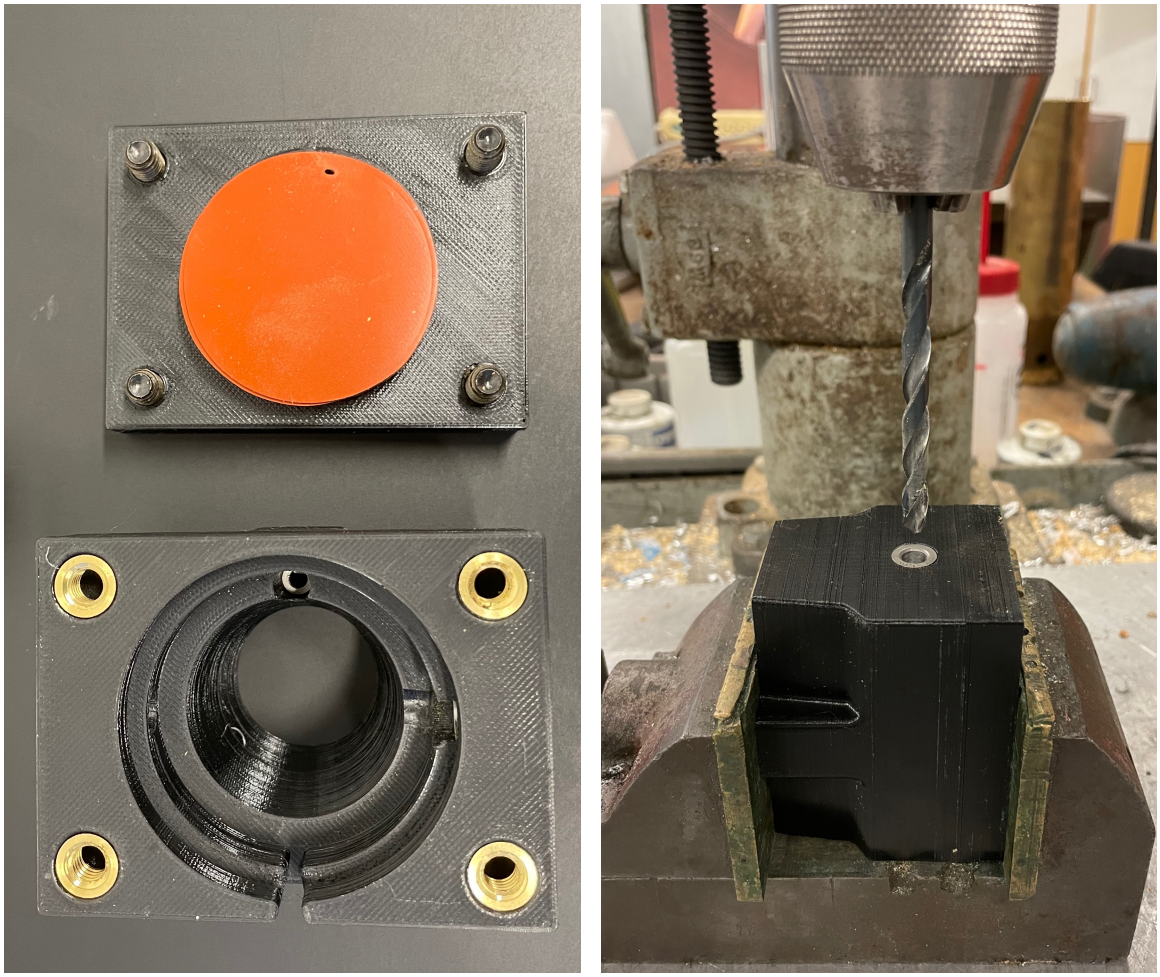

Figure A-4: A 3D printed drill jig with press fit bushings was made to ensure the holes in the aft insulator could be drilled simply and accurately.

Appendix B

Two-Piece Ceramic Nozzle with 3D Printed Cellular Ceramic Insulator

A two-piece nozzle configuration with a 3D-printed cellular ceramic nozzle insulator was previously proposed for use in low-thrust, long-endurance solid rocket motors for Firefly-like aircraft in Ref. [4]. The two-piece nozzle configuration, illustrated generally in Figure B-1, used a nozzle insulator and contoured nozzle insert which were manufactured separately, and then bonded together with a silica adhesive. The contoured nozzle insert was turned from boron nitride rod. The insulator, shown in Figure B-2, was printed on a Formlabs Form 2 printer using the Formlabs Ceramic resin (a silica particle-filled photopolymer). After printing, the insulator was fired in a kiln to burn out the cured photopolymer resin and sinter together the silica particles. The cells of the insulator were hand-packed with silica fibers to reduce radiative heat transfer through the cells. The nozzles were manufactured and tested successfully in small, long-endurance test motors. However, there were some manufacturing and performance drawbacks for this nozzle design.

Boron nitride is a relatively soft material, and consequently the tested nozzles using the boron nitride inserts showed nozzle erosion, which decreased the expansion ratio and specific impulse of the motor. For two motor tests using this nozzle (Static Fires D and E in Ref. [4]), the nozzle throat diameters increased by 4.6 % and 8.5 % by the end of the motor burn.

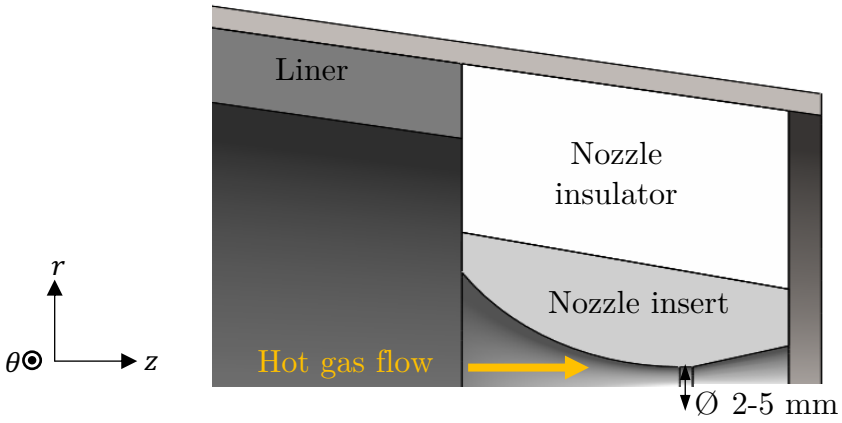

Figure B-1: The two-piece nozzle configuration uses a separate nozzle insulator and nozzle insert which must be bonded together.

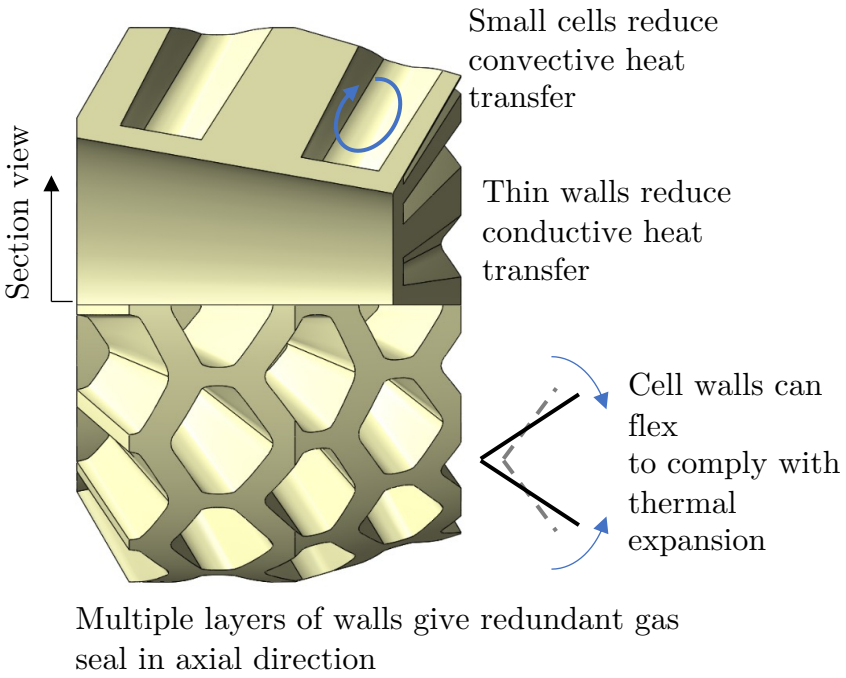

Figure B-2: A 3D printed fused silica insulator was used with the two-piece nozzle configuration. Reprinted from Ref. [4].

The manufacturing process for the 3D-printed cellular ceramic insulation was unreliable and time-consuming. The thin cell walls were printed near the minimum resolution of the printer, which led to inconsistent wall thicknesses. The silica filled polymer used for the printing process was especially viscous, and often led to failed prints where the insulator broke off from its supports mid-print. The insulators had inconsistent material shrinkage during the kiln firing process, which varied between

14 % to 20 % in the $r\theta$ directions and 15 % to 22 % in the z direction for 29 different nozzle insulator iterations. The process of packing the insulator cells with alumina fibers was time-consuming and relied on human dexterity. Additionally, the use of a two-piece configuration inherently required an additional machining step and a bonding step than would be required by a configuration where the nozzle insulator and insert was a single piece.

Appendix C

Single Line Group Parameter Surrogate Models

As discussed in subsubsection 6.3.6.5, C^1-continuous surrogate models for the single line group model molecular emission parameters $\bar{\kappa}_{\lambda i0}$ and $1/d_{\lambda i}$ (or equivalently with respect to wavenumber η, $\bar{\kappa}_{\eta i0}$ and $1/d_{\eta i}$) were developed by fitting the tabulated data provided by Ludwig et al. in Ref. [27]. As noted in subsubsection 6.3.6.5, C^1-continuity is only needed with respect to temperature, and not with respect to wavelength (or equivalently wavenumber). Differentiable, cubic splines were fit to the logarithm of the data using the `UnstructuredInterpolatedModel()` class described in subsection 6.2.3.

Models were developed for CO, CO_2, H_2O, and HCl, which represent the major molecular species present in the combustion products for ammonium perchlorate composite propellants. The outputs of the fitted surrogate models for $\bar{\kappa}_{\lambda i0}$ and $1/d_{\lambda i}$ for these species are plotted with the data from Ref. [27] in Figures C-1 to C-4 below. The fitted models show excellent agreement with the fitted data where it is available. For wavenumbers where data was not provided, the species do not produce any significant emission, and the surrogate model outputs sufficiently small values for absorption coefficient to reflect this.

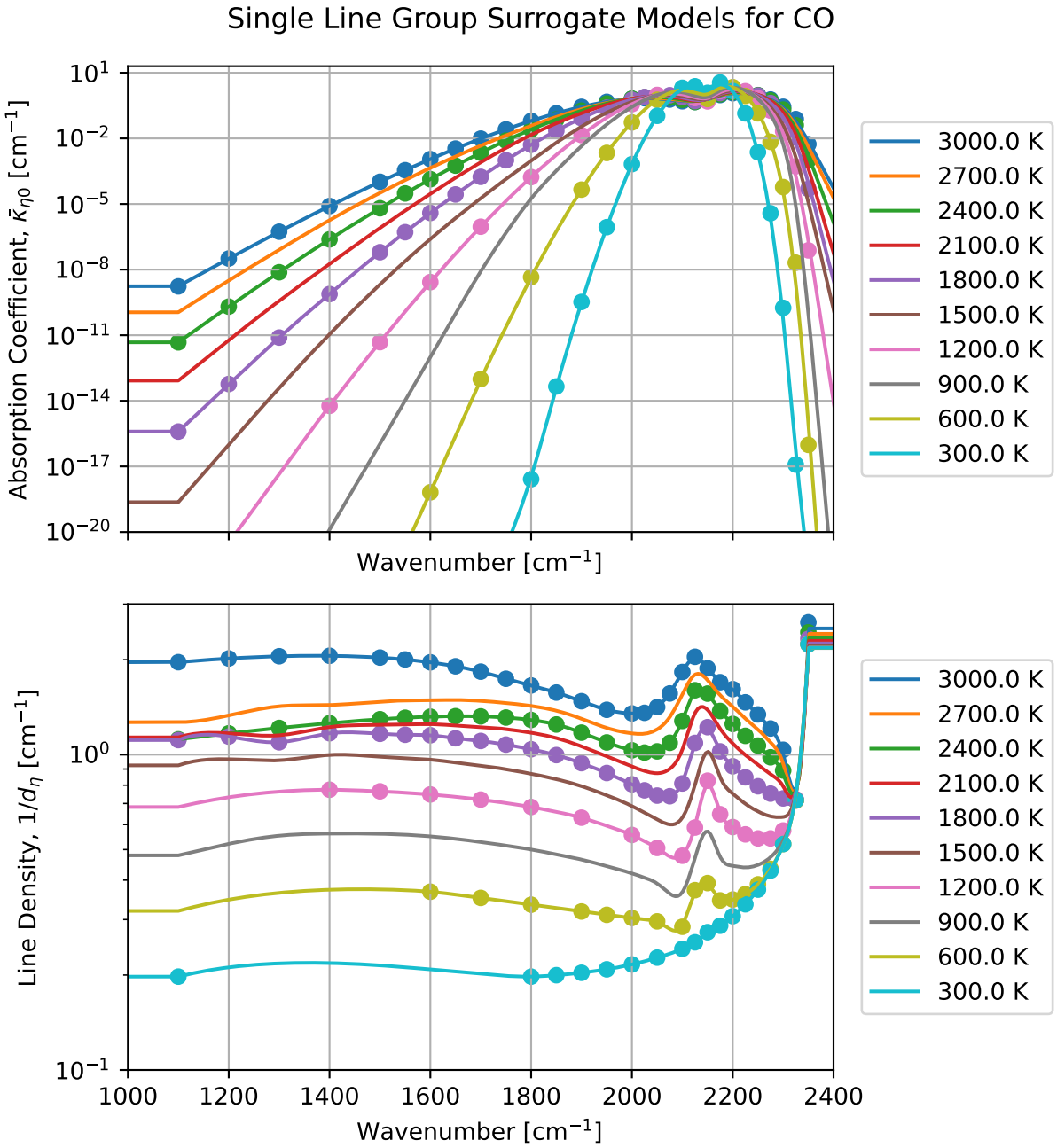

Figure C-1: Surrogate models for the mean absorption coefficient at standard temperature and pressure $\bar{\kappa}_{\lambda 0}$ and the average line density $1/d_{\lambda}$ for CO. For these figures, points plotted with circles are data points given in the data tables in Ref. [27]. The curves are the output of the surrogate model for the chosen wavelengths and temperatures.

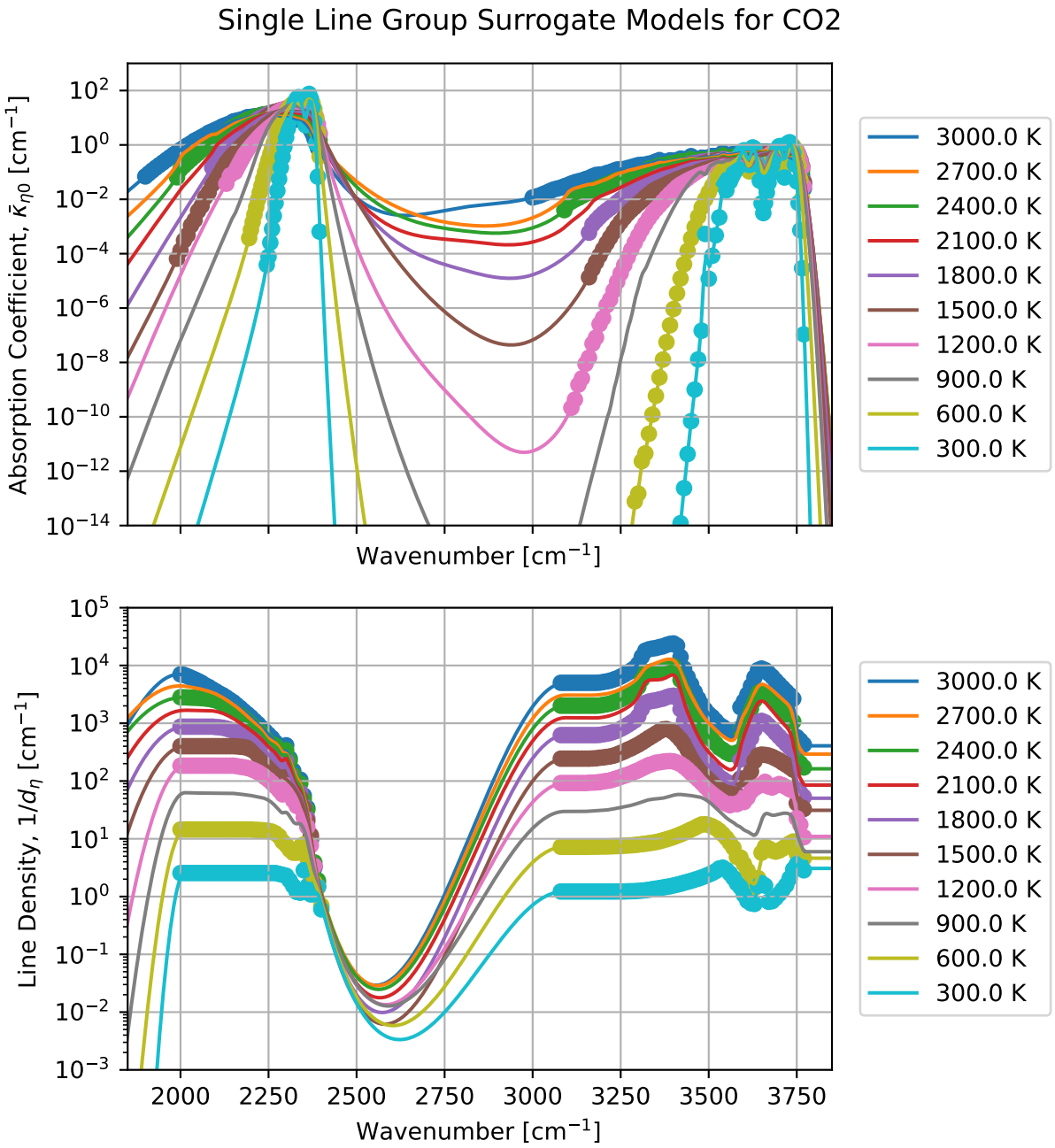

Figure C-2: Surrogate models for the mean absorption coefficient at standard temperature and pressure $\bar{\kappa}_{\lambda 0}$ and the average line density $1/d_\lambda$ for CO_2. For these figures, points plotted with circles are data points given in the data tables in Ref. [27]. The curves are the output of the surrogate model for the chosen wavelengths and temperatures.

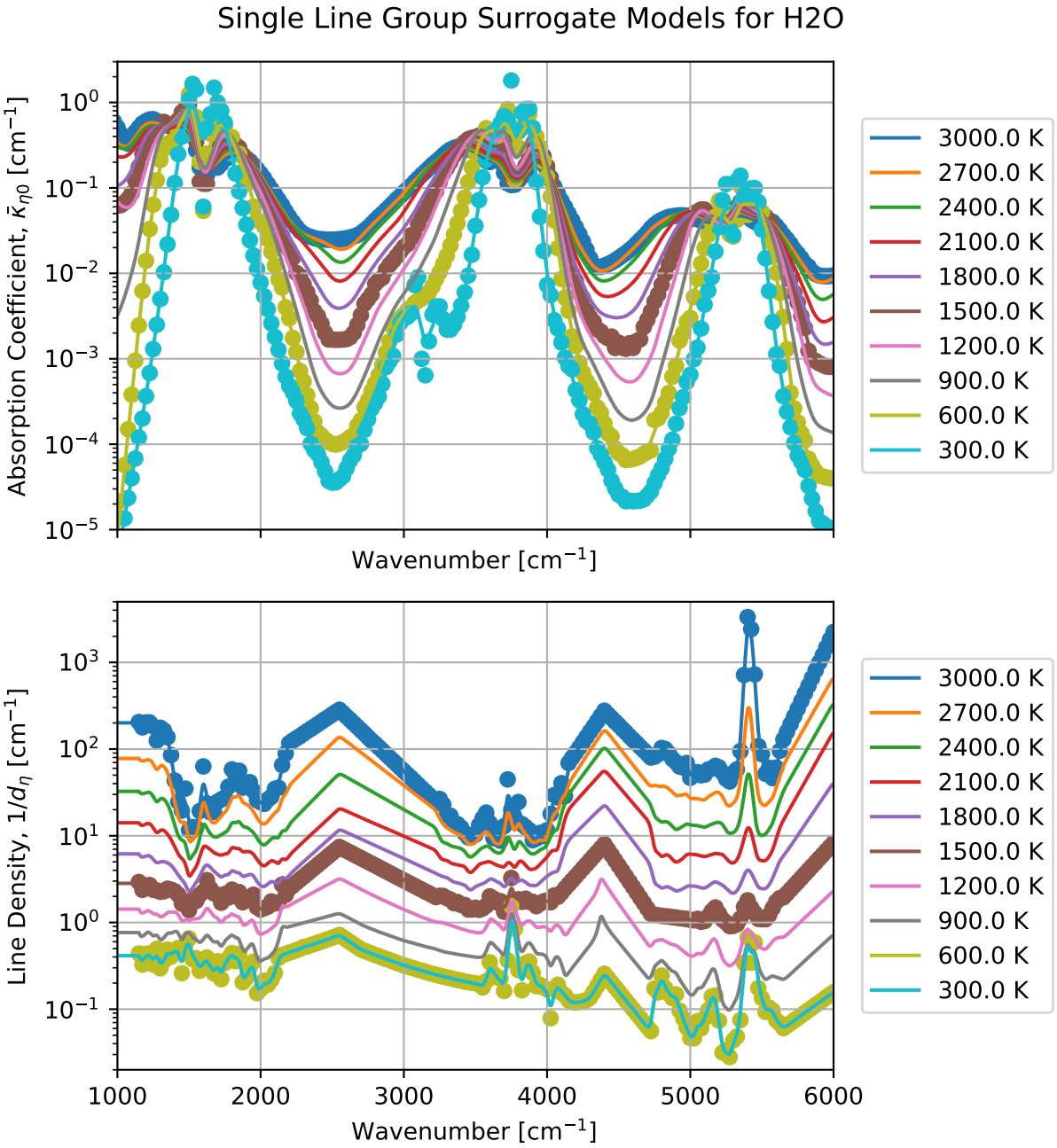

Figure C-3: Surrogate models for the mean absorption coefficient at standard temperature and pressure $\bar{\kappa}_{\lambda 0}$ and the average line density $1/d_{\lambda}$ for H_2O. For these figures, points plotted with circles are data points given in the data tables in Ref. [27]. The curves are the output of the surrogate model for the chosen wavelengths and temperatures.

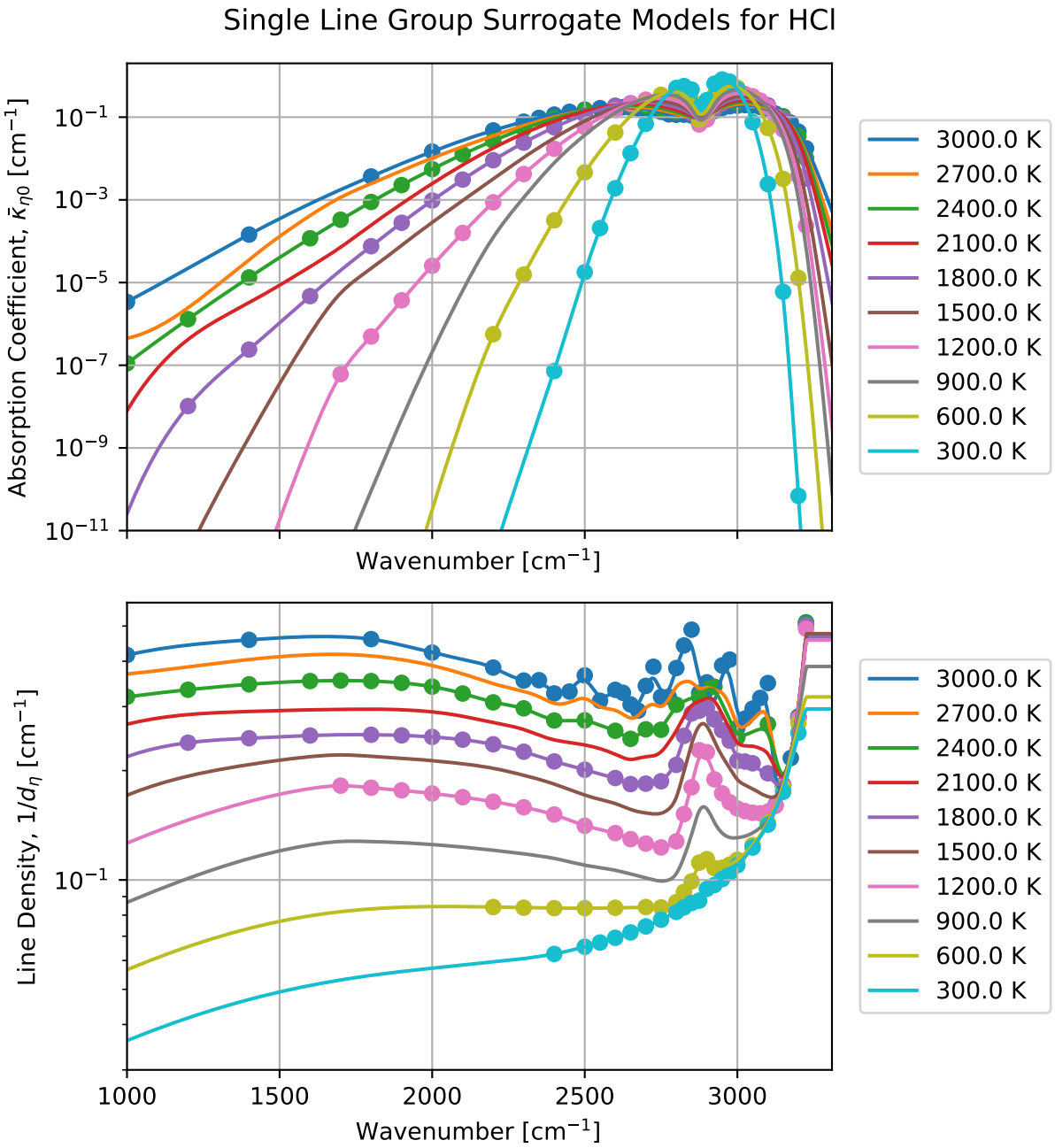

Figure C-4: Surrogate models for the mean absorption coefficient at standard temperature and pressure $\bar{\kappa}_{\lambda 0}$ and the average line density $1/d_\lambda$ for HCl. For these figures, points plotted with circles are data points given in the data tables in Ref. [27]. The curves are the output of the surrogate model for the chosen wavelengths and temperatures.

Appendix D

Validation of Developed Sub-models

This appendix contains more in-depth test cases for validation of the developed chamber thermodynamic equilibrium sub-model discussed in subsection 6.3.1 and the plume flow field sub-model discussed in subsection 6.3.4. Validation of the sub-models is discussed more generally in section 7.1.

D.1 Chamber thermodynamic equilibrium

The outputs of the developed chamber thermodynamic equilibrium model are compared to the outputs of the Rocket Propulsion Analysis (RPA) software [19]. For each test case, the chamber pressure and propellant formulation were pre-selected. The resulting chamber temperature and species mole fractions are then compared. Several test cases are given below in Tables D.1, D.2, and D.3. The chamber thermodynamic equilibrium model shows excellent agreement with the outputs from RPA.

Parameter	**Developed sub-model**	**RPA**	**Relative error [-]**
Propellant formula	baseline		
Pressure [MPa]	1		
Temperature [K]	2180.20	2180.31	5×10^{-5}
w_{CO} [-]	0.250 63	0.250 62	4×10^{-5}
w_{CO_2} [-]	0.055 49	0.055 49	$< 1 \times 10^{-5}$
w_{H_2} [-]	0.216 88	0.216 87	5×10^{-5}
w_{H_2O} [-]	0.250 27	0.250 27	$< 1 \times 10^{-5}$
w_{HCl} [-]	0.149 45	0.149 45	$< 1 \times 10^{-5}$
w_{N_2} [-]	0.076 04	0.076 03	1×10^{-4}

Table D.1: Test case for validating developed chamber thermodynamic equilibrium model using the baseline propellant formulation at a chamber pressure of 1 MPa.

Parameter	**Developed sub-model**	**RPA**	**Relative error [-]**
Propellant formula	baseline		
Pressure [MPa]	5		
Temperature [K]	2183.96	2184.08	5×10^{-5}
w_{CO} [-]	0.250 79	0.250 79	$< 1 \times 10^{-5}$
w_{CO_2} [-]	0.055 43	0.055 43	$< 1 \times 10^{-5}$
w_{H_2} [-]	0.216 94	0.216 91	1×10^{-4}
w_{H_2O} [-]	0.250 50	0.250 51	4×10^{-5}
w_{HCl} [-]	0.149 70	0.149 71	7×10^{-5}
w_{N_2} [-]	0.076 06	0.076 05	1×10^{-4}

Table D.2: Test case for validating developed chamber thermodynamic equilibrium model using the baseline propellant formulation at a chamber pressure of 5 MPa.

Parameter	**Developed sub-model**	**RPA**	**Relative error [-]**
Propellant formula	baseline w/ 8 % oxamide		
Pressure [MPa]	2		
Temperature [K]	1904.04	1904.16	6×10^{-5}
w_{CO} [-]	0.259 40	0.259 40	$< 1 \times 10^{-5}$
$w_{\mathrm{CO_2}}$ [-]	0.056 07	0.056 07	$< 1 \times 10^{-5}$
$w_{\mathrm{H_2}}$ [-]	0.241 01	0.240 99	8×10^{-5}
$w_{\mathrm{H_2O}}$ [-]	0.219 98	0.219 98	$< 1 \times 10^{-5}$
w_{HCl} [-]	0.135 17	0.135 18	7×10^{-5}
$w_{\mathrm{N_2}}$ [-]	0.088 23	0.088 22	1×10^{-4}

Table D.3: Test case for validating developed chamber thermodynamic equilibrium model using the baseline with 8 % oxamide propellant formulation at a chamber pressure of 2 MPa.

D.2 Flow field

Several methods are used to validate the flow field model. Woodroffe, who originally proposed the 1D plume flow field model used in this thesis, also derived a set of explicit equations to model the temperature, velocity, and diameter at every station throughout the plume [55]. This explicit model assumes either frozen or equilibrium chemistry in the plume, neglects changes to molecular weight in the plume due to afterburning and mixing with entrained air, and assumes the molecular weight of gas inside and outside of the plume are the same. The outputs of the explicit model can be compared to the outputs of the developed model for this thesis to validate the implementation. A comparison of the two models is shown in Figure D-1. Because the Woodroffe model assumes the molecular weight is fixed at the value at the start of the turbulent mixing region, the molecular weight throughout the plume is under-predicted, since the entrainment of air would increase the molecular weight in the plume. Because the molecular weight is under-predicted by the Woodroffe model, the density is then under-predicted as well, which explains why the Woodroffe model shows a lower density than the output from the developed plume flow field sub-model which includes changes to molecular weight.

For an additional test, the developed flow field model was modified to neglect changes to molecular weight throughout the plume. These new model outputs are compared to the explicit Woodroffe model below in Figure D-2. There is a slight deviation between the temperature and density predictions, but the agreement is excellent overall. This validates the implementation of the flow field sub-model for the frozen flow case.

The temperature flow field results are analyzed further to evaluate model behavior for non-frozen flow. Assuming identical nozzle exit and free stream conditions, the temperature of the plume at every station should be bounded on the lower side by the temperature if the plume exhibited frozen flow, and on the upper side by the temperature if the plume exhibited equilibrium flow. At the frozen flow boundary, the plume temperature is the result of simple mixing of the motor exhaust with

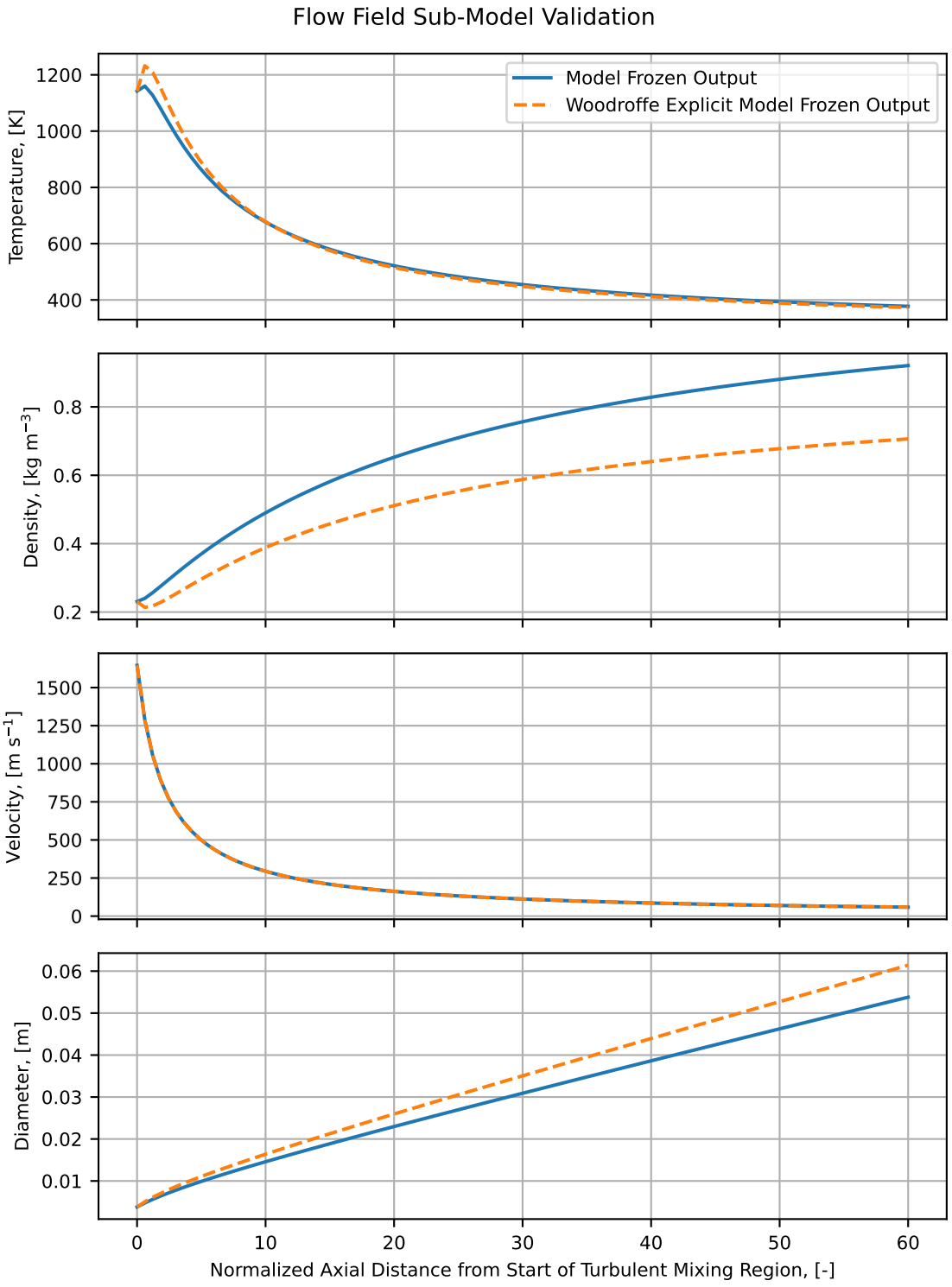

Figure D-1: The outputs of the developed flow field model can be compared to the explicit model developed by Woodroffe [55], assuming frozen flow and known parameters at the start of the turbulent mixing region. The agreement between the two models is generally good, although the Woodroffe model neglects changes in molecular weight as air from the free stream is entrained, which accounts for most of the difference between the two models.

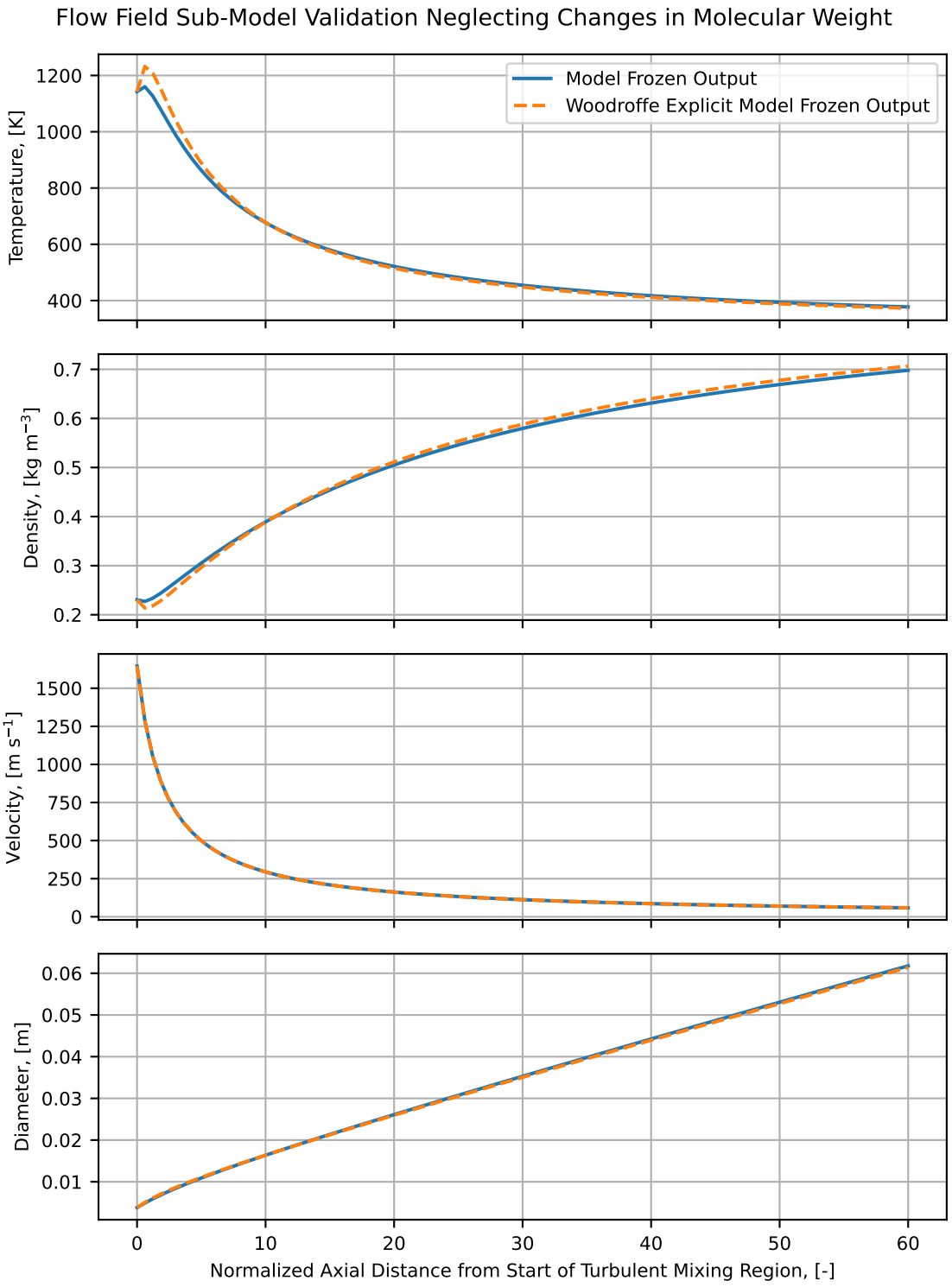

Figure D-2: The outputs of the developed flow field model are compared again to the explicit Woodroofe model, except the terms in the developed model accounting for changes in molecular weight are neglected. The agreement between the two models is now very close, which validates the implementation of the developed model for the frozen flow case.

colder ambient air as it is entrained, as well as a small amount of thermal "recovery" as the plume slows down and some kinetic energy is converted to thermal energy. At the equilibrium boundary, the plume temperature is the result of mixing due to entrainment, thermal recovery, and a conversion of species formation enthalpy (stored chemical energy) into sensible enthalpy (energy that changes the temperature). For equilibrium flow, the species production rate is still limited by the rate of oxygen entrainment into the plume.

The developed flow field model should converge onto the frozen and equilibrium flow temperature bounds for the appropriate reaction and species production rates. To verify this behavior, the plume temperature versus downstream distance in the plume is modeled for a sweep of different reaction rates. This is achieved by including (for demonstration purposes only) a reaction rate multiplier ϕ_{reac} in the species flow equation (repeated here from Equation 6.20):

$$\frac{d}{dx}\left(\rho d^2 u y_i\right) = y_{i\infty}\frac{d}{dx}\left(\rho d^2 u\right) + \phi_{reac}\dot{\omega}_i d^2 \tag{D.1}$$

The reaction rate multiplier ϕ_{reac} is swept through a range of values spanning several orders of magnitude. For sufficiently small values of ϕ_{reac}, the plume temperature should converge onto the frozen flow solution and not go lower even if ϕ_{reac} is reduced further; conversely, for sufficiently large values of ϕ_{reac}, the plume temperature should converge onto the equilibrium flow solution and not go higher even if ϕ_{reac} is increased further.

Theoretical curves for plume temperature versus distance from the start of the turbulent mixing region are calculated using the velocity and mass flow rate results from the flow field sub-model and the Cantera python package [21]. Following Woodroffe's analysis in Ref. [55], velocity and mass flow rate are not dependent on the plume temperature, species mass fractions, or mean molecular weight (and therefore do not change whether afterburning reactions are happening or not). This is evidenced by the velocity curves in Figures D-1 and D-2 – the velocity curves match exactly with the explicit model in both figures, and the values do not change (even though the

temperature, density, and diameter are affected) even when the parameters handling molecular weight are adjusted between the two plots. Therefore solved values for mass flow rate and velocity can be used in the Cantera calculations, as they are not dependent on the presence of afterburning.

For the Cantera calculations, at every station throughout the plume, the quantity and temperature of exhaust gas that actually exited the nozzle and the quantity and temperature of free stream air that would have been entrained into the plume up to that point are modeled as a combined mixture. The mass quantities are determined from the solved mass flow rate from the flow field sub-model. The temperature of the exhaust gas is taken as temperature T_0 at the start of the turbulent mixing region, and the temperature of the entrained air is taken as the temperature of the ambient air. The thermal recovery energy gained by the stagnation of the plume up to that station, calculated from the difference in velocities, is included as an extra enthalpy term in the mixture. The temperature of this unreacted mixture is the theoretical lower bound frozen flow temperature at that station in the plume. Then, this mixture can be equilibrated, and the resulting temperature of this reacted mixture is the theoretical upper bound equilibrium temperature at that station.

A plot showing the theoretical lower frozen and upper equilibrium temperature bounds calculated with Cantera, as well as the output of the flow field sub-model for a sweep of reaction rate multipliers is shown in Figure D-3. The flow field sub-model converges almost exactly onto the frozen flow lower bound predicted with Cantera. As the reaction rate multiplier is increased, the flow field temperatures increase as formation enthalpy is converted to sensible enthalpy. The flow field model results generally converge onto the equilibrium flow upper bound predicted with Cantera. At normalized downstream distances >10, the agreement between the Cantera equilibrium curve and the model outputs with large multiplier values is excellent.

Near the peak exhaust plume temperatures, however, the flow field model does over-predict slightly compared to the Cantera equilibrium curve. This over prediction is a result of the assumptions made in the developed global reaction mechanism (introduced in subsubsection 6.3.5.1). The global reaction mechanism does not enforce

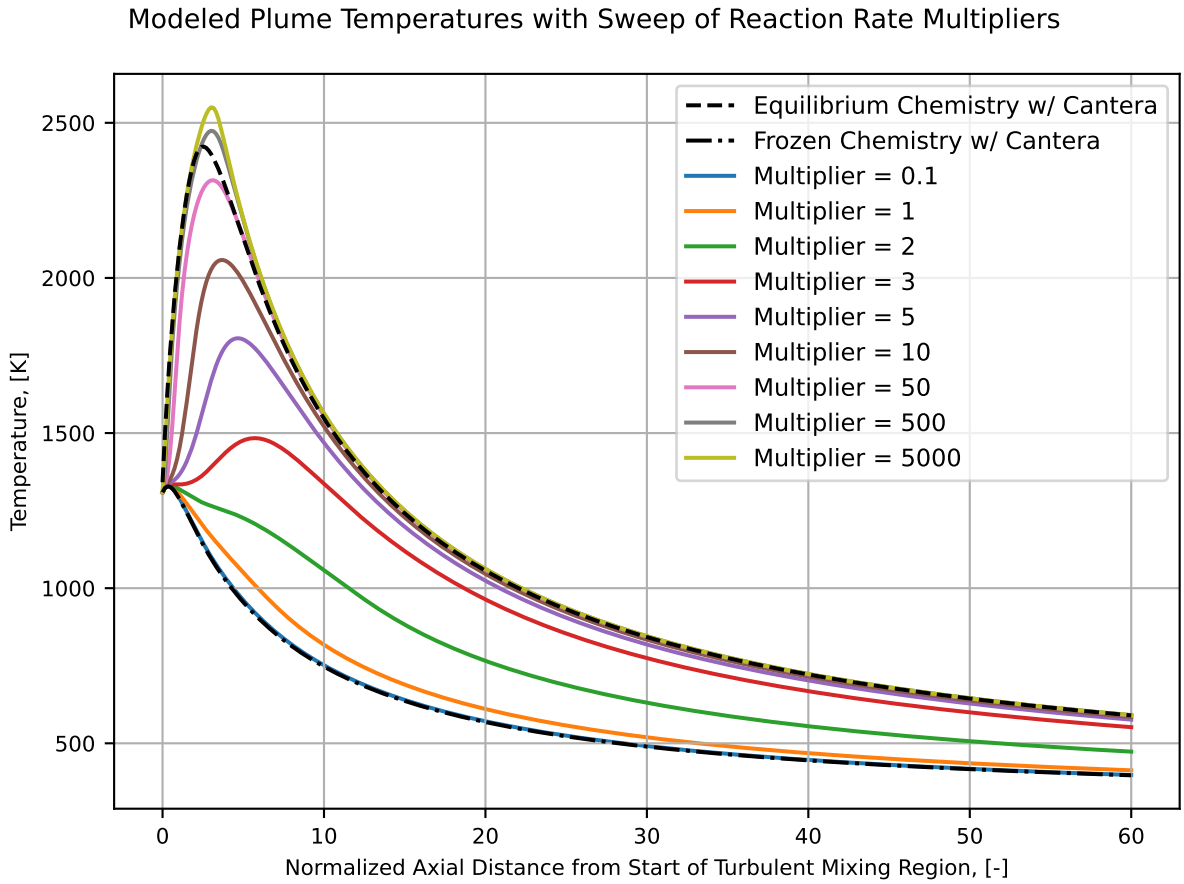

Figure D-3: The plume flow field sub-model temperature output should be bounded on the lower side by frozen flow and on the upper side by equilibrium flow. The sub-model converges almost exactly onto the the frozen flow lower bound for small reaction rate multipliers. For large reaction rate multipliers, the sub-model overshoots slightly near the peak temperatures for the equilibrium flow upper bound. This is due to slightly unrealistic reactions predicted by the developed global reaction mechanism.

the equilibrium condition of minimizing Gibb's free energy, and assumes forward only reactions with the same reaction rate (relative to the initial mole fractions) for all species. This mechanism models some reactions as occurring that, if modeled with a more rigorous reaction mechanism scheme, would not be favored. This ultimately leads to a disparity in the modeled quantities of formation and sensible enthalpies in the plume for the flow field sub-model and the Cantera calculations, even though the sum of the two enthalpies (the static enthalpy) are identical for both methods.

This disparity between the calculated Cantera equilibrium temperature and the flow field sub-model output with the multiplier $\phi_{reac} = 5000$ is shown in Figure D-4. In

the figure, the static enthalpy curves are identical for both Cantera and the sub-model (they are directly on top of each other in the figure, so the blue static enthalpy curve for Cantera is not actually visible). However, for normalized downstream distances from ∼3 to 6, the formation enthalpy calculated with the flow field sub-model is under-predicted relative to the Cantera output, and the sensible enthalpy for the flow field sub-model is over-predicted relative to the Cantera output. This explains why the flow field sub-model over-predicts the temperature compared to the Cantera equilibrium temperature prediction shown in Figure D-3.

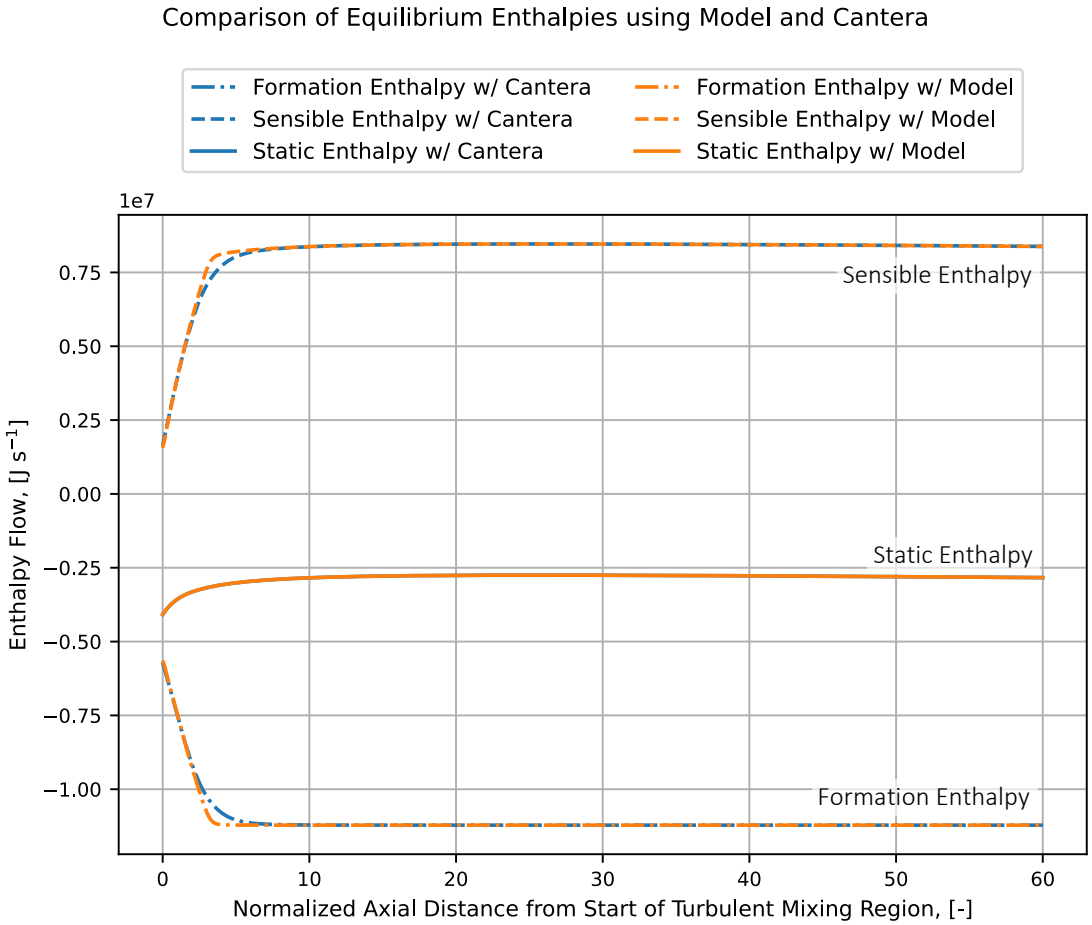

Figure D-4: The developed flow field model and global reaction rate mechanism under-predict the formation enthalpy and over-predict the sensible enthalpy relative to calculations completed with Cantera, even though the static enthalpy (the sum of the formation and sensible enthalpies) is the same.

Appendix E

Scaling Law for Small Solid Rocket Motors with Fixed Burn Area

A simple exhaust plume radiant intensity scaling law is desirable for gaining an intuitive understanding of how key design parameters influence radiant intensity. As discussed in subsection 2.1.1, for small, low-thrust aircraft using an end-burning motor configuration, propellant burn area is fixed, while the motor propellant composition and throat diameter (which sets the chamber pressure) are free variables. This scaling law attempts to capture the key physics relating chamber pressure and propellant oxamide content to exhaust plume radiant intensity for small, end-burning motors. The derived scaling law is:

$$J_\lambda \sim I_{b\lambda}(T_e(p_c, w_{om}))\ \frac{p_a}{T_e(p_c, w_{om})}\ \left[\frac{A_e}{A_t}(p_c)\ \frac{A_t}{A_b}(p_c, w_{om})\right]^{3/2} \equiv S \qquad \text{(E.1)}$$

This scaling law assumes that the propellant burn area A_b is fixed, nozzles have matched expansion and motors are operated at a fixed altitude such that $p_e = p_a = const.$, and motors are small enough such that the plumes are optically thin and the exhaust flow has frozen chemistry. The derivation of the scaling law given in Equation E.1 is given below in section E.1.

E.1 Derivation

As introduced in subsection 4.3.1 and Equation 4.7, a general first order scaling law for for exhaust plume radiant emission is:

$$J_\lambda \sim I_{b\lambda}(T)\epsilon_\lambda A_{projected} \sim I_{b\lambda}(T)\epsilon_\lambda D^2 \tag{E.2}$$

The choice of temperature T and diameter D could be taken at any consistent and representative point in the plume. Assuming that any nozzles for these motors are designed with matched expansion and are at constant altitude such that $p_e = p_a = const.$, a convenient choice is to chose properties at the nozzle exit plane as representative of the plume, and so nozzle exit temperature T_e and nozzle exit diameter D_e can be used in Equation E.3.

Small, low thrust rocket motors are often optically thin (optical depth $\tau_\lambda \ll 1$) across relevant wavelengths, as noted in section 8.1. For the optically thin plume, $\epsilon_\lambda \sim \kappa_\lambda D_e$. Additionally, to first order, the absorption coefficient κ_λ scales like $\kappa_\lambda \sim \rho_e \sim p_e/T_e = p_a/T_e$ (see Equation 6.43), again choosing exit plane properties as representative of the exhaust plume. Plugging all of these expressions back into Equation E.3, the updated scaling law is:

$$J_\lambda \sim I_{b\lambda}(T_e)\,\frac{p_a}{T_e}\,D_e^3 \tag{E.3}$$

T_e and D_e now need to be related back to p_c and w_{om}.

T_e can be expressed using simple isentropic flow theory. Assuming $p_e = p_a = const.$:

$$T_e = T_c(w_{om})\left[\frac{p_a}{p_c}\right]^{\frac{\gamma-1}{\gamma}} \tag{E.4}$$

T_c can be expressed as a function of oxamide content and γ is approximately constant across all oxamide contents, as introduced in subsubsection 2.4.2.2.

Because it is assumed that the burn area A_b is fixed, D_e can be expressed as a function of p_c and w_{om} by rewriting D_e as follows:

$$D_e \sim A_e^{1/2} \sim \left(\frac{A_e}{A_b}\right)^{1/2} = \left(\frac{A_e}{A_t}\frac{A_t}{A_b}\right)^{1/2} \tag{E.5}$$

A_e/A_t can be found as a function of p_c/p_e and γ using the Mach-area relation (see Equation 3-25 from Ref. [2]). A_t/A_b can be found by rearranging the equilibrium chamber pressure equation for solid rocket motors given in Equation 2.6:

$$\frac{A_t}{A_b} = \rho_p \, c^*(w_{om}) \, a(w_{om}) \, p_c^{n-1} \tag{E.6}$$

where the characteristic velocity $c^*(w_{om})$ is found as a function of oxamide content using the fit given in subsubsection 2.4.2.2 and the burn rate coefficient $a(w_{om})$ is found using the burn rate law for oxamide introduced in subsubsection 2.4.2.1. Propellant solid density ρ_p and burn rate exponent n do not vary significantly with oxamide content.

Combining the above expressions, the scaling law for small, fixed burn area solid rocket motors is:

$$J_\lambda \sim I_{b\lambda}(T_e(p_c, w_{om})) \, \frac{p_a}{T_e(p_c, w_{om})} \, \left[\frac{A_e}{A_t}(p_c) \, \frac{A_t}{A_b}(p_c, w_{om})\right]^{3/2} \equiv S \tag{E.7}$$

Bibliography

[1] Frederick S. Simmons. *Rocket Exhaust Plume Phenomenology*. El Segundo, Ca: Aerospace Press, 2000. ISBN: 1-884989-08-X.

[2] George P. Sutton and Oscar Biblarz. *Rocket Propulsion Elements*. 8th ed. Hoboken, New Jersey: John Wiley & Sons, Inc., 2010. ISBN: 978-0-470-08024-5.

[3] Matthew T. Vernacchia, Kelly J. Mathesius, and R. J. Hansman. "Slow-Burn Ammonium Perchlorate Propellants with Oxamide: Burn Rate Model, Testing, and Applications". In: *Journal of Propulsion and Power* 37.5 (Sept. 2021), pp. 792–800. ISSN: 0748-4658.

[4] Matthew T. Vernacchia, Kelly J. Mathesius, and R. John Hansman. "Low-Thrust Solid Rocket Motors for Small, Fast Aircraft Propulsion: Design and Development". In: *Journal of Propulsion and Power* 38.1 (2022), pp. 122–134. ISSN: 0748-4658.

[5] Peter Sharpe. "AeroSandbox: A differentiable Framework for Aircraft Design Optimization". SM thesis. Cambridge, MA: Massachusetts Institute of Technology, 2021.

[6] Joel A. E. Andersson et al. "CasADi: a software framework for nonlinear optimization and optimal control". In: *Mathematical Programming Computation* 11.1 (Mar. 1, 2019), pp. 1–36. ISSN: 1867-2957.

[7] Andreas Wächter and Lorenz T. Biegler. "On the implementation of an interior-point filter line-search algorithm for large-scale nonlinear programming". In: *Mathematical Programming* 106.1 (Mar. 1, 2006), pp. 25–57. ISSN: 1436-4646.

[8] Atılım Gunes Baydin et al. "Automatic Differentiation in Machine Learning: a Survey". In: *Journal of Machine Learning Research* (2018), p. 43.

[9] Alain Davenas. *Solid Rocket Propulsion Technology*. New York: Pergamon Press, 1993.

[10] Philip Hill and Carl Peterson. *Mechanics and Thermodynamics of Propulsion*. 2nd ed. New York: Pearson Education, Inc., 1992.

[11] Terry McCreary. *Experimental Composite Propellant*. Murray, KY, 2014.

[12] Kelly J. Mathesius. "Manufacturing Methods for a Solid Rocket Motor Propelling a Small, Fast Flight Vehicle". MS thesis. Cambridge, Massachusetts: Massachusetts Institute of Technology, June 2019.

[13] Matthew T. Vernacchia. "Development, Modeling and Testing of a Slow-Burning Solid Rocket Propulsion System". MS thesis. Cambridge, Massachusetts: Massachusetts Institute of Technology, 2017.

[14] Matthew T. Vernacchia. "Development of Low-Thrust Solid Rocket Motors for Small, Fast Aircraft Propulsion". PhD thesis. Cambridge, Massachusetts: Massachusetts Institute of Technology, May 2020.

[15] Vishwas Govindrao Ghorpade et al. "Study of Burn Rate Suppressants in AP-Based Composite Propellants". In: *Propellants, Explosives, Pyrotechnics* 35.1 (2010), pp. 53–56. ISSN: 1521-4087.

[16] L. H. Caveny et al. *Solid Propellant Flammability Including Ignitability and Combustion Limits*. Aberdeen, MD: Ballistics Research Laboratories, Mar. 1, 1974.

[17] D. Trache et al. "Effect of Amide-Based Compounds on the Combustion Characteristics of Composite Solid Rocket Propellants". In: *Arabian Journal of Chemistry* (Dec. 12, 2015).

[18] Irvin. Glassman. *Combustion*. 4th ed. Amsterdam ; Boston : Academic Press, 2008. ISBN: 0-12-088573-5.

[19] Alexander Ponomarenko. *RPA: Tool for Liquid Propellant Rocket Engine Analysis*. Neunkirchen-Seelscheid, Germany, May 2010.

[20] B. McBride and S. Gordon. *Chemical equilibrium with applications*.

[21] David G. Goodwin et al. *Cantera: An object-oriented software toolkit for chemical kinetics, thermodynamics, and transport processes.* 2021.

[22] N. Eisenreich, H. P. Kugler, and F. Sinn. "An Optical System for Measuring the Burning Rate of Solid Propellant Strands". In: *Propellants, Explosives, Pyrotechnics* 12.3 (1987), pp. 78–80. ISSN: 1521-4087.

[23] Rm Muthaiah et al. "Rheology of HTPB Propellant: Effect of Mixing Speed and Mixing Time". In: *Defence Science Journal* 43.2 (1993). Number: 2, pp. 167–172. ISSN: 0976-464X.

[24] Luthfia H. Abdillah et al. "Effect of Mixing Time to Homogeneity of Propellant Slurry". In: *IPTEK Journal of Proceedings Series* 4.1 (Jan. 29, 2018), p. 94. ISSN: 2354-6026.

[25] John R. Howell, Robert Siegel, and M. Pinar Mengüç. *Thermal radiation heat transfer*. 5th ed. Boca Raton, Fla: CRC Press, 2011. ISBN: 978-1-4398-0533-6.

[26] M. F. (Michael F.) Modest. *Radiative heat transfer*. 2nd ed. Amsterdam ; Boston : Academic Press, 2003. ISBN: 0-12-503163-7.

[27] C. B. Ludwig et al. *Handbook of Infrared Radiation from Combustion Gases*. NASA SP-3080. NASA Marshall Space Flight Center, 1973.

[28] "Emission and Absorption of Thermal Radiation". In: *Theory and Calculation of Heat Transfer in Furnaces*. Ed. by Yanguo Zhang, Qinghai Li, and Hui Zhou. Oxford: Academic Press, 2016, pp. 45–74. ISBN: 978-0-12-800966-6.

[29] *Rotations Accompany Vibrational Transitions*. LibreTexts. May 11, 2021. URL: https://chem.libretexts.org/@go/page/2402.

[30] Chickos, Garin, and D'Souza. *Infrared Spectroscopy*. University of Missouri - St. Louis. URL: http://www.umsl.edu/~orglab/documents/IR/IR2.html (visited on 08/18/2021).

[31] Michael Richmond. *Optical Depth RIT Overview*. URL: http://spiff.rit.edu/classes/phys440/lectures/optd/optd.html (visited on 11/16/2020).

[32] I. E. Gordon et al. "The HITRAN2016 molecular spectroscopic database". In: *Journal of Quantitative Spectroscopy and Radiative Transfer* 203 (2017), pp. 3–69. ISSN: 0022-4073.

[33] Richard M. Goody. *Atmospheric radiation*. Oxford monographs on meteorology. Oxford: Clarendon Press, 1964.

[34] Jeremy Tatum. "Combination of Profiles". In: *Stellar Atmospheres*. University of Victoria, Dec. 30, 2020.

[35] Walter M. Elsasser. *Heat transfer by infrared radiation in the atmosphere*. Harvard meteorological studies ; no. 6. Milton, Mass: Harvard University, Blue Hill Meteorological Observatory, 1942.

[36] W. Malkmus. "Random Lorentz Band Model with Exponential-Tailed 1/S Line-Intensity Distribution Function". In: *JOSA* 57.3 (1967). Publisher: Optical Society of America, pp. 323–329.

[37] R. M. Goody and Y. L. Yung. *Atmospheric Radiation: Theoretical Basis*. 2nd ed. NY: Oxford University Press, 1989. 544 pp. ISBN: 978-0-19-505134-6.

[38] D. K. Edwards and W. A. Menard. "Comparison of Models for Correlation of Total Band Absorption". In: *Applied Optics* 3.5 (1964). Publisher: Optical Society of America, pp. 621–625. ISSN: 2155-3165.

[39] D. K. Edwards. "Molecular Gas Band Radiation". In: *Advances in Heat Transfer*. Ed. by Thomas F. Irvine and James P. Hartnett. Vol. 12. Elsevier, Jan. 1, 1976, pp. 115–193.

[40] Lord Rayleigh. "On the light from the sky, its polarization and colour". In: *Philosophical Magazine* 41 (1871).

[41] Gustav Mie. "Beiträge zur Optik trüber Medien, speziell kolloidaler Metallösungen". In: *Annalen der Physik* 330.3 (1908), pp. 377–445.

[42] Gustav Mie. *Contributions on the Optics of Turbid Media, Particularly Colloidal Metal Solutions - Translation*. SAND78-6018. Sandia National Laboratories, Albuquerque, New Mexico: National Translation Center, Chicago, IL, 1978.

[43] H. C. van de Hulst. *Light scattering by small particles*. Publication Title: Light scattering by small particles. New York: Dover Publications, 1981. ISBN: 0-486-64228-3.

[44] Chiao-Min Chu and Stuart W. Churchill. "Representation of the Angular Distribution of Radiation Scattered by a Spherical Particle*". In: *JOSA* 45.11 (Nov. 1, 1955). Publisher: Optical Society of America, pp. 958–962.

[45] Hsueh-chia Chang and T. T. Charalampopoulos. "Determination of the wavelength dependence of refractive indices of flame soot". In: *Proceedings of the Royal Society of London. Series A: Mathematical and Physical Sciences* 430.1880 (Sept. 8, 1990). Publisher: Royal Society, pp. 577–591.

[46] Qinglin Niu, Zhihong He, and Shikui Dong. "IR radiation characteristics of rocket exhaust plumes under varying motor operating conditions". In: *Chinese Journal of Aeronautics* 30.3 (2017), pp. 1101–1114. ISSN: 1000-9361.

[47] G. Avital et al. "Experimental and Computational Study of Infrared Emission from Underexpanded Rocket Exhaust Plumes". In: *Journal of Thermophysics and Heat Transfer* 15.4 (Oct. 2001), pp. 377–383. ISSN: 0887-8722, 1533-6808.

[48] A. Devir et al. "Comparison of calculated and measured radiation from a rocket motor plume". In: *39th Aerospace Sciences Meeting and Exhibit*. 39th Aerospace Sciences Meeting and Exhibit. Reno,NV,U.S.A.: American Institute of Aeronautics and Astronautics, Jan. 8, 2001.

[49] Weichen Wang et al. "Infrared radiation signature of exhaust plume from solid propellants with different energy characteristics". In: *Chinese Journal of Aeronautics* 26.3 (June 1, 2013), pp. 594–600. ISSN: 1000-9361.

[50] Xiaoying Zhang and Rui Li. "Numerical Study on Similarity of Plume's Infrared Radiation from Reduced Scaling Solid Rocket". In: *Journal of Applied Mathematics* 2015 (2015), pp. 1–11. ISSN: 1110-757X, 1687-0042.

[51] Robert Stowe et al. "Effect of Flight and Motor Operating Conditions on IR Signature Predictions of Rocket Exhaust Plumes". In: *International Journal of Energetic Materials and Chemical Propulsion* 14 (Jan. 1, 2015).

[52] V Rialland et al. "Infrared signature modelling of a rocket jet plume - comparison with flight measurements". In: *Journal of Physics: Conference Series* 676 (Jan. 2016), p. 012020. ISSN: 1742-6588, 1742-6596.

[53] Qinglin Niu et al. "A simplified model for fast estimating infrared thermal radiation of low-altitude under-expanded exhaust plumes". In: *International Journal of Heat and Mass Transfer* 136 (June 1, 2019), pp. 276–287. ISSN: 0017-9310.

[54] Sangmin Kim et al. "Infrared signature of NEPE, HTPB rocket plume under varying flight conditions and motor size". In: *Infrared Physics & Technology* 112 (Jan. 1, 2021), p. 103590. ISSN: 1350-4495.

[55] J. Woodroffe. "One-dimensional model for low-altitude rocket exhaust plumes". In: *13th Aerospace Sciences Meeting*. Aerospace Sciences Meetings. American Institute of Aeronautics and Astronautics, Jan. 20, 1975.

[56] *GASP*. AeroSoft. URL: `https://www.aerosoftinc.com/gasp_main.php`.

[57] Stephen J. Young. "Nonisothermal band model theory". In: *Journal of Quantitative Spectroscopy and Radiative Transfer* 18.1 (July 1, 1977), pp. 1–28. ISSN: 0022-4073.

[58] A Berk, L. S. Bernstein, and D. C. Robertson. *MODTRAN: A Moderate Resolution Model for LOWTRAN*. Section: Technical Reports. 1987.

[59] K. Franklin Evans. "The Spherical Harmonics Discrete Ordinate Method for Three-Dimensional Atmospheric Radiative Transfer". In: *Journal of the Atmospheric Sciences* 55.3 (Feb. 1, 1998). Publisher: American Meteorological Society Section: Journal of the Atmospheric Sciences, pp. 429–446. ISSN: 0022-4928, 1520-0469.

[60] Qinglin Niu et al. "Numerical analysis of point-source infrared radiation phenomena of rocket exhaust plumes at low and middle altitudes". In: *Infrared Physics & Technology* 99 (June 1, 2019), pp. 28–38. ISSN: 1350-4495.

[61] Hongxia Mao, Debin Fu, and Xingdong Bao. "Engineering Method of Predicting Rocket Exhaust Plumes at Middle and Low Altitudes". In: *Journal of Spacecraft and Rockets* 54.5 (May 25, 2017). Publisher: American Institute of Aeronautics and Astronautics, pp. 1170–1177. ISSN: 0022-4650.

[62] *Modeling Chemical Reactions*. Cantera. Sept. 26, 2022. URL: `https://cantera.org/science/kinetics.html` (visited on 11/03/2022).

[63] S. Rudman and B. A. Hibbeln. "Scaling of optically thick plume signatures". In: *2000 IEEE Aerospace Conference. Proceedings (Cat. No.00TH8484)*. 2000 IEEE Aerospace Conference. Proceedings (Cat. No.00TH8484). Vol. 3. ISSN: 1095-323X. Mar. 2000, 265–270 vol.3.

[64] F. M. Tayler and L. L. Bircumshaw. "The Thermal Decomposition of Oxamide". In: *Journal of the Chemical Society* (1956).

[65] J.W. Knowlton and E.J. Prosen. "Heat of combustion and formation of cyanogen". In: *Journal of Research of the National Bureau of Standards* 46.6 (June 1951), p. 489. ISSN: 0091-0635.

[66] *Spectral Results: Ultra Flat Black Paint*. ECOSTRESS Spectral Library. URL: `https://speclib.jpl.nasa.gov/library` (visited on 05/17/2023).

[67] *Wonderstone Technical Datasheet*. Wonderstone. URL: `http://wonderstone.co.za/wp-content/uploads/2020/04/02-Wonderstone-Technical-Datasheet-2018.pdf`.

[68] W. D. Kingery. "Factors Affecting Thermal Stress Resistance of Ceramic Materials". In: *Journal of the American Ceramic Society* 38.1 (1955), pp. 3–15. ISSN: 1551-2916.

[69] "Strength and engineering design". In: *An Introduction to the Mechanical Properties of Ceramics*. Ed. by David J. Green. Cambridge Solid State Science Series. Cambridge: Cambridge University Press, 1998, pp. 285–315. ISBN: 978-0-521-59913-9.

[70] John B. Wachtman, W. Roger Cannon, and M. John Matthewson. *Mechanical Properties of Ceramics (2nd Edition)*. 2nd ed. Publisher: John Wiley & Sons. John Wiley & Sons, 2009.

[71] Randall F Barron and Brian R Barron. "Thick-Walled Cylinders and Spheres". In: *Design for Thermal Stresses*. Hoboken, New Jersey: John Wiley & Sons, Inc., 2011, pp. 378–415. ISBN: 978-1-118-09318-4.

[72] *Aluminum Silicate (Lava) (2000°F+ Machine and Fire Ceramic)*. Foundry Service & Supplies, Inc. URL: https://www.foundryservice.com/product/aluminum-silicate-lava-2000of-machine-and-fire-ceramic/ (visited on 11/28/2022).

[73] *Lava (Grade "A")*. URL: https://www.ceramics.net/ceramic-materials-solutions/silicates/lava-grade-a (visited on 11/28/2022).

[74] *Machinable Ceramics — Aremcolox™ — Aremco*. Nov. 29, 2020. URL: https://www.aremco.com/machinable-ceramics/ (visited on 11/29/2022).

[75] Matthew Kelly. "An Introduction to Trajectory Optimization: How to Do Your Own Direct Collocation". In: *SIAM Review* 59.4 (Jan. 2017). Publisher: Society for Industrial and Applied Mathematics, pp. 849–904. ISSN: 0036-1445.

[76] Alexander Ponomarenko. *RPA: Tool for Liquid Propellant Rocket Engine Analysis C++ Implementation*. 2010.

[77] Bonnie J. McBride, Michael J. Zehe, and Sanford Gordon. *NASA Glenn Coefficients for Calculating Thermodynamic Properties of Individual Species*. NTRS Author Affiliations: NASA Glenn Research Center NTRS Report/Patent Number: NASA/TP-2002-211556 NTRS Document ID: 20020085330 NTRS Research Center: Glenn Research Center (GRC). Sept. 1, 2002.

[78] Matthew T. Vernacchia. *proptools: Rocket Propulsion Design Tools*. 2017.

[79] Peter O. Witze. "Centerline Velocity Decay of Compressible Free Jets". In: *AIAA Journal* 12.4 (1974). Publisher: American Institute of Aeronautics and Astronautics _eprint: https://doi.org/10.2514/3.49262, pp. 417–418. ISSN: 0001-1452.

[80] Tobias Ecker, Sebastian Karl, and Klaus Hannemann. "Combustion Modeling in Solid Rocket Motor Plumes". In: Proceedings of the 8th European Conference for Aeronautics and Space Sciences. Madrid, Spain, 2019, 17 pages.

[81] Matthew Newville et al. *LMFIT: Non-Linear Least-Square Minimization and Curve-Fitting for Python*. Sept. 21, 2014.

[82] A. A. Alexeenko et al. "Modeling of Flow and Radiation in the Atlas Plume". In: *Journal of Thermophysics and Heat Transfer* 16.1 (Jan. 2002), pp. 50–57. ISSN: 0887-8722, 1533-6808.

[83] K. Viswanath et al. "Investigation of Soot Combustion in Underexpanded Jet Plume Flows". In: *Journal of Thermophysics and Heat Transfer* 19.3 (July 2005). Publisher: American Institute of Aeronautics and Astronautics, pp. 282–293.

[84] Ahmed Ghoneim. “Chemical Kinetics”. In: *2.28 Combustion Notes*. 2009.

[85] H. Yoshihara. *Gasdynamics of Rocket Exhaust Plumes*. Conference Name: The Middle Ultraviolet: Its Science and Technology Pages: 269 ADS Bibcode: 1966must.conf..269Y. Jan. 1, 1966.